UNIVERSITY OF SOUTHAMPTON

FACULTY OF ENGINEERING AND THE ENVIRONMENT

Fluid Structure Interaction Group

Predicting radiated noise of marine propellers using acoustic analogies and hybrid Eulerian-Lagrangian cavitation models

by

Artur K. Lidtke

Thesis for the degree of Doctor of Philosophy

June 2017

UNIVERSITY OF SOUTHAMPTON

ABSTRACT

FACULTY OF ENGINEERING AND THE ENVIRONMENT
Fluid Structure Interaction Group

Doctor of Philosophy

PREDICTING RADIATED NOISE OF MARINE PROPELLERS USING ACOUSTIC ANALOGIES AND HYBRID EULERIAN-LAGRANGIAN CAVITATION MODELS

by Artur K. Lidtke

Anthropogenic noise from a variety of merchant ships has been reported to be a major factor adversely affecting marine organisms. Consequently, scientists and regulators have become more vocal about encouraging, and possibly enforcing, quieter ships in the future. For this to be feasible from an engineering standpoint, a range of numerical methods must be made available to allow acoustic performance of vessels to be evaluated at the design stage.

Cavitation is a major contributor to the hydroacoustic signature of a merchant vessel. The reason for this is the relatively high drop of pressure induced by the propeller, which in turn promotes the growth of vapour bubbles and cavities, oscillation and collapse of which act as strong acoustic sources. The entire process is made more dynamic by the non-uniform wake of the ship, propeller rotation, as well as the fact that vessels travel in a seaway. Because of its complexity, the problem of marine propeller noise is thus not widely studied numerically, which translates to the lack of tools readily available to designers willing to reduce the noise generated by ships.

A set of numerical utilities are proposed which could be employed at the late design stage of a merchant ship in order to allow the designer to estimate the radiated noise and make informed decisions on how to improve the design. The methodology involves solving the turbulent flow over the propeller using Detached Eddy Simulation (DES) and modelling cavitation using a mass-transfer model. The porous Ffowcs Williams-Hawkings acoustic analogy is used to infer far-field radiated noise caused by the blade rotation, pulsating cavitation, as well as non-linear noise sources in the propeller slip-stream. The cavitation model is also extended to incorporate Lagrangian bubbles dispersed downstream of the large cavities modelled using the baseline Schnerr-Sauer model via the volume fraction equation approach. This allows the broadband nature of cavitation noise to be captured.

The methods are applied to a NACA 66 and the Delft Twist 11 hydrofoil test cases. Although there are limited validation data allowing all of the methods to be validated simultaneously, relatively good agreement is seen at intermediate validation stages. These include comparing the non-cavitating noise of the Insean E779a propeller to reference data, conducting acoustic predictions for idealised acoustic sources, as well as comparing cavitation patterns, cavity cloud shedding frequencies, and induced pressures to experimental data for hydrofoils and propellers.

It is concluded that the presented methodology may be used to predict low-frequency noise due to cavitation in a relatively robust manner, although the method is yet to be tested and validated on more complex geometries. The hybrid Eulerian-Lagrangian model is still at an early stage and a range of areas for improvement have been identified, such as implementation of more realistic cavity break-up models as well as better coupling between the fluid and bubble solvers. Nonetheless, the method is demonstrated to be a promising tool at tackling the broadband cavitation noise components as it can capture the contribution of the mass of small, oscillating bubbles on the radiated pressure which would otherwise be unaccounted for in the baseline Eulerian framework.

Contents

Contents ix

List of Figures xiii

List of Tables xv

Declaration of Authorship xv

Acknowledgements xvii

Nomenclature xix

1 Introduction 1
- 1.1 Motivation . . . 1
- 1.2 Aims & Objectives . . . 3
- 1.3 Structure of the thesis . . . 5

2 Marine Propeller Noise 7
- 2.1 Introduction . . . 7
- 2.2 The noise problem . . . 7
  - 2.2.1 Underlying physics . . . 7
  - 2.2.2 Shipping noise . . . 10
- 2.3 Turbulence . . . 12
  - 2.3.1 Physics and Origin of Turbulence . . . 12
  - 2.3.2 Turbulence in Marine Propeller Context . . . 13
  - 2.3.3 Noise due to turbulence . . . 14
- 2.4 Cavitation . . . 16
  - 2.4.1 Physics and Origin of Cavitation . . . 16
  - 2.4.2 Cavitation on marine propellers . . . 17
  - 2.4.3 Cavitation noise . . . 21
  - 2.4.4 Cavitation and turbulence . . . 23
- 2.5 Review of relevant published work . . . 23
  - 2.5.1 Experimental measurements . . . 24
  - 2.5.2 Simulating cavitation . . . 25
  - 2.5.3 Simulating marine propeller noise . . . 30
- 2.6 Modelling challenges . . . 34
- 2.7 Summary . . . 37

3 Methodology **39**
3.1 Introduction . . . 39
3.2 The OpenFOAM framework . . . 39
3.3 Flow motion and the finite volume method . . . 40
3.3.1 Governing equations . . . 40
3.3.2 The finite volume method . . . 41
3.3.3 Numerical schemes . . . 42
3.3.4 Linearised equation solution . . . 43
3.3.5 Pressure-velocity coupling . . . 44
3.4 Reynolds Averaged Navier-Stokes equations . . . 44
3.4.1 Overview . . . 44
3.4.2 Averaging of the Navier-Stokes equations . . . 45
3.5 Large and Detached Eddy Simulation . . . 46
3.5.1 Overview . . . 46
3.5.2 Filtering of the Navier-Stokes equations . . . 47
3.5.3 Boundary Treatment . . . 49
3.5.4 Detached Eddy Simulation . . . 50
3.6 Multiphase flow modelling . . . 51
3.6.1 Overview of available methods . . . 51
3.6.2 The volume of fluid approach . . . 53
3.6.3 Mass transfer cavitation models . . . 54
3.6.4 Schnerr-Sauer cavitation model . . . 56
3.6.5 Aspects of post-processing . . . 57
3.7 Summary . . . 58

4 Propeller modelling **59**
4.1 Introduction . . . 59
4.2 Background to the Podsdam Propeller Test case (PPTC) . . . 59
4.3 Simulation set-up . . . 60
4.4 Results . . . 62
4.5 Discussion . . . 63
4.6 Summary . . . 65

5 Acoustic modelling of marine propeller noise **67**
5.1 Introduction . . . 67
5.2 Review of Numerical Acoustic Methods . . . 67
5.2.1 Governing equations of sound . . . 67
5.2.2 Computational Approaches to Acoustics . . . 69
5.2.3 Selection of a suitable acoustic method . . . 71
5.3 Ffowcs Williams-Hawkings acoustic analogy . . . 72
5.4 Present implementation of the acoustic analogy . . . 75
5.4.1 Practical considerations . . . 75
5.4.2 Implementation Strategy . . . 75
5.4.3 Analytical acoustic sources . . . 79
5.5 Acoustic analogy verification and validation . . . 80
5.5.1 Basic validation . . . 80
5.5.2 Sensitivity Studies . . . 83

5.6 Application to the Insean E779a propeller . . . 88
5.6.1 Aims of this study . . . 88
5.6.2 Background . . . 90
5.6.3 Simulation set-up . . . 90
5.6.4 Results . . . 92
5.6.5 Discussion . . . 98
5.7 Summary . . . 102

6 Cavitation modelling 105
6.1 Introduction . . . 105
6.2 Background to the Delft Twist 11 hydrofoil . . . 106
6.3 Simulation set-up . . . 107
6.4 Results - NACA 0009 . . . 110
6.5 Discussion - NACA 0009 . . . 112
6.6 Results - Delft Twist 11 . . . 114
6.7 Discussion - Delft Twist 11 . . . 117
6.8 Summary . . . 123

7 Application of the FW-H analogy to a NACA 0009 foil 125
7.1 Introduction . . . 125
7.2 Simulation set-up . . . 126
7.2.1 General simulation parameters . . . 126
7.2.2 Span-wise domain size . . . 127
7.2.3 Acoustic analogy set up . . . 128
7.3 Results . . . 130
7.3.1 Identification of primary source mechanisms . . . 130
7.3.2 Effect of FW-H control surface choice . . . 133
7.3.3 Sound source identification . . . 136
7.3.4 Sound field characterisation . . . 138
7.4 Discussion . . . 140
7.5 Summary . . . 145

8 Modelling pressures induced by a cavitating NACA 66 foil 147
8.1 Introduction . . . 147
8.2 Background . . . 148
8.3 Simulation set-up . . . 148
8.4 Results . . . 151
8.4.1 Capturing different cavitation regimes . . . 151
8.4.2 Flow details for dynamics 1 . . . 153
8.4.3 Cavitation induced pressures for dynamics 1 . . . 155
8.4.4 Acoustic analysis for dynamics 1 . . . 156
8.5 Discussion . . . 157
8.6 Summary . . . 161

9 Multi-scale cavitation modelling 163
9.1 Introduction . . . 163
9.2 Theory behind mixed Eulerian-Lagrangian modelling . . . 164
9.2.1 Bubble motion . . . 164

9.2.2 Eulerian cavity reconstruction . . . 166
9.2.3 Bubble transfer between Eulerian and Lagrangian frames . . . 168
9.3 Present implementation . . . 171
9.3.1 Implementation strategy . . . 171
9.3.2 Code organisation . . . 171
9.4 Verification . . . 172
9.5 Application to the Delft Twist 11 hydrofoil . . . 174
9.5.1 Aims of this study . . . 174
9.5.2 Simulation set-up . . . 174
9.5.3 Results . . . 176
9.5.4 Discussion . . . 180
9.6 Summary . . . 182

10 Conclusions and future work **183**
10.1 Conclusions . . . 183
10.2 Review of scientific contributions . . . 185
10.3 Future work . . . 187

A Schnerr-Sauer model derivation **191**

B Ffowcs Williams-Hawkings acoustic analogy derivation **195**

References **201**

List of Figures

1.1 Knudsen ambient noise spectrum 2

2.1 Examples of idealised acoustic noise sources 9
2.2 An example Kolmogorov spectrum 13
2.3 Schematic illustration of noise sources on an airfoil moving through fluid . 16
2.4 Schematic illustration of types of cavitation on a hydrofoil 19

3.1 Principle of the finite volume method 41

4.1 View of the Potsdam Propeller Test Case (PPTC) 60
4.2 Predicted non-cavitating force coefficients for the PPTC propeller 62
4.3 Cavitation pattern predicted for the PPTC case 2.3.1 63

5.1 Illustration of the principle of how the FW-H integrals get solved 73
5.2 Illustration of the retarded time concept 77
5.3 Workflow of the key steps of the FW-H stand-alone utility 78
5.4 Analytical and computed pressure time derivatives for a monopole 81
5.5 Time signal of pressure induced by a monopole showing the effect of redarted time 82
5.6 Breakdown of a pressure signal induced by a monopole showing contributions of different terms of the FW-H equation 82
5.7 Breakdown of a pressure signal induced by a dipole showing contributions of different terms of the FW-H equation 83
5.8 The effect of sampling rate on the FW-H prediction accuracy 84
5.9 The effect of mesh density relative to wavelength on the FW-H prediction accuracy 85
5.10 The effect of distance between the control surface and the source on FW-H result 86
5.11 Effect of source frequency on the relative magnitude of FW-H terms . . . 87
5.12 Effect of receiver distance on the relative magnitude of FW-H terms . . . 88
5.13 The effect of axial length of an open-ended control surface on dipole directivity predicted using FW-H 89
5.14 View of the Insean E779a propeller blade 90
5.15 Locations of receivers used in the E779a study 92
5.16 Mean force coefficients predicted for the Insean E779a propeller 93
5.17 Instantaneous pressure coefficient contours for the E779a 94
5.18 Iso-contours of vorticity around the E779a propeller 94
5.19 Flow field comparison for E779a between OpenFOAM and ReFRESCO . 95
5.20 Predicted pressure signal for E779a at the propeller plane 96

5.21 Blade harmonics of pressure signals for E779a at the propeller plane . . . 97
5.22 Influence of closing the FW-H control surface for the E779a study, receiver 27 . . . 98
5.23 The effect of closing the FW-H control surface for a downstream receiver for E779a . . . 99
5.24 Distribution of the pseudo-thickness FW-H term on the two control surfaces used for E779a . . . 100

6.1 Overview of the Delft Twist 11 hydrofoil geometry . . . 106
6.2 Overview of numerical domains for the Delft Twist 11 hydrofoil and initial NACA 0009 studies . . . 109
6.3 Details of the computational mesh used to simulate the Delft Twist 11 hydrofoil . . . 110
6.4 Time history snapshots of total cavitation volume predicted for the 2D NACA 0009 hydrofoil . . . 111
6.5 Instantaneous vapour fraction contours for RANS and LES NACA 0009 simulations at the time when a new cavity sheet starts to develop . . . 112
6.6 Instantaneous iso-contours of vapour fraction and vorticity magnitude for explicit and implicit LES for the NACA 0009 case . . . 113
6.7 Grid convergence of the Delft Twist 11 hydrofoil steady-state, non-cavitating simulation . . . 116
6.8 Non-cavitating surface pressure coefficient on the Delft Twist 11 hydrofoil compared to the experimental measurements . . . 117
6.9 Mean surface pressure and volume fraction at the mid-span of the Delft Twist 11 hydrofoil . . . 118
6.10 Mean value and standard deviation of the volume fraction at stations along the Delft Twist 11 hydrofoil . . . 119
6.11 Time history of volume fraction at a station at x/c 0.15 from the leading edge of the Delft Twist 11 hydrofoil sampled at mid-span . . . 119
6.12 Instantaneous iso-contours of vapour fraction compared to the experimental cavitation observations on the Delft Twist 11 hydrofoil . . . 120
6.13 Time histories of total cavity volume and lift coefficient on the Delft Twist 11 hydrofoil . . . 121
6.14 Power spectral density functions of total cavity volume and lift coefficient on the Delft Twist 11 hydrofoil . . . 122

7.1 Overview of the C-grid topology used to simulate the NACA 0009 foil for acoustic analysis . . . 126
7.2 Positions of the receivers and FW-H surfaces used in the NACA 0009 noise study . . . 129
7.3 Characteristic sheet and cloud cavitation pattern on the NACA 0009 hydrofoil . . . 130
7.4 Effect of cavitation sheet and clouds on the stream-wise velocity over the NACA 0009 foil . . . 131
7.5 Time-averaged pressure coefficient distribution at mid-span of the foil surface, also showing the standard deviation, σ, at each location along the chord. . . . 132
7.6 Distribution of the mean and standard deviation of the volume fraction on the upper surface of the foil, sampled at mid-span. . . . 132

7.7 Power spectral density of the local pressure coefficient on the upper surface of the foil at x/c=0.08, 0.25, 0.55, and 0.95, sampled at mid-span. . . 133
7.8 Source-time derivative of the total cavity volume time trace for the NACA 0009 foil . . . 134
7.9 Power spectral density function of the time derivative of the total cavity volume for the NACA 0009 foil . . . 134
7.10 Breakdown of the sound pressure level for two receivers above and downstream of the NACA 0009 foil . . . 136
7.11 Time trace of the pseudo-thickness and pseudo-loading FW-H terms for a receiver above the NACA 0009 foil . . . 137
7.12 Distribution of the derivative part of the pseudo-loading FW-H term for a receiver downstream of the NACA 0009 foil . . . 137
7.13 Time history of pressure predicted above the NACA0009 foil shown in the source time . . . 138
7.14 Snapshots showing pressures induced on the NACA 0009 foil during cavity collapse . . . 141
7.15 Time trace of the total cavity volume predicted over the NACA 0009 . . . 141
7.16 Pressure time histories predicted at different receivers around the NACA 0009 foil . . . 142
7.17 Change of sound pressure levels above the NACA 0009 foil with receiver distance . . . 143
7.18 Comparison of the peak sound pressure levels above the NACA 0009 with an ideal monopole source . . . 143

8.1 FW-H integration surface and mesh used for the NACA 66 foil case . . . 150
8.2 Total cavity volume traces and spectral characteristics for NACA 66 across a range of conditions . . . 151
8.3 Snapshots of the experimental and computational cavity extents for NACA 66 - cavitation dynamics 1 . . . 153
8.4 Snapshots of the cavity extents for NACA 66 - cavitation dynamics 2 . . . 154
8.5 Time history of L/D ratio for the dynamics 1 NACA 66 simulation . . . 155
8.6 Surface distribution of mean flow quantities for the NACA 66 dynamics 1 case . . . 156
8.7 Local surface pressure time history on the NACA 66 foil compared to experimental data . . . 157
8.8 Time histories of local pressure on the suction of the NACA 66 foil . . . 158
8.9 Time series of pressure and second derivative of the total cavity volume upstream of the NACA 66 . . . 159
8.10 Comparison of the FW-H and direct pressures induced by cavitation in front of the NACA 66 (dynamics 1) . . . 159
8.11 FW-H predictions for a monopole source and its reflections . . . 160
8.12 Illustration showing the effect of nearby solid walls on an acoustic source . 160

9.1 Principle of operation of the cavity reconstruction algorithm . . . 167
9.2 Parallel data exchange strategy for the cavity reconstruction algorithm . . 169
9.3 Example result of the interface reconstruction algorithm . . . 170
9.4 Time histories of bubbles used for validation of the Rayleigh-Plesset equation solver . . . 175

9.5 Positions of bubbles over a backward facing step used for validation of the Lagrangian motion solver . . . 176
9.6 Time series of wall pressure induced by cavitation around the Delft Twist 11 foil . . . 176
9.7 PSD of wall pressures around the Delft Twist 11 hydrofoil . . . 177
9.8 Comparison of the cavitation pattern on Delft Twist 11 foil between experiment and hybrid cavitation model . . . 178
9.9 Detailed view of cavitation patterns predicted by the hybrid cavitaiton model for the Delft Twist 11 foil . . . 179
9.10 Wall pressures predicted for the Delft Twist 11 foil with the hybrid cavitation model . . . 180
9.11 PSD of wall pressures predicted for the Delft Twist 11 foil with the hybrid cavitation model . . . 180
9.12 Example time history of position and radius of a Lagrangian bubble flowing over the Delft 11 foil . . . 181

List of Tables

2.1 Dominant noise sources for a commercial ship 11

4.1 Parameters of the VP1304 (PPTC) propeller 60
4.2 Fluid properties and cavitation model constants used for the VP1304 (PPTC) propeller 61

5.1 Particulars of the Insean E779a propeller 91
5.2 Receiver locations for the Insean E779a propeller study 92
5.3 Comparison of the mean propulsive coefficients for the E779a case 93

6.1 Summary of conditions used to simulate the Delft Twist 11 hydrofoil . . . 107

7.1 Locations of receivers used for the NACA 0009 acoustic analogy study . . 129
7.2 Convergence of the mean and standard deviation of the lift coefficient for the NACA 0009 foil 130

8.1 Flow conditions for the NACA 66 simulations 150

9.1 Parameters describing idealised bubble simulations used to test the Rayleigh-Plesset equation solver 173

Declaration of Authorship

I, Artur K. Lidtke , declare that the thesis entitled *Predicting radiated noise of marine propellers using acoustic analogies and hybrid Eulerian-Lagrangian cavitation models* and the work presented in the thesis are both my own, and have been generated by me as the result of my own original research. I confirm that:

- this work was done wholly or mainly while in candidature for a research degree at this University;
- where any part of this thesis has previously been submitted for a degree or any other qualification at this University or any other institution, this has been clearly stated;
- where I have consulted the published work of others, this is always clearly attributed;
- where I have quoted from the work of others, the source is always given. With the exception of such quotations, this thesis is entirely my own work;
- I have acknowledged all main sources of help;
- where the thesis is based on work done by myself jointly with others, I have made clear exactly what was done by others and what I have contributed myself;
- parts of this work have been published as: [119], [120],[121],[122] [124],[125],[126],[133]

Signed:.....

Date:.....

Acknowledgements

First of all, I would like to thank my supervisors, Professor Stephen Turnock and Professor Victor Humphrey, for their involvement in my work and their priceless input. They helped to shape me academically and professionally, but also shared many of my joys and sorrows over the several years it took me to complete this thesis.

Also, many thanks to Dr Thomas P. Lloyd from MARIN, the Netherlands, for his support in learning OpenFOAM at the beginning of this project and countless consultations on the topics of hydroacoustics and the secrets to completing a PhD. He also provided me with the Insean E779a propeller geometry and computational grids, as well as helped shape the part of the thesis which concerns it.

I would furthermore like to thank my parents, who have always encouraged me to pursue my interests and education. Without their support none of this would have been possible. Great thanks also go to my partner Agnieszka, my brother Alek, and all my friends and colleagues at the University, who have made my time here a much more pleasant and enriching experience.

Finally, I would also like to acknowledge the use of the OpenFOAM open-source CFD package and the IRIDIS High Performance Computing Facility, and associated support services at the University of Southampton, that enabled the completion of this work.

Nomenclature

Symbols

α	fluid volume fraction	$[-]$
α_{TH}	threshold value of the volume fraction	$[-]$
c	chord length	$[m]$
c_0	sound speed in a medium	$[ms^{-1}]$
C_L	lift coefficient	$[-]$
C_D	drag coefficient	$[-]$
C_m	pitch moment coefficient	$[-]$
C_P	pressure coefficient	$[-]$
D	propeller diameter	$[m]$
η_0	open water efficiency	$[-]$
F	pressure induced by an arbitrary sound source	$[Pa]$
J	advance coefficient of a propeller	$[-]$
K_T	thrust coefficient	$[-]$
K_Q	torque coefficient	$[-]$
λ	wavelength	$[m]$
L	reference length scale	$[m]$
μ	dynamic viscosity	$[kgs^{-1}m^{-1}]$
Ma	Mach number	$[-]$
ν	kinematic viscosity of the fluid	$[m^2s^{-1}]$
n	revolutions per second of a propeller	$[s^{-1}]$
n_0	number of cavitation bubbles per unit volume	$[m^{-3}]$
$\hat{\mathbf{n}}$	unit normal vector	$[-]$
ω	vorticity	$[s^{-1}]$
p	local pressure of the liquid	$[Pa]$
p_v	saturated vapour pressure	$[Pa]$
p_∞	reference pressure value	$[Pa]$
Q	propeller torque	$[Nm]$
ρ	fluid density	$[kgm^{-3}]$
$\mathbf{r}$	radiation vector	$[m]$
R	bubble radius	$[m]$
R_0	equilibrium bubble radius	$[m]$

Re	Reynolds number	$[-]$
σ	cavitation number	$[-]$
σ_{ST}	surface tension	$[kgm^{-2}]$
s	span	$[m]$
t	receiver time	$[s]$
τ	source time	$[s]$
T	propeller thrust	$[N]$
$\mathbf{U}$	velocity vector	$[ms^{-1}]$
u_i	component of the velocity vector in tensor notation	$[ms^{-1}]$
$\mathbf{U}_B$	velocity vector of a bubble	$[ms^{-1}]$
U_∞	reference velocity scale	$[ms^{-1}]$
V	total volume of cavitation in the numerical domain	$[m^{-3}]$
V_a	advance velocity of a propeller	$[ms^{-1}]$
$\mathbf{x}$	position of a receiver in a Cartesian frame	$[m]$
x^+	non-dimensional cell spacing along the chord	$[-]$
$\mathbf{y}$	sound source position in a Cartesian frame	$[m]$
y^+	non-dimensional wall-normal distance (inner scaling)	$[-]$
z^+	non-dimensional cell spacing along the span	$[-]$

Operators

$\overline{\mathbb{D}}^2$	the D'Alembert operator $= \left(\frac{1}{c_0^2}\frac{1}{\partial t^2} - \nabla^2\right)$
$dB\,re\,1\mu Pa$	sound level defined with respect to a $1\,\mu Pa$ reference

Abbreviations

AQUO	Achieving Quiet Oceans
CFD	Computational Fluid Dynamics
DES	Detached Eddy Simulation
DNS	Direct Numerical Simulation
EU	European Union
FW-H	Ffowcs Williams-Hawkings acoustic analogy
ILES	implicit Large Eddy Simulation
LES	Large Eddy Simulation
PDS	porous data surface
PPTC	Potsdam Propeller Test Case
PSD	power spectral density function
RANS	Reynolds Averaged Navier-Stokes
SONIC	Suppression Of underwater Noise Induced by Cavitation
SPL	sound pressure level
R/V	Research vessel

Chapter 1

Introduction

1.1 Motivation

In recent years, the interest in limiting the input of energy and, in particular, noise into the oceans has increased. This resulted in, amongst others, European Union initiatives investigating the potential at reducing this component of human impact on the environment [54, 55, 189, 197]. While of course there are multiple sources of noise in the Oceans, natural and anthropogenic alike, shipping as a whole contributes to a large proportion of the total ambient sound level, particularly in the 10-1000 Hz frequency range [75, 194] (see Figure 1.1). Although certain aspects of this problem are understood it is, in general, an open field with multiple questions remaining unanswered. It has been recognised, however, that the elevated noise levels induced by shipping have multiple adverse effects on marine life [203]. As a result, the marine scientific community needs to and recently has been paying more attention to the noise problem in order to limit the harm to the crew and increase their comfort, but also to reduce the impact on the environment [91]. This has direct implications for designers and operators of ships and has therefore sparked a debate on whether the current regulations need to be amended or extended in any way [106].

Merchant ships are expected to be one of the largest contributors to the overall shipping noise as their propulsion requires a significant amount of power to pass through the relatively confined region of a propeller disc. The resulting high power density associated with operating the propeller close to its optimum efficiency induces a local pressure drop and causes an enhanced risk of cavitation [12, 94, 104, 177]. Severity of cavitation therefore increases with the speed of the vessel, as sailing faster generally requires the propeller to generate more momentum, and thus induce a stronger pressure difference across the propeller disc [203]. The wake flow developed along the ship, in which the propeller must operate at all times, produces a large boundary layer region which contains unsteady turbulent flow. The combined risk of cavitation and unsteady inflow result in

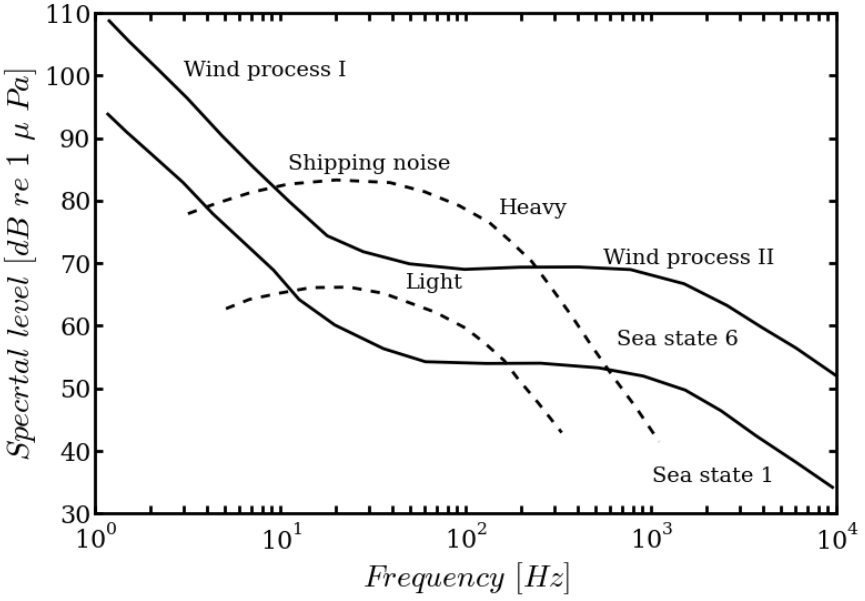

Figure 1.1: Knudsen spectrum of ambient noise in the Oceans (reproduced from data by Urik [194]; originally deduced from noise measurements at different locations world-wide at various depths).

the potential for significant underwater noise. Out of the multiple noise sources present in the ship-propeller system, the low-frequency cavitation noise is of primary concern from an environmental impact point of view [17, 203]. That is because it propagates at large distances due to high power and low attenuation and is typically in the frequency band many organisms are capable of hearing [136].

Currently, one of the primary means of assessing the radiated noise of a ship is full-scale testing, or sea trials. This involves placing an array of hydrophones at a remote location with low ambient noise and favourable noise propagation conditions, such as an apt water depth and seabed type, and recording the noise from a passing ship. This, while shown to be feasible from an academic and environmental assessment standpoint [4, 29, 144], would be far too expensive and difficult if, for instance, regulation requiring the noise from each newly built ship to be assessed were to be introduced.

An alternative to this approach is the use of model-scale testing in facilities like cavitation tunnels or de-pressurised towing tanks. This method is significantly cheaper and more available than full scale testing, but still only affordable enough in a limited number of cases. The difficulty here is also finding an appropriate method of scaling the near-field measurements to full scale and deducing the correct far-field noise level from them [17].

Due to the limitations of the experimental methods, making trade-offs and performing optimisation, or at least sensitivity studies, of the radiated noise against propulsive performance is an expensive and challenging endeavour. These limitations also pose a

major obstacle to truly understanding the commercial shipping noise and being able to conclude whether an action is required of the maritime community in order to reduce the environmental impact in this respect.

Fortunately, this gap in the understanding of the problem may be overcome using numerical analysis tools, as acknowledged in the recent IMO guidelines for the reduction of underwater noise from commercial shipping [94]. For example, Ianniello *et al.* [92] investigated the noise induced by a full scale ship in non-cavitating conditions using a porous Ffowcs Williams-Hawkings (FW-H) analogy coupled with a RANS solver. Furthermore, more recent work by Bensow *et al.* [15] adopted similar acoustic techniques to study the noise induced by turbulence and cavitation on a research vessel. Pan & Zhang [155] studied the non-cavitating noise for the DTMB 4118 propeller in non-uniform inflow conditions using FW-H analogy evaluated on the propeller blade and a Detached Eddy Simulation (DES) flow solver. Studies by Seol et al. [177] and Salvatore & Ianniello [169] both described using a potential flow solver and a semi-empirical sheet cavitation model with the FW-H analogy evaluated on the blade surface to compute the noise of a propeller in cavitating and non-cavitating conditions. Additionally, work by Lloyd [136] saw the use of Large Eddy Simulation (LES) with an inflow turbulence model to evaluate the broadband noise signature of a tidal turbine from an environmental impact point of view. This shows that there is a growing interest in the use of advanced acoustic methods, such as acoustic analogies, in the marine and maritime contexts. An important observation is, however, that until very recently only relatively simple flow modelling techniques were being employed and that few recent studies have concerned themselves with modelling cavitation noise. This has guided the focus of the thesis on bringing in established acoustic approaches, cavitation modelling methods, and turbulence simulation techniques in order to deduce the noise of marine propellers.

1.2 Aims & Objectives

The main aim of this work was to numerically study the multi-scale nature of marine propeller noise associated with low-frequency components, for instance due to sheet cavitation and non-uniform inflow, occurring around the blade passage, typically between 10 and 50 Hz for large merchant vessels [17]. The broadband noise components above several hundred Hertz, occuring due to turbulence and small-scale bubbles, are also addressed. Including the latter in the analysis is viewed as the next step in accurate propeller noise prediction, as methods for predicting the large-scale phenomena do exist but generally fail to account for the more intricate flow features.

In order to address these questions the work presented here aims to establish a computational framework for marine propeller noise prediction which will:

- provide more insight into the nature of noise generating mechanisms, particularly the relative magnitude of the broadband and low-frequency noise sources;
- enable far-field noise signature of an arbitrary propeller to be evaluated, allowing optimisation and trade-off studies to be performed in the future;
- help in bridging the gap between the model- and full-scale measurements by providing a third, alternative source of data which may be compared against the former two;
- provide a partial answer to the fundamental question of whether the marine community should take immediate steps in remedying the effects of shipborne noise on the environment.

In order to achieve the above the following objectives were set at the beginning of the project

- Compare the available cavitation models and assess their usefulness in terms of propulsive performance and noise prediction.
- Assess how applicable acoustic analogy noise prediction methods are to the problem at hand.
- Explore available alternatives to the aforementioned method and select the most suitable approach.
- Implement the chosen acoustic prediction method in the OpenFOAM framework.
- Perform validation and sensitivity studies of the acoustic utility, highlighting any limitations and/or problems that need to be resolved in the future.
- Combine the cavitation model and acoustic analogy in application to a simple test case, such as a vortex generator or a hydrofoil, to gain first-hand experience in using it, perform further validation and exploration of the limits of applicability of the chosen method.
- Implement a framework for predicting high-frequency, broadband, noise of a marine propeller due to turbulence and cavitation in order to simulate cavitation tunnel conditions more closely.
- Summarise the work, comment on any drawbacks and problems, suggesting future improvements and research questions which will remain open at the end of the project.

1.3 Structure of the thesis

In the remaining part of this thesis, Chapter 2 first gives a background to the propeller noise problem. Overview of how shipping affects the marine environment through noise pollution is first given. The chapter then explains where both turbulence and cavitation originate from in a ship propulsion system, what are the key underlying physical processes associated, and how both of the phenomena may act as noise sources. A review of the published work aiming to tackle these problems is also given, which is summarised by an outline of the largest challenges at the front of numerical modelling of marine propeller noise.

Chapter 3 builds up on the introduced physics and discusses numerical means of modelling them. An outline is given of how cavitation and flow in general may be solved numerically. Focus is put on discussing various alternative techniques and their relative advantages and disadvantages, paving the way to a discussion of how these relate to the modelling challenges involved in predicting marine propeller noise. This is then used to justify the choice of methodology used throughout this work.

Subsequent Chapters 4 and 5 demonstrate how the introduced methodology may be used to solve practical flows around propellers. A review of the methods available to deduce far-field pressure fluctuations is also given, which concludes with the selection of the porous Ffowcs Williams-Hawkings acoustic analogy for the purpose of carrying out acoustic predictions throughout this thesis. The mathematical formulation of the analogy and its codified representation are first described, followed by a series of sensitivity studies using analytical noise sources. Results for a rotating propeller are then given and discussed with the focus on the low-frequency non-cavitating noise, as well as highlighting potential limitations of the acoustic analogy.

In the following Chapter 6, a more in-depth analysis of the applicability of the selected mass transfer cavitation model to the problem of cavitation noise modelling is presented. The results cover the concepts of using advanced turbulence modelling techniques, such as LES and DES, to solve flows over the Delft Twist 11 and NACA 0009 hydrofoils subject to significant amounts of highly unsteady cavitation. The data serve to further validate the proposed methodology and show that it can potentially be used in conjunction with the developed acoustic analogy. This is then carried out and is described in Chapter 7 in application to the NACA 0009 hydrofoil. The study indicates the dependence of the radiated noise on the second derivative of the volume of oscillating cavities as well as shows the monopole nature of the associated dominant noise source.

The following Chapter 8 is concerned with further validating the developed methodology using published experimental data for a NACA 66 foil, which is also far more representative of real propeller blade sections that a 4-digit NACA profile. The Chapter also

aims to apply the FW-H methodology in a small numerical domain representative of a cavitation tunnel environment to comment on its applicability in such scenarios.

The drawback of the acoustic analogy method and the selected cavitation model is their inability to account for the broadband noise due to small bubbles present in the flow. Chapter 9 explores the theory behind and the implementation of a hybrid Eulerian-Lagrangian cavitation model developed with the aim of providing a fuller description of the entire sound spectrum generated by cavitation. The chapter closes with qualitative validation of the model based on simple test cases, as well as application to the Delft Twist 11 foil.

Chapter 2

Marine Propeller Noise

2.1 Introduction

Before discussing the details of the numerical approaches adopted in this work in order to model cavitating marine propeller noise, it is important to first introduce the complicated physics that govern this issue. In this Chapter, the fundamental principles of noise propagation are first highlighted and put in the context of shipping. Subsequently, the phenomena of turbulence and cavitation, which are the two main culprits contributing to ship-induced noise, are briefly described with noise generation in mind. A brief review of numerical and experimental work by other authors aimed at tackling the marine propeller noise problem is given. This is summarised in order to point out the main modelling challenges still persistent in the field and thus indicating the possible paths for computational method development to be undertaken in the following chapters.

2.2 The noise problem

2.2.1 Underlying physics

Sound is a mechanism of energy transfer through a medium via propagating pressure, density and velocity fluctuations. These oscillations are of small amplitude compared to the state of rest of the fluid [43]. Motions of fluid particles associated with acoustic disturbances are governed by the same laws as any other fluid motion, namely the compressible Navier-Stokes and continuity equations. For acoustic wave propagation it is conventional to neglect the effects of viscosity and linearise the momentum conservation equations by assuming $p = c_0^2 \rho$, where p is the local pressure, c_0 is the speed of sound in the considered medium, and ρ is its density. This allows the inhomogeneous wave

equation to be written,

$$c_0^2 \left(\frac{1}{c_0^2} \frac{1}{\partial t^2} - \nabla^2 \right) \rho' = c_0^2 \overline{\mathbb{D}}^2 \rho' = F(\mathbf{y}, t), \tag{2.1}$$

where $\overline{\mathbb{D}}^2$ is the D'Alembert operator and ρ' is the instantaneous density fluctuation constituting a sound wave [43]. This formulation describes the propagation of sound due to an arbitrary source, $F(\mathbf{y}, t)$, whose acoustic contribution tends to zero in the far field. It should also be noted that the source is located at a position $\mathbf{y}$ and any disturbance it produces will arrive at the receiver at $\mathbf{x}$ after a finite amount of time equal to the ratio of the source-receiver distance and the speed of sound, possibly creating a phase difference in the excitation and perceived signals.

The simplest idealised noise source is the monopole, which generates pressure waves radiating equally in all directions [77]. Physically, this may be imagined to be a sphere expanding and shrinking in an oscillatory manner, periodically pushing the fluid away from and attracting it towards the centre of the sphere. Higher order sources can also be constructed by taking spatial derivatives of the monopole. The first order derivative yields a dipole and the second order derivative describes a quadrupole [77]. All of these provide valid solutions to the inhomogeneous wave equation, Eq. (5.4). It is useful to visualise the behaviour of acoustic sources by examining the pressure waves they produce, as shown in Figure 2.1. It may be seen that higher order sources behave as superpositions of multiple out-of-phase monopoles placed a fixed distance apart, and as such exhibit directional behaviour.

In practice, different types of acoustic sources often present themselves as one of or a combination of the idealised sources. For example, periodic cavitation occurring on a propeller may be seen as an oscillating volume pushing the fluid away and attracting it back, and hence tends to act as a monopole source [156, 177]. Free, isentropic turbulence on the other hand tends to produce noise which is quadrupole in nature [128].

How much noise a sound source will produce depends on its strength, which will dictate the amplitude of pressure waves created. Another factor is the distance to the receiver, which affects the geometric spreading of the wave energy as it travels further from the source. Furthermore, absorption of the acoustic energy by the medium leads to damping of the sound waves away from the source [141]. The foremost is dictated by the physical phenomena causing the sound, such as the amount of cavitation or turbulence intensity. Spreading of acoustic energy typically follows the spherical model. This means that as the source-receiver distance increases, the corresponding acoustic intensity decays proportionally to the increase in the area of a sphere centred at the source and with a radius extending to the receiver. The absorption loss is tied to the dissipation of fluid particle motions and its magnitude depends on the fluid properties [141]. Understanding these basic behaviours is key to appreciating how different aspects of the complex flow

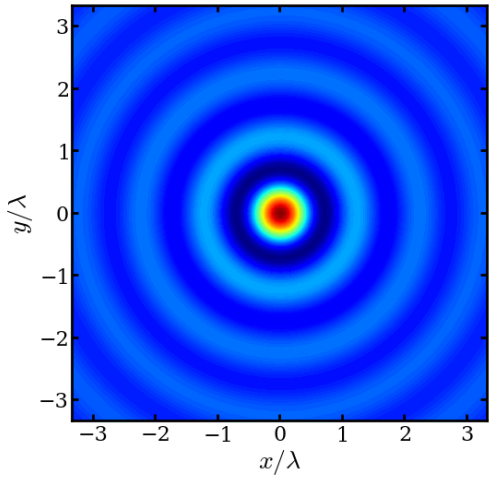

(a) Monopole

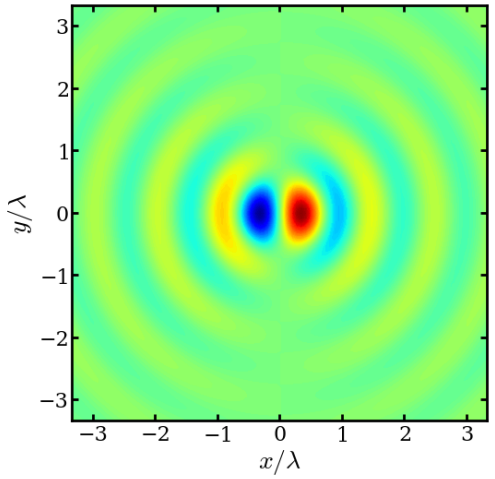

(b) Dipole

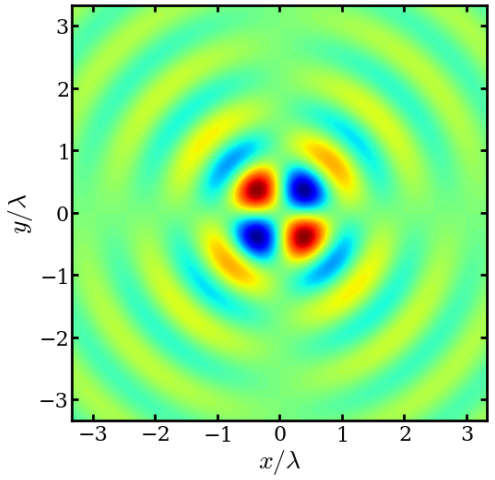

(c) Quadrupole

Figure 2.1: Examples of idealised acoustic noise sources showing pressure iso-contours non-dimensionalised using maximum values over a 2D plane shown as a function of wavelength, λ.

environment generated by a propeller-driven ship moving through a seaway contribute to the vessel's overall noise signature.

2.2.2 Shipping noise

The ultimate aim of the present work is to aid in developing realistic design tools and standards of ship design promoting efficiency and responsible environmental practices. It is therefore important to highlight how shipping noise affects aquatic wildlife and develop analysis tools capable of providing the most promising impact on minimising marine noise pollution.

Most marine animals rely on sound to sense their environment, which affects all aspects of their lives, from searching for food to avoiding danger [47]. Thus, even sound levels not directly detrimental to the health of the animals may affect them adversely by modifying their behaviour, displacing species from their original habitats or masking frequencies the animals rely on for their existence [47].

According to a comprehensive review published by the ITTC Specialist Committee on Hydrodynamic Noise, hydroacoustic noise sources for a commercial ship cover a wide range of frequencies, as seen in Table 2.1 [17]. What is more, noise from commercial shipping is said to dominate ambient noise levels in many regions around the world [47]. In this context, it is worrying that there is a trend for the continuous increase of shipping noise levels in the oceans, which has been quoted to be as high as 3 dB re 1μPa per decade between the 1950s and 1980s [38]. This tendency has recently showed signs of slowing down but still remains positive [38]. Overall, it is thought that shipping has raised the ambient noise in the seas by approximately 20 dB since pre-industrial conditions [113].

In favourable conditions, a single vessel may be heard at distances as large as tens of kilometres due to the high speed of sound in water [47], which is a clear indicator of the scale of the problem at hand. From an environmental impact point of view, the low frequency, tonal sources are of primary importance, because they will have the highest sound power and lowest attenuation, thus affecting the largest area [17, 141].

It follows that the noise due to the vibration of the hull structure induced by its interaction with the propeller and due to machinery, such as the main engines, drive shafts, auxiliaries, cooling systems, pumps, etc., will be of much smaller interest as far as marine wildlife is concerned. This is because their effect will be primarily seen at short distances, despite being of key importance for the crew and passenger comfort [94]. The tonal noise sources associated with the propeller, cavitating and non-cavitating, should therefore be focused on when assessing the environmental impact of shipborne noise pollution. The former is known to be of monopole nature, meaning it will radiate in all directions approximately equally, thus having the greatest environmental impact. The

Table 2.1: Dominant noise sources for a commercial ship (data from [17, 30, 85, 92, 107, 136, 203], environmental impact assessment from [17]).

Source	**Frequency range [Hz]**	**Environmental impact**
Machinery	1-10000	medium
Slamming	1-100	low
Hull boundary layer	100-1000	low
Wave breaking	100-10000	low
Appendage cavitation	100-20000	medium
Propeller-hull interaction	Blade rate	low
Propeller singing	100-2000	high
Open-water propeller noise	Blade rate	low/medium
Non-uniform inflow	Blade rate	medium
Unsteady, turbulent inflow	1 - 20000	low
Inflow and loading changes due to ship motions	<1	low
Periodic propeller cavitation	Blade rate	high
Unsteady propeller cavitation	10-20000	low

loading noise of the propeller is typically of dipole nature, affecting primarily the areas upstream and downstream of the propeller disc. It should be noted, however, that propeller noise is also likely to be associated with a significant broadband component due to cavity instabilities, presence of small oscillating and collapsing bubbles in the flow, vortices from the hull impinging on the propeller blade, and interaction of turbulence and cavitation.

Ships often operate in shallow, coastal waters where a large fraction of the sensitive marine habitats are placed. One may therefore postulate that if the true nature of the problem is to be fully understood, the broadband phenomena may not be completely overlooked on the basis of it only having an effect at short distances. Instead, this part of the noise spectrum should be studied and its real consequences ought to be better understood. This would allow a quantitative comparison of the extent to what the high- and low-frequency contributions are likely to affect marine life. Performing such a multi-scale analysis would also offer an opportunity to achieve an agreement between the computational and experimental results across the entire frequency spectrum. Doing so would allow for more thorough validation of the predictions with cavitation tunnel measurements.

2.3 Turbulence

2.3.1 Physics and Origin of Turbulence

Turbulence may be described as irregular and seemingly random fluctuations of fluid velocity in space and time. As such, it may be treated as a statistical process and so is often expressed in terms of the mean and fluctuating components

$$\begin{aligned} p(\mathbf{x},t) &= p_0(\mathbf{x}) + p'(\mathbf{x},t), \\ \mathbf{U}(\mathbf{x},t) &= \mathbf{U}_0(\mathbf{x}) + \mathbf{U}'(\mathbf{x},t), \end{aligned} \tag{2.2}$$

where p and $\mathbf{U}$ refer to the total value of pressure or fluid velocity at any one location, p_0 and $\mathbf{U}_0$ denote the mean (typically ensemble average) values and p' and $\mathbf{U}'$ the fluctuating components.

The ratio of inertial to viscous forces acting on an element of fluid in non-dimensional terms may be defined as the Reynolds number,

$$Re = \frac{U_\infty L}{\nu}, \tag{2.3}$$

where U_∞ and L are the significant velocity and length scales, respectively, and ν is the kinematic viscosity of the fluid. This non-dimensional quantity also acts as an indicator of whether a given flow is likely to be laminar or turbulent. The regime at which the flow will transition to a turbulent state will vary significantly, depending on such parameters as the shape of the geometry, presence of pressure gradients, and surface roughness.

In any turbulent flow there will exist a range of turbulent scales, as postulated by Kolmogorov [108, 109]. His original hypothesis also states that the largest eddies present in the flow will have the size in the order of the significant dimensions of the body in motion, while the size of the smallest ones will be dictated by the local Reynolds number and the turbulent energy dissipation rate, ϵ. Together with all the intermediate scales, these will form the so-called Kolmogorov energy spectrum, which is schematically depicted in Figure 2.2.

It has been postulated that there will be an exchange of energy between the eddies in which the energy is primarily passed from the large to the small scales, where the viscosity of the flow manifests its action by dissipating the energy into heat. This indicates that in order for turbulence to persist an external input of energy is required [160]. For a marine propeller this is delivered in the form of shaft rotation and the vessel moving.

Moreover, at high Reynolds numbers, typically encountered in engineering flows, the small-scale turbulent motions may be assumed to be isotropic, meaning their statistics do not vary with respect to any spatial direction [108]. Their size may be characterised

using the so-called Kolmogorov length scale,

$$l_K \equiv (\nu^3/\epsilon)^{1/4}, \tag{2.4}$$

where ϵ is the turbulent energy disspiation rate. This gives a useful indication as to the size of the discretisation size required for a particular problem when considering higher fidelity methods, such as Direct Numerical Simulation (DNS) or Large Eddy Simulation (LES). However, for more complex problems of engineering relevance, such as complete propellers, determining this parameter may not be trivial due to local flow effects.

Close to a fixed wall, fluctuating velocity components become affected by the no-slip condition, as well as the fact that there may be no flow through the wall. Accordingly, the velocity fluctuations will be altered, possibly leading to even smaller scales in the flow than would otherwise exist if the wall were not present [160].

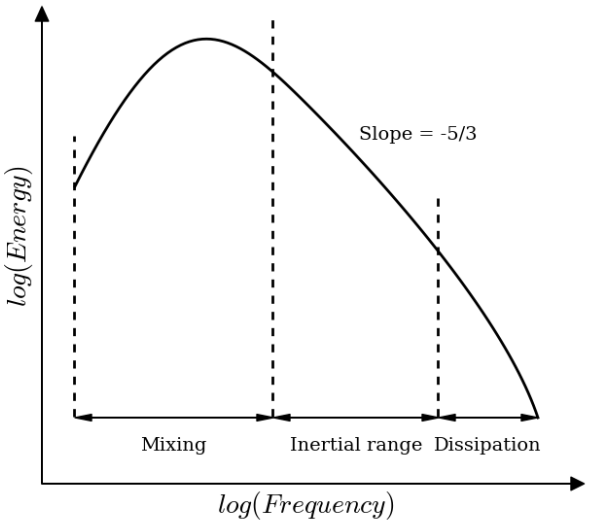

Figure 2.2: An example Kolmogorov spectrum showing how energy is distributed across a range of eddies of different sizes. In the lower frequency range large eddies responsible for most of the mixing exist, while the high frequency eddies govern dissipative processes in the flow.

2.3.2 Turbulence in Marine Propeller Context

In most engineering flows the Reynolds number is likely to be high. For instance, for a typical container ship one may expect this parameter to reach 4 billion for the hull boundary layer and 600 million for the propeller itself [1] . This is far beyond the turbulent transition point for any relevant wing section used on propellers, indicating

[1]This assumes: hull length of 300 m, speed of 25 knots, propeller diameter of 10 m operating at 120 rpm.

that turbulence will play a crucial role in the associated flow. Specifically, it will lead to turbulent boundary layers developing on all elements of the system and a wide range of turbulent length scales, varying from between the characteristic hull dimension down to the Kolmogorov length scale (see Eq. (2.4)) forming.

Moreover, the propeller will have to operate in the wake of the hull. This will firstly act to introduce a momentum loss to the fluid and cause the load of a particular propeller blade section to vary over a single revolution. As a result, periodic fluctuations of the boundary layer flow over the blade will be present. Furthermore, since the wake of the ship will contain a large range of turbulent length scales itself, it will cause each blade element to experience highly unsteady load variations on top of the periodic component associated with the mean inflow.

Finally, ships are expected to operate in a seaway. This, first of all, often induces significant motions on the hull, which will act to modify the inflow velocity to the propeller, thus changing the blade loading, as well as interacting with the boundary layer and other flow features directly. On top of that, each wave has a velocity and pressure field associated with it. As these pass along the hull, they will interact with the flow around the ship, further modifying it. Altogether, waves may therefore be expected to add a substantial amount of complexity and unsteadiness to the hull-propeller system, likely increasing rather than reducing the radiated noise levels.

2.3.3 Noise due to turbulence

Noise due to turbulence is typically associated with vorticity,

$$\omega = \nabla \times \mathbf{U}, \tag{2.5}$$

where $\nabla = \hat{x}_i \frac{\partial}{\partial x_i}$. The presence of solid boundaries will affect the vorticity field and the production and destruction of turbulence, as well as have an effect on the subsequent radiation of sound [79].

One may distinguish six principle categories of noise due to turbulence for a body moving through a fluid, which are also schematically depicted in Figure 2.3:

- **Turbulent boundary layer trailing edge noise** - originates from vorticity present in the boundary layer and the wake. It can be predicted if the pressure surface field is known [30, 31]. The generated sound pressure levels typically depend on the velocity to the 5^{th} power [31, 198]. One needs to account for the history of turbulence, not just the mean characteristics for this to be captured well [31].

- **Laminar boundary layer instabilities noise** - only important at intermediate and low Re since a proportion of the flow must be laminar over the chord for this to occur [31]. This originates from Tollmien-Schlicting instabilities in the laminar boundary layer. This is one of transition mechanisms whereby a disturbance (like sound) interferes with the leading edge roughness [31]. Thickness of the laminar layer is the relevant length-scale of this process (e.g. for Strouhal no. estimation or scaling attempts) [31].

- **Separation noise** - originates due to a large stall vortex being present and is broadband in nature [142]. For a wing section it increases the sound pressure level by approximately 10 dB relative to the trailing edge noise encountered at lower angles of attack [31]. At moderate angles of incidence the noise is centred at the trailing edge but in deep stall it emanates from over the entire chord [31]. One needs to capture separation well to predict this accurately [31].

- **Blunt trailing edge vortex shedding noise** - might contribute to the high-frequency broadband noise and is of dipole nature [30]. It will become increasingly important for wing sections or objects with large thickness at the trailing edge where a local recirculating flow region will be present [31, 198].

- **Tip vortex noise** - local separated flow due to the presence of the vortex is the main source of this high frequency broadband noise source [30, 31]. It is induced by the passing of the turbulence over the trailing edge near the tip of the wing [31].

- **Inflow turbulence noise** - originates from a vortex from an upstream body impinging on a downstream one, for instance tip vortex of a propeller blade interacting with the rudder. The resulting local change of the angle of attack, as well as a direct change in local pressure, yield a broadband noise source [136, 142].

It may be seen that turbulence itself is a major source of noise. As such, in order for any simulation to yield a satisfactory numerical prediction, one needs to ensure that appropriate turbulence modelling techniques are used [136, 142]. This stresses out the importance of using methods such as Large Eddy Simulation over, for instance, instead of unsteady RANS or potential flow methods, as the latter do not resolve but only model turbulence. Admittedly, the simpler methods are appreciably more computationally efficient and so may be successfully used to provide quick estimates for the purpose of guiding a design in the early stages of the design process. However, due to the simplifications they introduce, it is doubtful that they may be applied on a large scale in a study whose purpose is to gain a more in-depth insight into the nature of marine propeller noise.

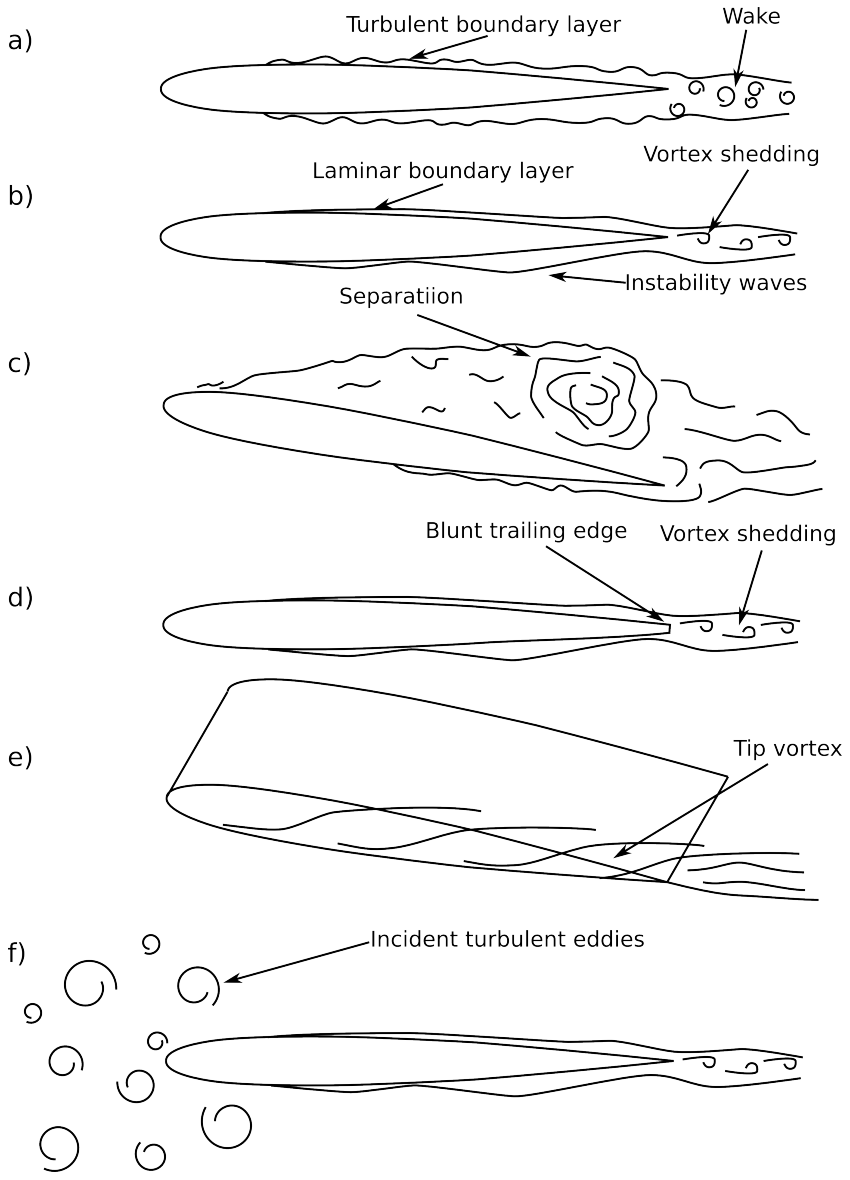

Figure 2.3: Schematic illustration of noise sources on an airfoil moving through fluid.

2.4 Cavitation

2.4.1 Physics and Origin of Cavitation

Cavitation is an event during which the liquid changes its state to gaseous due to being subject to low pressure. This originates from small gas nuclei present in the liquid being acted upon by the tensile stress, which leads to their expansion [158]. Depending on the local conditions and fluid properties, this may yield different types of cavitation [196]. Similarly, when the cavity passes to a higher pressure region it collapses or condensation takes place.

The saturated vapour pressure of a liquid, p_v, is one the key parameters governing the cavitation event. It defines how big a pressure drop may be sustained by the fluid without the cavities forming. In a non-dimensional form, one may express it as the cavitation number,

$$\sigma = \frac{p - p_v}{\frac{1}{2}\rho U_\infty^2}, \tag{2.6}$$

where p refers to the pressure of the liquid, ρ is the fluid density and U_∞ is a representative velocity scale. Typically, lower cavitation number corresponds to more pronounced and severe cavitation.

One of the first systematic attempts at tackling the cavitation problem was the analysis performed by Rayleigh in 1917 whereby the problem of the collapse of a single empty cavity in a large mass of fluid was considered [164]. The equation proposed by Rayleigh governs the expansion and shrinking of a bubble and has since received much attention and seen many modifications. One of the most mentionable ones was that discussed by Plesset in 1977, where the effects of surface tension and viscosity have been taken into account [158]. Since then, further research has been conducted in the area and the effect of other factors, such as thermodynamics and compressibility, have been accounted for [81]. In the most general form the Rayleigh-Plesset equation is

$$R\ddot{R} + \frac{3}{2}\left(\dot{R}\right)^2 = \frac{1}{\rho}\left(p_B - p - \frac{2\sigma_{st}}{R} - \frac{4\mu}{R}\dot{R}\right), \tag{2.7}$$

where the term p_B refers to the pressure inside the bubble consisting of the sum of the saturated vapour pressure, p_v, and the local gas pressure, p_g. R is the bubble radius, σ_{st} is the surface tension constant and μ is its dynamic viscosity.

It follows that the content and size of cavitation nuclei are key factors governing cavity inception and collapse [158, 196]. According to Plesset, the dynamics of the bubble at other stages of bubble life are not so greatly affected by the content of the gas [158]. More recent research does suggest, however, that the tensile strength of water is greatly affected by this parameter, which will influence the cavitation characteristics [95]. It has been reported that in a cavitation tunnel test an insufficient amount of nuclei will cause cavitation to be intermittent and appear less severe than it will be in reality. On the other hand, too many nuclei will cause cushioning during cavitation collapse and reduce the extent of erosion and dynamics observed [95]. This makes accurate scaling and quantitative CFD validation difficult.

2.4.2 Cavitation on marine propellers

Cavitation on a marine propeller induces multiple problems, such as [204]:

- **performance degradation** - e.g. breakdown of thrust and torque due to presence of large, persistent cavities on the propeller blades;

- **erosion** - high pressures and temperatures associated with the shock wave from a collapsing bubble (implosion) may cause the metal forming the propeller blade to be chipped away with time; once erosion occurs it is accelerated by the increasing turbulence and cavitation in the flow due to the eroded pits;
- **vibration** - due to instabilities and fluctuations of thrust and torque transmitted along the shaft to machinery and through hull shell to the main girder, as well as pressure pulses impinging on the hull shell and induced by the cavities themselves;
- **noise** - occurs due to pressure and velocity fluctuations induced by the displacement of cavity interfaces as its volume varies and due to implosion of cavities which emit a shock wave as a result.

Traditionally, the first two of the phenomena were the main concern of ship designers as they directly affect the ability of the vessel to fulfil its purpose. Vibration has also become a major concern as increasing crew comfort has become an important design factor. Radiated noise from commercial ships, however, has not received substantial interest until very recently.

There are several factors affecting the extents, severity and type of cavitation occurring on a marine propeller [204].

- Strongly non-uniform flow field causing local angle of attack and pressure variations.
- Turbulent inflow into the propeller disc causing transient fluctuations of blade loading.
- Limitted propeller area due to draught constraints resulting in high propeller loading and significant pressure drops.
- Increasing power demand output of ever growing ships which necessitates higher loads.
- Strong wake peaks for a traditional, V- or U-shaped single-screw merchant hull.
- Change of flow field during manoeuvres and ship motions.

These give rise to various types of cavitation phenomena, the most common of which are depicted in Figure 2.4. In general, one may distinguish two principle forms of cavitation [131].

- Attached cavitation - interface between the liquid and vapour is partly attached to the solid surface; it is called a sheet when the cavity forms a thin and quasi-steady stable cavity.

- Convected cavitation - typically takes the form of bubble cavitation or travelling bubble cavitation, whereby individual transient bubbles are created and travel with the flow, expanding and shrinking as they encounter varying local pressure.

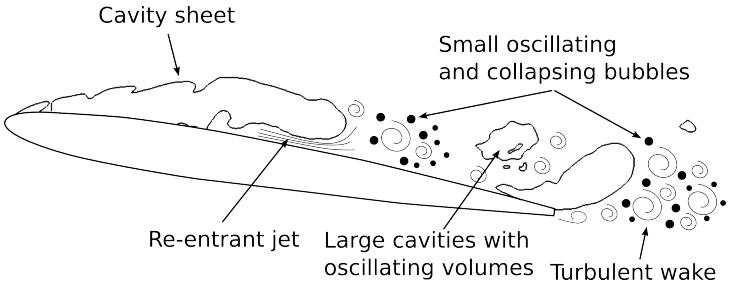

Figure 2.4: Schematic illustration of types of cavitation on a hydrofoil.

In practice, these will often occur simultaneously and interact with each other. For instance, on the edges of the sheet cavitation there are typically small regions of bubble cavitation being generated. Clouds of bubbles are also often generated at the downstream extent of sheet cavitation when the cavity lifts off the surface of the body it is attached to, thus creating a jet of liquid moving rapidly upstream along the cavity-body interface. This is referred to as the re-entrant jet. In certain cases, this may also cause the sheet to collapse completely [12]. Moreover, sheet cavitation may lead to the excitation of cavitation nuclei, for instance through interaction with a turbulent boundary layer or by creating pressure fluctuations close to the body. Shear and mixing of the flow while the re-entrant jet fills the cavity or other types of reversed flow or rebound may also interfere with cavitation phenomena [139].

A more detailed classification of cavitation phenomena may also be devised based on the mechanism responsible for the inception and its location in a marine propeller-rudder-hull system.

- **Bubble cavitation** - takes place when the number density of nuclei subject to macroscopic cavitation is low. Typically, the mid-chord region in non-separated flows is most prone to this type of cavitation due to a strong low pressure peak. Rayleigh-Plesset equation, Eq. (2.7), is a valid approximation for describing the growth and collapse of individual bubbles but more care may be needed to account for the dynamics of complete clouds [19, 20, 35, 204]. Also, in reality bubbles are not perfectly spherical due to pressure gradients, shear forces, and presence of solid surfaces [19]. It has the potential to result in a violent collapse and erosion towards the trailing edge and may be remedied through unloading the blade section [204].
- **Sheet cavitation** - if enough bubbles become subject to low pressure and are allowed to interact with each other, they may connect and form a larger pocket of gas. This type of cavitation is one of the primary blade-rate related cavitation phenomena. On propeller blades and hydrofoils this is typically attached to

the surface of the body and starts around the leading edge, extending chord-wise. These cavities may cause a significant change in thrust and toque by effectively altering the profile of the blades. Depending on the flow conditions, the sheet may become unsteady or intermittent, often due to non-uniform inflow, or the ratio between the cavitation and Reynolds numbers and the angle of attack. Sheet cavitation is associated with large cavity volume variations which may induce pressure peaks on the hull at multiples of the blade passing frequency; these will most likely be much bigger than the excitation cuased by the blade loading itself [204]. The collapse usually occurs through the formation of a re-entrant jet which travels in the upstream direction until impinging on the upstream cavity interface [46], as shown in Figure 2.4. As a result, a major part of the cavity will become detached from the surface of the body and form a cloud which will then be convected downstream. The shed volume of cavities is since then referred to as cloud cavitation. Depending on the flow conditions, this process may be two- or inherently three-dimensional, as well as stable, cyclic and unstable [62, 63, 202]. Irregular shedding will occur when there is not enough momentum in the re-entrant jet the to overcome the viscous forces present close to the solid boundary and the interaction with other cavity extent. This prevents the jet from reaching the leading edge every time it is formed. As a result, the shedding will become irregular in frequency and location chord-wise. It will be mainly induced by the interaction of the jet and outer cavity interface and the resultant disturbances rather than the typical regular shedding mechanism [46].

- **Cloud cavitation** - often occurs due to periodic disturbances of sheet cavitation which cause shedding of clouds of small bubbles or from bursting of tip vortex cavitation. Shedding of the cloud will affect the pressure distribution around the propeller blade and, in case where it originates from sheet cavitation, the re-entrant jet impinging on the upstream cavity end will likely lead to instabilities being introduced to the flow [200]. As the shed cloud travels downstream following the break-off, it will undergo collapse [12, 46, 139], which is known to cause some of the most violent erosion and is also a prominent source of noise [204].

- **Tip vortex cavitation** - a main bubble forms at the core of the vortex due to nuclei being subject to low pressure there and becomes elongated downstream [41]. Vortex-vortex interactions may lead to stretching and modification of the axial flow in the core of the main vortex, thus incepting cavitation at relatively high ambient pressure levels and on lightly loaded propellers [41, 139], which is one of the reasons why this type of cavitation is so often seen in experiments. Typical collapse of this type of cavitation reportedly occurs through necking of the downstream part of the bubble, eventually causing the cavity to split. This behaviour may potentially induce radiant pressure waves and is largely dependent on the radius of the bubble prior to the collapse [41]. At low blade loading, the

vortex bubble is said to often appear at a distance from the trailing edge; as the load is increased it becomes attached to the blade [204] and may sometimes merge with a sheet cavity [139], leading to complex flow patterns.

- **Secondary cavitation** - occurs in an element of fluid which has undergone primary cavitation (any of the other mentioned types) and which then enters a new low pressure region. This causes new inception or growing of present cavities to take place. Dynamics of the new cavity may be modified by the element of fluid possibly having a different distribution of cavitation nuclei and dissolved gas than what is present in the free-stream. A typical example is remnants of propeller hub vortex cavitation impinging on a rudder [11].

- **Hub cavitation** - associated with the hub vortex and so is generally similar to the tip vortex cavitation in terms of the driving force (low pressure region inside a vortex core) [204].

- **Root vortex cavitation** - occurs when there is a root vortex present, for instance on propellers with very short chord lengths near the hub (such as a controllable pitch propeller, Potsdam Propeller Test Case being a fine example [187])).

- **Propeller-hull vortex cavitation** - when there is a small clearance between the propeller tip and the hull shell, pressure drop at a low advance coefficient may cause detached cavitation in this region [204].

- **Air bubbles trapped in the hull flow** - air bubbles generated by the motion of the ship and its wave system are often trapped in the vortical structures of the wake and yield a large acoustic cross section when passing through the propeller region where they become excited [81]. While not strictly associated with a vaporisation process, these should still be included in the analysis, particularly when one acknowledges the fact that interactions between these bubbles play a crucial role in concentrating the collapse energy, for instance via inducing the collapse cascade when the first pressure pulse is emitted by a cavity undergoing rapid destruction [19, 196].

2.4.3 Cavitation noise

Cavitation is known to induce low-frequency and broadband noise components, which for full-scale ships span between 5 and 100,000 Hz, with maximum spectral levels typically occurring around 50 Hz [107, 203]. This noise is generally induced through the following mechanisms

- **Fluctuation of cavity volume** - as a bubble volume changes it induces a pressure fluctuation to the surrounding fluid. This will give rise to a disturbance which

may travel as an acoustic wave and form a monopole source [156, 177]. For large structures, such as prominent sheet cavities or large tip vortex cavities, the associated frequency of this type of pressure fluctuation may be relatively low. It will also often be close to the blade pass frequency, as it will be the non-uniform wake into the propeller that will act as the primary driver for inception. If the cavity is assumed to be quasi-stable, it may also be viewed as changing the thickness of the blade and thus having a direct influence on the associated blade-pass noise [169]. Non-periodic factors, such as turbulent eddies and ship motions, will also have a prominent effect on cavity volume oscillations, although they will interfere with the remaining noise sources as well [107]. Smaller bubbles will also follow this mechanism. However, as may be shown from the Rayleigh-Plesset equation (2.7), their frequency of response is likely to be significantly higher, thus typically giving rise to higher frequency noise [115]. As will be discussed and demonstrated later, in a turbulent flow small-scale deformations on the surface of larger cavities will also be present, further adding to the high frequency component.

- **Shockwave** - final stages of the collapse of a cavity yield very high interface velocities and may cause the formation of a shockwave [107, 156, 177]. The pressure induced by the acoustic wave generated by a collapsing bubble may be estimated from the rate of collapse of the bubble [196]. While the global flow quantities may well remain in the incompressible region, locally the growth rate may approach the speed of sound and yield high pressures [9, 196]. This phenomenon will occur in large (sheet) and small (bubble) scale cavitation structures and so it will likely have a prominent effect on the overall emitted sound pressure levels [176]. Factors such as presence of a solid boundary, other bubbles, or the cavity having a non-spherical shape will all affect the shockwave formation process [19, 196]. Shockwave formation is known to give rise to concentrated noise peaks, thus making it broadband in nature [107, 156, 177].

- **Oscillation of small bubble volumes** - while the mechanism associated with generating noise from this phenomenon encompasses the mechanisms listed above, it is useful to consider it separately. As may be deduced from the Rayleigh-Plesset equation, Eq. (2.7), a collapsing bubble may be caused to rebound, or re-grow in size, following a collapse. This is caused largely by the non-condensable gas pressure delivering a restoring action to the system [9, 12, 14, 139, 196]. This has the potential to induce a series of strong pressure peaks and thus cause broadband noise. During the oscillations the non-condensable gas diffuses across the bubble interface at a rate which is dependent on the gradient of its concentration [81]. This implies that after a certain number of rebounds there may not be enough of it left in the nucleus for the oscillations to continue and the process stops. This process is highly dependent on the interactions between bubbles, which play a crucial role in concentrating the collapse energy, for instance via inducing a collapse cascade

when the first pressure pulse is emitted [196]. An important observation is that this mechanism will not only apply to cavitation bubbles, but also, for instance, air bubbles entrapped in the hull boundary layer due to the presence of a free surface or if an air lubrication system is used [81]. For simple spherical shapes, relatively accurate approximations of the natural frequency and radiated pressure may be obtained using the Rayleigh-Plesset equation [19, 115, 143].

2.4.4 Cavitation and turbulence

The unsteadiness of the flow may affect cavitation in many ways. Firstly, turbulent mixing may force more nuclei into the boundary layer which may alter the form and nature of cavitation present, particularly in the case of sheet cavitation [196]. On a larger scale, the bubbles may follow turbulent motions or accumulate in certain areas causing localised cavitation. Similarly, the unsteady flow may lead to additional low pressure regions being created and thus being more prone to cavitation.

Turbulence may also introduce non-periodic fluctuations of the cavity interface, especially in the downstream region of the propeller blade where the wake field is far more developed. This will be greatly amplified by the presence of turbulent inflow causing large amplitude variations of the local angle of attack of the blade. As a result, the load distribution will see an oscillating component leading to unsteady cavitation.

Cavitation will interfere with the flow as well. The change of bubble volume will affect the vorticity distribution and modify the turbulent structures. For instance, for a vortex cavity expanding the flow is displaced and the pressure on the interface increases, modifying the vortex core [41]. Also, the presence of a disperse phase, such as clouds of bubbles, may affect the turbulent kinetic energy and dissipation rate if the turbulent and particle length scales are comparable [23]. This is of particular importance given that the viscous sublayer is usually thinner than the bubble dimension, and so may be subject to interactions with cavitation near the body surface [204]. Finally, for larger cavities the complex momentum exchange due to the presence of a re-entrant jet and three-dimensionality will play an important role in establishing the flow field characteristics [46, 185]. The aforementioned points show why it is imperative to model both cavitation and turbulence as accurately as possible if a true understanding of the dynamic flow processes is to be developed.

2.5 Review of relevant published work

This section reviews some of the most notable works from the literature treating on marine propeller flows, cavitation, and noise. The aim is to highlight the state of the art in the respective fields and allow the most pressing challenges to be formulated.

2.5.1 Experimental measurements

A range of sets of experimental data related to the topic of marine propeller cavitation and noise modelling have been identified in the literature. However, from the perspective of the current work, the primary focus was put on identifying studies which could be reproduced numerically for the purpose of validation. For this reason, the chosen test cases had to be well documented, present a wide range of data directly comparable with CFD results, and any relevant geometries had to be easily obtainable. Unfortunately, much of the data in the literature does not stand up to these criteria and hence only a handful of experiments were short listed. The chosen test cases also had to cover a possibly wide range of complexity levels in order to allow basic validation, as well as more focused and detailed studies on realistic geometries. Following this logic, they could be broadly categorised into studies involving hydrofoils, rotating propellers, as well as fully appended ships.

A number of test cases focused on hydrofoil shapes is available in the literature. Several series of experiments were available for NACA 0015 aerofoil shapes. For example, the study by Arndt *et al.* [5] reports on the effect of changing the angle of attack and cavitation number on the force coefficients, cavitation patterns and shedding frequencies. An investigation by Bretschneider *et al.* [27] reports similar results by also extending the observations into the bubble cavitation regime. While certainly informative, these studies were not widely used in the literature, which reduced the amount of numerical results that could be referred to for additional comparison.

A wide range of experimental studies has been discussed in a series of publications by Ducoin, Astolfi and Leroux *et al.* [6, 50, 51, 116, 117]. They studied the modified NACA 66 profile over a wide range of conditions. The advantage of this series of experimental work is that it describes phenomena occurring on a blade section typical of marine propellers and that, thanks to the work having been continued for several years, it explores the observed behaviours and the mechanisms involved in them in detail. Importantly, the data set includes unsteady surface pressure measurement at various locations along the foil, which makes the test case extremely valuable from the CFD validation perspective.

Another compelling test case identified was the Delft Twist 11 hydrofoil [62, 63]. It is based on a 9% thick NACA 4-digit section, similar to the first studies mentioned, but covers a hydrofoil which employs a span-wise variation of the angle of attack. This implies that the observed cavitation patterns are three-dimensional but, unlike on a propeller, are not, at least theoretically, affected by the formation of tip vortices. This allows the phenomena of sheet and tip cavitation to be studied independently. An additional advantage of this test case is the wide range of numerical studies devoted to it, which inaugurated with the test case being used in the first SMP workshop on

cavitation [78]. Force measurements, cavitation pattern observations, and mean surface pressure measurements are among the experimental data available for this test case.

At the time of writing, there were two main propeller cases widely discussed in the literature in the context of cavitation studies: the Potsdam Propeller Test Case (PPTC) [187, 188], and the Insean E779a propeller [33]. The latter test case is a four-bladed modified Wageningen-series propeller and has been tested in uniform and non-uniform inflow, as well at an inclined shaft condition. Therefore, observations of a wide range of cavitation patterns have been reported in the literature, mainly by means of high-speed camera photographs and associated force measurements. The PPTC case involves a much more modern, five-bladed, highly-skewed VP1304 propeller design. This is appreciably more representative of propellers fitted to contemporary commercial ships. At the outset of the present project, cavitation observations for this case were only available at level shaft and uniform inflow conditions and the data was presented as high-speed camera photographs and force coefficients. During the second SMP Workshop [188] an additional set of measurements was presented where the propeller had been tested with an inclined shaft and pressure pulse measurements in both cavitating and non-cavitating were used to complement standard cavitation observations.

Given the preliminary nature of the present work, it was recognised from the early stages of the project that cases involving fully appended ships and full-scale measurements would likely be excluded from the current work scope due to their expected high computational cost and complexity. It was still useful to identify the available data, however, to inform future research. At present, the most useful data sets in this area appear to be the outcomes of the EU SONIC project, whose experimental side is well summarised by Brooker *et al.* [28] and Aktas *et al.* [2, 3]. The authors describe a range of hydroacoustic measurements of the Newcastle University research vessel, R/V Princess Royal, carried out during sea trials and cavitation tunnel experiments. For the former, the ship sailed up and down a fixed track while noise measurements were taken at various depths using a series of hydrophones deployed overboard of an observer vessel. The accompanying cavitation tunnel measurements involved observations of the propeller alone as well as operating behind a scaled model of the real vessel. Together, the studies present a very informative data set. Particularly valuable is the ability to use the data to study the intricacies of sound reverberation and model-scale noise measurement scaling.

2.5.2 Simulating cavitation

Before considering computational works by individual authors, it is informative to summarise the major workshops during which participants were presented with particular experimental test data they had to reproduce using simulations. Salvatore [171] reviews the submissions for the 2008 VIRTUE workshop, which involved simulations of cavitation

on the Insean E779a propeller in uniform and non-uniform inflow conditions. Reportedly, 6 of the participants utilised unsteady RANS and only one submission relied on LES for turbulence modelling. Furthermore, all but one team depended on mass-transfer cavitation models, with the outlier utilising a compressible barotropic model. The major conclusion from the workshop was that while non-cavitating flow may be simulated to within several percent of accuracy in terms of force coefficients and, quantitative prediction of cavitation was not particularly reliable in terms of cavitation extents and pressure fluctuations. Hoekstra *et al.* [78] summarise the results of the subsequent SMP'11 workshop during which the Delft Twist 11 hydrofoil was meant to be simulated. Again, only two submissions used LES or DES methods and the remaining participants employed RANS codes. All of the presented cavitation results were obtained using mass transfer models, with four users utilising the Schnerr-Sauer and one the Zwart implementations. The workshop concluded by pointing out dependency of cavitation predictions on the grid and time step resolutions, but highlighted a relatively good agreement in the predicted cavitation shedding frequencies. The most recent SMP'15 workshop is described by Luebke and Barkmann [140]. In this study, the participants were asked to simulate the Potsdam Propeller Test Case at level and inclined shaft, paying attention to the cavitation patterns and generated pressure pulses. In line with the previous workshops, LES and DES methods were still largely outnumbered by RANS and mass transfer models were most widely used. In general, the magnitudes of pressure pulses and cavitation patterns were represented well by the participants, indicating a certain degree of maturity of the methods used.

Wikstrom, Huuva, and Lu [87, 139, 202] successively explored how LES and mass transfer models may be used together in order to produce reliable cavitation predictions. Their studies are largely focused on initial applications to hydrofoil shapes and pay particular attention to the issues associated with interactions of the LES models with water-vapour interfaces, as well as issues of grid resolution and practicalities of applying LES to high-Re geometries. They conclude that wall-modelled implicit LES, while more challenging to use than RANS, offers significant improvements in the prediction of unsteady cavitation. The subsequent work by Lu aimed to extend the results to better characterise erosion and noise using LES instead of focusing solely on global cavitation dynamics. This study also applies the implicit LES and mass transfer methods to real models of skewed propellers. The reported qualitative flow comparisons suggest relatively good agreement with cavitation tunnel observations, but point to the challenges of resolving small-scale flow features important for the prediction of erosion and noise. An important finding is also that substantial care must be taken when designing numerical grids on which re-entrant jet mechanisms are to be resolved, as the mesh must be fine enough to allow the thin feature to gain sufficient momentum.

Usefulness of LES and mass-transfer cavitation models was also reported by two studies focused around the Clark-Y hydrofoil test case. Roohi *et al.* [165] used Kunz and

Schnerr-Sauer models and found both of them to predict the chord-wise pressure distributions and qualitative cavitation dynamics relatively well, while the drag was reportedly over-estimated. Huang *et al.* [86] employed the Kubota cavitation model and showed that vortical and cavity structures experience a substantial amount of interactions, which effect the predicted dynamics. They also pointed out that the presence of cavitation affects the way the leading and trailing edge vortices interact, and thus has an impact on the frequency of the resultant load changes.

Furthermore, a study by Ponkratov *et al.* [159] has demonstrated successful use of Detached Eddy Simulation (DES) and mass transfer cavitation models in order to compute the flow around a full scale ship, accounting for the unsteady wake effects. The authors also utilised a range of erosion prediction functions, thus hoping to quantitatively assess the risk of damage due to cavitation to the ship stern gear in service.

An important set of studies was presented by Bensow *et al.*. The first study [11] focused on solving the flow past the Delft Twist 11 hydrofoil using RANS, DDES, and implicit LES, as well as the Schnerr-Sauer cavitation model. The authors reported relatively good agreement between the turbulence-resolving methods and the experiments in terms of the predicted shedding frequency and cavitation patterns, however the latter were under-predicted. A major discrepancy was reported in the mean lift coefficient. The authors also found that the RANS approach, unless modified with a turbulence viscosity reducing correction, does not predict the dynamics of cavitation well and hence a recommendation was made to move to LES or DES approaches. In the next study [13], the authors modelled the the Insean E779a propeller subject to uniform and non-uniform inflow conditions. The reported set up relied on implicit LES and the Kunz mass transfer model while solving the flow on a 4.5 million cell, wall-modelled, unstructured mesh. The authors reported good agreement of the simulations with PIV measurements of the wake, but admitted that their results under-predicted the intensity of the tip vortex. Cavitation pattern predictions were reported to stand in satisfactory agreement with the experiment for non-uniform inflow conditions, but deviated from reality in the uniform flow. It is also interesting to turn attention to the study in which the authors model the flow past a NACA 0015 [16] with the intention of tackling erosion by using ILES and mass transfer models, as in the aforementioned studies. Important findings are that inclusion of compressibility and non-condensible gas content in the simulations is almost certainly necessary for erosion to be predicted accurately. Furthermore, the authors point out the importance of small-scale bubbles to erosion and noise, which cannot be reliably solved for using the mass transfer model without prohibitively large mesh densities. A related study by Eskilsson [53] did, in fact, describe the use an early implementation of a compressible cavitation model based on the equilibrium relationship to model the flow over a NACA 0015. The authors reported very small time steps being needed, which led to high cost of the simulations.

Compressible cavitation models were also used by several other authors. Arndt *et al.* [5] studied a NACA 0015 foil using LES and a barotropic cavitation model across a range of conditions. They pointed out a strong relationship between the cavitation behaviour and a non-dimensional parameter $\sigma/2\alpha$, where α is the angle of attack. Interestingly, said parameter is derived from linearised inviscid thin plate theory but yet still manages to describe the frequency of oscillation of cavities on a hydrofoil to within several percent over a wide range of conditions. Leroux *et al.* [117] combined experiments and 2D RANS with a compressible cavitation model based on the barotropic law in order to study the flow past a NACA 66. Their study paid particular attention to cavitation patterns and surface pressure measurements, as well as pressures induced by the collapse of cavity clouds in the wake and how these affect the flow on the foil itself. Through their analysis they were able to show that the pressure waves from collapsing cavitation play an important role in the unsteady cavitation dynamics by interacting with the growth of cavitation upstream of the location of the collapse. Wang *et al.* [200] describe the use of a single-fluid cavitation model and LES to study the flow over a NACA 0015 foil. They use a polynomial expression to express the compressible relationships between density and pressure. The authors argue they can capture the collapse pressures well using the proposed method. Furthermore, they point out the important role of interactions between cavitation and vortices on the overall flow patterns on the foil. Yakubov *et al.* [207] also demonstrated the use of RANS and a compressible flow model in application to a NACA 0015 foil. Their model derives from the Zwart approach but accounts for the compressibility of vapour and water phases. They reported that the reference incompressible results predict much higher pressure peaks and fewer oscillations in forces and local pressures compared to the improved model. These were likely due to rebounds being ignored. The most recent studies considered here are those by Budich *et al.* [32, 32], in which the authors present studies of the PPTC (VP1304) propeller using inviscid Euler equations and implicit LES. They employ a compressible homogeneous mixture cavitation model similar to the aforementioned studies. The major focus of the investigations was to validate the numerical approach by comparing the predicted cavitation patterns and pressure pulses to experimental data, and then allow the risk of erosion to be estimated. The authors reported satisfactory agreement with the validation data and described their method as promising yet expensive.

Ji *et al.* have conducted a series of studies in which they explored the applicability of incompressible mass-transfer cavitation models to engineering flow simulations. Their initial work [100] focused on applying standard RANS models to study the Seiun-Maru model-scale propeller in an artificially generated wake, making the study similar to the E779a propeller investigated by other authors during the 2008 VIRTUE workshop [171]. The authors reported that cyclic cavitation has a noticeable reinforcing effect on the pressure pulses generated by the propeller at the blade pass harmonics, which stood in good agreement with the experiment. Two subsequent studies [101, 102] then investigated the use of LES and partially-averaged Navier-Stokes equations to the Delft

Twist 11 hydrofoil. Cavitation was reportedly modelled suing the Schnerr-Sauer and Zwart approaches. Despite relatively coarse meshes of 3 and 4.5 million cells being used, the authors reported satisfactory prediction of the shedding frequency and cavitation patterns. They also indicated that the interaction of the cavities with a major horseshoe vortex being formed on the twisted hydrofoil plays an important role in the incipient flow dynamics. The most recent publication by the authors [99] applied LES and Schnerr-Sauer to model the flow past a NACA 66. The authors investigated the effect of the spanwise mesh resolution and highlighted the importance of matching the mean inlet pressure to the experimental conditions, contrary to the typically followed approach where the outlet pressure is used to fix the cavitation number of a CFD simulation. Using a 4 million cell mesh the authors showed relatively good agreement of the unsteady surface pressure on the surface of the foil, as well as highlighted the dependence of the pressure pulses on the second time derivative of the total cavity volume from first principles.

The NACA 66 was also studied by Tran *et al.* [193] using incompressible Kubota and Merkle cavitation models and unsteady 2D RANS. The authors focused on a single condition from the orignal experiments by Leroux *et al.* [117]. In their work they showed that, with a modification to the turbulent viscosity aiming to represent the effect of vapour compressibility, the RANS model may predict the cavitation dynamics relatively well in terms of the shedding frequency. A similar study was presented by Kanfoudi *et al.* [104] who applied the k-ϵ RNG RANS model with Kunz and Merkle cavitation models to NACA 66. They, too, saw the unsteady pressures on the foil surface agree relatively well with the experimental data by Leroux *et al.*, but reported their CFD to predict far more high-frequency content.

Woo Shin [204] investigated the use of mass transfer models by Kunz, Singhal and Zwart models to predict 2D and 3D flows over foils and skewed propellers with RANS. The author reported reasonable agreement with experiments but also highlighted the underestimation of cavity extents and problems with predicting vortex cavitation. Importantly, he also pointed out the inability of the method to resolve cloud cavitation and at high angles of attack. A similar observation was made by Yakubov *et al.* [207] in the aforementioned NACA 0015 study. This has led to some authors aiming to alleviate the deficiencies of the commonly used cavitation models by moving to hybrid Eulerian-Lagrangian methods. Vallier [196] developed such a model based on the Schnerr-Sauer approach and used it to simulate flows past simple hydrofoils with LES. The author reported that the hybrid method can be a promising tool for assessing induced pressures and erosion. A large and persistent amount of information has been presented by Hsiao, Choi, and Chahine *et al.* over a period of several years. In their more recent work these authors have presented a novel approach to modelling the two phase problem associated with cavitation using a Lagrangian-Eulerian framework to model different scales of cavities [80, 84]. At the time of writing, this approach has not been reportedly used to predict far-field noise, but has the potential to allow this. The authors have also

advanced the use of bubble-dynamic models together with a RANS solver to model the effect of cavitation and bubbly flows in general on the performance and noise characteristics of propellers [37, 41, 83]. One of the most important findings they present is the indication of the influence of nuclei distribution on the tip vortex and other types of cavitation. The studies have also shown that the mechanism of noise generation associated with the tip vortex is relatively similar to that observed in many other aspects of cavitation. Namely, it is said to occur due to the oscillation of the cavity volume and when necking of the elongated bubble trapped in the viscous vortex core takes place. When the tip vortex cavity finally collapses, it generates a strong pressure wave [42].

Several groups of authors paid particular attention to better understanding the effect of grid- and time-step dependence on the unsteady cavitation dynamics. Lloyd *et al.* [135] studied the PPTC at an inclined shaft using RANS and Schnerr-Sauer model. They utilised unstructured trimmed hexahedral meshes up to 16 million cells and pointed out that increasing the near-wall resolution has a limited effect on the obtained results and the use of a wall function does not affect the results significantly. They also highlighted the importance of achieving sufficient mesh resolution around the high curvature areas of the propeller. Their preliminary results reportedly showed promising agreement of the generated pressure pulses with the experimental data. Negrato *et al.* [150] conducted a similar study in the sense that the authors focused on the effect of grid resolution and type on cavitation over a simple 2D NACA 0015 hydrofoil shape. By using RANS and the Schnerr-Sauer cavitation model they showed that structured and unstructured meshes predict qualitatively similar patterns but the location of the shed clouds and downstream collapses are different between them. This was reported despite relatively low numerical uncertainty computed using traditional grid refinement studies. Recently, Wu *et al.* [205] also investigated the issue of mesh resolution by simulating cavitation around the Delft Twist 11 hydrofoil with the Kunz cavitation model and LES. They employed a structured meshing strategy and investigated the change of results when increasing mesh resolution from 2 to 10 million cells. They observed significant influence of mesh resolution on the predicted size of cavitation, its shape, and shedding frequency. In particular, they highlighted the need to achieve sufficient span-wise resolution in order to resolve the three-dimensional re-entrant jet mechanism accurately.

2.5.3 Simulating marine propeller noise

Despite the recent significant surge of interest in modelling cavitation noise on marine propellers, there exist few large-scale studies involving high-fidelity numerical techniques. Methods such as potential flow coupled with boundary element methods are still in use, as seen in the studies presented by Salvatore *et al.* [169, 170] for the DTRC 4148 and E779a propellers and Seol *et al.* [177] for the DTMB 3119 design. Both groups of

authors utilised the Ffowcs Williams-Hawkings (FW-H) acoustic analogy evaluated on the blade surface to deduce the noise radiated by the propeller.

To the author's knowledge, the most complex study related to cavitation noise modelling presented in the literature is that by Seo et al [176]. In this work the flow over a circular cylinder was simulated using a compressible DNS solver coupled with a density-based cavitation model in order to predict the radiated sound waves. An appreciably high level of detail was shown to be resolved using the proposed method with the monopole character of the collapsing cavities clearly interacting with the dipole sound source of the cylinder itself.

A thorough approach to predicting propeller noise has been proposed by Matusiak [143]. He computed the flow making an inviscid assumption and utilised a simple cavity sheet model in order to account for the large monopole noise contribution this induces while the blade passes through the ship wake. Moreover, small bubbles in the flow were introduced as part of the sheet cavity break-up and their motion was then solved in a Lagrangian manner. The associated broadband noise component was accounted for by time integration of the Rayleigh-Plesset equation by neglecting bubble-bubble interaction. The latter is quite a significant assumption and may be expected to remove some complex physics from the flow [20]. The overall agreement between the discussed method and experimental noise data does indicate that at least some of the cavitation mechanisms may be captured in this way. However, due to the simplicity of the flow modelling employed, the model canno account for viscous flow features and turbulence.

An important study was presented by Park *et al.* [157] who solved the flow around a NACA 0015 hydrofoil with a tip using RANS and seeded Lagrangian bubbles into the flow in order to simulate tip vortex cavitation. They then use the radiation equation in order to predict the noise radiated by each bubble. The authors were able to predict a significant amount of high-frequency, high-amplitude peaks due to collapse of the bubbles. A similar approach was followed by Sunil *et al.* [186] who used Lagrangian tracking of bubbles around a 2D NACA 0012 in order to compute the noise they generate. The authors paid particular attention to accounting for compressibility effects when solving the Rayleigh-Plesset equation, as well as achieving realistic distributions of the seeded bubbles.

Interesting results have been presented by Seo *et al.*, where Reynolds Averaged Navier-Stokes methods were used for a compressible fluid in conjunction with a density-based, homogeneous model [175]. In their study, a 2D NACA 66 wing section was considered and the near-field pressure radiated from the collapse of the cavity was captured thanks to the use of high-order schemes. Overall, the investigation concluded with satisfactory results but stressed the importance of using more advanced turbulence modelling techniques, such as LES. In the study the authors did not consider propagation into the far-field, however.

Ianniello *et al.* investigated the noise induced by a model- and a full- scale ship and propeller in non-cavitating conditions using a porous Ffowcs Williams-Hawkings analogy coupled with a RANS solver [89, 90, 92]. The open water propeller study was also recently extended with the use of a DES solver [88]. The authors indicated that, unlike in aeroacoustic problems, the nonlinear sources are relevant to the marine propeller problem despite significantly lower Mach numbers observed. They also recommended computing the volume integral of the quadrupole source instead of conveniently neglecting them. This conclusion also indicated the importance of capturing the vorticity in the wake of the propeller, and not just the surface pressures on the blades, for a reliable acoustic analysis to be possible, and thus highlighted the necessity of employing more advanced turbulence modelling techniques. The authors also challenged the common view that cavitation is in most cases the dominant noise source, given the significant noise levels they predicted in non-cavitating conditions. They also postulated that the current state-of-the-art in cavitation modelling is unlikely to be sufficient to accurately capture the associated noise, mainly due to the compressibility effects typically being excluded from the analysis.

A more recent study by Ianniello [93] presents further theoretical analysis of the FW-H analogy applied to a marine propeller and also refers to E779a data computed using RANS and DES in the earlier studies mentione above. The author argues that non-linear flow phenomena and not the blade pass frequency-related ones are the main noise sources in the marine propeller context. Reportedly, this is because the relative efficiency of the rotating source becomes comparable to that of a quadrupole, unlike in a stationary case for which the low-order sources are much more efficient. For a marine propeller this phenomenon is said to arise due to the low rotational speeds and the consequently low Mach numbers, as well as multi-bladed design of propellers. The author hence argues that an accurate description of the entire flow field, including the wake, is needed to yield an accurate prediction of the acoustic signature of the non-linear problem. A related conclusion is that the noise due to the quadrupole sources may not be disregarded at low rotational speeds, which necessitates either the use of the porous FW-H analogy or the solution of the volume integral for the quadrupole source contribution. For the porous approach, careful treatment of the outlet FW-H integration surface is needed in order to avoid contamination of the far-field pressure predictions by the spurious noise source from quadrupole sources in the wake interacting with the FW-H surface. Following the author's logic, one may deduce that the presence of small bubbles in the wake of the propeller and their interaction with the vortical structures in the wake may also be important for the full acoustic description of the problem to be devised.

In a different study Pan & Zhang [155] studied the non-cavitating noise for the DTMB 4118 propeller in non-uniform inflow conditions using FW-H analogy evaluated on the propeller blade and a Detached Eddy Simulation (DES) flow solver. Tonal character of both propeller blade loads and radiated sound was reported and was expected due to

the cyclic nature of the inflow used in the study. Authors also reported a broadband contribution originating from the high blade-pass harmonics.

More recently, Lloyd *et al.* focused on using the FW-H acoustic analogy in order to compute the low-frequency, non-cavitating noise of the model-scale Insean E779a propeller [132, 133, 134]. Unsteady, incompressible RANS solver was reportedly used with the porous formulation of the acoustic analogy. The authors compared near-field viscous solver results with the pressure signals computed using the FW-H approach and found the two to be in satisfactory agreement. In this work authors cross-validate some of the findings by Ianniello *et al.* and also explore the influence of the FW-H porous surface orientation and grid structure on the predicted results.

A similar study was recently presented by Nitzkorski *et al.* [152] who studied the effect of trailing edge treatment on the radiated noise using an incompressible LES code and porous FW-H analogy implementation. The authors used dynamic end cap treatment to avoid problems with the vortices penetrating the control surface and were able to validate their code on a low Mach number cylinder test case. The work further develops the works by Ianniello *et al.* and Lloyd *et al.*.

Finally, a key study was recently presented by Bensow *et al.* [15] as this thesis was nearing completion. The authors solved the flow past the R/V Princess Royal using wall-modelled implicit LES and the Schnerr-Sauer cavitation model. The authors also applied the FW-H Formulation 1, both porous and surface-based, to predict the noise radiated by the propeller of the vessel. The authors assume $Ma \approx 0$, since it reaches the maximum of 0.02 for the propeller considered. They authors also validate their FW-H code on a low-Ma cylinder case, similarly to Nitzkorski *et al.*. In the final simulation 22 million unstructured, hex-dominant cells are reportedly used for the hull and 5 million for the propeller itself, which is meshed with a structured boundary layer and unstructured tetrahedra inside the rotating domain. The authors sample the acoustic data at 15 kHz and report little increase in the sound pressure levels due to cavitation. In the reported data the volume of cavitation was not particularly prominent, which offers a possible explanation for this behaviour. Importantly, the authors report noisiness in the SPL above 1 kHz, the origin of which they cannot explain. Around the medium frequency range above 400 Hz, relatively good agreement with the experimental noise data is reported, but below that range a rapid decrease of the SPL of approximately 20 dB with respect to the experiment is reported, which the authors were not able to explain either. Furthermore, the authors report little directivity in the predicted noise signature, which would not necessarily be expected in reality. An interesting observation is that the authors saw no substantial differences between evaluating FW-H on the porous surface or the hull shell itself. The authors hypothesise that the lack of the tip vortex cavitation may be responsible for some of the underwhelming acoustic results and point to the lack of simple, well-described in-depth validation data as a key obstacle in further developing the numerical methods.

2.6 Modelling challenges

High-fidelity turbulent flow modelling has become increasingly more popular with the rising computational resources available to the researches, but also industrialists, in recent years. This has led to methods such as DNS being used to study performance of aerospace gas turbines or aerofoil noise [103, 172]. Industrial applications of LES have seen wide use in studying the flows around aircraft wings in stall condition, bluff bodies, and jets [70, 73, 162, 166].

In the marine context, however, the inherently high Reynolds numbers make it rather challenging to use such methods on a regular basis, particularly when predicting full scale values. This is evident from relatively few authors abandoning RANS in lieu of LES or DES. The reason is mainly due to the high cell counts required to simulate fully appended ships at full scale. This may be better visualised by examining the non-dimensional cell size required at a wall,

$$y^+ = \frac{U_\tau u}{\nu} = \frac{y\sqrt{\tau_{wall}/\rho}}{\nu}. \tag{2.8}$$

In the above, the local wall shear stress, τ_{wall}, will increase with velocity so that for constant viscosity ν and higher Reynolds number, y^+ will rise for a fixed wall spacing y. For the ship considered in the example in Section 2.3.2 this would imply a wall-normal mesh spacing of $2.5{\cdot}10^{-5}$ m on the hull for $y^+ = 1$ at model scale (1:40) and $6.5{\cdot}10^{-6}$ m for the same criterion to be satisfied at full scale. Unfortunately, the cell size requirements in the remaining two directions for Large Eddy Simulation, between $x^+ \leq 100$ and $z^+ \leq 20$ [40] and $x^+ \leq 150$ and $z^+ \leq 40$ [68], are also quite strict. For a Reynolds Averaged Navier-Stokes (RANS) simulation similar wall-normal spacing is required but higher expansion ratios may be used and a much coarser discretisation can be employed in the directions parallel to the wall, making it significantly more affordable. This explains why prevailing majority of authors focus on RANS methods in the marine hydrodynamic world, both academically and industrially.

The nature of turbulence dictates that the largest flow scales present in the flow will be of the order of the characteristic dimensions of the body. Following on the example above, one could expect the largest eddies for a large container ship to be in the order of 10 - 20 m in size. For a full-scale, directly driven propeller the acoustic wavelength associated with the periodic cavitation and loading noise will be larger than 500 m. This difference of scales implies that finding a flow solution method applicable to both problems simultaneously may prove challenging due to the mesh size and fidelity requirements being different [136].

Moreover, a significant difficulty in computing marine flows is also associated with the relatively high speed of sound, c_0, in water compared to air, approximately 1500 against 340 m s^{-1}. Continuing with the example ship from Section 2.3.2, the expected Mach

numbers of the tip of the blade of a marine propeller would be less than 0.05. This implies that the speed of the wavefronts that need to be captured for a hydroacoustic simulation is over four times greater in water than in air, which in turn limits the maximum time steps possible. For example, in the very recent studies by Budich *et al.* and Yakubov *et al.*, time steps as small as 10^{-7} and 10^{-9} s were used [32, 207].

Furthermore, the higher density and speed of sound in water imply it has acoustic impedance, $z = \rho c_0$, 3500 higher than air. This means that for a pressure source of the same amplitude the induced particle velocity will be much smaller for water. From a numerical standpoint, the associated computational effort required to achieve full convergence using high order schemes, and mesh density necessary to keep the dissipation and dispersion errors low, may thus be expected to be higher for a computation in water than in air. It also follows that the amount of acoustic energy in the flow, compared with that contained in the other range of wave numbers, will be relatively low and hence difficult to discern [136].

Cavitation may be of periodic or random character. One should hence pay special care when analysing the time history of a particular quantity to distinguish between the periodic and random events. This imposes a need for long and statistically relevant data records, which are expensive to obtain computationally [96]. Another associated difficulty is that of the lack of validation data which would allow the predictions of unsteady, time-resolved phenomena, to be validated in detail [140].

There is also a large uncertainty in how different types of cavitation, in particular sheet and bubble cavitation, may be distinguished in a volume-of-fluid approach, which is currently used in a vast majority of studies. This method, discussed in more detail in the various sections of this thesis, describes the cavities using a scalar field which denotes what proportion of a given cell is filled with gas. As such, it is deemed appropriate for modelling well-defined cavities, such as sheet cavitation [87, 200, 202]. However, in the presence of bubble cavitation, occurring separately or during dynamics of sheet cavitation, this method does not provide any insight into the physics of the flow other than modelling the effect of the bulk of bubbles on the momentum and mass conservation equations. Moreover, it neglects some of the fundamental phenomena, such as bubble-bubble interactions, which will have a key effect on the radiated pressure [20].

Most of the cavitation models used in research, and more importantly, day-to-day fluid dynamic computations, utilise the incompressible flow assumption. This of course cannot propagate the shockwaves occurring during the collapse of the cavities, nor account for effects such as rebound or cushioning of the collapse due to the gas inside the cavities compressing [91]. Several methods using compressible flow are in use today but these are typically reported to be computationally expensive due to small time steps and high mesh densities required, as well as the necessity to incorporate elaborate discretisation schemes and pressure-velocity coupling algorithms [32, 67].

Nearly all of the reported cavitation models today are based on highly empirical expressions, which have not seen any significant change for well over a decade. These often neglect some of the underlying physics of cavitation, such as thermodynamic processes, presence of non-condensible gas, and different types of nucleation, all of which are expected to have an important effect on the predicted pressure pulses and, subsequently, noise [11, 12]. An interesting alternative to this are the Euler-Lagrange models which resolve the motion of small bubbles, or even individual cavitation nuclei [80, 195]. This category of approaches is by no means young [143], but it appears that only now do we have sufficient computational means to truly utilise it, despite it still being relatively expensive [202, 204].

It is conventional to carry out large parts of hydrodynamic analysis at model scale, both for industrial and validation purposes. This of course raises a question about accuracy of scaling the complex phenomena observed in a ship propulsion system, particularly when it comes to cavitation [96]. For example, the aforementioned study by Ponkratov *et al.* looked at predicting cavitation erosion at model and full scale [159]. The authors found that often very different approaches are needed to yield an accurate prediction at the two scales, indicating the difficulty in predicting the cavitation induced pressures. Comprehensive data allowing for these kind of scaling issues to be better understood is still very scarce, largely due to it being commercially sensitive, thus impeding the progress made in the open literature.

It is also important to note that at model and full scale the boundary layers will behave differently due to the Reynolds number typically being mismatched. This may significantly affect the cavitation [41] and make validation more challenging. Moreover, the water quality parameters are difficult to scale accurately even in experimental conditions [82]. Dependence of the cavitation models on the adopted values may thus lead to significant errors when full-scale performance is to be predicted based on model-scale simulations [159] or when numerical models validated in model-scale are applied to full-scale problems.

Irrespective of the modelling approach used, maintaining a precise description of the cavity interface remains challenging, particularly using the most commonly used volume-of-fluid models [10, 87, 139, 202]. This requires high mesh densities and high-order, specially designed numerical schemes which are likely to be expensive compared to the ones used in standard multiphase flow problems. If this is not ensured, capturing of the strong gradients of liquid and flow properties across the interface will not be possible and the obtained predictions will be non-physical [202].

Accurately resolving the cross-interface gradients may be expected to play an important role in minimising dispersion and dissipation errors for a sound wave to be predicted in the far-field. For this to be done successfully, the numerical schemes usually used in

cavitating flow simulations may be too dissipative, which poses a significant difficulty from the numerical accuracy and stability point of view [176].

Single-fluid cavitation models are said to capture the low frequency behaviour, including terms proportional to global flow quantities and their derivatives reasonably well [163, 171, 176]. However, due to the fact that typically the grid resolution used in combination with these methods is far too small to capture and resolve the small scale bubbles, the capturing of certain noise components is practically impossible to achieve in this way [139, 202, 204]. Few of these models account for the presence of incondensable gas, with exceptions of models such as the ones proposed by Singhal and the modified Schnerr-Sauer model introduced by Lu [139, 182]. If this is unaccounted for, even if compressibility is included in the analysis, accurate prediction of events such as rebound or pressure pulse generation may prove difficult [11, 12, 139].

2.7 Summary

It has been shown that marine propeller noise is a complex, multi-scale phenomenon and it has not been widely studied using modern fluid dynamic modelling techniques. This is because fully tackling all of its complexities, accounting for issues such as fully resolving the effect of hull boundary layer on the turbulence impinging on the propeller blades or incorporating the effect of ship motions on the flow will most likely remain computationally unachievable for the foreseeable future from a practical point of view. On the other hand, the growing computational resources allow one to depart from using simplistic methods, such as potential flow with empirical cavity models, and move on to more realistic high-fidelity methods [169]. These offer the potential to gain far more insight into the flow physics and relate those to the radiated noise.

Based on the review of the current state of the art, it has been concluded that while RANS methods may sometimes yield satisfactory predictions of unsteady cavitation behaviour, LES and DES are much better suited to such problems, despite the need for high mesh densities and small time steps. Furthermore, the use of compressible methods appears to offer significant advantages in modelling cavitating flows and will likely become increasingly more adopted as computational power increases. However, at present it has been decided to pursue the incompressible mass-transfer modelling approach due to its lower cost and satisfactory capabilities at capturing large scale cavitation presented in the literature.

Three main challenges to be addressed in this thesis have been identified.

- Being able to accurately resolve the turbulent, cavitating flow around a propeller.
- Developing a capability to predict far-field noise propagation from near-field CFD simulations

- Being able to account for a wide range of frequencies affected by cavitation noise.

Addressing these would allow the noise generated by a marine propeller to be fully modelled using CFD. In the next Chapter means to numerically model the flow past a marine propeller, accounting for cavitation, will be discussed, paving the way for developing a numerical framework aiming to address the remaining major milestones.

Chapter 3

Methodology

3.1 Introduction

In order to allow marine propeller noise to be modelled and accomplish the objectives of this thesis, a wide range of methods had to be adopted but also implemented, allowing equations describing unsteady, cavitating flow to be solved and the generated noise modelled. The purpose of this Chapter is to introduce the basic methods utilised in order to numerically solve the governing equations of multiphase fluid motion. First, the open-source OpenFOAM framework for solving partial differential equations is introduced and the justification for using it is given. Then, the Navier-Stokes and continuity equations are discussed, and the principle ideas behind the finite volume method are outlined. This is followed by highlighting a range of turbulence modelling techniques varying in the range of complexity and associated computational expense. The Chapter concludes by summarising the fundamental methods for solving multi-phase flow.

3.2 The OpenFOAM framework

Throughout this thesis the open-source OpenFOAM framework [190] has been used in order to solve the partial differential equations governing the fluid flow. This comprises a wide range of libraries and executables that may be used to model fluid flow, but also a much wider range of phenomena, such as magnetics or chemical reactions. The most distinguishable feature of the code is that is distributed under the GNU licence agreement, which gives the users full access to the underlying source code and allows them to implement their own solvers and utilities, building upon the basic code. This speeds up the development of novel techniques and has been relied upon strongly throughout the present project when new acoustic analysis and cavitation models were being developed.

3.3 Flow motion and the finite volume method

3.3.1 Governing equations

Any fluid may be shown to follow the equations of conservation of mass, termed the continuity equation,

$$\frac{\partial \rho}{\partial t} + \nabla \cdot (\rho \mathbf{U}) = 0, \tag{3.1}$$

where ρ denotes the fluid density and $\mathbf{U}$ its velocity. The above equation implies that no mass may be created or destroyed at any one time.

Furthermore, the fluid is also required to obey the conservation of momentum, also called the Navier-Stokes equation,

$$\frac{\partial (\rho \mathbf{U})}{\partial t} + \nabla \cdot ((\rho \mathbf{U}) \otimes \mathbf{U}) = -\nabla p + \mu \mathbf{D}. \tag{3.2}$$

Here p is the fluid perssure, μ is the dynamic viscosity of the fluid, and $\mathbf{D}$ denotes the deviatoric stress tensor. This equation implies that the action of all forces on an element of fluid is accounted for and results in acceleration. The stress tensor $\mathbf{D}$ may also be written as

$$\mathbf{D} = 2\left(\mathbf{S} - \frac{1}{3}(\nabla \cdot \mathbf{U})\,\mathbf{I}\right), \tag{3.3}$$

where $\mathbf{I}$ is the identity matrix and $\mathbf{S}$ the symmetric part of the strain rate tensor,

$$\mathbf{S} = \frac{1}{2}\left(\nabla \mathbf{U} + (\nabla \mathbf{U})^T\right). \tag{3.4}$$

In the the form showin in Eq. (3.1) and (3.2), the equations of motion of a fluid do not make any assumption on whether the medium is compressible or not. In other words, they allow for the density to vary in space and time. If mass per unit volume of the fluid is fixed, one may simplify Equations (3.1) and (3.2) by arriving at the so-called incompressible formulation,

$$\nabla \cdot \mathbf{U} = 0, \tag{3.5a}$$

$$\frac{\partial (\mathbf{U})}{\partial t} + \nabla \cdot (\mathbf{U} \otimes \mathbf{U}) = -\frac{1}{\rho}\nabla p + \nu \mathbf{D}, \tag{3.5b}$$

where ν is the kinematic viscosity.

No analytical solution exists to Equations (3.5) for a general case. This implies that they need to be solved using numerical methods. In the presented work this is done by first rewriting the governing equations into an integral form, following the finite volume approach, then discretising the gradients of variables, and finally iteratively solving for pressure and velocity until both momentum and mass of the fluid are considered conserved down to a specified tolerance.

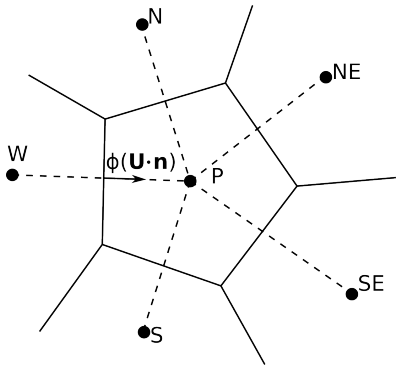

Figure 3.1: Principle of the fnite volume method. Sum of fluxes of the scalar ϕ is used to compute a balanced scalar field. $\mathbf{n}$ is a surface area vector of the face joining cells P and W.

3.3.2 The finite volume method

Several ways allowing differential equations, such as Equations (3.5), to be described using a finite set of values, or in other words discretised, exist. In this work the finite volume approach is utilised. This is based on dividing the space occupied by the fluid flow into a set of non-overlapping control volumes, or cells, as shown in Figure 3.1. The governing equations are then rearranged and integrated over the finite volume of each cell [148].

For instance, the incompressible continuity equation, Eq. (3.5a), can be integrated over a cell of volume V, yielding

$$\int_V \nabla \cdot \mathbf{U} \mathrm{d}V = 0. \tag{3.6}$$

Integral in Eq. (3.6) may be rewritten using the Gauss' theorem in order to express the integral in the form of fluxes on the surface of the cell. This yields

$$\int_S \mathbf{U} \cdot \mathrm{d}\mathbf{A} = 0, \tag{3.7}$$

where S is the surface area of the cell and $\mathbf{A}$ is the surface area vector of an infinitesimal element of this surface. Physically, the above equation implies that, for mass to be conserved in an incompressible flow, the sum of volume fluxes into any given cell must be zero. The same process may be repeated for the momentum equations, Eq. (3.5b), or any transport equation of an arbitrary variable. For more complex equations it is also usual to include sources and sinks located at the centre of each cell, which are used to model physical phenomena like generation of turbulent kinetic energy of phase change.

3.3.3 Numerical schemes

Numerical solution of differential equations using the finite volume method requires flow quantities, such as pressure and velocity, to be known at face centres in order for the surface integral over faces of each cell (see Equation (3.7), for instance) to be solved. Possibly the simplest shape assumption is linear interpolation, which for two neighbouring cells P and E, whose centroids are spread along the x-axis, yields

$$\phi_e = \frac{\phi_E - \phi_P}{x_E - x_P}(x_e - x_P) + \phi_P, \tag{3.8}$$

where ϕ is an arbitrary variable, subscripts P and E refer to cell centre values, and e denotes a value defined at the cell face. If for the sake of example the grid is assumed to be unifrom and of a constant grid spacing Δx, the above expression reduces to

$$\phi_e = \frac{\phi_E + \phi_P}{2}, \tag{3.9}$$

as one might intuitively expect. It is also important to obtain the values of gradients at cell faces in order to solve partial differential equations using the finite volume method. First, expanding the face centre value using both cells P and E yields

$$\phi_E = \phi(x_e + \frac{\Delta x}{2}) = \phi(x_e) + \frac{\Delta x}{2}\phi'(x_e) + \frac{(\frac{\Delta x}{2})^2}{2!}\phi''(x_e) + \mathrm{O}[\Delta x^3], \tag{3.10a}$$

$$\phi_P = \phi(x_e - \frac{\Delta x}{2}) = \phi(x_e) - \frac{\Delta x}{2}\phi'(x_e) + \frac{(\frac{-\Delta x}{2})^2}{2!}\phi''(x_e) + \mathrm{O}[\Delta x^3]. \tag{3.10b}$$

Subtracting the above equations from each other and rearranging to yield $\phi'(x_e)$ gives

$$\phi_E - \phi_P = \Delta x \phi'_e + \mathrm{O}[\Delta x^3], \tag{3.11}$$

or

$$\phi'_e = \frac{\phi_E - \phi_P}{\Delta x} + \mathrm{O}[\Delta x^2]. \tag{3.12}$$

Therefore, for a uniform grid, the linear scheme is second order accurate as the truncated terms are proportional to Δx^2. Similar procedure may be followed to approximate higher order derivatives. It may be expected that some of the accuracy will be lost for a non-uniform grid. This is because structured meshes can be aligned with the flow, making the calculation of fluxes less susceptible to numerical errors.

It may shown that in certain conditions the linear scheme may become unbounded, meaning it may produce over- or under-shooting values with respect to the boundary condition values during solution. This is detrimental to numerical stability and so first order schemes, such as the upwind scheme, are therefore sometimes employed in computational fluid dynamic approaches. This simply assigns the cell face value equal to that

at the cell centre *upstream*,

$$\phi_e = \begin{cases} \phi_P, & \text{if } U_x \geq 0 \\ \phi_E, & \text{otherwise} \end{cases}. \tag{3.13}$$

Low-order schemes are detrimental to numerical accuracy and so ought to be avoided when possible, particularly when computing cavitating flows which require fine flow features to be computed. Mixed, or hybrid, approaches trying to bring the best of two worlds also exists. These are typically constructed in such a way as to be at least second order accurate but satisfy boundedness of the solution. For this reason they are sometimes referred to as total variation diminishing, or TVD, schemes [98].

In OpenFOAM two such schemes are readily implemented. The limited linear scheme attempts to linearly weigh the amount of central and upwind parts of the interpolation quantity,

$$\phi_f = \phi_f^u + \gamma \left(\phi_f^c - \phi_f^u \right), \tag{3.14}$$

where subscript f denotes a face value interpolated either using an upwind or central scheme, marked using superscripts u or c, respectiely, and γ is a weighting factor.

A more complex filtered linear scheme attempts to automatically control and adjust the amount of upwinding applied locally for each face. This is done by computing a limiter value,

$$\Phi = (1 + \Pi) - \Gamma \left[\frac{\min([\Delta J - (\nabla J)_P], [\Delta J - (\nabla J)_E])}{\max([(\nabla J)_P], [(\nabla J)_E])} \right], \tag{3.15}$$

where J is the flux between cells P and E, and Π and Γ are the scaling coefficients $(\Phi, \Gamma) \in < 0, 1 >$. If the difference in flux between the two cells, ΔJ, is larger than the gradient of the flux, ∇J, the scheme favours the upwind approach at the face shared by the two cells to increase stability. Otherwise it makes the interpolation more centred. In the present work the filtered linear approach, or `filteredLinear2V` in OpenFOAM terms, is preferred, due to the increased numerical stability and accuracy it offers [136].

3.3.4 Linearised equation solution

Once a differential equation has been linearised using appropriate numerical schemes, it may be expressed in a matrix form

$$\mathbf{A}\mathbf{x} = \mathbf{b}, \tag{3.16}$$

where $\mathbf{A}$ is the coefficient matrix depending on, for instance, the fluid parameters or mesh properties, $\mathbf{x}$ is the vector of unknowns describing a field such as velocity or pressure, and $\mathbf{b}$ is the boundary conditions vector which will enforce the action of boundaries of the domain, as well as introduce additional source terms.

For a typical computational fluid dynamic problem the coefficient matrix is sparse, meaning most of its elements are filled with zeros, indicating that only neighbouring cells affect the solution for any given mesh element. The number of the adjacent elements which have an effect will increase with using higher order schemes, as they require more data points to make an assumption about the profile of the variable [148].

A wide range of linear solvers is available in the OpenFOAM framework and listing all of them is beyond the scope of this section of the Chapter. Typically, the multi-grid `GAMG` solver was used for solving the unsteady pressure equation. In most cases the problem was first smoothed with the diagonal incomplete-Cholesky solver mixed with the Gauss-Seidel solver (`DICGaussSeidel`). For most unsteady simulations, other fields, including individual components of the velocity, were preconditioned using the diagonal incomplete-LU method and solved with the preconditioned bi-conjugate gradient solver, `PBiCG`. These general rules were not always observed, particularly in the earlier simulations when the used numerical set up was still evolving. Hence settings for each individual case are also introduced individually in the subsequent chapters where appropriate. These differences in set up do not affect the validity of current results as convergence criteria were strictly observed for all simulations carried out.

3.3.5 Pressure-velocity coupling

Unless any additional modelling is involved, the Navier-Stokes and continuity equations have two unknowns, namely pressure and velocity. This implies that for both of the equations to be satisfied at the same time, coupling between these two variables needs to be solved. In OpenFOAM this is done in an implicit way, either using the Pressure-Implicit Splitting of Operators (PISO) or PIMPLE (hybrid of PISO with the SIMPLE, or Semi-Implicit Method for Pressure Linked Equations) algorithms [45]. Full description of these two algorithms is provided by Wan *et al.* [199]. In the present work, the PISO algorithm was preferred. It has been found to typically require smaller time steps to achieve the same iterative convergence as the PIMPLE method. However, time steps for most of the considered cavitating flow simulations are also limited by the physics they attempt to predict, which means satisfactory level of convergence may often be achieved with just a single outer solver loop.

3.4 Reynolds Averaged Navier-Stokes equations

3.4.1 Overview

The velocity and pressure of the flow at a given point may be seen as as a sum of a time-averaged value, denoted by an overline, and a fluctuating component, marked by

a prime symbol,

$$p = \overline{p} + p', \tag{3.17a}$$

$$\mathbf{U} = \overline{\mathbf{U}} + \mathbf{U}'. \tag{3.17b}$$

Since it is often the mean quantities that are of interest in an engineering context, a substantial amount of effort has been devoted to creating numerical models capable of predicting these without having to resolve the computationally expensive unsteady components. This has given rise to the formulation of the Reynolds Averaged Navier-Stokes (RANS) equations.

These may also be used to solve unsteady flow in the form of unsteady RANS, or URANS. In a physical sense, an URANS solution postulates that the time and space scales of the mean flow can be separated from the turbulent motions in the fluid. In many applications, such as turbulent jets, the aptness of this assumption may be questioned. However, in case of a marine propeller one may expect large changes to the mean flow due to the rotating motion being the dominant feature in the flow and so URANS can potentially be used in this context. In an acoustic application the disadvantage of URANS is that the broadband part of the noise spectrum associated with the turbulent motions may not be captured. This is because RANS only models the effect of turbulent fluctuations rather than resolves them. For a marine propeller case, an URANS solution may be able to resolve the low-frequency blade-pass component of the radiated noise, however, and so is still of interest in this work, given its relatively low computational cost [89, 132, 134].

3.4.2 Averaging of the Navier-Stokes equations

By utilising the assumption that any flow quantity may be described by a Reynolds time-averaged mean and a fluctuating component, and substituting Equation (3.17) into the incompressible mass and momentum conservation equations, Eq. (3.5),

$$\nabla \cdot \overline{\mathbf{U}} = 0, \tag{3.18a}$$

$$\frac{\partial \overline{\mathbf{U}}}{\partial t} + \nabla \cdot \left(\overline{\mathbf{U}} \otimes \overline{\mathbf{U}}\right) + \nabla \cdot \left(\overline{u'u'}\right) = -\frac{1}{\rho}\nabla \overline{p} + \nu \nabla^2 \overline{\mathbf{U}}. \tag{3.18b}$$

To arrive at this form, one has to use the property that the mean of the fluctuating component is zero, $\overline{\phi'} = 0$. The additional term in (3.18), $\rho\nabla \cdot \left(\overline{u'u'}\right)$ is termed the Reynolds' stress tensor and represents the action of turbulence on the mean flow. It arises due to the observation that the mean of the product of two quantities with a zero mean does not necessarily tend to zero.

Several decades of research have been devoted to coming up with appropriate models for the non-linear stress tensor created by the Reynolds' averaging process. The most basic ones adopt simple analytical expressions derived from boundary layer theory and the more complex approaches solve up to several additional transport equations. Its beyond the scope of this work to describe them in detail as main focus of this thesis is about using more advanced modelling techqniques, such as LES or DES.

One of the most popular models in the marine community is the $k-\omega\,SST$ [146]. It uses two additional variables, the turbulent kinetic energy, k, and the specific dissipation rate, ω, to provide expressions for the turbulent length and time scales. These are then used to yield a scalar variable, the turbulent viscosity ν_T. This quantity aims to relate the rate of strain in the mean flow to the action of turbulence turbulence to the mean flow following the Boussinesq hypothesis. Exact details of the model are discussed by Menter [146]. This model was utilised in most of the early simulations as it is, by far, the most common turbulence model used by the maritime community [149].

3.5 Large and Detached Eddy Simulation

3.5.1 Overview

Large Eddy Simulation (LES) is a method of computing the flow motion with a higher degree of fidelity than URANS, as it resolves the larger eddies forming the turbulent flow. It follows that this approach is only applicable to time-resolved simulations as no mean quantities are used during the solution. The fundamental principle of this category of methods is filtering the equations of motion of a fluid, which allows the motions with more kinetic energy to be resolved directly, while the smaller ones responsible for dissipative effects are modelled. Relative proportions of the turbulent energy spectrum which remain resolved and modelled depend on the filtering operation applied to the flow equations. LES is, in general, more expensive than RANS as it requires much finer time steps and grid resolution. It does allow the broadband components of the noise due to fluid motion to be captured, however, and so has seen significant use in the aeroacoustic field, both from research and industry perspectives [70, 162, 179].

In order to obtain an accurate solution capable of providing reliable noise data, it is not uncommon in the aeroacoustic field to use numerical schemes of order 4 and higher [103, 172]. This does impose a significant demand on the numerical methods used to obtain a stable solution at an acceptable computational effort. Such high-order schemes are not commonly used in marine context due to the incompressible flow assumption making their use much more difficult. Also, and high density gradients present in many marine-related contexts necessitate the use of increasingly dense grids as larger stencils become introduced, further increasing computational costs.

Moreover, as one moves closer to a solid boundary, the resolution required to resolve the spectrum of eddies becomes prohibitively expensive as the relevant scales become very small. A potential solution to this issue is the use of Detached Eddy Simulation (DES) where the near-wall region is solved for using unsteady RANS calculations and LES is used further away [159]. This potentially offers some computational cost reductions but requires a more complex solution method. Another alternative is using a wall-model to approximate the physics in the inner boundary layer [15, 136].

LES has traditionally been considered too expensive for marine simulations. Advanced turbulence modelling techniques have been, however, gaining ground in this context, particularly in the field of cavitation modelling. For instance, work by Bensow *et al.* [11, 87, 139, 202] has reported using LES successfully in various marine-related contexts. More recently Budich *et al.* have reported using a compressible LES code for computing cavitating flow around the Potsdam Propeller Test Case [32]. Furthermore, the work by Ponkratov *et al.* has seen the use of DES for industrial applications of cavitation modelling showing a strong incentive for such advanced turbulence modelling techniques to be applied to unsteady ship flows [159]. This is further evident in work by Fujiyama who has described development of a compressible, cavitating flow solver based on scale-adaptive simulations (SAS) and applied it to a flow around a marine propeller [67]. This trend may be explained by the fact that cavitation modelling itself imposes quite stringent grid and time step requirements. Thus, it becomes affordable to sacrifice a little more computational power to use higher fidelity methods, given their increased accuracy in predicting the unsteady cavitation behaviour [202].

3.5.2 Filtering of the Navier-Stokes equations

By applying the filtering operator, denoted by an overline $\overline{\phi}$, to the mass and momentum conservation equations, Eq. (3.5), the effect of the small, unresolved (or subgrid) scales, on the flow may be removed, yielding

$$\nabla \cdot \overline{\mathbf{U}} = 0, \tag{3.19a}$$

$$\frac{\partial \overline{\mathbf{U}}}{\partial t} + \nabla \cdot \left(\overline{\mathbf{U}} \otimes \overline{\mathbf{U}}\right) = -\frac{1}{\rho}\nabla p + \nu \nabla^2 \overline{\mathbf{U}} - \nabla \cdot \boldsymbol{\tau}, \tag{3.19b}$$

where the subgrid stress tensor, $\boldsymbol{\tau}$, represents the effect of the scales that have been filtered out. This may be written as [45]

$$\boldsymbol{\tau} = \overline{\mathbf{U} \otimes \mathbf{U}} - \overline{\mathbf{U}} \otimes \overline{\mathbf{U}}. \tag{3.20}$$

The low-pass filtering removes smaller eddies from the velocity field and is performed using a convolution operator, G, whose kernel is defined by the filter width, δ, as

$$\overline{u}_i = G u_i \quad and \quad \overline{p} = G p. \tag{3.21}$$

The physical effect of this operation is better visualised by, for instance, looking at the convective term of the momentum equations [202]

$$\nabla \cdot (\mathbf{U} \otimes \mathbf{U}) = \nabla \cdot \left(\overline{\mathbf{U}} \otimes \overline{\mathbf{U}}\right) + O[\delta^2], \tag{3.22}$$

which indicates how the scales smaller than the filter width are separated from the resolved scales.

One way to provide an expression for the subgrid stress tensor is to use scale similarity hypothesis, which states that the largest filtered and smallest resolved scales are fundamentally similar [168]. The effect of subgrid scales on the computed flow field is said to be well accounted for using this category of models [136]. Following this approach, the subgrid stress tensor may be defined following the work by Bardina [8] using a double filtering operator, yielding

$$\boldsymbol{\tau} \approx \overline{\overline{\mathbf{U}} \otimes \overline{\mathbf{U}}} - \overline{\overline{\mathbf{U}}} \otimes \overline{\overline{\mathbf{U}}}. \tag{3.23}$$

Alternatively, the subgrid stress tensor may be modelled in a similar fashion to the turbulent eddy viscosity in RANS models by using the Boussinesq hypothesis. The latter assumes that the needed tensor may be described using a product of the fluid strain rate, $\mathbf{S}$, and an assumed subgrid viscosity, ν_{SGS}, yielding

$$\boldsymbol{\tau} - \frac{1}{3}\boldsymbol{\tau} \cdot \mathbf{I} = -\nu_{SGS}\mathbf{S}, \tag{3.24}$$

where $|\mathbf{S}| = (2\mathbf{S} \cdot \mathbf{S})^{1/2}$.

One of the simplest available models of this category is that by Smagorinsky, according to which the subgrid viscosity may be defined using the filter width, Δ, and a calibration constant, C_S, as

$$\nu_{SGS} = \left(C_S\overline{\Delta}\right)^2 |\mathbf{S}| \,. \tag{3.25}$$

This is said to be of limited accuracy for complex geometries, as a constant value of the calibration constant does not allow for local flow phenomena to be predicted accurately. One may thus chose to dynamically evaluate the proportional coefficient. According to Germano *et al.* [69], a resolved stress tensor may be defined as

$$\mathbf{L} = \widehat{\overline{\mathbf{U}} \otimes \overline{\mathbf{U}}} - \hat{\overline{\mathbf{U}}} \otimes \hat{\overline{\mathbf{U}}}, \tag{3.26}$$

where the caret operator denotes the test filter operator. The latter is defined similarly to the grid filter but utilises a different width and describes the range of scales between the test and grid filters. Equation (3.26) may be compared with (3.24), allowing for an expression to be derived for the proportional constant in (3.25) [129].

The most advanced model used in the present study is the dynamic mixed Smagorisnky model which aims to provide enhanced accuracy by combining the Smagorinsky-, or

functional-, type models with the scale similarity, or structural, ones. Following Zang et al. [208], this may be expressed as

$$\boldsymbol{\tau}^S - \frac{1}{3}\tau^S \cdot \mathbf{I} = \frac{1}{2}\left(-2\nu_{SGS}\overline{\mathbf{S}} + \tau^B - \frac{1}{3}\tau^B\mathbf{I}\right). \tag{3.27}$$

In Equation (3.27), B denotes the contribution from the Bardina model. An expression for the dynamic Smagorinsky constant may now be written as

$$C_{\mathrm{S}}^2 = \frac{1}{2}\left(\frac{(\mathbf{L}-\mathbf{B})\cdot\mathbf{M}}{\mathbf{M}\cdot\mathbf{M}}\right), \tag{3.28}$$

where

$$\mathbf{M} = 2(\overline{\Delta}/\hat{\Delta})^2\hat{\overline{|\mathbf{S}|}}\hat{\overline{\mathbf{S}}} - \hat{\Delta}^2\widehat{\overline{|\mathbf{S}|}\overline{\mathbf{S}}}, \tag{3.29a}$$

$$\mathbf{B} = \widehat{\overline{\overline{\mathbf{U}}\otimes\overline{\overline{\mathbf{U}}}}} - \hat{\overline{\overline{\mathbf{U}}}}\otimes\hat{\overline{\overline{\mathbf{U}}}}. \tag{3.29b}$$

A completely different alternative to treating the LES problem is neglecting the subgrid model completely and instead using the numerical diffusion provided by the computational grid and numerical schemes to imitate the dissipative effect of the neglected scales [11, 87, 139, 202]. This method is often called implicit-LES (ILES). Aside from simplifying the overall numerics, this approach has been reported by Bensow *et al.* to reduce the problems associated with sharp fluid property gradients occurring at the cavity interface [13]. The ILES method has also been shown not to over-predict the subgrid scale viscosity in the cavity closure region, which has been reported as a significant issue in capturing cavitation dynamics [202]. However, as shown in the study by Lloyd [136], non-uniformity of grid in different directions may lead to the different velocity components being affected to a different degree when an implicit model is used. This implies that an additional level of care needs to be taken when undertaking the mesh design, especially for cases involving complex geometries such as marine propellers, potentially reducing the practical benefits of using ILES.

3.5.3 Boundary Treatment

An important issue with conducting an LES simulation with acoustic analysis in mind is the need to avoid pressure waves reflecting back into the numerical domain. This may be achieved by using non-reflective boundary conditions on the external domain boundaries [39]. In modern CFD, buffer zones are considered as the most flexible means of reducing the effect of the boundaries. These simply add additional terms to the flow equations to damp out the oscillations [39].

An alternative method is to use a large domain with cell stretching in order to destroy fluctuations in the direct vicinity of the domain [39]. This is, however, often impractical

due to the associated unnecessary computational cost. Unfortunately, to the authors knowledge, no readily available implementation of these boundary conditions exists in the official OpenFOAM version, and hence large domains with cell stretching are often adopted.

Even if incompressible flow is being solved, the wake of the propeller may have an effect on the upstream solution, particularly if the turbulent eddies impinge on the domain outlet while still having a considerable amount of energy in them. Again, this may be avoided by designing the numerical grid to be very long and with a significant amount of coarsening downstream. An alternative is the use of a convective outlet boundary condition which allows the eddies to leave the domain freely [136]. This uses a prescribed convection velocity, U_C, typically equal to the mean flow speed, and makes sure the boundary values of the velocity field satisfy

$$\frac{\partial \mathbf{U}}{\partial t} + U_C \left(\nabla \cdot \mathbf{U} \right) = 0. \tag{3.30}$$

This method was utilised in some of the early simulations of hydrofoil cavitation but was then replaced by a conventional outlet boundary condition due to problems with numerical stability. Longer domains with cell stretching were thus used to dissipate the eddies before they reach the downstream end of the domain.

As already mentioned, the issue of high mesh density required in the wall region is a significant obstacle limiting the use of LES in the marine context. One of the ways to overcome this is to use wall functions in order to model the effect of the wall on the flow [87, 202]. This assumes pre-defined boundary layer characteristics and so reduces the accuracy of the prediction in the cases where this behaviour would not be followed. This approach has been reportedly used positive results in multiple studies focused on marine propellers and hydrofoils [87, 139, 202]. Potentially, however, it may not cope well with very strong adverse pressure gradients or prediction of recirculating flows, both of which may be expected in case of severely cavitating bodies. In the present studies, simulations both with and without wall functions were used, with preference being given to the latter in order to reduce the amount of assumptions made.

3.5.4 Detached Eddy Simulation

In order to allow accurate modelling of the unsteady flow but reduce the computational expenses associated with the use of pure LES, Detached Eddy Simulation (DES) model, based on the Spalart-Allmaras RANS formulation [183], was also used in several of the presented studies. In general, it has been found to offer a satisfactory balance between fidelity and cost, which was deemed necessary if the proposed methods are to be adopted on a wider scale throughout the maritime community.

In this approach, the RANS equation, Eq. (3.18), is solved in the attached boundary layer and gets blended into a Large Eddy Simulation (LES) formulation, given by Eq. (3.19), further away from the solid wall. This is done based on defining a limiting length for which RANS equation is solved,

$$l_{DES} = \min(d_w, C_{DES}\Delta), \tag{3.31}$$

which is dependent on the wall distance d_w, a constant C_{DES}, and grid size Δ. This gives rise to issues for cells inside the boundary layer if the numerical mesh is fine [183] and hence a fix has been used to delay the transition to the LES mode by the use of additional blending functions similar to the ones used in the shear stress transport (SST) RANS model [147]. This gives rise to the so-called Delayed Detached Eddy Simulation (DDES), utilised in the present work.

In the underlying RANS model, the Boussinesq hypothesis is used in order to provide an expression for the Reynolds stress tensor. The model solves an additional transport equation for a variable $\hat{\nu}$,

$$\frac{\partial \hat{\nu}}{\partial t} + \nabla \cdot (\mathbf{U}\hat{\nu}) = c_{b1}\hat{S}\hat{\nu} - c_{w1}f_w\left(\frac{\hat{\nu}}{d}\right)^2 + \frac{1}{\sigma}\left[\nabla \cdot ((\nu + \hat{\nu})\nabla\hat{\nu}) + c_{b2}(\nabla\hat{\nu})^2\right], \tag{3.32}$$

with details of the constants discussed at length in the original reference [183]. Once $\hat{\nu}$ has been obtained, it may be used to compute the turbulent eddy viscosity

$$\mu_t = \rho\hat{\nu}f_{v1} \tag{3.33}$$

as a function of $\chi = \hat{\nu}/\nu$ and

$$f_{v1} = \frac{\chi^3}{\chi^3 + c_{v1}^3}. \tag{3.34}$$

3.6 Multiphase flow modelling

3.6.1 Overview of available methods

Multiphase flow entails transport of several fluids mixed above the molecular level and may refer to applications such as propeller cavitation, flow past a ship hull, mixing in industrial processes, or river bank erosion, to name a few [24]. It follows that a wide range of approaches are available in the literature, many of them having been derived with very specific objectives in mind. Several main categories of multiphase flow models may be distinguished, the following summarises those of them which have been most commonly used to model cavitation or similar problems [24, 87, 110, 138, 196, 206, 207].

- **Lagrangian** - these methods trace the motion of individual bubbles (or larger, representative particles) by analysing the forces acting on each of them individually [81, 131, 195]. One needs to treat every bubble independently, which allows the effect of its time history to be accounted for, for instance by incorporating thermodynamic effects into the the governing equation, which will most likely take the form of one of the variants of the Rayleigh-Plesset equation. Mass and momentum of the fluid are solved for the main phase using standard finite volume procedures and the particles are tracked by their equation of motion being integrated in time. Various degrees of fidelity exist in accounting for the exchange of momentum, mass and energy between the two phases, ranging from one-way coupling, where bubbles do not affect the flow, to accounting for complex effects the bubbles have on the flow and each other [80, 196, 207].

- **Euler** - this set of approaches relies on the use of traditional finite volume meshes to resolve both the fluid flow and cavitation. The multiphase problem must then be described using an appropriate method, such as volume of fluid or level-set. An expression describing the phase change is required in order to model the dynamic creation and destruction of cavities.

- **Hybrid** - combine both of the above categories into a single model. These methods have reportedly been seen as an efficient way of tackling the multi-scale cavitation problem because they are capable of tracing the smaller bubbles on relatively coarse grids while still resolving the dominant cavitation phenomena [80, 143, 163, 196]. A more in-depth discussion will be devoted to this methodology in subsequent parts of this thesis, particularly Chapter 9.

Within the Euler methods, by far the most prevalent in the scope of marine applications, one may distinguish between the following categories of models, which differ in the way in which they deal with the presence of two fluids.

- **Level-set** - solve for a distance function governed by a scalar transport equation. This function represents the cavity interface explicitly and so its reconstructionis not necessary. This method makes it difficult to satisfy the mass conservation at all times, particularly if one considers adding source terms accounting for vaporisation and condensation [145, 196]. Having access to the exact position of the interface makes it easier, however, to better account for the effects of surface tension and removes the ambiguity associated with deciding on where the interface between the fluids actually is.

- **Marked particles** - an individual cell is either empty or full at any one time, depending on whether there is a particle present or not; this often yields a smeared interface separating the two fluids, but can capture complex phenomena with a

large amount of mixing; there is an associated high computational cost as there is a need to solve many equations of motion simultaneously [87, 145, 196].

- **Inhomogeneous** - both liquid and vapour phases occupy the same space but are governed by two sets of mass and momentum equations. Coupling is achieved by matching the velocity fields of both fluids at the interface [71]. This is done by using a void fraction and by including source terms in the momentum equations [71, 130, 196].
- **Homogeneous Volume of Fluid (VOF)** - solves for a scalar field representing the fraction of a cell filled with the vapour [130, 131, 145]. The fluid properties are interpolated between the two extreme possibilities (all-water or all-vapour) and the weighted values are used to solve a single set of momentum and continuity equations for the mixture [131, 196]. Reported to be versatile and robust but suffers from difficulties with keeping the interface sharp and makes identifying the exact interface difficult [111, 112, 173, 182].

At the time of writing, the VOF methods appear to be the world-wide standard in terms of high-fidelity cavitation modelling techniques and have seen a plethora of successful application [87, 171, 195, 202, 204]. As such, it has been decided to pursue this methodology as the baseline for this project. The biggest disadvantage these models from a hydroacoustic point of view is that they use a field representing a region where cavitation will occur without modelling the individual bubbles, and thus neglect the broadband noise component [111, 112, 173, 182]. This occurs due to the inherent averaging of fluid properties over each grid cell. Lack of detailed information about the cavity interface is also a drawback of the VOF approaches. Their strong suit are their ability to observe the mass continuity and relative ease of implementation of the base model and modifications building upon it.

3.6.2 The volume of fluid approach

The volume of fluid (VOF) approach treats the two fluids as an immiscible mixture occupying the same space, or volume, and assumes its motion to be governed by a single set of momentum and mass conservation equations, in this case Equation (3.5) [24]. This implies that for small particles on a coarse numerical mesh averaging of the effect of the transported vapour phase, in case of cavitation, is approximate and undergoes inherent averaging [24].

The VOF method defines an additional scalar, termed the volume fraction α, which describes what percentage of a given cell is filled with water ($\alpha = 1$) and what with vapour ($\alpha = 0$). Once the relative proportions of water and vapour have been established throughout the numerical domain, individual fluid properties for both phases are

assumed to be constant and are interpolated locally according to the cell volume fraction value,

$$\rho = \alpha\rho_{\mathrm{v}} + (1-\alpha)\rho_{\mathrm{l}}, \tag{3.35a}$$

$$\mu = \alpha\mu_{\mathrm{v}} + (1-\alpha)\mu_{\mathrm{l}}. \tag{3.35b}$$

In the above, ρ and μ refer to the density and dynamic viscosity of the individual phases denoted by subscripts l for liquid and v for vapour. In an actual simulation the interface between the two phases is typically denoted by $\alpha = 0.5$ and in most applications it is expected that the region of intermediate volume fraction values will be small and confined to few cells. This is not true for cavitation where clouds of bubbles characterised by intermediate volume fraction values are expected.

The distribution of the volume fraction obeys the same laws as any other scalar. Thus, its motion may be described by virtue of a general transport equation,

$$\frac{\partial\alpha}{\partial t} + \nabla\cdot(\alpha\mathbf{U}) = \frac{\dot{m}}{\rho_{\mathrm{l}}}, \tag{3.36}$$

where the source term on the right hand side of the equation, termed the mass transfer rate, denotes the rate of destruction (or creation, depending on the reference system) of the liquid (or vapour) phase [11, 87, 145, 195, 202, 204].

Presence of a non-zero source term on the right hand side of Equation (3.36) implies that the velocity field will not be divergence free [11, 196], which introduces an important modification to the equations of motion of the fluid. This may be shown by substituting Equations (3.35) into the general continuity equation, Equation (3.1), which yields

$$\nabla\cdot\mathbf{U} = \left(\frac{1}{\rho_{\mathrm{v}}} - \frac{1}{\rho_{\mathrm{l}}}\right)\dot{m}. \tag{3.37}$$

The non-zero right hand side indicates that the source term will affect both the α transport equation and the pressure equation [11].

3.6.3 Mass transfer cavitation models

Given the popularity of the volume-of-fluid multi-phase modelling approach, a range of cavitation models relying on its fundamental principles have emerged. These utilise the source term on the right hand side of the volume fraction transport equation to model the phase change as a rate of mass transfer between vapour and liquid. As such, they are often referred to as mass transfer models.

A detailed review of 15 models presented in the literature is given by Niedzwiedzka *et al.* [151], who discusse the relative differences between them. These typically entail different ways of including higher-order terms of the fundamental Reyleigh-Plesset equation into

the source term, or attempts at accounting for additional physics, such as the influence of Reynolds number on the bubble behaviour. At the time, some of the most commonly referenced phase change models of this category are [87, 145, 195, 202, 204]:

- Kubota et al. 1992 [111],
- Singhal et al. 2002 [182],
- Sauer & Schnerr 2001 [173],
- Kunz et al. 2000 [112].

They differ in the expression used for providing the mass transfer source term and the control parameters required. Typically, one needs to supply the model with parameters describing the water quality or general state of the flow, such as a time and length scale. These may be different in controlled experimental facilities and at full scale, and so matching the experimental results in a simulation may not always lead to results which are readily scalable [41, 95, 96]. Other parameters may often be, in fact, empirical constants. Scaling effects of using various of these will play an important role in the predictions, especially if a wide range of conditions is being considered (e.g. highly different Re between full- and model-scale) [87].

In the present work, each of the individual simulations carried out had its parameters set to reproduce the reported cavitation tunnel conditions as closely as possible. Where not enough data were available about the experimental set up, typical values reported in the literature were used. These assumed the nucleus radii found in water to range between 2 and 50 μm, the vapour pressure to be temperature dependent and taking values between 2300 and 3100 Pa, and the surface tension of water under normal conditions to be 0.0728 N m^{-}1 [204]. In a cavitation tunnel environment nuclei densities between 0.1 up to 100 nuclei per cm^3 were typically assumed [66].

Substantial discrepancies exist in the literature as to which cavitation model truly yields the most accurate results in terms of cavity extent and predicted forces, with the model by Sauer and Schnerr seemingly seeing the most reported applications [87, 104, 165, 171, 204]. A brief comparison with the Kunz model was carried out based on a 2D hydrofoil. With appropriately chosen control parameters, agreement to within several percent was observed between the two approaches in terms of mean force and pressure coefficients, as well as dominant frequencies of dynamic cavitation. This is consistent with the authors in the literature finding different models to yield relatively similar results [78, 140]. The Kunz model did, however, require tuning of its empirical coefficients, which was thought to be disadvantageous with the perspective of studying complex, three-dimensional geometries. It was hence decided to utilise the Schnerr-Sauer model in the present work.

3.6.4 Schnerr-Sauer cavitation model

The Schnerr-Sauer model was first introduced in order to strictly tie the bubble physics to the overall flow dynamics [173]. A full version of the derivation, together with a detailed view of the OpenFOAM implementation of the source terms for the pressure equation and volume fraction transport equations, is given in Appendix A. What follows is a summary listing the main source terms and governing equations.

The rate of change of mass induced by the phase change is modelled using the simplified version of the Rayleigh-Plesset equation, Eq. (2.7), whereby the effects of viscosity, surface tension and thermal effects are neglected and the higher order term is omitted, yielding

$$\dot{R} = \sqrt{\frac{\frac{2}{3}(p - p_\mathrm{v})}{\rho_\mathrm{l}}}. \tag{3.38}$$

This is then fed into an equation derived from the continuity equation, Eq. (3.1), and fluid property interpolation, Eq. (3.35), which allows the rate of change of mass of the fluid due to the phase change to be estimated as

$$\dot{m} = \frac{\rho_\mathrm{l}\,\rho_\mathrm{v}}{\rho}(1-\alpha)\alpha\frac{3\dot{R}}{R}. \tag{3.39}$$

From the implementation point of view, Equation (3.39) is inconvenient as it requires the local bubble radius, R, to be known. In OpenFOAM this is overcome by first computing α_nuc, which denotes the contribution of the nuclei to the vapour volume. It is assumed the local radius is equal to the characteristic equilibrium radius of cavitation nuclei, or $R = R_0$, yielding

$$\alpha_\mathrm{nuc} = \frac{\frac{4}{3}\pi R_0^3 n_0}{1 + \frac{4}{3}\pi R_0^3 n_0}. \tag{3.40}$$

One may now use the relationship between the volume fraction of liquid and vapour,

$$n_0\frac{4}{3}\pi R^3 = \frac{\alpha_v}{\alpha} = \frac{1 + \alpha_\mathrm{nuc} - \alpha}{\alpha}, \tag{3.41}$$

in order to arrive at an expression for the inverse bubble radius that may be substituted directly into (3.39)

$$\frac{1}{R} = \left(\frac{4}{3}\pi n_0 \frac{\alpha}{1 + \alpha_\mathrm{nuc} - \alpha}\right)^{\frac{1}{3}}. \tag{3.42}$$

Finally, substituting Equations (3.38), (3.40), and (3.42) into (3.39) yields the expression for the mass transfer rate used in the present model

$$\dot{m} = \frac{3\rho_\mathrm{l}\,\rho_\mathrm{v}}{\rho}(1-\alpha)\alpha\left(\frac{4}{3}\pi n_0 \frac{\alpha}{1 + \frac{\frac{4}{3}\pi R_0^3 n_0}{1+\frac{4}{3}\pi R_0^3 n_0} - \alpha}\right)^{\frac{1}{3}} \mathrm{sign}(p_\mathrm{v} - p)\sqrt{\frac{\frac{2}{3}\,|p - p_\mathrm{v}|}{\rho_\mathrm{l}}}. \tag{3.43}$$

In the actual implementation the mass transfer rate described by Equation (3.43) is split into condensation and vaporisation parts, depending on the sign of the $p - p_{\mathrm{v}}$ term originating from Equation (3.38). Doing so allows for a more stable implementation and introduction of additional tuning coefficients serving to adjust the rates of creation and destruction of vapour, C_{vap} and C_{con}, respectively. In the present work, values of 1 are used for both in order not to artificially affect the cavitation behaviour but rather to depend on the physics that is being modelled.

3.6.5 Aspects of post-processing

In the maritime CFD context, volume of fluid methods are typically used to model free surface flows where the interface between the liquid and gas is generally well defined. It is therefore common to assume the interface is located at an iso-contour $\alpha = 0.5$, provided the intermediate region $0 < \alpha < 1$ is spread across only a small number of cells.

In cavitating flows, however, this rule is no longer relevant as intermediate vapour fraction values are expected to occur, for instance, in areas where a large number of small, sparsely concentrated bubbles would occupy relatively large regions of cloud cavitation. This makes comparing snapshots of α iso-contours to experimental photographs challenging, as the numerical interfaces are somewhat arbitrarily chosen. It has therefore become more common to compare the photographs against a few iso-contours for different volume fraction values [140], which can allow for a more fair comparison.

An interesting quantity to monitor a cavitating flow simulation is the total amount of vapour volume inside the numerical domain,

$$V = \int_0^{\alpha_{TH}} (1 - \alpha) \mathrm{d}V \approx \sum_{i=0, \alpha_i \leq \alpha_{TH}}^{N_{cells}} (1 - \alpha_i) V_i, \tag{3.44}$$

where V_i is the volume of an individual cell and α_{TH} is an arbitrarily chosen volume fraction threshold value. In this work, typically values of 0.1, 0.5 and 0.9 are used to esimate how much of the cavitation has a sharply defined interface ($\alpha \leq 0.1$) and how much of it is due to large swathes of low vapour concentration ($0.1 < \alpha \leq 0.9$).

Alternative sources of comparison data to photographs may come from several sources. Laser based techniques, such as the hydrodynamic nuclei concentration (HDNC) or shadowography, may be used to measure the concentration of small bubbles, for instance [52, 167]. The range of bubbles which may be captured is within 10 and 300 μm, which allows these methods to be used to analyse bubbly wakes but not large-scale cavitation patterns, such as sheets or tip vortices. Another promising experimental method relies on using x-rays in order to measure extents of cavitation along the line of sight from the measuring device [105]. As such, the method is limited in providing three-dimensional

data, and is thus perhaps less applicable to complex propeller geometries, but has the potential to deliver highly-accurate validation information for two-dimensional hydrofoils. Unfortunately, all of these more advanced methods are not yet in wide use and hence there are few well documented test cases for which such information is available. For this reason, the present work still largely relies on comparing vapour fraction iso-contours to cavitation tunnel photographs.

3.7 Summary

A range of fundamental numerical methods useful for modelling cavitating flows around hydrofoils and marine propellers have been introduced. These make multiple assumptions on the nature of the physics involved in the flow, such as postulating that the mixture of the two fluids is incompressible and performing local averaging of fluid properties. Before any attempts could be made at using the described methods at modelling the acoustic signatures of cavitating flows, a thorough understanding of the effect of the aforementioned assumptions on the predicted results had to be developed. This need is addressed in the subsequent chapters.

Chapter 4

Propeller modelling

4.1 Introduction

Before any advancements could be made in modelling the noise generated by cavitating marine propellers, a set of benchmark simulations had to be established to allow basic validation of the available turbulence and cavitation models. In this part of the study, it was decided to evaluate the flow around a rotating propeller in order to assess the applicability of the selected models to real geometries. The Potsdam Propeller Test Case (PPTC) was chosen as the basis for the simulations, due to its modern design and the rich experimental data available. The focus of the study was put on first developing a suitable meshing strategy, then validating the non-cavitating results using the available experimental data, and finally simulating some of the reported cavitating conditions using the chosen cavitation model. The results were then analysed with emphasis on the accuracy of predictions, necessary fidelity required, and associated computational costs. These aims are addressed in the subsequent parts of this Chapter.

4.2 Background to the Podsdam Propeller Test case (PPTC)

Geometry of the Potsdam Propeller Test Case is shown in Figure 4.1 and its main particulars are summarised in Table 4.1. The key facts standing out are the relatively high pitch-diameter ratio and high skew, which also drive the characteristic shape of the propeller blades seen in the Figure.

Due to its shape, the propeller produces a relatively strong tip vortex and associated cavitation over a wide range of test conditions. At higher advance ratios the propeller also develops significant root cavitation associated with the large fillet radii where the

blade joins the hub. At inclined shaft, the propeller exhibits periodic, unsteady behaviour with pronounced tip, sheet, and bubble cavitation all being present at various parts of the blade throughout one revolution [140].

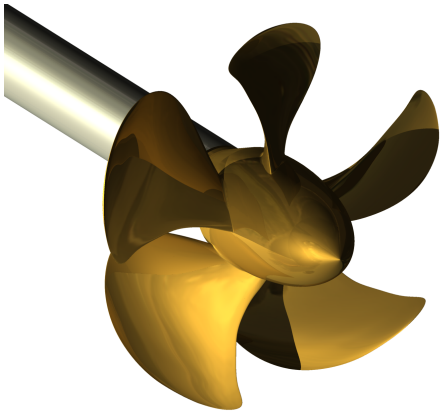

Figure 4.1: View of the Potsdam Propeller Test Case (PPTC).

Table 4.1: Parameters of the VP1304 (PPTC) propeller.

Parameter	**Value**	**Unit**
Diameter	0.250	m
Pitch ratio at r/R=0.7	1.635	-
Chord at r/R=0.7	0.10417	m
Skew	18.837	deg
Hub ratio	0.3	-
Number of blades	5	-

4.3 Simulation set-up

In order to first evaluate the non-cavitating force coefficients across a range of advance ratios, $J = V_a/nD \in$ <0.3, 1.6>, the rotational speed of the propeller, n, was fixed at 10 s^{-1} and the advance velocity, V_a, was changed accordingly for a fixed diameter, D. These operating points corresponded to the published open-water data tests [187]. It has been decided to then focus the investigation on the experimental condition 2.3.1 from the original data [187], as it involved the presence of strong tip vortex and root cavities, which were seen as particularly important from the point of validating the model in a real-life scenario. Hence, the advance coefficient was set to 1.019, advance speed to 7.204 ms^{-1}, and the rps-based cavitation number was fixed by adjusting the outlet pressure, p_∞, by assuming $\sigma = \frac{p_\infty - p_{sat}}{\frac{1}{2}\rho(nD)^2}$=2.024.

Due to the complex geometry of the propeller involved, an unstructured meshing approach was followed using the OpenFOAM native snappyHexMesh tool. This generates

a predominantly hexahedral grid with refinement based on surface curvature and specified volumetric regions and extrudes prismatic cells off the propeller body. A coarse mesh consisting of 4.7 million cells was utilised for the non-cavitating force coefficient prediction. In order to increase the resolution for the cavitating conditions, maximum mesh refinement level based on curvature was increased by 1 and additional volumetric refinement regions were added around the propeller hub and tip where cavitation was expected to occur. This increased the cell count to approximately 5.8 million elements. For both grids, obtaining a wall-resolved boundary layer grid was found to be difficult with the mesher used. It was therefore decided to apply wall functions to the propeller, thereby relaxing the required size of the first cell to $y^+ \in$<30, 300> and making it easier for a high quality mesh to be created. For the non-cavitating simulations the same grid, designed for the average advance velocity, was used for all advance ratios. The numerical domain in all cases extended 5 propeller diameters in the upstream and radial directions and 10D in the downstream direction. In order to enable rotation of the part of the mesh containing the propeller, interpolation was performed between the stator and the rotor zones using an Arbitrary Mesh Interface (AMI) available in OpenFOAM.

For all cases, turbulence was modelled using the k-ω shear stress transport (SST) RANS model. Fixed velocity and turbulence inlets were chosen to simulate uniform inflow conditions. Ambient pressure required to achieve the desired cavitation number was imposed using a fixed pressure value at the outlet. The outer walls were assumed to be slip, while no-slip condition was applied to the propeller, hub, and shaft. Suitable fluid and cavitation model parameters, shown in Table 4.2, were used to match the experimental conditions.

Table 4.2: Fluid properties and cavitation model constants used for the VP1304 (PPTC) propeller

Parameter	**Value**	**Unit**
Water density	997.44	kg m^{-3}
Vapour density	0.023	kg m^{-3}
Water viscosity	$9.337 \cdot 10^{-7}$	m^2 s^{-1}
Vapour viscosity	$4.273 \cdot 10^{-6}$	m^2 s^{-1}
Saturation pressure	2818	Pa
C_{vap}, C_{con}	1.0	-

First order time discretisation was used, and the convection term of the RANS equation was resolved using the mixed first-second order upwind scheme. First order schemes were used to model the turbulent quantities and van Leer scheme with interface compression was applied to the volume fraction field. The simulations were run with adjustable time step in order to bound the maximum Courant number to less than 1.

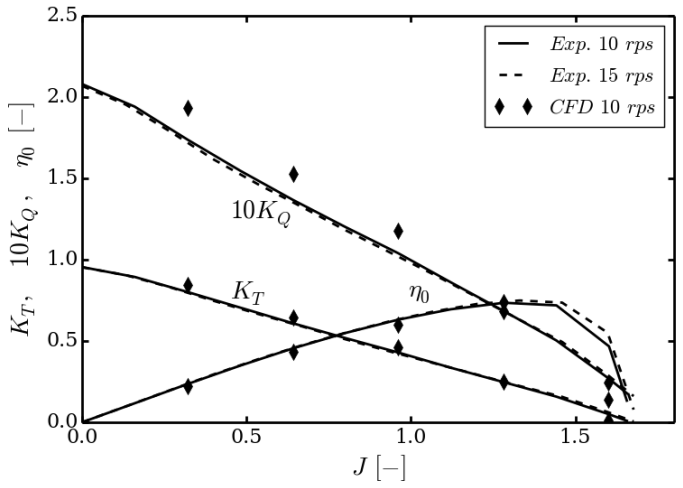

Figure 4.2: Predicted non-cavitating force coefficients for the PPTC propeller. Experimental data from [187].

4.4 Results

Figure 4.2 presents mean thrust and torque coefficients,

$$K_T = \frac{T}{\rho n^2 D^4}, \tag{4.1a}$$

$$K_Q = \frac{Q}{\rho n^2 D^5}, \tag{4.1b}$$

as well as the open water efficiency,

$$\eta_0 = \frac{JK_T}{2\pi K_Q}, \tag{4.2}$$

predicted for the PPTC propeller using non-cavitating RANS simulations. Experimental data from [187] are also presented for 10 and 15 rps. Overall, despite a coarse mesh with fixed cell spacing at the wall being used across all J values, the trends in force coefficients are relatively well represented with errors in K_T and η_0 being within 5% from the experimental values. Noticeably, the torque exhibits larger errors up to a maximum of 10% compared to the experiment. Insufficient mesh resolution has been identified as the root cause of this since initial non-cavitating simulations on the fine, 5.8 million cell, mesh reduced the errors to 0.3, 4.6 and 4.2% for the thrust coefficient, torque coefficient, and open water efficiency, respectively.

Figure 4.3 shows the predicted cavitation pattern as well as the corresponding sketch and photograph made during the experimental tests reported in [187]. A well-defined tip cavity and a less pronounced root cavity may be seen in both the calculated and observed results. Moreover, the numerical data allows the tip vortices and a root vortex

on the pressure side of the blade downstream of the trailing edge to be observed as vorticity iso-contours. A hub vortex and an associated cavity are also present. Total cavity volume time history was also computed but showed little to no variation and hence is not shown for brevity.

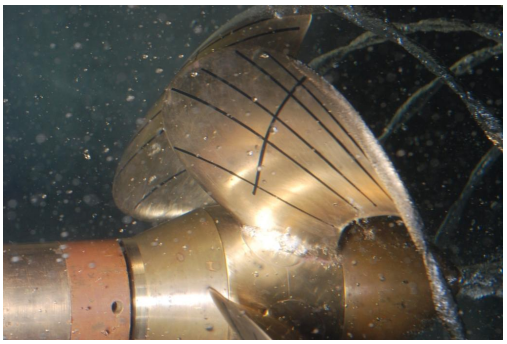

(a) Experimental observation - photograph

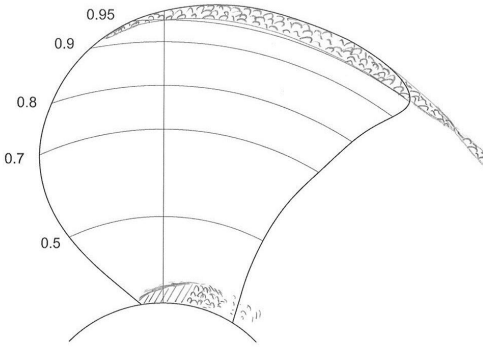

(b) Experimental observation - sketch

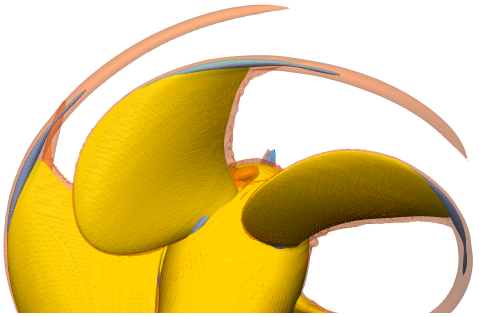

(c) Predicted cavity extent - blue ($\alpha = 0.5$) and tip vortex - orange ($|\omega| = 1500\,s^{-1}$)

Figure 4.3: Cavitation pattern predicted for the PPTC case 2.3.1. Experimental data from [187].

4.5 Discussion

Despite their preliminary nature, the presented results allowed several interesting observations to be made which would then steer the overall direction of the project. Most importantly, achieving satisfactory mesh resolution and quality using the employed gridding technique has proven to be challenging. Initial attempts were also made to increase the mesh density and quality sufficient for Large Eddy Simulation. However, the rapidly increasing cell count and difficulty of improving mesh quality when using the present meshing tool augured high computational costs for the simulations. This was unexpected, as a previous study by Lloyd [136] used an identical meshing strategy in application to a tidal turbine with satisfactory results. However, the geometry considered in

the present work was much more complex, making achieving high mesh quality more challenging. Also, the propeller operates at significantly higher Reynolds numbers of 1.4 million compared to 400 thousand in the reference study, which causes a rapid increase in the cell count required.

Another major issue observed was the discrepancy of the torque coefficient compared to the experiments. Part of this problem has been shown to be related to insufficient grid resolution but even eliminating this factor yielded differences of just under 5%. A significant amount of torque on a propeller blade comes from the friction force, which is of course governed by the behaviour of the boundary layer. Due to the relatively low Reynolds number and lack of turbulence stimulators in the experiment, it is likely a small amount of laminar or transitional flow was present during the experiment, which would not have been accounted for by the RANS model used [201]. This could have been alleviated for through the use of a more advanced turbulence model accounting for transition or by calibrating the turbulent quantities of the inlet to better represent the experimental conditions. None of these were seen as necessary at this stage as the intention was to move towards more complex turbulence modelling strategies, such as LES or DES, at subsequent stages of this project, thereby removing the need to model transition implicitly.

A further incentive for using the more sophisticated turbulence modelling approaches was the fact that they are better suited to predict the structure of vortices, such as those developed at the tip and the root of the propeller. As was seen in the cavitating simulations, these features play a major role in the process of cavitation inception. Hence, one should aim to resolve them as accurately as possible if unsteady flow dynamics around the propeller are to be studied and understood.

The predicted cavitation behaviour was seen to be qualitatively similar to the one observed in the experiments, however its extent was under-predicted. This was expected from published numerical studies [13, 204], but could likely be improved by tuning the cavitation model parameters. An issue with doing so, however, would be the risk of forcing the model to conform to the experimental observations for this particular case while making it diverge from reality in other scenarios not considered thus far. It was therefore decided not to pursue this line of investigation, at least until a larger database of validation cases has been built up.

Finally, the computed cavities have been found to be rather stable in volume and location. This is symptomatic of a relatively stable cavitation behaviour associated with a persistent tip vortex, constant low pressure region around the root radius and uniform, steady inflow. This further emphasised the need for a different test case with more dynamic cavitation behaviour to be found so that the noise generated by rapidly oscillating volumes may be predicted.

4.6 Summary

Simulations have been presented in which cavitating and non-cavitating flows for a propeller geometry highly relevant to modelling of marine propeller noise were computed. The results have shown agreement to within 5% with the experiment in terms of the thrust coefficient and efficiency. The predicted cavitation patterns also agreed with the experimental observations, although the volume of the cavities was less in the present simulations that was reported in the measurements. Torque, however, could not be predicted well. This indicated that the present method should allow for the blade-pass-dependent part of marine propeller noise to be studied. The major discrepancies seen between the present results and the experiments have been caused by the limitations of the underlying cavitation model and coarse mesh used due to the overall high cost of the simulations. Before the developed simulation framework could be used to study the far-field pressures induced by the blade rate of a propeller, a suitable hydroacoustic method had to be devised, which is described in the following chapter.

Chapter 5

Acoustic modelling of marine propeller noise

5.1 Introduction

This Chapter aims to first review hydroacoustic methods which could potentially be used in conjunction with modern computational fluid dynamic tools in order to predict marine propeller noise. Their relative strengths and weaknesses are weighed and it is concluded that the "porous" Ffowcs Williams-Hawkings (FW-H) acoustic analogy appears to offer the greatest potential in achieving the aims of this project. This methodology is then discussed in more detail and the undertaken OpenFOAM implementation is described. Furthermore, a series of sensitivity studies are carried out in order to provide basic verification and validation, as well as to allow a better understanding of the limitations of the method. The Chapter then concludes with an application to the Insean E779a propeller in non-cavitating conditions, the results for which are compared against the literature.

5.2 Review of Numerical Acoustic Methods

5.2.1 Governing equations of sound

As already explained in Section 2.2.1, sound may be defined as a fluctuating pressure wave moving through a compressible fluid [43]. As such it is governed by the compressible form of the momentum and mass conservation equations, Eq. (3.1) and (3.2), which,

upon neglecting the effects of viscosity, may be written as

$$\frac{\partial \rho}{\partial t} + \nabla \cdot (\rho \mathbf{U}) = 0, \tag{5.1a}$$

$$\frac{\partial}{\partial t}(\rho \mathbf{U}) + \nabla \cdot (\rho \mathbf{U} \otimes \mathbf{U}) = -\nabla p + F(\mathbf{y}, t), \tag{5.1b}$$

where $F(\mathbf{y}, t)$ is a generalised source term tending to zero in the far field. This may take the form of a monopole, dipole or a quadrupole. The momentum equation may be linearised by assuming that $p = c_0^2 \rho$, where c_0 is the speed of sound in the considered medium, yielding

$$\frac{\partial}{\partial t}(\rho \mathbf{U}) + c_0^2 \nabla p = F(\mathbf{y}, t). \tag{5.2}$$

In practice, it is the fluctuating components of pressure and density, p' and ρ', that are of interest from the sound generation point of view. Given the mean values p_0 and ρ_0 these may be defined as

$$p = p_0 + p', \tag{5.3a}$$

$$\rho = \rho_0 + \rho', \tag{5.3b}$$

in a very similar fashion to the separation of variables discussed for the Reynolds Averaged Navier-Stokes (RANS) equation in Chapter 3.

Now, by subtracting the spatial derivative of Eq. (5.2) from the time derivative of Eq. (5.1a), one may arrive at the inhomogeneous wave equation

$$c_0^2 \left(\frac{1}{c_0^2} \frac{1}{\partial t^2} - \nabla^2 \right) \rho' = c_0^2 \overline{\mathbb{D}}^2 \rho' = F(\mathbf{y}, t). \tag{5.4}$$

This formulation describes the propagation of sound due to an arbitrary source, F, and has already been stated at the beginning of Section 2.2.1.

One may also consider a more accurate description of the sound generated by an arbitrary source by comparing the linearised momentum equations, (5.2), and the full Navier-Stokes equations, (5.1b) [127]. Doing so allows a more complete expression, termed the acoustic analogy, to be written as

$$c_0^2 \overline{\mathbb{D}}^2 \rho' = \nabla^2 \mathbf{T}, \tag{5.5}$$

where the Lighthill stress tensor, $\mathbf{T}$, describing the volumetric distribution of sources generating noise through turbulent stresses in the fluid, is defined as

$$\mathbf{T} = \rho \mathbf{U} \otimes \mathbf{U} - p\mathbf{I} + \mathbf{D} - c_0^2 \rho' \mathbf{I}. \tag{5.6}$$

For low Mach number flows it may be approximated to [127, 136]

$$\mathbf{T} \approx \rho \mathbf{U} \otimes \mathbf{U}. \tag{5.7}$$

The presence of a solid boundary will modify the acoustic field by forcing the surface-normal Reynolds stress to be zero on the wall. In other words, the product of velocity and a wall normal vector, $\hat{\mathbf{n}}$, must be zero on the wall ($\mathbf{U} \cdot \hat{\mathbf{n}} = 0$) for there to exist no flow through the solid surface. This allows the inhomogeneous wave equation, Eq. (5.5), to be rewritten for a solid moving surface as [44]

$$c_0^2 \overline{\mathbb{D}}^2 \rho' = \nabla^2 \mathbf{T} + \nabla \left(p\mathbf{I} \cdot \hat{\mathbf{n}} \right). \tag{5.8}$$

5.2.2 Computational Approaches to Acoustics

Several ways to provide the expression for the sound source term $F(\mathbf{y}, t)$ in Eq. (5.4), as well as to solve the entire equation exist.

- **Direct Compressible Navier-Stokes solution** - Sound generation and propagation may be computed directly using a compressible set of Navier-Stokes equations, Eq. (5.1). One would typically be interested in using advanced turbulence modelling techniques, such as DES, LES or DNS, in order to capture the sound waves accurately enough [34, 39, 162, 178, 184]. A typical example of such an approach is described by Sandberg *et al.* where DNS is used to compute tonal noise due to laminar flow past an airfoil section [172]. This method accounts for all the physics directly with minimum amount of modelling and so is expected to be highly accurate. However, if high quality of the acoustic solution is to be maintained, the numerical grid must remain fine out to the point of interest to avoid dissipation and dispersion errors. In many practical engineering applications, where large source-receiver distances are considered, such as for a marine propeller far-field noise, this will be prohibitively expensive.

- **Unsteady RANS with modelling** - it is possible to reduce the compressible Navier Stokes equations to Reynolds averaged form, following the rationale given in Section 3.4. For very low frequencies, such as the blade pass frequency of a marine propeller, this approach should be capable of predicting the associated pressure signal. Broadband contributions could be modelled using empirical or semi-empirical relationships [7, 49]. This approach, while offering substantial reductions in the computational time, is heavily limited by the availability of appropriate empirical expressions describing the noise sources. Such an approximation may be readily obtained for a spherical bubble in a quiescent medium, for instance, but the process becomes less reliable as one moves towards the full propeller cavitation problem

[20, 79, 143]. Furthermore, it also suffers from the need of solving the simplified Navier-Stokes equations out to the point of interest.

- **Euler equations solution** - This method is based on separating the flow and acoustic problems due to the difference in the length scales and energy distribution in the two. It entails a standard fluid dynamic solution in a near-field domain and then uses linearised Euler perturbation equations, thus simplifying the Navier-Stokes solution substantially, compared to Equation (5.1), in a larger acoustic domain. One-way coupling between the two solvers is achieved using appropriate source terms whose values are computed from the CFD data [56]. This approach is far more flexible than directly solving the governing equations in the same form everywhere. It requires a secondary domain, however, and appropriate numerical means to treat the compressible Euler and Navier-Stokes equations without introducing significant errors out to the locations of interest.

- **Lighthill's acoustic analogy** - Lighthill's acoustic analogy, seen in Eq. (5.5), is derived from rearranging the equations of motion of a fluid into a linear wave equation and modelling the noise sources using the mean and turbulent flow fields [127]. This approach is widely used in the aeroacoustic field, see for instance work by Self in application to a turbulent jet [174]. The main advantage stems from the fact that the method solves a volume integral of quantities dependent on the flow field and uses them to deduce sound at an arbitrary location. This removes the need for solving additional equations numerically, as in the case of linearised Euler equations, making the methodology simpler and capable of working as a post-processing tool. From a cavitation modelling point of view, however, this is also a major setback as it implies that the integration volume would encompass a non-homogeneous region filled with two fluids, thus complicating the formulations. Moreover, Lighthill's analogy does not account for the presence of solid walls and the associated sound generation and scattering effects, rendering it of little use to a marine propeller problem [74].

- **Curle's acoustic analogy** - work by Curle extended the applicability of the Lighthill's analogy by accounting for reflection and diffraction of sound due to the presence of solid boundaries and incorporating additional sound generation mechanisms occurring there, yielding Equation (5.8) [44]. This allowed overcoming the biggest limitation of the original formulation in application to external fluid dynamic problems. In cavitation noise modelling context, however, it still suffers from the the fact that it requires a volume integral.

- **Kirchhoff method** - this approach is a surface integral method capable of computing sound generated by moving bodies by solving an inhomogeneous wave equation. This is potentially a very attractive approach as it does not require a volume integral to be solved, potentially making it more straightforward to deal with the presence of cavitation, for instance [25, 57].

- **Ffowcs Williams-Hawkings acoustic analogy** - further extension to the analogies formulated by Lighthill and Curle was done by Ffowcs Williams & Hawkings in order to account for arbitrary motion of the body for which the flow is being calculated [61]. In this method the acoustic analysis is performed by solving a surface integral for the loading and thickness terms and a volume integral to account for the quadrupole source from the original formulation by Lighthill.

5.2.3 Selection of a suitable acoustic method

As can be seen, a wide range of approaches may be used to model noise generated by the propeller. For the purpose of this project, the method to be selected had to be affordable and capable of dealing with high sound speeds and high attenuation in water. This ruled out the solution of Euler equations and direct solution of compressible Navier-Stokes equations because of the fine meshes and small time steps make these methods too computationally expensive at present. At the outset of the present project precious few sources in the open literature could be referred to regarding the choice of an alternative method. As highlighted in Section 2.5, most of the early literature on the topic of marine noise relied on the Ffowcs Williams-Hawkings acoustic analogy, for instance as in the studies by Lloyd [136] or Ianniello et al. [90]. This choice stands in agreement with lessons drawn from the aeroacoustics field, where various versions of the simpler Curle analogy and Kirchhoff method appear to have lost some of the ground to the FW-H.

There are several reasons to prefer the FW-H analogy over the alternatives in a marine propeller-oriented study. The FW-H approach is derived from conservation equations, rather than the wave equation, meaning it is said to be valid even if the integration surface is placed in the non-linear flow region, such as a wake, which is not true for the Kirchhoff approach [25]. This implies that much smaller computational domains may be used together with the FW-H approach, reducing the overall cost of the prediction substantially and making it a favourable choice for the present work. Furthermore, the method has been successfully applied to rotating geometries such as marine propellers [90, 169, 177] and helicopter rotors [26], which demonstrates its capability. While none of the early maritime studies used flow and cavitation solvers with the level of fidelity applied in the present work, the proof of concept demonstration being available in the literature provided increased confidence in the FW-H method. One of the disadvantages of the FW-H compared to the Kirchhoff method is that the former analogy suffers from the nonlinear flow effects not being included in the surface integration, which may be alleviated, but arguably not completely, when the permeable formulation of the former is used [89].

This strategy, introduced by Di Francescantonio, involves rewriting the FW-H equations so that the integrals are solved on a surface surrounding and not coinciding with the body

moving through the fluid [48]. Doing so also reduces the risks associated with solving the volume integrals in regions where intermittent cavitation may occur. This was considered advantageous as it was realised the present cavitation models may not necessarily be able to accurately represent the flow regime in those areas. Additionally, account would not have to be taken of the fact that the sound waves would be propagating through a bubbly medium. Moreover, using a porous formulation also allows for noise sources located further away from the body, such as strong wake non-linearities, to be more easily included in the analysis without the need to resort to expensive volume integrals over large parts of the numerical domain. Given these considerations, it was decided to implement the porous Ffowcs Williams-Hawkings in OpenFOAM for the purpose of this project. This is described in detail in the following section.

5.3 Ffowcs Williams-Hawkings acoustic analogy

Ffowcs-Williams Hawkings (FW-H) acoustic analogy uses the extended Lighthills equation, Eq. (5.5), to predict noise originating from turbulence when moving surfaces are present [48, 61, 91, 155, 171]. It may be derived by rearranging the mass and momentum conservation equations in order to yield a solution to the inhomogeneous wave equation, Eq. (5.4). The solution to this equation computed using the FW-H acoustic analogy then allows one to predict the noise propagation from a moving noise source to the far-field. A full derivation of the method is described in detail by Brentner and Farassat [26] and given in Apendix B. The key concepts and steps are summarised below.

In the general form the FW-H solution may be expressed as a summation of three different terms yielding the total pressure disturbance at at the location of a receiver, given as

$$p'(\mathbf{x},t) = p'_T(\mathbf{x},t) + p'_L(\mathbf{x},t) + p'_Q(\mathbf{x},t). \tag{5.9}$$

In the above, p' denotes the acoustic pressure disturbance and its individual elements are denoted with with subscripts referring to: T - thickness (monopole), L - loading (dipole), Q - non-linear (quadrupole) contributions [142, 169]. The multipole order of these terms holds only for a rigid control surface coinciding with the surface of the body in motion [142].

The FW-H equation makes use of two intermediate variables, defined for a stationary control surface as

$$U_i = \frac{\rho^{'} + \rho_0}{\rho_0} u_i, \tag{5.10a}$$

$$L_i = P_{ij}\hat{n}_j + (\rho^{'} + \rho_0)u_i(u_i \cdot \hat{n}_i), \tag{5.10b}$$

where $\hat{n}$ is a unit vector normal to the control surface, $\rho^{'}$ is the density disturbance and P_{ij} is the compressive stress tensor. Given the pressure field of a fluid, p, and its value

when the fluid is at rest, p_0, one may simplify the P_{ij} tensor to $p - p_0$ [142, 169]. For an incompressible flow the density disturbance will, by definition, be zero [137]. Thus, the final expressions for the acoustic variables may be written as

$$U_i = u_i, \tag{5.11a}$$

$$L_i = (p - p_0)\hat{n}_j + \rho_0 u_i (u_i \cdot \hat{n}_i). \tag{5.11b}$$

For a stationary control surface, the general forms of the first two of the FW-H terms may be written as [142]

$$4\pi p'_T(\mathbf{x}, t)H(f) = \int_S \left[\frac{\rho_0 \dot{U}_n}{|\mathbf{r}|}\right]_\tau \mathrm{d}S, \tag{5.12a}$$

$$4\pi p'_L(\mathbf{x}, t)H(f) = \frac{1}{c_0}\int_S \left[\frac{\dot{L}_r}{|\mathbf{r}|}\right]_\tau \mathrm{d}S + \int_S \left[\frac{L_r}{|\mathbf{r}|^2}\right]_\tau \mathrm{d}S. \tag{5.12b}$$

In the above, $H(f)$ is the Heaviside function equal to 1 outside of the control surface S, $\int_S [...]\mathrm{d}S$ denotes integration over the control surface, the dot defines a time derivative with respect to the source time, and subscripts r and n refer to the dot product of the quantity in question with the normal unit vector along either radiation or surface normal directions, respectively. The concept of solving the surface integrals is best visualised by Figure 5.1 which shows how the FW-H method may be applied to a marine propeller.

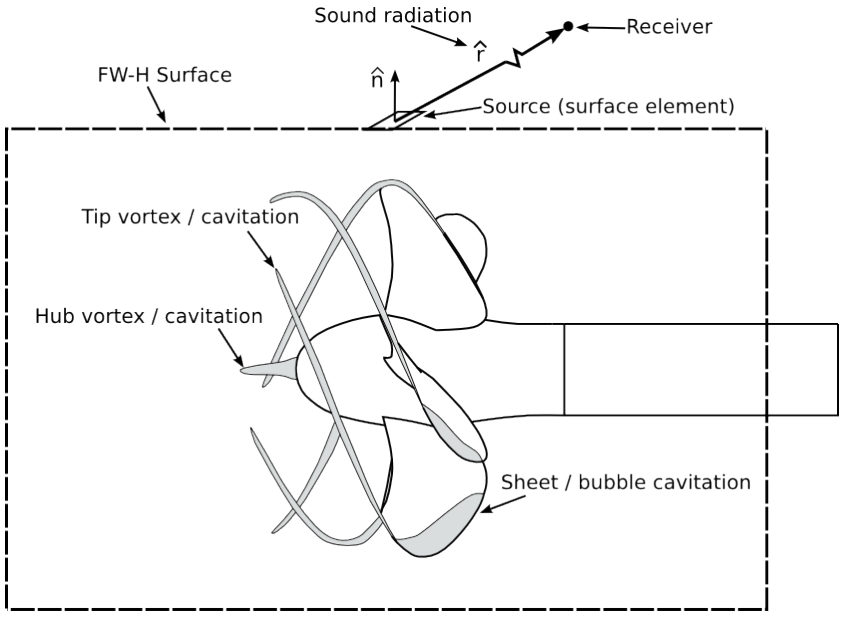

Figure 5.1: Illustration of the principle of how the FW-H integrals get solved around a marine propeller.

Equation (5.12) is the so-called Farassat 1A formulation, where the time derivatives are incorporated into the integrals [26]. An alternative would be to evaluate the surface

integrals first and then take the derivatives of the results, an approach called Farassat formulation 1. The only major difference is the need to supply time derivatives of the flow field quantities to formulation 1A, which are not required by formulation 1. This implies more data being saved and hence higher hard drive usage, which may be a limitting factor for large simulations. However, formulation 1A is said to be less expensive and marginally more accurate [26, 142]. This approach was therefore followed, although the current implementation is capable of using formulation 1 as well.

Furthermore, each term in Eq. (5.12) is evaluated at the retarded time, denoted by $[...]_\tau$. This captures that the sound propagates from different elements of the discretised control surface will take a finite amount of time to reach the receiver [39, 91, 142, 169]. Thus, the contribution of an individual located at $\mathbf{y}(\tau)$ element at the emission (retarded) time τ will affect the receiver at $\mathbf{x}(t)$ at time

$$t = \tau + \frac{|\mathbf{x}(x) - \mathbf{y}(\tau)|}{c_0}. \tag{5.13}$$

At present both the source and receiver are assumed to be stationary and so their positions do not change in time. Following Lloyd *et al.* [137], it is useful to rewrite Eq. (5.12) by substituting the acoustic variables defined in Eq. (5.11) and inserting the resultant expressions into Eq. (5.9), yielding the total pressure at the receiver

$$\begin{aligned} 4\pi p'(\boldsymbol{x},t)H(f) = &\underbrace{\int_S \frac{\rho_0 \dot{u}_n}{|\mathbf{r}|}\bigg|_\tau dS(\boldsymbol{y})}_{\text{monopole, } p'_0} + \underbrace{\int_S \frac{p\hat{\boldsymbol{n}}\cdot\hat{\boldsymbol{r}}}{|\mathbf{r}|^2}\bigg|_\tau dS(\boldsymbol{y})}_{\text{dipole, } p'_1} + \underbrace{\int_S \frac{\rho_0 u_n u_r}{|\mathbf{r}|^2}\bigg|_\tau dS(\boldsymbol{y})}_{\text{non-linear dipole, } p'_2} \\ &+ \underbrace{\int_S \frac{\dot{p}\hat{\boldsymbol{n}}\cdot\hat{\boldsymbol{r}}}{c_0|\mathbf{r}|}\bigg|_\tau dS(\boldsymbol{y})}_{\text{unsteady dipole, } p'_3} + \underbrace{\int_S \frac{\rho_0 \dot{(u_n u_r)}}{c_0|\mathbf{r}|}\bigg|_\tau dS(\boldsymbol{y})}_{\text{unsteady, non-linear dipole, } p'_4} + p'_Q(\mathbf{x},t). \end{aligned} \tag{5.14}$$

This shows how for an FW-H integration surface defined on the body, each of the terms may be associated with a physical source of a given order. For a permeable, or porous, formulation, however, terms in Equation (5.9) lose their physical meaning and shall henceforth be referred to as pseudo-thickness and pseudo-loading to make this disctly clear [142].

It is also worth noting that, for a porous formulation, the quadrupole term, $p'_Q(\mathbf{x},t)$, denotes the non-linear contributions from the volume not enclosed by the control surface and is described by a volume integral [48]. Thus, if the porous data surface is defined to cut across a region where turbulence or other noise sources exist, solution of the volume integral is still required if an accurate representation of the noise source is to be obtained [89].

5.4 Present implementation of the acoustic analogy

5.4.1 Practical considerations

To perform a successful implementation it is important to understand the key practical steps that need to be achieved to integrate the solution of the FW-H equation into a CFD code.

1. Constructing a porous data surface (PDS).
2. Sampling flow field data on the surface and passing them to an acoustic solver or storing them while working in parallel.
3. Understanding the retarded time for each face-receiver combination.
4. Effectively performing the surface integration.

The following section describes how each of these steps were tackled.

5.4.2 Implementation Strategy

The acoustic analysis framework has been divided into three main parts.

- Core library `fwhlib`, which contains the algorithms for manipulating the data surface, reading and writing data, as well as mathematical formulations used to solve the FW-H equations and deal with retarded time. The ability to re-use code makes the dependent sofware pieces more compatibile and significantly easier to maintain.
- Runtime post-processing objects, `fwhRuntime` and `saveFaceZoneData`, which may be attached to an OpenFOAM simulation in order to solve the FW-H equation while the computation is running or to simply save the flow field data to a data file for future use.
- Stand-alone post-processing tools, `sampleFaceZoneData` and `fwhPostProcess`. The former can be used to sample flow field data from saved time steps, which is typically used to obtain the mean flow quantities. The latter is the main analysis utility used to solve the FW-H equations. It is preferred to the runtime version as it allows the same set of data files to be re-used, thus allowing new acoustic results to be computed from the same flow field as the analysis of a particular case progresses.

Currently, the data surface, also referred to as the control surface, is defined using a `faceZone` and the cells contained by it are grouped inside a `cellZone`. Both of these are OpenFOAM-native objects, which reduces the amount of bespoke code needed and makes the utilities more compatibile with an arbitrary solver. This also enables straightforward exchange of the data between the acoustic tools and the main solver, as well as using the built-in `topoSet` utility in order to create the surface. A disadvantage of this solution is, however, that for complex meshes describing the control volume in this way has proven to be time consuming. Moreover, for fine grids, the integration resolution may be higher than required and thus contribute to higher computational times, disk space and memory usage. It may therefore be useful to considere using a surface description independent of the mesh in the future and interpolate the fields onto it. This could be, for instance, done using a stereolitography (stl) file, but would run the risk of introducing additional interpolation errors corrupting the input data.

In the OpenFOAM mesh format, the normal vectors of every cell face are stored in the mesh object and may be accessed via the `Sf()` operator. However, FW-H requires the surface-normal vectors to point outside of the control volume. Because of that, a routine is employed when the solution is being initialised in order to verify whether any of the normal vectors need to be inverted. This is done by analysing the owner-neighbour connectivity of the mesh cells since, by convention, OpenFOAM keeps the face normals for a particular face pointing from its owner to its neighbour cell. Therefore, if a given normal points into a cell enclosed by the control surface, the direction of the vector must be inverted for the purpose of acoustic analysis.

Special treatment of faces coincident with the domain boundaries is necessary as the OpenFOAM mesh properties, such as face centre locations, are stored separately for boundary faces. Therfore, the acoustic tools perform a check to identify whether a given face is internal or belongs to a boundary before sampling the data and performing other operations. Moreover, in OpenFOAM processor patches are constructed of *baffles*, which means each face on the processor boundary is duplicated with respect to the initial mesh. This requires one of the faces from each pair to be ignored. The face to be abandoned is chosen by virtue of belonging to a subprocess with a greater MPI ID. It is still advisable to avoid defining the control surface on the processor boundaries as much as possible to limit the computational effort associated with the aforementioned checks.

In order to account for the retarded time, the acoustic pressure signals need to be interpolated onto a coherent time grid given a unique arrival time, t, value for each face-receiver combination. In the present method this is done by extending the CFD time axis using a fixed time step beyond the time covered by the underlying hydrodynamic simulation, as depicted in Figure 5.2. Thus, the time record may be seen as being divided into bins Δt wide, as seen is Figure 5.2. For a contribution released at $\tau = t_0$ for a receiver R away from the surface element, the computed receiver time falls between simulation times t_i and t_{i+1}, onto which the acoustic pressure is interpolated. One may

see how large size of the time step may lead to the high-frequency content of the signal being lost, which emphasises the use of sampling rates sufficient for the required analysis.

An important step of the process is accounting for the proportion of the acoustic contributions which would arrive at the listener after the fluid dynamic solution has been. This may be done by either assigning an individual acoustic contribution to the time indices closest to its analytically computed listener time, or by distributing the contribution proportionally to how close it is to the neighbouring indices on the listener time axis. Both of these approaches have been implemented and tried but did not show significant differences in the results. The interpolation approach was therefore followed.

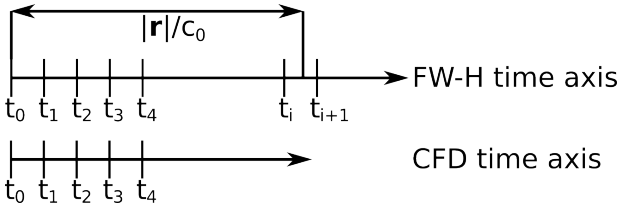

Figure 5.2: Illustration of the retarded time concept. Sound source emits a pressure wave at t_0 in the direction of a receiver $\mathbf{r}$ but the sound does not reach the listener $|\mathbf{r}|/c_0$.

At this time, the acoustics utility, both in runtime and post-processing variants, follows a simple structure whereby two iterations are performed, one over all the receivers and then one over all faces of the control surface. Thus a total acoustic contribution for each receiver is computed. For the simple validation test cases considered this did not yield long computational times but has been found to increase substantially as more complex control surfaces are evaluated. Currently, the post-processing version of the code is not parallelised, however, so substantial potential for improvement exists in this respect. OpenMPI parallelisation of the runtime version is achieved through executing all of the FW-H term evaluations independently on each processor, following the main OpenFOAM framework. The data is the gathered on the master thread, then the values are categorised according to their retarded time and written when necessary. The post-processing program follows the same structure except the data is read from the file instead of retrieved from the flow solver directly. A more detailed overview of the workflow of the post-processing analysis tool is depicted in Figure 5.3.

The post-processing FW-H tool has been found to poses significant memory requirements if all of the flow field data collected for a complex surface with many elements over a long simulation period is to be read at once. Therefore, a set of controller features have been added into the main loop of the program in order to allow the geometry of the control surface to be read and prepared independently from the actual flow field data. Moreover, it is possible to import the flow data in smaller portions, run the analysis on them, and then clear the memory and move to the next segment of data. This allows the process to be run even on a desktop machine with input data files as large as hundreds of gigabytes.

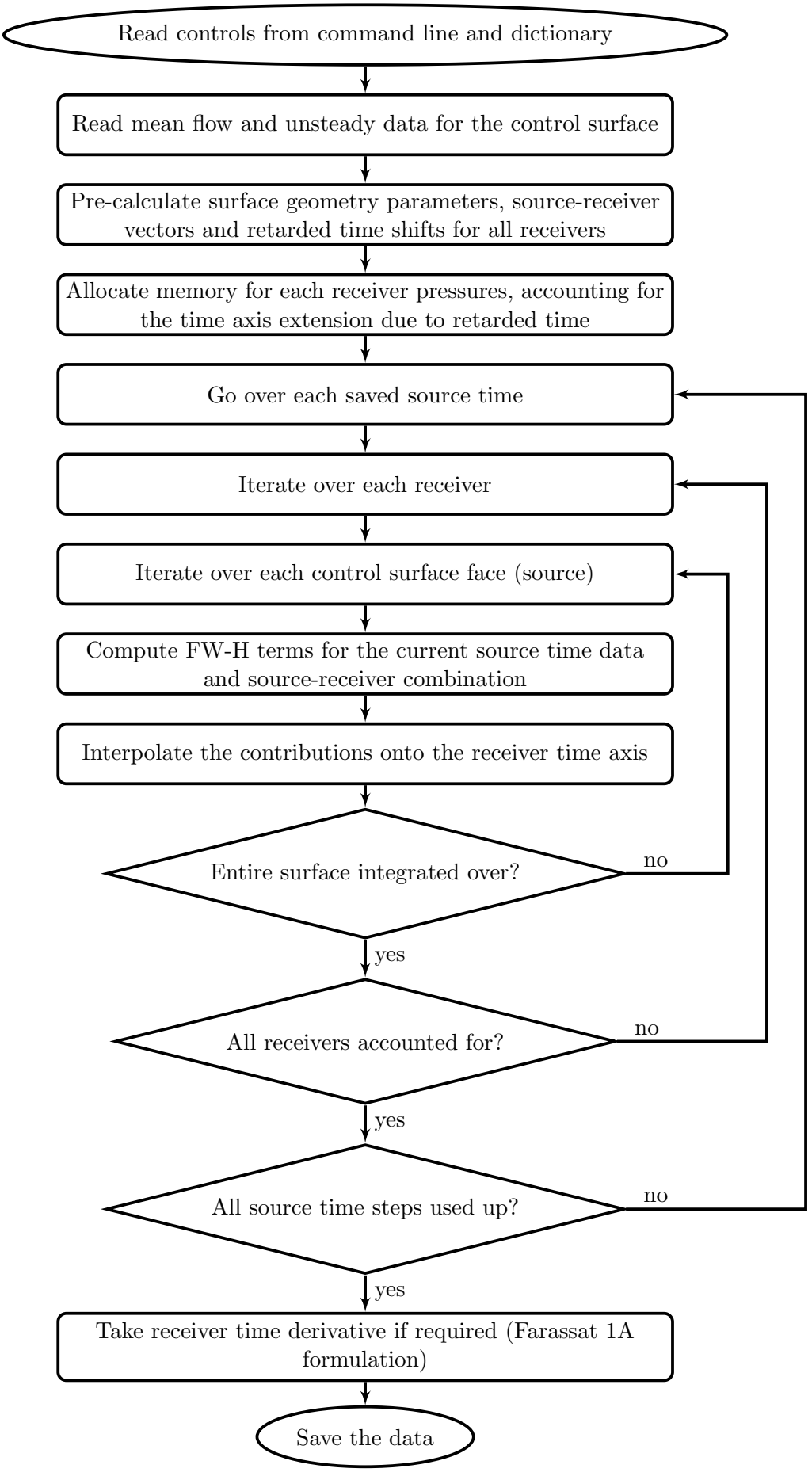

Figure 5.3: Workflow of the key steps of the FW-H stand-alone utility.

In order to allow a more detailed insight into the flow physics, the utility allows the contributions of each face constituting the control surface to be saved. The output file contains all the information about the surface geometry, allowing for it to be reconstructed afterwards. A set of Python scripts have been developed to complete this task and save the data for each collected time step into vtk or Tecplot formats. This allows for the noise term distribution to be compared against the flow field data and a discussion to be made about the origin and nature of the noise generation mechanisms. It should be noted that the size of the generated files is significant and so this feature is aimed to be used for very targeted studies rather than as a standard procedure.

5.4.3 Analytical acoustic sources

In order to provide the means for validating the acoustic tools, a dedicated flow solver has been devised in order to generate the required flow field data. Instead of solving the equations of motions of the fluid, the solver was made to assign the solution of idealised source equations, which allowed for the analysis to be focused on finding errors in the acoustic tools themselves and not the flow solver.

The solver uses the analytical expression for sound pressure generated by a harmonic point source, expressed as

$$p'(\mathbf{x},t) = \frac{j\omega\rho_0 Q e^{j(\omega t - k|\mathbf{x}-\mathbf{y}|)}}{4\pi\,|\mathbf{x}-\mathbf{y}|}, \tag{5.15}$$

where $\mathbf{y}$ is the location of the source, $\mathbf{x}$ is the point at which the sound pressure is being evaluated, k is the wave number, ω the frequency of oscillation, and Q is the strength of the source describing the amount of volume flow it induces [97]. This may be simplified by letting $|\mathbf{x}-\mathbf{y}| = r$, where r is the distance between the source and the point of interest.

A similar expression is used to describe the particle velocity of the source,

$$\begin{aligned}\mathbf{U}'(r,t) = &-\frac{1}{j\omega\rho_0}\frac{\partial p'(r,t)}{\partial r} = \frac{p'(r,t)}{\rho_0 c_0}\left(1+\frac{1}{jkr}\right) = \\ &\frac{jkQe^{j(\omega t-kr)}}{4\pi r}\left(1+\frac{1}{jkr}\right).\end{aligned} \tag{5.16}$$

From a practical standpoint, the Real components of (5.15) and (5.16) are of interest, namely

$$\mathfrak{r}\left\{p'(r,t)\right\} = -\frac{\omega\rho_0 Q}{4\pi r}\sin(\omega t - kr), \tag{5.17a}$$

$$\mathfrak{r}\left\{\mathbf{U}'(r,t)\right\} = -\frac{\omega Q}{4\pi c_0 r}\left(\sin(\omega t-kr) - \frac{1}{kr}\cos(\omega t-kr)\right). \tag{5.17b}$$

In the implemented solver, sources of higher order are described using a collection of monopoles placed at correct locations and assigned appropriate phase angles. An example representation of a monopole and dipole pressure distributions has already been shown in Figure 2.1.

Before validating the acoustic analogy, the flow solver alone was used in order to explore the influence of the time derivative scheme used as it was recognised this would heavily influence the solution of Eq. (5.14). For this investigation a simple cubic domain centred at the origin and with the edge length of 2 m was used. The domain was discretised with 10^3 elements. A monopole was placed at the origin and its source strength was arbitrarily chosen so that

$$-\frac{\omega\rho_0 Q}{4\pi} = 1, \tag{5.18}$$

thus making the pressure signal 1 m away from the origin vary between ± 1 Pa. The frequency of oscillation of the source was chosen as 100 Hz, which was considered representative of low frequency noise encountered in marine applications (see Table 2.1). Based on this, the time step of the simulation was set to Δ t=10^{-5} s, ensuring high density of data. Water of standard properties, i.e. ρ_0=1000 kg m^{-3} and c_0=1500 m s^{-1}, was used. The exact values were not important at this stage as they were utilised for the purposes of verification.

The results shown in Figure 5.4 compare the analytically obtained derivative of pressure with its numerically obtained counterparts at a cubic control surface with the side length of 0.1 m. One may note how the higher order `backward` scheme agrees much better with the analytical results than the first order `Euler` scheme, despite the time step of the simulation being fine. This highlighted the need of using the more accurate but less stable approach in the future work.

5.5 Acoustic analogy verification and validation

5.5.1 Basic validation

Following the implementation of the FW-H utilities and a simple acoustic source solver, a simulation was devised in order to validate the implemented acoustic analogy. For this purpose, a spherical control surface was used to limit any possible errors or inaccuracies coming from sharp corners, as could be possible for a cubic surface, for instance. This was constructed using the OpenFOAM unstructured mesher, `snappyHexMesh`, using a background mesh with edge length of 0.1 m and refining it twice on the surface of a sphere with radius of 0.2 m. The obtained mesh faces were then assembled into the control surface. The monopole strength was still kept such as to keep the signal at 1 m between ± 1 Pa at source frequency of 100 Hz.

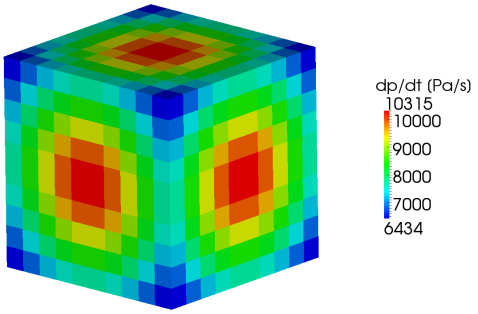

(a) Analytical

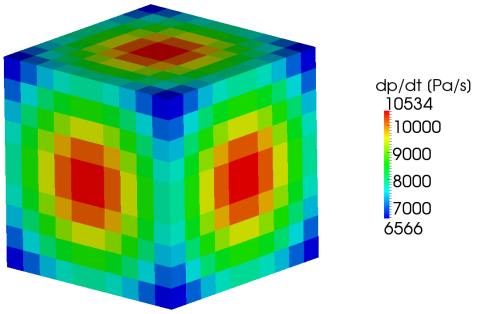

(b) Explicit - Euler scheme (1^{st} order)

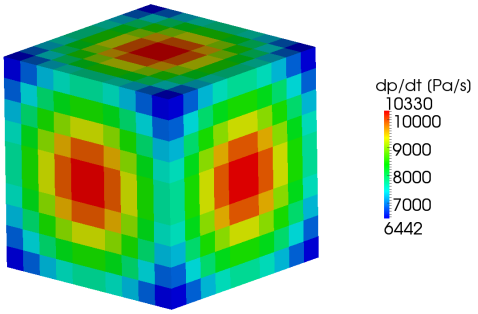

(c) Explicit - Backward scheme (2^{nd} order)

Figure 5.4: Comparison of the analytical and explicit pressure time derivatives for the monopole case as evaluated on the cubic control surface at source time τ=0.001 s.

Figure 5.5 shows the predicted receiver pressure. Two data sets are presented for the FW-H analogy, one where the retarded time was accounted for and another where it was ignored. One may see that agreement to under 1% is achieved between the predicted and analytical data in terms of magnitude and all of the waveforms have very comparable shapes.

As expected, for this simple case the retarded time acted to simply introduce a phase shift to the data. However, for a more complex source with complicated distribution of the hydrodynamic variables on the control surface, omitting the retarded time could potentially lead to less obvious errors. One may visualise this by considering several simple sources of different magnitudes and frequencies distributed throughout a volume

of fluid. If their contributions to an arbitrary receiver are not corrected for the difference between arrival and emission times, it could happen that the differences in phases of the sources would cause amplification or cancellation of the predicted pressure waves.

Figure 5.6 depicts the time series of the predicted time signal, showing its breakdown into individual terms of Eq. (5.14). It may be seen that a surpassing majority of the signal is constituted by the pseudo-thickness term of the equation.

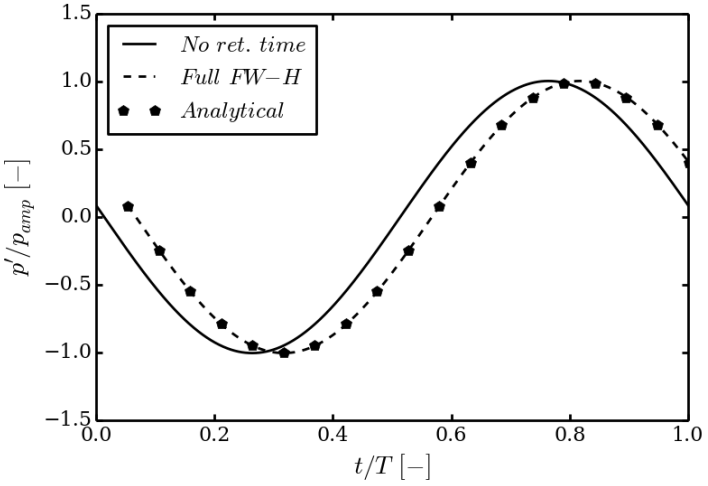

Figure 5.5: Time signal of pressure induced by a monopole predicted using the FW-H analogy for a receiver 1 m away, also showing the effect of retarded time.

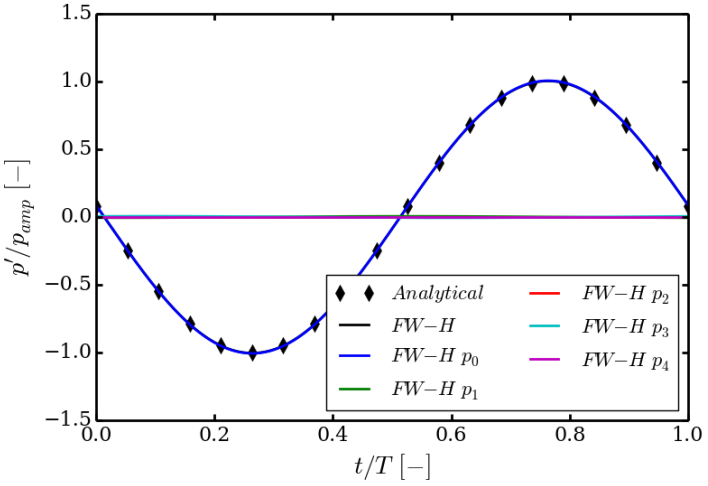

Figure 5.6: Breakdown of a pressure signal induced by a monopole oscillating at 100 Hz predicted using FW-H for a receiver 1 m away showing contributions of different terms of the FW-H equation. p_{amp} is the analytical signal amplitude and $p'_{0,\ldots,4}$ are the individual FW-H components, as defined in Eq. (5.14).

To validate the other terms of the FW-H equations, a dipole source was used. This was centred at the origin, with the source and sink separated by 0.02 m along the x-axis. The magnitudes of their individual strengths were kept the same and adjusted to yield the total signal at the receivers to vary between ±1 Pa.

By analysing the time histories shown in Figure 5.7 one may note that, as expected, the higher order terms of the FW-H equation have non-zero contribution to the total signal, except for the non-linear velocity terms of Eq. (5.14). This was expected as the simple source does not produce non-linear excitations. Overall, good agreement to under 1% is seen between the analytical and computed data in terms of phase and magnitude.

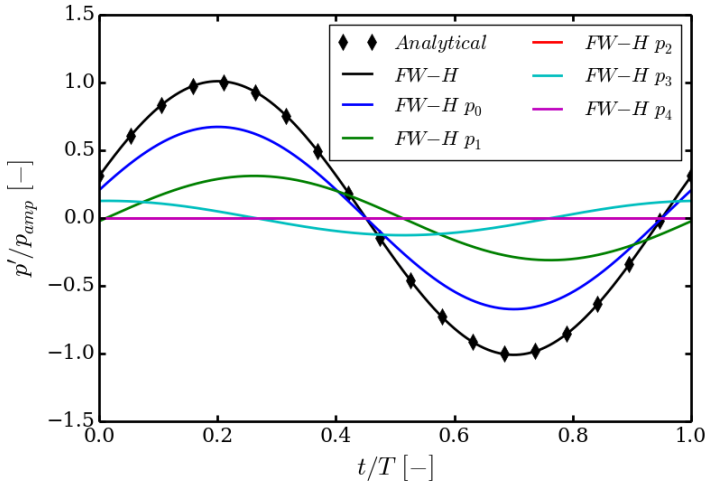

Figure 5.7: Breakdown of a pressure signal induced by a monopole oscillating at 100 Hz predicted using FW-H for a receiver 1 m away in the direction parallel to the dipole axis. Contributions of different terms of the FW-H equation may be seen.

5.5.2 Sensitivity Studies

Following the basic validation of the acoustic analogy, it was necessary to establish its limits of applicability before real geometries could be studied. This stage was particularly important as it allowed basic guidelines relating to the mesh size and time step requirements needed for a given degree of accuracy to be developed. The obtained information was also used to better understand the issues relating to how the data surface is defined in relation to the source region.

5.5.2.1 Sampling rate

Figure 5.8 shows the change in the ratio of predicted to analytical value of the root-mean-square of the receiver pressure for a monopole source with varying the sampling frequency. A trend may be seen whereby the lower the temporal resolution, the quicker the FW-H diverges from the analytical value as source frequency is increased. This may be associated with the finite time derivatives used in the acoustic analogy not being well posed and thus introducing errors. Also, as the sampling rate is reduced, the sampled points do not represent the waveform well enough. Nonetheless, it may be seen that for the frequency range below 1 kHz, relevant for low- and medium-frequency cavitation noise on a propeller, even the coarsest time step provides results in agreement with the analytical values down within 2%. This is an important observation as it shows that the low frequency noise for a typical marine propeller flow may, in theory, be captured, even with a relatively coarse time resolution.

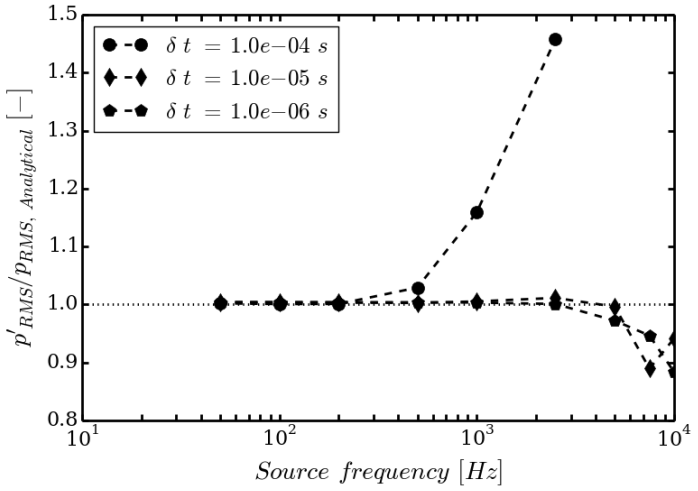

Figure 5.8: The effect of samling rate on the FW-H prediction accuracy. Results for a monopole at three different sampling rates.

5.5.2.2 Mesh density

Next, the effect of the size of the control surface elements relative to the wavelength was studied, as shown in Figure 5.9. The refinement level for the baseline mesh was varied between 1 and 4.

As the grid becomes refined, the FW-H solution tends to the analytical value. However, it has also been noted that the ratio of mesh face size to wavelength over the range of typical frequencies is relatively small, even for the coarsest grid and highest wave number. Importantly, the baseline mesh with refinement level 2 was seen to be within a 0.5% error margin compared to the finest one, indicating a mesh-independent solution.

Given that the cell size used may be considered relatively coarse for a marine propeller simulation, it has been concluded that it is likely the hydrodynamic solution that will put more stringent requirements on the mesh density rather than the acoustic analogy itself. Still, for this study there were no dissipation nor dispersion errors since the flow field was prescribed directly to the cells. In a real simulation this will not be the case and so additional mesh refinement will be required in order to preserve the flow features of interest out to the control surface.

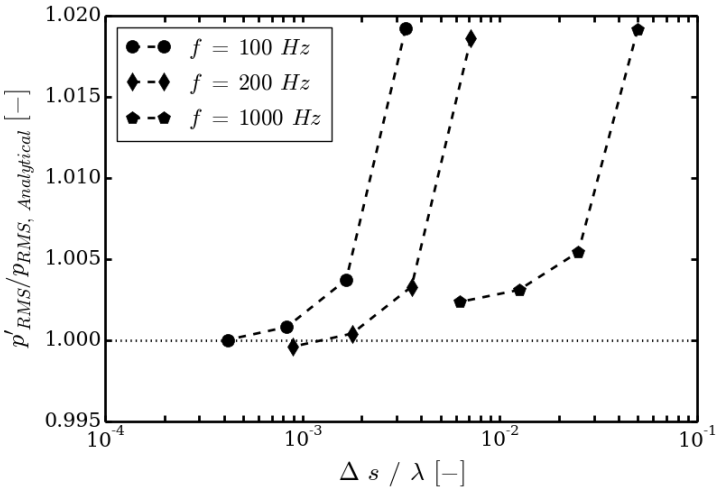

Figure 5.9: The effect of mesh size, Δs, relative to wavelength, λ, on the FW-H prediction accuracy. Results for a monopole at three different source frequencies.

5.5.2.3 Control surface size

The relative size of the control surface to the wavelength of the source was also considered an important parameter, as it will dictate the strength of the signal perceived by the control surface and the number of faces available to describe the source. For this reason, a simulation with spherical control surfaces of 5 different radii, 0.1, 0.2 (baseline), 0.3, 0.4 and 0.5 m was carried out for a dipole source. Figure 5.10 shows the RMS of pressure for three different receivers placed around the origin. As expected, with increasing the control surface size the error reduces as there are more elements representing the control surface and providing a finer resolution. Notably, beyond R/λ of 0.01 the relative error becomes smaller than 1%, again indicating that the chosen baseline mesh resolution was sufficient to capture the source characteristics.

5.5.2.4 Source frequency

It has been reported that for a porous FW-H formulation the terms in Eq. (5.14) lose their physical meaning, namely, a loading term contribution may not always be

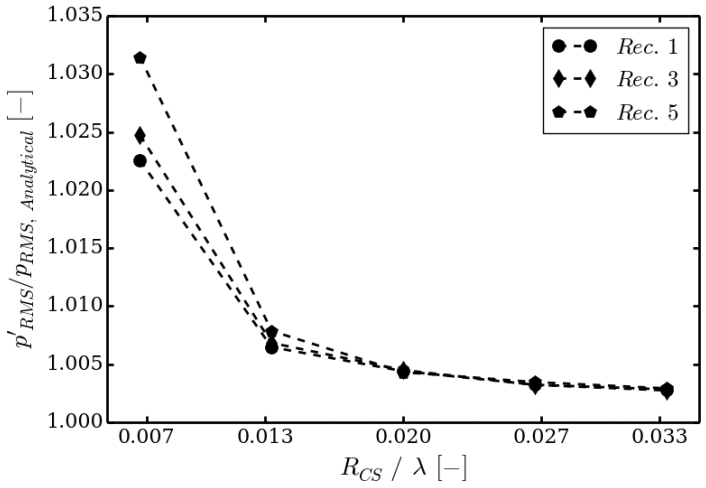

Figure 5.10: The effect of distance between the control surface and the source on FW-H result. Data for a dipole oscillating at 100 Hz.

associated with a dipole source [142]. An observation has been made by comparing Figures 5.7 and 5.6, showing the time traces for a monopole and dipole at 100 Hz, with the same data predicted for sources oscillating at 1000 Hz, shown in Figure 5.11.

Firstly, one may observe that for the monopole at high frequency, new terms of the FW-H equation start contributing to the total signal. For the dipole, increasing frequency may be seen to cause a phase shift in the pseudo-loading terms and also change their relative magnitude. This illustrates that indeed the terms of the porous FW-H formulation may not be directly attributed to a noise source of particular order. Consequently, their relative importance will vary depending on the nature of the noise generation mechanism being studied and the particular simulation set up.

5.5.2.5 Receiver distance

The distance from the source to the receiver was also found to have an effect on the FW-H term phase and magnitudes, as seen in Figure 5.12. For a receiver placed 75 m (5λ) instead of 1 m away, the proportional pressure pseudo-loading term may be seen to become negligible as the listener moves away from the source. This may be explained by analysing the denominators in Eq. (5.14) and noting that for this term these increase proportionally to the receiver distance squared.

5.5.2.6 Open control surface

Reportedly, the FW-H analogy should cope well with the control surface being placed in the non-linear region of the fluid [25]. In the literature, however, one may often see

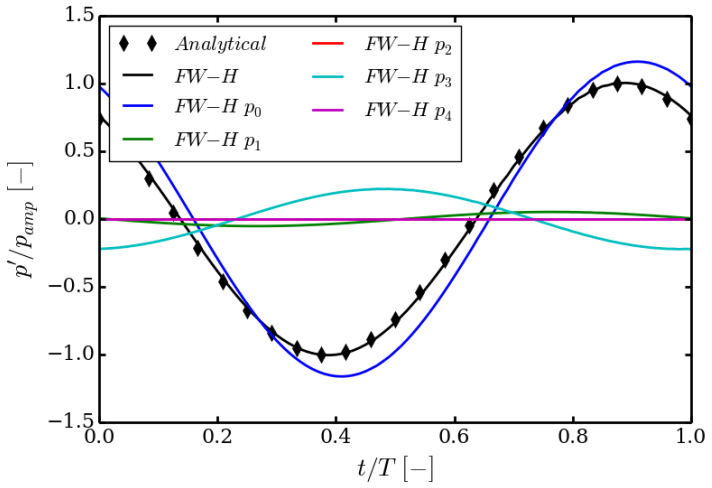

(a) Monopole

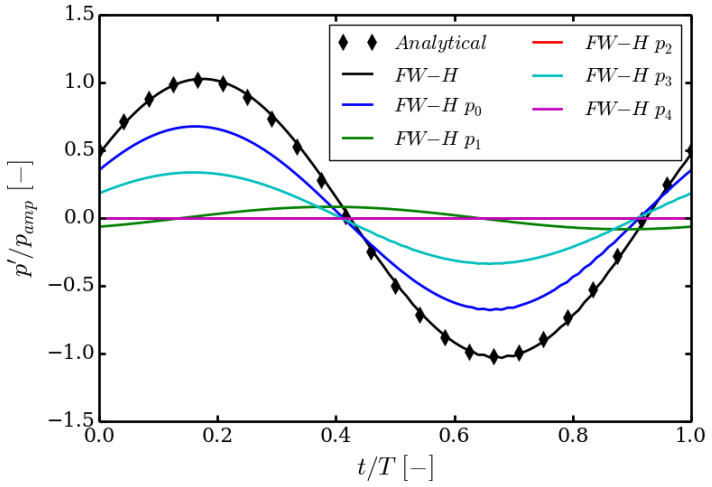

(b) Dipole

Figure 5.11: Effect of source frequency on the relative magnitude of FW-H terms shown for a monopole and a dipole at 1000 Hz.

the elements of the control surface experiencing vortical flow features being omitted, for instance for turbulent jet flows or even for some of the published marine propeller studies [90, 162]. This stands in contradiction with the need to enclose all of the possible noise sources present in the fluid inside the control surface but, to a certain extent, allows the expensive volume integral needed to obtain the p'_Q to be ignored. It was therefore decided to investigate what effect does removing the end of the control surface has on the predicted noise by enclosing a dipole inside a cylinder whose length was varied between 0.5 and 2.0 m. The result is shown in Figure 5.13.

One may note how, with increasing the length of the cylindrical control surface in the

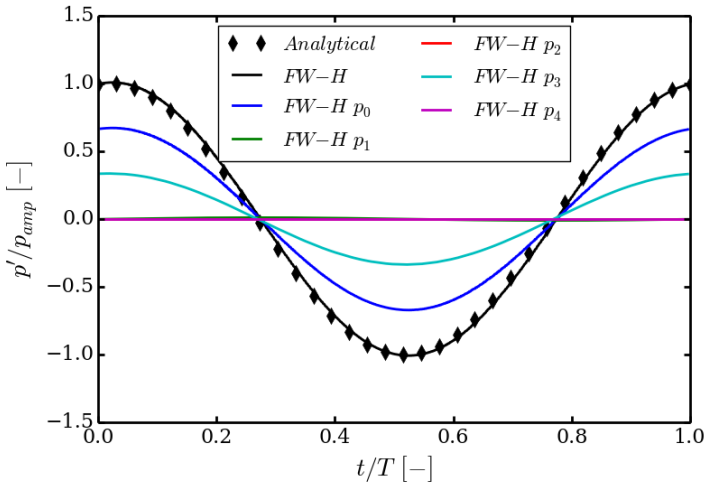

Figure 5.12: Effect of source-receiver distance on the relative magnitude of FW-H terms shown for a dipole at 100 Hz with receivers placed 5λ away from the source.

x-direction, the error is small for the receivers for which the line of sight to the source penetrates the control surface. For angles closer to the control surface axis, the error is approximately halved each time the cylinder length is increased by a factor of two, but yet does not become zero in the range investigated. It therefore seems possible to reduce it even further but only at an expense of storing more flow field data and thus making the analysis more intensive in terms of computational resources required. It is also unlikely that reliable estimates will be possible directly along the shaft line if an open-ended control surface is used. This finding is of key importance to studying the loading noise due to non-uniform inflow to the propeller race, which will be of dipole nature and see most prominent fluctuations perpendicular to the propeller disc. Therefore, if aiming to study this particular problem one should consider the volume integral or employ some of the outlet disc averaging and other similar techniques discussed in the literature [152, 181].

5.6 Application to the Insean E779a propeller

5.6.1 Aims of this study

The initial PPTC study discussed in Chapter 4 has indicated that RANS equations can be successfully used in order to model the large scale flow motions induced by a rotating propeller. It was therefore aimed to extend the available simulation to include the newly implemented acoustic analogy. However, there was no comparison data available at the

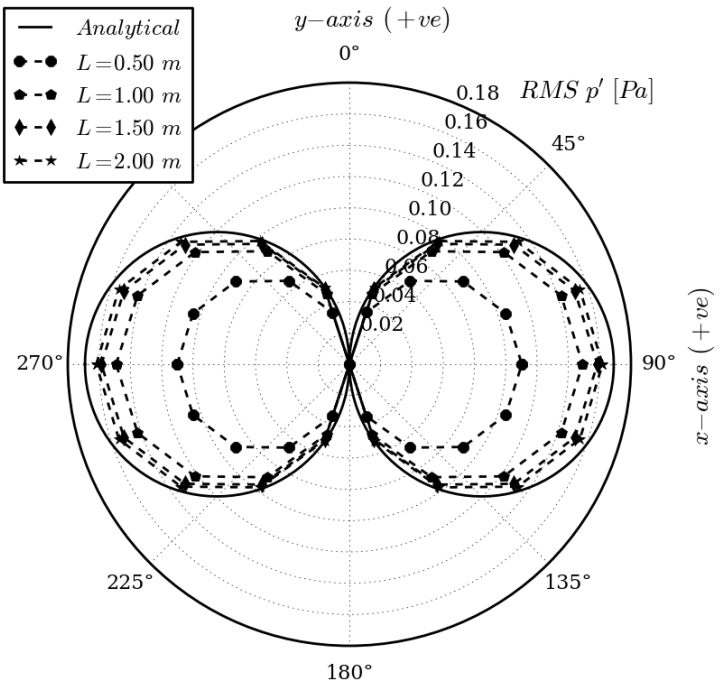

(a) Directivity pattern (p'_{RMS})

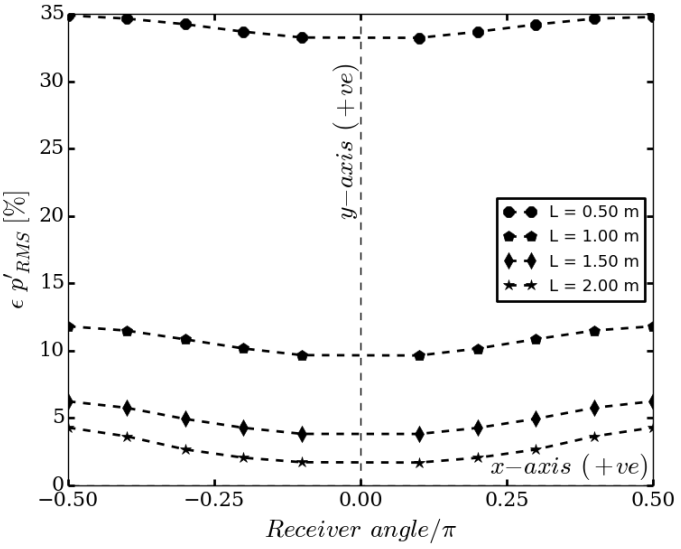

(b) Error in RMS

Figure 5.13: The effect of axial length of an open-ended control surface on dipole directivity predicted using FW-H. Data for a dipole oscillating at 100 Hz. Errors shown only for receivers above the x-axis for clarity.

time to allow the present results to be benchmarked against. It was therefore decided to switch the attention to the Insean E779a propeller [33].

As already mentioned, this test case does not represent a modern geometry but has been studied by Ianniello et al. [89] and Lloyd et al. [134] using their FW-H analogy codes in non-cavitating conditions. While no experimental hydroacoustic data is available in the open literature for the E779a propeller, comparison with other numerical studies at the very least increases the confidence in the present implementation. To compensate for the lack of the measurement data, the approach by the other authors was decided to be followed, where FW-H predictions for near-field receivers would be compared with the direct RANS solution.

5.6.2 Background

The presented study formed part of a joint research effort with Lloyd *et al.* [133]. The numerical grids and intended simulation set-up used were provided by the collaborators. The author of this thesis conducted all of the OpenFOAM simulations, took active part in preparing the post-processing scripts, as well as in drawing conclusions from the analysis.

Table 5.1 summarises the particulars of the Insean E779a propeller and a close-up view of one of its blades is shown in Figure 5.14. It may be seen that the propeller is characterised by a relatively low pitch ratio, has a high blade area ratio and nearly no skew.

Figure 5.14: View of the Insean E779a propeller blade.

5.6.3 Simulation set-up

Only a single advance ratio of 0.88 was considered in this case. This translates to a rotational speed of 25 rps and inflow velocity of 5 ms^{-1}. Fixed velocity and turbulence

Table 5.1: Particulars of the Insean E779a propeller.

Parameter	**Unit**	**Value**
No. blades	-	4
Diameter	m	0.227
Expanded area ratio	-	0.689
Pitch ratio at 0.7 R	-	1.1
Hub ratio	-	0.1

inlets were used to simulate uniform inflow conditions. Mixed outlet conditions were used, following the approach by Lloyd *et al.* [134], where Neumann boundary condition was applied to pressure and velocity fields where the accelerated flow impinges on the downstream end of the domain. The remaining part of the outlet was assigned a fixed value of pressure and free pressure outlet condition for velocity. The outer walls were assumed to be slip, while no-slip condition was applied to the propeller, hub, and shaft. Since the mesh met the $y^+ \leq 1$ condition, no additional treatment was applied to the solid boundaries and instead the full boundary layer profile was simulated. To match the experimental conditions, the water was assigned density of 997.44 and kinematic viscosity of $9.337 \cdot 10^{-7}$ m^2 s^{-1}.

Second order time discretisation was used, and the convection term of the RANS equation was resolved using the second order QUICK scheme. First order schemes were used to model the turbulent quantities. The PIMPLE algorithm was used to solve the pressure-velocity coupling. five outer loops were applied with time step of $5 \cdot 10^{-6}$ s, corresponding to a Courant number of approximately 6.

Two structured hexahedral numerical grids were used. These consisted of 1.6 and 13 million elements for the coarse and fine variants, respectively. An outline of the control surface used for FW-H computation, also showing the mesh arrangement for the coarse grid, is demonstrated in Figure 5.15. The numerical domain extended five propeller diameters in all directions from the centre of the propeller plane. The coarse grid was only used for the force coefficient calculation, the flow field and acoustic analyses were carried out on the fine mesh.

In order to compute the acoustic signature of the propeller, two FW-H integration surfaces were used. The baseline was chosen to follow Lloyd *et al.* [134] and Ianniello *et al.* [89], namely 0.179 m upstream and 0.5 m downstream of the propeller plane with a radius of 0.18 m. The longer variant reached 0.25 m further downstream, as seen in Figure 5.15. Each of the control surfaces was split into the main cylinder and two end caps, allowing for bigger flexibility when analysing the data. Same set of receivers as in the study by Lloyd *et al.* was employed, and is given in Table 5.2 and depicted in Figure 5.15.

Table 5.2: Receiver locations for the Insean E779a propeller study (x-axis parallel to the shaft, x=0 m is the propeller plane).

		x [m]				
		0.1403	0.0000	-0.1279	-0.2677	-0.4569
y [m]	0.1477	1	2	3	4	5
	0.1704	6	7	8	9	10
	0.1932	11	12	13	14	15
	0.2159	16	17	18	19	20
	0.2386	21	22	23	24	25
	0.2648	26	27	28	29	30

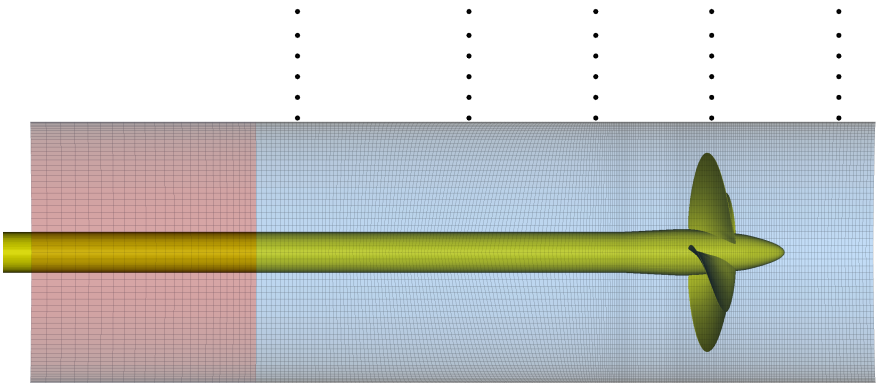

Figure 5.15: Locations of receivers used in the E779a study relative to the geometry and the baseline (blue) and extended (red) FW-H control surfaces. Flow from right to left.

5.6.4 Results

Figure 5.16 and Table 5.3 compare mean propulsive coefficients with respect to the experimental data [89, 132]. Agreement to within 3% with the experiment has been reached for the thrust and torque coefficients, which is satisfactory but greater than would be desirable. It is also important to note that increasing the mesh size by nearly a factor of 10 did not have an obvious effect on the convergence of forces, also in the reference study by Lloyd *et al.* [134]. This may possibly be explained by the mesh refinement not being uniform but focusing on better resolving the wake of the propeller, thus perhaps causing the surface pressure distribution on the blades to be underestimated.

Figure 5.17 shows iso-contours of pressure coefficient,

$$K_P = \frac{p}{\rho n^2 D^2}, \tag{5.19}$$

at a snapshot in time. One may note how the core of the tip vortices is captured relatively well until approximately 3 revolutions downstream, but then loses focus and disappears completely as the mesh begins to coarsen downstream of the end of the baseline FW-H

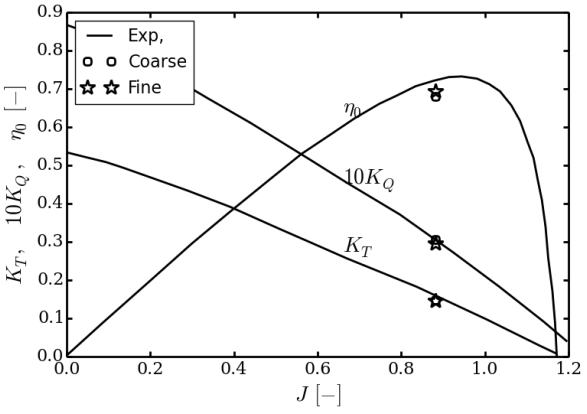

Figure 5.16: Mean force coefficients predicted for the Insean E779a propeller.

Table 5.3: Comparison of the mean propulsive coefficients for the E779a case. Errors with respect to the experimental values denoted with ϵ. EFD are the experimental data by [33], Lloyd *et al.* refers to numerical data from [134] computed on the same coarse and fine meshes as used in the present study.

Source	$\mathbf{K_T}$	$\mathbf{10K_Q}$	$\boldsymbol{\epsilon K_T}$	$\boldsymbol{\epsilon K_Q}$
EFD	0.1510	0.3050	-	
CFD - Lloyd *et al.*, coarse	0.1463	0.2977	-3.1%	-2.4%
CFD - Lloyd *et al.*, fine	0.1445	0.2931	-4.3%	-3.9%
CFD - coarse	0.1487	0.3063	-1.5%	0.4%
CFD - fine	0.1467	0.2961	-2.9%	-2.9%

control surface. It is also interesting to note the dipole-like pressure distribution caused by the rotation of the propeller blades in the uniform flow.

Figure 5.18 compares two iso-contours of the vorticity field and their relative position to the FW-H control surface arrangement. An important observation is that the baseline control surface sees reasonably well defined vortical structures at its downstream extent. The longer variant, located in the region with a significantly higher stream-wise cell expansion ratio, experiences far more broken-up vortices, which have merged into a toroidal structure by the time they impinge on the downstream extent. It is also worth noting strong root vortices being created by the propeller, visible particularly well in Figure 5.18a.

Figure 5.19 presents a similar set of data and compares it to the results obtained by Lloyd et al. [133] using a different finite-volume CFD code on an identical numerical grid and the same turbulence model. Similar strength of the tip vortices is seen between the two cases but OpenFOAM simulation appears to have predicted a stronger vorticity further downstream.

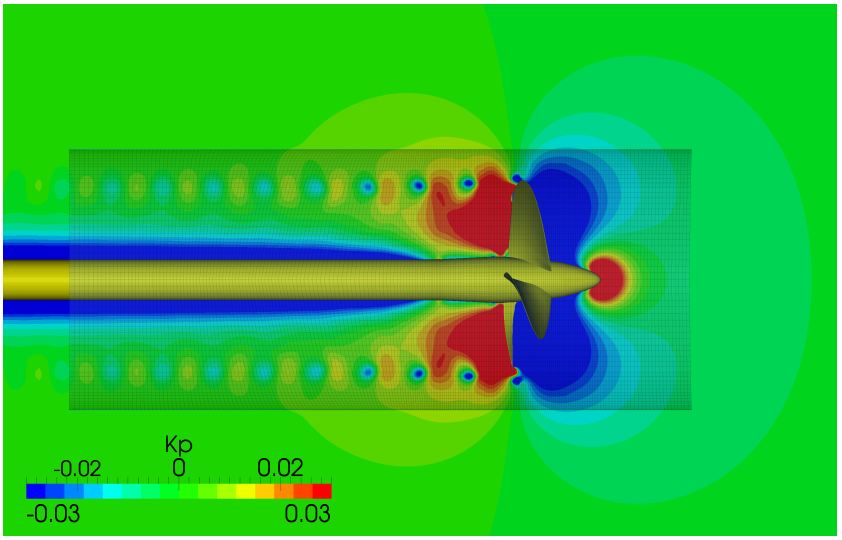

Figure 5.17: Instantaneous pressure coefficient contours for the E779a showing locations of tip vortex core and the extent of the baseline FW-H integration surface in light grey.

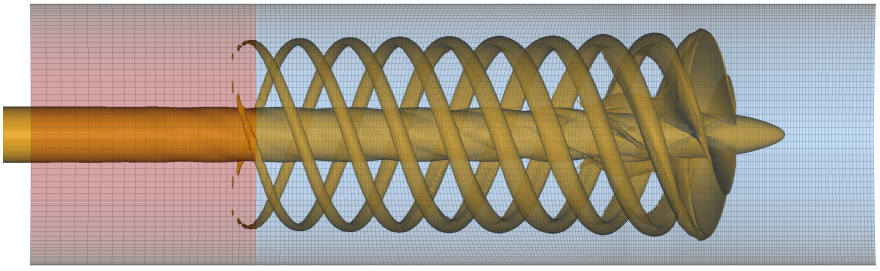

(a) $|\omega| = 125.0\, s^{-1}$

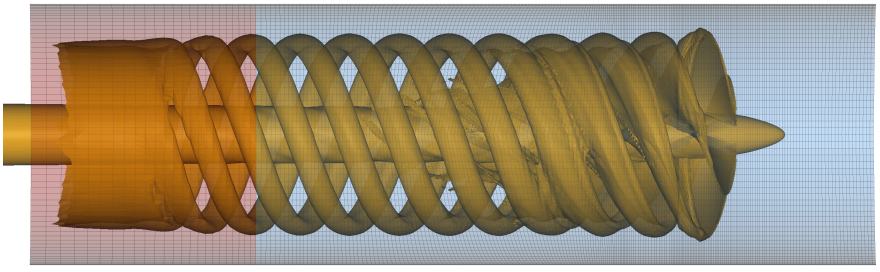

(b) $|\omega| = 62.5\, s^{-1}$

Figure 5.18: Iso-contours of vorticity around the E779a propeller also showing the extents of the baseline (blue) and extended (red) FW-H control surface.

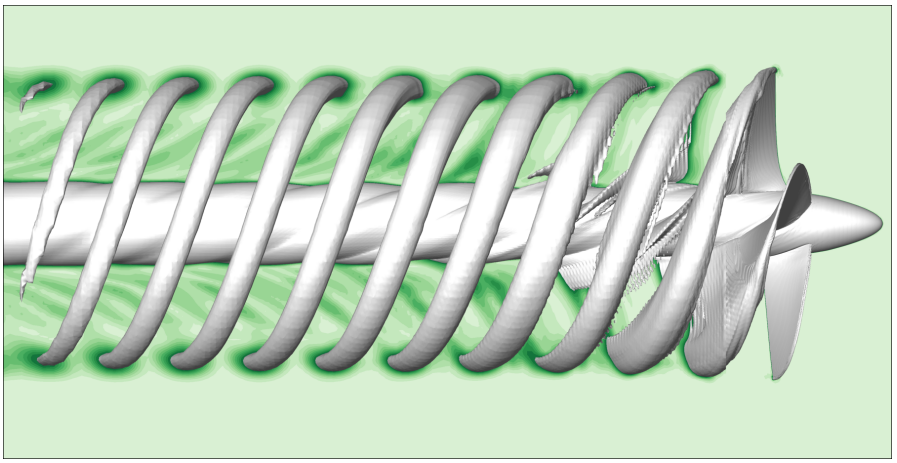

(a) OpenFOAM

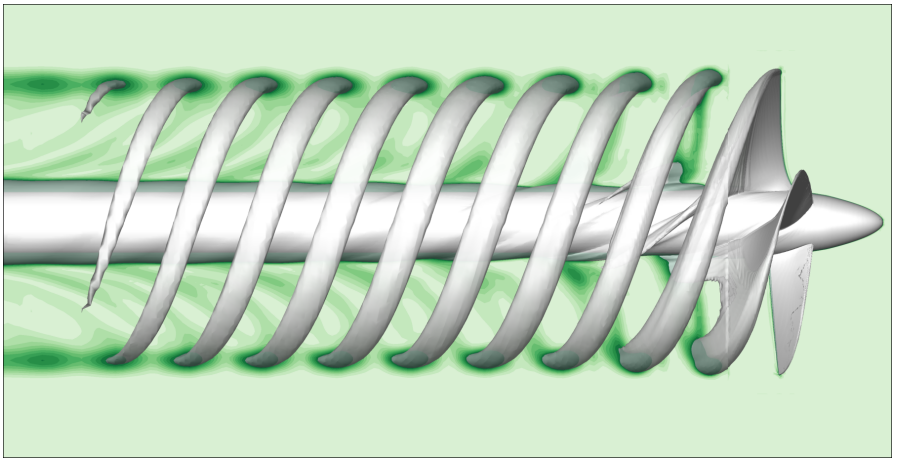

(b) ReFRESCO

Figure 5.19: Flow field comparison for the E779a propeller between OpenFOAM and ReFRESCO results showing vorticity iso-contours $|\omega| = 100\,s^{-1}$. OpenFOAM data forms part of the present project, the ReFRESCO result and the actual figures provided by Lloyd et al. [133].

Figure 5.20 presents time histories of pressure predicted for receiver 7 located on the propeller plane using an open variant of the baseline FW-H control surface. A comparison with the results by Lloyd *et al.* is also shown. Good agreement may be seen between both the total signals and their individual terms, as well as the RANS solution itself. The positive and negative peak values of all the signals are within 6% of each other and their wave forms and phases show very little difference. As expected, the unsteady FW-H terms (p'_4 and p'_5 in Eq. (5.14)) have a negligible contribution due to the time derivatives of the flow being small.

Figure 5.21 presents the first 5 harmonics of the blade pass frequency present in the total pressure signals in Figure 5.20, as well as for receiver 22 further away from the blade tip but still on the propeller plane. For the former, the first harmonics are within 5% of each other, with the error being similar for the second harmonic but growing for higher

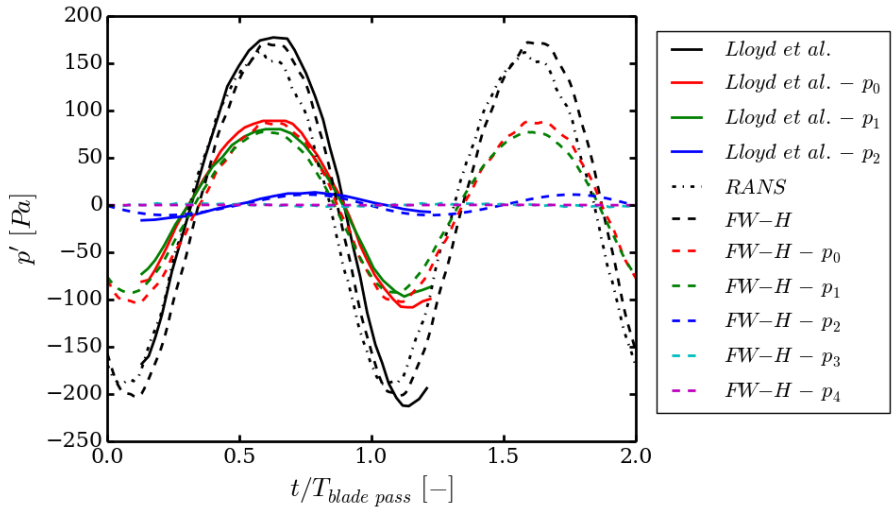

Figure 5.20: Breakdown of the predicted pressure signal for the E779a at the propeller plane compared against results presented by Lloyd *et al.* [132], receiver 7. Data presented as a function of non-dimensional time defined based on the blade pass period.

frequency components. The receiver further away also sees reasonable consistency of results in terms of the first harmonic with the values being within 4% of each other. Higher frequency components, however, exhibit significantly larger discrepancies. This may be partly caused by the fact that their magnitude is indeed very small and so capturing them is very challenging and would be affected by factors such as iterative convergence of the flow solution and details of the discretisation scheme implementation.

The ultimate aim of this study was to further investigate the effect of the wake and its interaction with the downstream parts of the FW-H control surface on the predicted pressure signals. Acoustic analysis was therefore performed for both of the considered control surfaces in open, upstream end closed, and fully closed variants. Figure 5.22 shows the time signals for the three variants of the baseline control surface predicted at receiver 7. All of the data series may be seen to agree well, implying there is merit in including the caps of the cylindrical control surface.

Different results may be seen in Figure 5.23, which presents the same data for the baseline and extended control surfaces and receiver 5 above the wake of the propeller. Firstly, it may be seen that the magnitude of the pressure oscillation disagrees between the RANS and FW-H significantly. It is difficult to establish the reason for this discrepancy as it could be both due to problems with the acoustic analysis as well as insufficiently accurate predicitons of the flow solver in this region. The latter appears likely, given the noticeable coarsening of the grid and the fact that the flow in this area is strongly dependent on resolution of the gradients. An important observation can be made about the phase of the FW-H and direct pressure signals. When the control surface is open

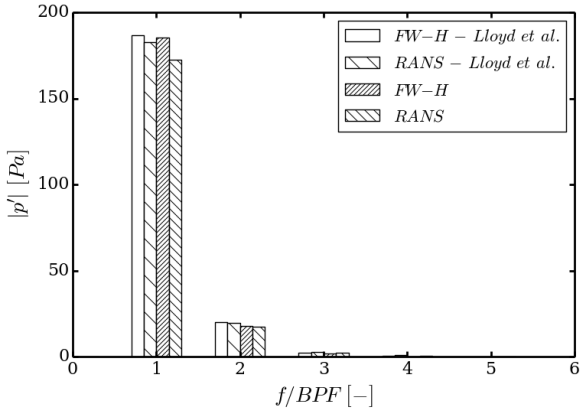

(a) Receiver 7

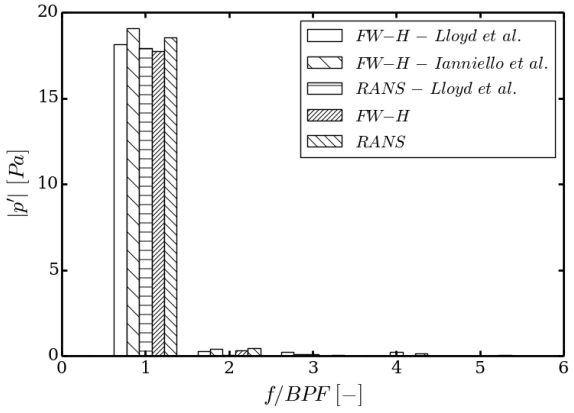

(b) Receiver 22

Figure 5.21: Blade pass harmonics of pressure signals for E779a at the propeller plane, open control surface. Compared against results presented by Lloyd *et al.* [132] and Ianniello *et al.* [89] (where available).

at the downstream end, there appears to be no phase shift between the two series, as was seen in the results for upstream receivers. However, when the short control surface is closed, a visible phase shift occurs. This disappears when the long control surface is used to perform the FW-H analysis.

The origins of this issue may be better visualised when examining the distribution of the dominant p'_0 FW-H term on the control surface, shown in Figure 5.24 for receivers 1 and 5 computed using the baseline and extended control surfaces. For the listener located at the propeller plane the effect of individual blades may be seen on the control surface, with elements facing the receiver directly contributing the most. One may also observe a zebra-like pattern corresponding to the tip vortices travelling downstream of the propeller and acting as noise sources in the wake. An important observation is the presence of strong sources at the downstream end of the baseline control surface, caused

by the wake penetrating it. For the longer control surface this effect may no longer be seen as the wake turbulence dissipate and lose coherence by the time they reach the end of the longer control surface.

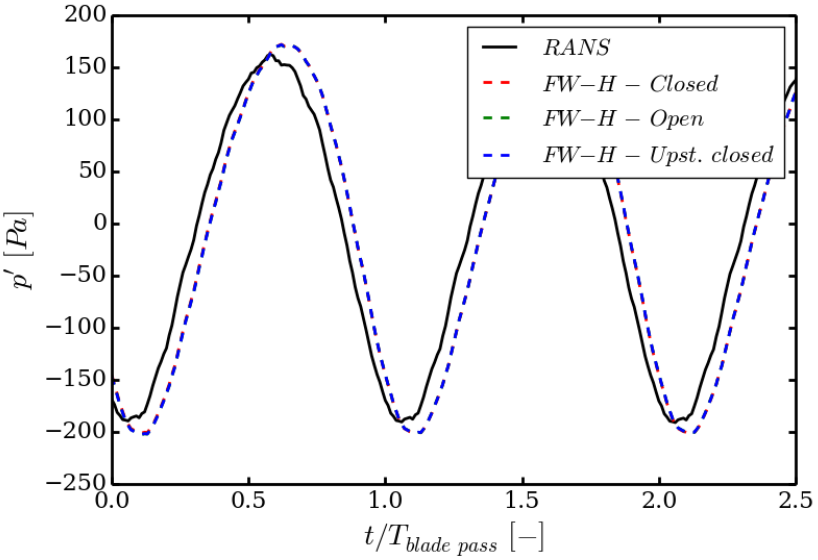

Figure 5.22: Influence of closing the FW-H control surface for the E779a study, receiver 27 (propeller plane), baseline control surface.

5.6.5 Discussion

It was worrying to observe the under-prediction of the thrust coefficient in the present results. An aspect to note is that the error appears to be mesh independent and consistent between the present code and the data by Lloyd *et al.*, although there is a relatively consistent 2% difference between them in both thrust and torque. The origin of this discrepancy was not identified but it is not expected to have a large effect on the comparison made between the FW-H and the RANS solver, which was the primary objective of the present study. This is because pressure and velocity distributions of RANS are used to evaluate the FW-H, which should make both results consistent.

At the outset of the study, it was not expected that the tip vortex will be resolved with an unsteady RANS method as well as it was in the presented case. This may be attributed to the high-quality mesh with an approximately uniform density being used in the wake and high order convection schemes being used for the discretisation. The presented results indicate how coarsening the mesh just slightly causes the wake structure to be lost due to numerical dissipation. This has implications for the subsequent studies, indicating that maintaining a fine mesh structure in the wake is important if acoustic contribution of that region of the flow is to be accounted for. It also follows that careful

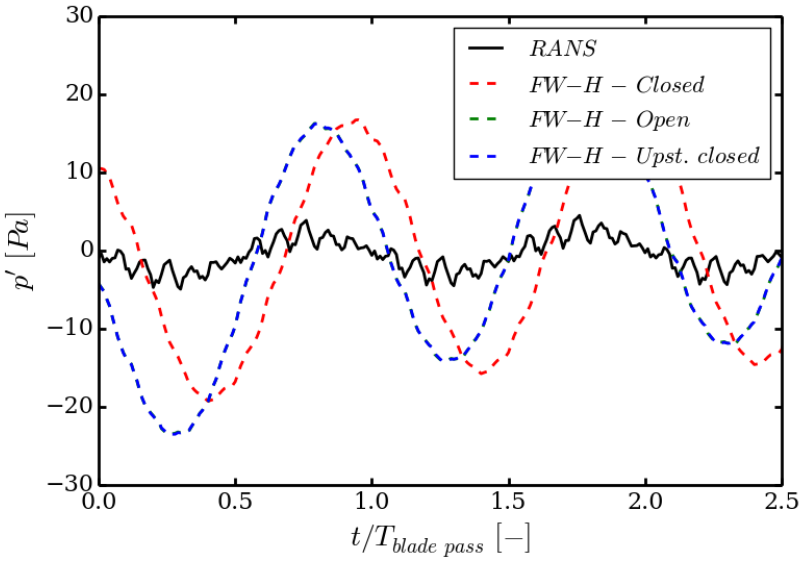

(a) Baseline control surface

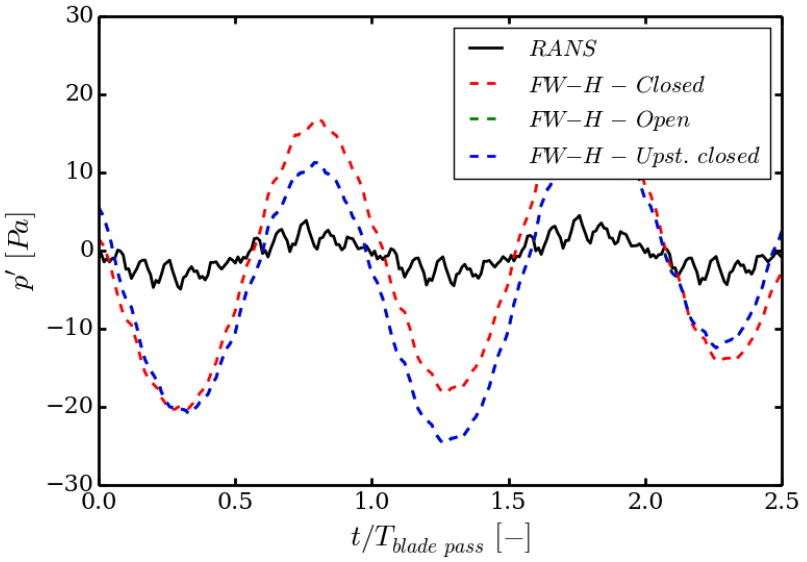

(b) Extended control surface

Figure 5.23: The effect of closing the FW-H control surface for a downstream receiver (rec. 5) for control surfaces placed in different flow regimes (baseline and extended).

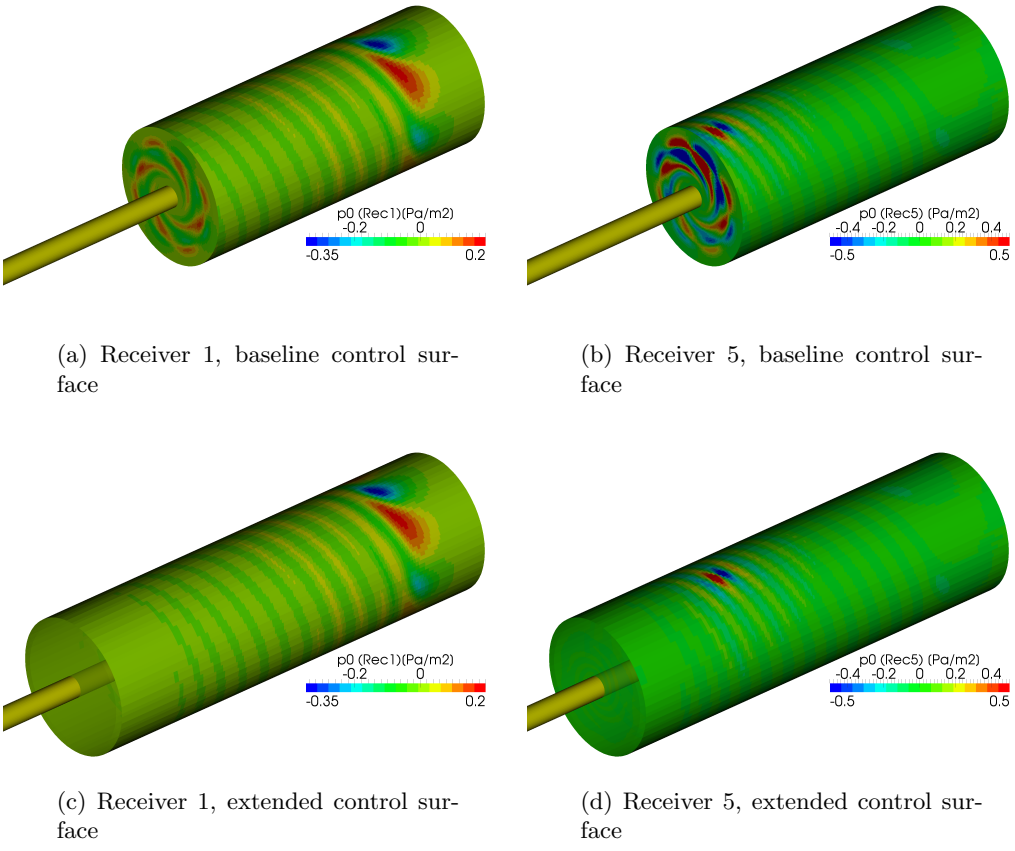

(a) Receiver 1, baseline control surface

(b) Receiver 5, baseline control surface

(c) Receiver 1, extended control surface

(d) Receiver 5, extended control surface

Figure 5.24: Distribution of the pseudo-thickness FW-H term on the two control surfaces used for E779a.

consideration must be given to how the porous data surfaces are placed relative to the body.

Moreover, comparison of the wake structure predicted using the currently used code, OpenFOAM, with results by Lloyd et al. [133] obtained with ReFRESCO indicates very good agreement. This is an important observation as it increases the confidence in the presently used numerical set-up and serves as a reminder that fundamentally similar codes should produce very comparable results given the same input parameters.

Very good agreement was observed for the FW-H results for receivers at the propeller plane. This applies to both the FW-H comparison from the present simulation as well as benchmarking against data by Lloyd et al. [133] and Ianniello et al. [89]. It is also worth noting that the individual terms of the FW-H equation agreed very well with the former published data set. This is particularly important from the point of view of verification of the present implementation, as it indicates that for nearly identical input flow field data the FW-H code developed as part of this project responds with the same outputs as the codes used by other authors. The initial sensitivity studies also indicated that the same physical source may be represented by different porous FW-H terms depending on

the source-receiver orientation, source frequency and its multipole order. Thus, being able to reproduce the magnitude of each of the terms accurately given a realistic data set, is crucial and has been achieved.

An important topic is the influence of the control surface size and orientation relative to the flow field, notably the propeller slip stream. It has been shown that a completely closed control surface getting penetrated by coherent vortical structures at the downstream extent leads to a spurious noise signal for receivers further downstream from the propeller plane. In the present results this manifested itself in the form of a phase and amplitude shift relative to the results obtained using an open data surface. Unfortunately, the RANS pressure data at that location appear to have lost accuracy and thus their magnitude differs significantly from the FW-H time histories. Thus, only its phase information may be used for the purpose of comparison. Nonetheless, it has been demonstrated that extending the control surface to the region where the vortices are no longer coherent, but have dissipated due to the mesh getting coarser, removes the spurious noise source nearly completely.

The origin of the spurious noise source may be observed from analysing how much specific parts of the data surface contribute to the signal predicted at a given receiver location. It has been shown that the downstream receiver is affected primarily by the faces close to it, meaning the noise sources present in the wake will play a dominant role in determining its noise signal. This observation, first of all, explains the small magnitude of the predicted pressure signals, as the magnitude of the flow quantities contributing to the noise in this part of the domain is going to be significantly smaller than at the propeller plane. A similar behaviour may be seen whereby the downstream end of the baseline control surface contributes significantly to the predicted pressure signals. This contribution is particularly strong at locations where vortices were observed to penetrate the data surface.

A similar observation was made in a recent study by Ianniello & Bernardis, where the authors observed the downstream receivers to be dominated by a shaft-rate pressure signal originating primarily from the downstream end cap of a cylindrical control surface [88]. In a different study, Rahier *et al.* examined a the effect of removing the downstream control surface end when computing aeroacoustic properties of hot jets [162]. They recommended excluding the downstream end of the control surface completely for receiver angles outside of the "missing" control surface element to avoid the integration surface cutting through the source region. This recommendation stands in agreement with the results presented earlier for analytical acoustic sources. It should be noted, however, that for a marine propeller, the rate of decay of vorticity downstream will be smaller due to the presence of a co-flow and different fluid properties than in the case of aeroacoustic flows. This makes removing the downstream end of the control surface risky, as it could lead to a significant part of sound sources being well outside the control surface. Indeed, more recent results by Ianniello *et al.* suggest that in non-cavitating

conditions, the propeller wake is a relatively strong acoustic source [88, 93]. A study by Nitzkorski *et al.* [152] showed how a dynamic end cap treatment method may be used in order to avoid solving the volume integral outside the porous data surface while removing the spurious data source. It entails modifying the acoustic contributions of the end cap perpendicular to the flow direction. Such methods are mature and there is, therefore, little scientific merit in implementing them in the current version of the code. Instead, the open control surface approach is followed. If the developed acoustic code were to be more widely adopted it would be beneficial, however, to implement both the end cap treatment and the volume integral at a later stage to minimise the dependence on the skill of the user in defining the control surface extent.

On the final note, it is worth considering how the present method might be used if turbulent structures were to convect onto the propeller. Such a scenario would be representative of what might be expected in reality when a propeller operates in a turbulent wake of a ship. Based on the current observations, it is likely that the incident eddies would enter and leave the control surface at unpredictable locations and hence the only way to prevent them from generating a spurious noise source would be to solve the volume integral everywhere outside of the porous data surface. This will therefore need to be addressed as more complex geometries are being investigated in subsequent studies.

5.7 Summary

It has been shown that the implemented acoustic analogy is capable of predicting the noise emitted by analytical acoustic sources satisfactorily well for a wide range of source and control surface parameters, with the errors in pressure amplitude typically being within a few percent of analytical or reference results. The sensitivity study carried out showed that the developed acoustic tool should be capable of capturing the noise signature of a typical marine propeller, as long as accurate enough input data may be provided. It has been demonstrated that this may be achieved without putting extra requirements on the actual simulation, apart from ensuring the dissipation and dispersion errors are small enough for the flow field on the control surface to be accurately predicted. Orientation of the control surface inside the flow domain has also been identified as a key factor affecting the acoustic prediction, particularly as one moves towards simulating complex geometries with full stern gear. The results obtained using analytical sources also reinforce the statement reported in the literature that pressure terms computed using the porous acoustic analogy may not be directly attributed to noise sources of particular order. This highlights a potential difficulty in interpreting the results for a complex problem with several noise generation mechanisms being active simultaneously. It is expected that this may be overcome with careful simulation design and data analysis.

Presented results for the E779a propeller show good agreement with the published acoustic data, with differences in the harmonics being less than 5% and phase angles and waveforms showing qualitative agreement [88, 89, 132]. As such, the results prove the successful implementation of the Ffowcs Williams-Hawkings analogy during the course of this project. The data also indicate the existence of a non-negligible sound source in the propeller wake, supporting the hypothesis by Ianniello *et al.* [89]. The data also suggest that placing the control surface in such a way as to cut through the source region may lead to erroneous results. Hence, it is recommended to remove the downstream end of the control surface in practical applications after ensuring that the data surface is long enough to enclose all of the source region which is being modelled accurately. The only way to avoid doing this is including the expensive volume integral of the FW-H equation in the present acoustic method or adding special treatment of the downstream extent of the data surface [152]. The latter approach has been discussed at length in the literature and hence could be readily implemented, but little merit was found in undertaking this for the present project since the straightforward removal of the downstream control surface extent was observed to produce satisfactory results.

Following the successful implementation and validation of the acoustic analogy, it was necessary to apply it to a case experiencing severe unsteady cavitation. However, the Potsdam propeller case discussed in Chapter 4 has been shown to experience fairly stable cavitation, which was not expected to produce substantial radiated pressure. Moreover, the two discussed propeller cases presented so far have proven to be computationally expensive. It was therefore necessary to shift attention towards simpler hydrofoil simulations, which would still be representative of the unsteady cavitating flow regimes expected on real propellers. The next Chapter is devoted to setting up such test cases and validating them with the view of ultimately using the FW-H method to predict unsteady pressures induced by cavitation.

Chapter 6

Cavitation modelling

6.1 Introduction

The objective of this chapter was to further develop and validate the cavitation modelling methodology first applied to the PPTC propeller, discussed in Chapter 4. Based on the previous results for both of the considered propellers, it was also decided to focus on simpler yet representative hydrofoils to allow higher quality flow data to be predicted with less computational effort. The Delft Twist 11 hydrofoil, originally tested by Foeth [62, 63, 64], has been selected to fill this role. It was known from the literature that this test case was affordable enough to allow new computational methods to be tested, it was supported by high quality experimental data for validation purposes, and provided a realistic set of conditions representative of unsteady, cavitating flows seen on propellers.

This part of the investigation focused on first advancing the methodology applied to the PPTC propeller, by employing more advanced turbulence modelling techniques and high quality meshes. The aim was to test two popular LES approaches: implicit, where the subgrid stress tensor is assumed to be zero and dissipation is provided by the numerical grid [11], and explicit Smagorinsky model. Furthermore, a DDES model would also be tested, given its potential advantage of requiring coarser grid resolution near the wall and, consequently, its better applicability to full scale geometries [159]. For comparison, the k-ω SST model used in the PPTC and E779a studies would also be used. This part of the study was conducted on a finite-span, 2D hydrofoil identical to the foil section at the centreline of the original Delft Twist 11. The point of this simplification was to provide an even cheaper test case and focus on relative comparison of the results obtained with different models.

Once the most promising LES-family turbulence model has been selected, the full D11 geometry would be simulated and in-depth validation performed. The aim was to compare the produced results to as much of the cavitating and non-cavitating experimental

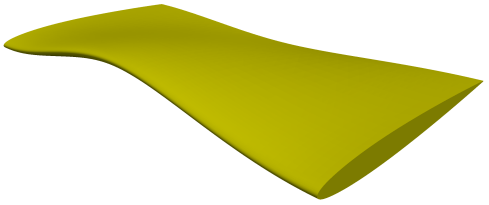

Figure 6.1: Overview of the Delft Twist 11 hydrofoil geometry.

data as possible, to establish how successful the present methodology is in modelling complex cavitation behaviours. This would allow confidence to be gained in the models before they would be used to make predictions about the hydroacoustic nature of cavitation in subsequent Chapters. Better understanding of the limitations of the models was also crucial in order to highlight possible paths for improving them as the project progressed.

6.2 Background to the Delft Twist 11 hydrofoil

The Delft Twist 11 hydrofoil consists of a NACA 0009 profile with varying twist angle along the span, yielding an angle of attack of -2 degrees at the wall of the cavitation tunnel up to 9 degrees at the centreline. This is better illustrated by Figure 6.1, which shows a rendering of the hydrofoil. The constant chord length of the foil is 150 mm, its span is 300 mm, and the width of the cavitation tunnel in which the original tests were conducted is 300 mm, or two chord lengths.

While the considered geometry is relatively simple, the test case is subject to significant sheet cavitation, making it representative of some the key modelling challenges found on a marine propeller. For this reason it presents a unique challenge for the numerical models used and has thus been studied by, for instance, Bensow *et al.* and Ji *et al.* [11, 101, 102]. It is now, arguably, one of the best established practical test cases in the field of cavitation modelling. The difficulty in capturing the cavitation behaviour on the foil lies in the complex nature of re-entrant jets moving towards the leading edge and along the span of the foil and causing complex shear off mechanism of the cavity sheet. The most common drawbacks of studies presented in the literature are the inability of the models to predict the maximum extent of cavities well and the re-entrant jets exhibiting slightly different behaviour and causing the cloud break off not to occur over the entire span of the foil. These issues typically manifest themselves in the shedding frequency being either over- or under-predicted in comparison to the experiment [78]. During the present validation these symptoms would be looked at in detail in order to compare the current set up with state of the art models presented in the literature.

6.3 Simulation set-up

While several sets of test conditions were considered in the original experiments, this investigation focused on the set up used in the SMP'11 workshop [78]. The exact conditions used, as well as relevant cavitation model settings are presented in Table 6.1. The nuclei density and diameter were chosen based on a study by Bensow [11] and were considered with other cases considered throughout this work, as described in Chapter 3. The choice of these values will affect the cavitation model results to a certain extent but lack of experimental measurements of these quantities forces the use of the most likely values rooted in typical fluid properties.

Table 6.1: Summary of the test conditions used to simulate the Delft Twist 11 hydrofoil [11, 62, 78].

Parameter	**Value**	**Unit**
Inlet velocity	6.97	m s^{-1}
Outlet pressure	29	kPa
Cavitation number, σ	1.07	-
Water temperature	24	°C
Water density, ρ_l	998	kg m^{-3}
Vapour density, ρ_v	0.023	kg m^{-3}
Water kinematic viscosity, ν_l	$0.923 \cdot 10^{-6}$	m^2 s^{-1}
Vapour kinematic viscosity, ν_v	$4.273 \cdot 10^{-6}$	m^2 s^{-1}
Mean nucleation radius, R_0	50	μm
Nuclei density, n_0	10^8	m^{-3}
Saturated vapour pressure	2970	Pa
Schnerr-Sauer tuning coefficient	1.0	-

For both the 2D NACA 0009 and the actual Delft Twist 11 geometries, structured meshing approach was followed. This allowed the grid resolution to be precisely controlled to refine the mesh where necessary. For the NACA 0009 case, a C-grid, shown in Figure 6.2a, was used in the boundary layer region and extended further away from the foil to generate fine, orthogonal cells where sheet and cloud cavitation was expected. H-blocks were used to model the cross-section of the virtual cavitation tunnel. The foil was assigned a span of 0.7c and 80 cells were placed along the span. Wall spacing of 0.2 mm was assigned to the first cell, corresponding to maximum y^+ of approximately 30. Following [11], Spalding law of the wall was used for all of the RANS, LES, and DDES cases to reduce the resolution requirements. 220 cells were placed along the foil chord and 50 were located in the near-field refinement zone responsible for resolving the cavities. The overall mesh layout is presented in Figure 6.2a. The grid was generated using a bespoke Python program that interfaces with the native OpenFOAM blockMesh utility. In total, 5.7 million cells were used.

Due to the more complex geometry of the full Delft Twist 11 hydrofoil, a commercial meshing tool Pointwise was used instead of blockMesh, to cope with the variable angle of attack. Furthermore, the variable loading of the foil causes the wake to follow different trajectories depending on the span-wise position. Following preliminary RANS simulations, the wake H-grid was deformed to concentrate the cells inside the wake. A similar domain shape and meshing strategy as in the NACA 0009 case was used, with the details depicted in Figure 6.2b. Major differences were that an O-grid topology was used in the near-field to resolve the finite trailing edge thickness of the foil and a symmetry plane was added at mid-span. Consequently, only half of the foil was modelled, similarly to nearly all studies in the literature. This could mean that span-wise asymmetry effects would not be captured, but based on experimental results this was not expected to be a major factor. The wall function was disabled in the hope that doing so will allow the complex re-entrant jet mechanisms to be modelled better. This imposed the $y^+ \leq 1$ requirement, which was met with using a wall spacing of 5 μm. 150 cells were placed across the span of the foil, yielding z^+ of 300 and x^+ of 230 was achieved with 240 cells in the stream-wise direction. These values would not be sufficient for a wall-resolved LES simulation, which typically requires $x^+ \leq 100$, $y^+ \leq 1$, and $z^+ \leq 20$ [40]. However, a DDES model was used in this case, for reasons which will be explained later, and thus the mesh resolution was deemed sufficient.

The mesh was subject to grid sensitivity studies for steady, non-cavitating flow computed using a RANS model. The effect of the number of cells on the integral force coefficients, as well as the maximum and minimum pressure coefficient values, believed to be important from cavitation inception point of view, were compared. This allowed the aptness of the present mesh to be confirmed, as will be shown in Section 6.6. The final grid used, consisting of 7.3 million cells, is shown in Figure 6.3.

For all of the NACA 0009 and the D11 cases, turbulence intensity of 1% and significant turbulent length scale of 4% of tunnel width were assumed to compute the necessary turbulent properties at the inflow. Note that these were not required by the LES simulations as the subgrid stress tensor for these cases is modelled locally rather than computed from a transport equation. A fixed value pressure outlet was used to adjust the cavitation number and slip boundaries were used to model the cavitation tunnel walls. As mentioned in Chapter 3, the NACA 0009 simulations used a convective velocity outlet but this was replaced with a standard pressure outlet for the Delft Foil computations due to issues with numerical stability. The second order `limittedLinear2V` convection scheme was used to resolve the convection term of the Navier-Stokes equation [136], time derivatives were approximated using the second order backward scheme, and first order schemes were used for the turbulent quantities, where necessary. For the NACA 0009 cases, care was taken to ensure that the turbulence model is the only thing changing between the individual simulations to ensure a fair and informative comparison. Each simulation was run with a maximum Courant number of 0.5, which for the Delft Foil

corresponded to time step of approximately 2 and for NACA 0009 5 micro-seconds. This highlights the large computational effort savings offered by the wall function.

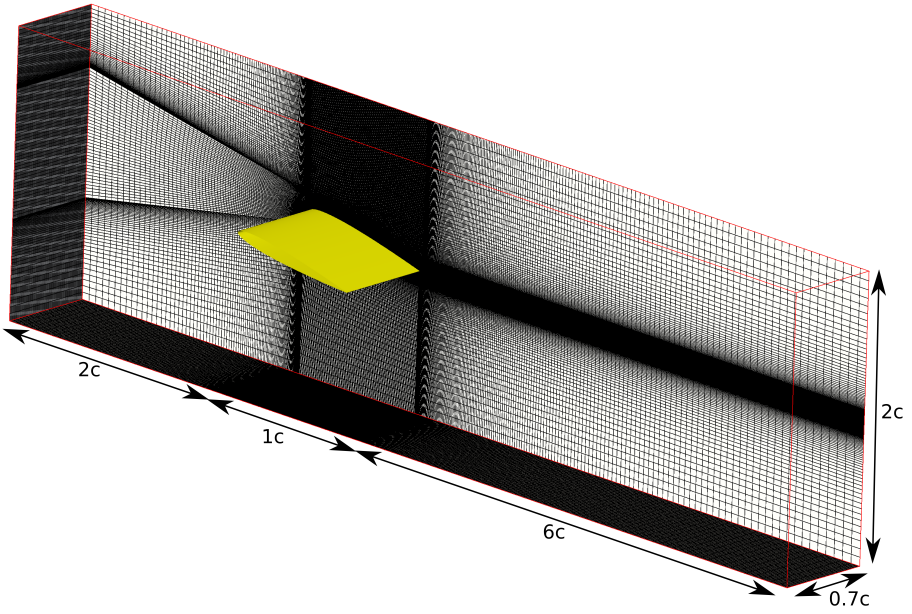

(a) Numerical domain used for the 2D NACA 0009 simulations

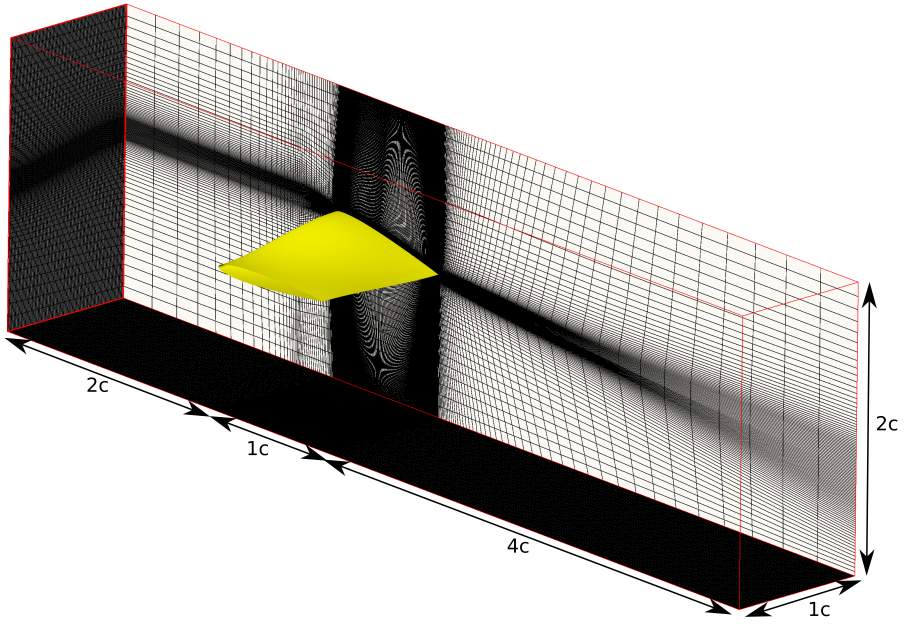

(b) Domain used to model the Delft Twist 11 hydrofoil

Figure 6.2: Overview of numerical domains for the Delft Twist 11 hydrofoil and initial NACA 0009 studies.

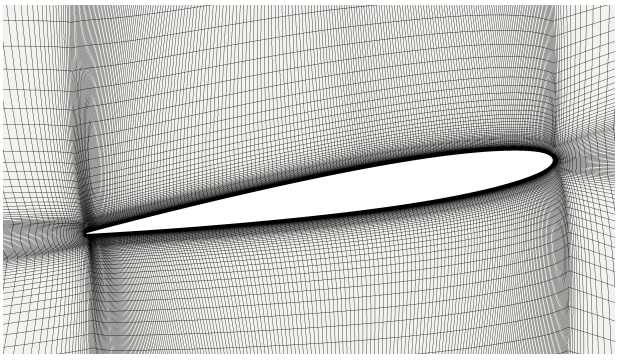

(a) O-grid mesh topology around the foil

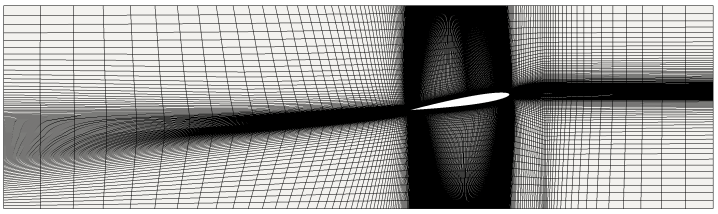

(b) Computational domain and wake adaptation of the mesh

Figure 6.3: Details of the computational mesh used to simulate the Delft Twist 11 hydrofoil.

6.4 Results - NACA 0009

Figure 6.4 presents chosen time histories of total cavitation volume computed inside the numerical domain with four different turbulence models. An immediate observation is that all of the signals follow a sinusoidal-like pattern but the fundamental frequency of the RANS case is much lower than that of the more advanced turbulence models. This is associated with periodic growth of sheet cavities and their subsequent shedding, leading to cavitation clouds being convected downstream. Both LES and the DDES case show a very similar peak-to-peak period, but the implicit LES exhibits more repeatable cycles than the DDES and explicit LES simulations within the time range chosen. All of the more expensive models show nearly identical maximum and minimum amplitudes, which hints that the observed difference are due to the highly unsteady nature of the flow rather than particular differences between the turbulence models themselves. The amount of vapour located inside less clearly defined cavitation clouds is also very similar between the LES and DDES models. The same cannot be said about the RANS simulation that shows a distinct period t$\in$ (0.07, 0.12) s over which few diffused cavitation clouds appear to exist, which is evident by the integrals for the two α threshold values returning nearly identical results.

The origin of the different shedding frequency for the RANS and other cases may be better understood by examining the volume fraction contours depicted in Figure 6.5. These instantaneous values are shown at a time during the shedding cycle when a new

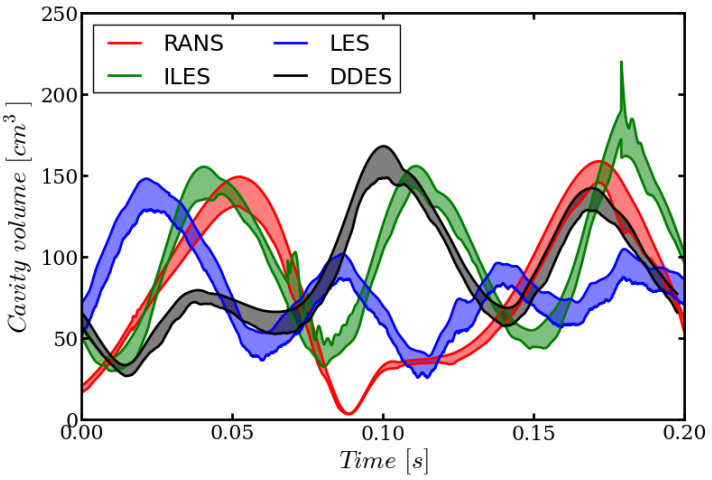

Figure 6.4: Time history snapshots of total cavitation volume predicted for the 2D NACA 0009 hydrofoil verification test case. Upper and lower solid lines correspond to integration of vapour fraction up to $\alpha \leq 0.9$ and $\alpha \leq 0.5$, respectively, and the shaded areas denote the differrence between the two integration limits.

cavity sheet has just started to develop. It may be seen that for the LES case shown this occurs when there are still cavity clouds present above the foil. The same pattern has been observed for the explicit LES and DDES cases. However, the RANS simulation only starts to develop the sheet once nearly all of the clouds have disintegrated. This leads to longer shedding cycles and explains why the other cases do not see the total cavity volume approaching zero, which happens for the RANS case.

Finally, one may compare the explicit and implicit LES models in more detail by analysing the instantaneous cavity and vorticity iso-contours depicted in Figure 6.6. These were sampled at approximately the same point during the cavitation cycle when a re-entrant jet appears to have just sheared off a major part of the cavity sheet around the leading edge when a large cloud structure is present above the trailing edge of the foil. Qualitatively, both models predict identical behaviour. Detailed inspection, however, reveals that the scale of turbulent eddies predicted by ILES is much smaller and the turbulence for this case predicts far more isotropic behaviour. In contrast, the explicit model gives rise to elongated vortical structures showing visible interactions with streaks of vapour volumes. It is also important to note how the turbulent structures affect the cavity walls by causing dents and irregularities. The scale and number of these fine features are visibly related to the scale of turbulence predicted.

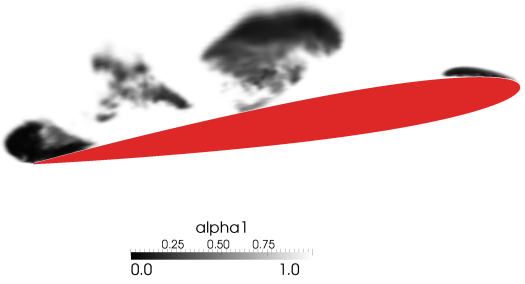

(a) Implicit LES

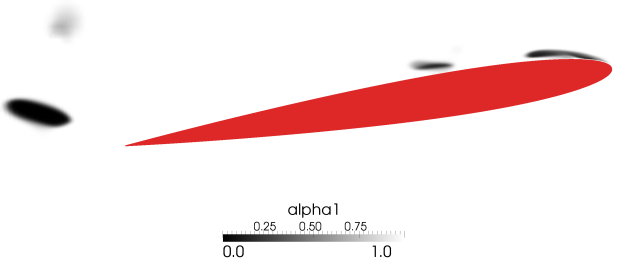

(b) k-ω SST RANS

Figure 6.5: Instantaneous vapour fraction contours for RANS and LES NACA 0009 simulations at the time when a new cavity sheet starts to develop.

6.5 Discussion - NACA 0009

The most important observation drawn from the comparison between the explicit LES, implicit LES, DDES and RANS models is that the former three show agreement to within 10% in the predicted cavitation cycle frequency and overall cavitation behaviour. These properties are predicted to be completely different with the RANS model. This stands in very good agreement with the comments made by other authors in the literature [11, 87, 202], who have identified the over-predicted eddy viscosity predicted by the RANS model to be the primary culprit for this behaviour. This is a fundamental disadvantage of Reynolds averaged flow models in application to unsteady multiphase flows. Ad-hoc corrections reducing eddy viscosity in the cavity closure region have been proposed and reportedly yielded promising results [11, 193]. It has been decided not to follow these procedures in this work and instead focus on the more advanced turbulence modelling techniques to reduce the amount of assumptions introduced to the overall methodology. This would also become important at the later stages of the project, since using DDES or LES would allow noise due to turbulence to be accounted for in the hydroacoustic simulations.

Comparing the two LES and DDES models yielded a somewhat unexpected conclusion, namely that they all predict nearly identical flow features and the only differences between them become evident in the secondary flow features. Several authors have

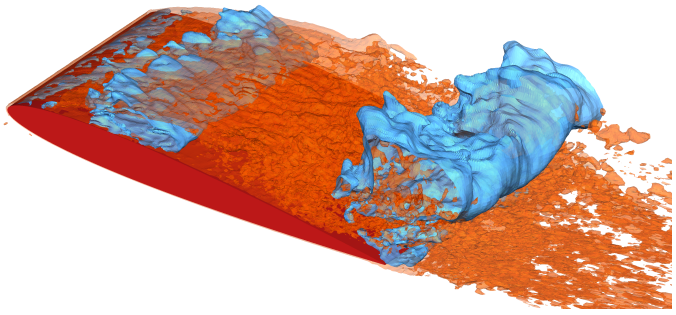

(a) Implicit LES

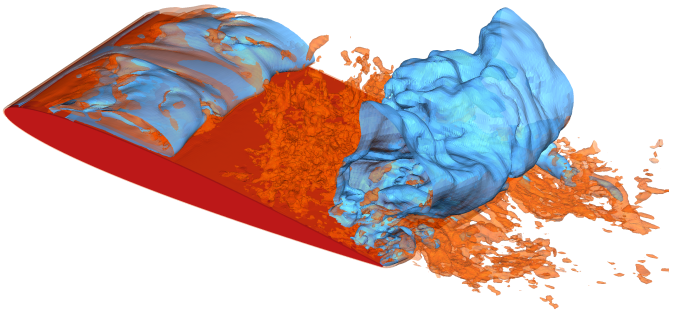

(b) Explicit Smagorinsky model

Figure 6.6: Instantaneous iso-contours of vapour fraction ($\alpha = 0.5$) and vorticity magnitude ($|\omega| = 3000\,s^{-1}$) computed for the explicit and implicit LES for the NACA 0009 case.

recommended using ILES for cavitating flow simulations and supported this reasoning with compelling arguments, such as reduced computational time, greater simplicity of the model and lower risk of over-prediction of subgrid viscosity inside of the cavities [11, 87, 202]. However, it has been shown that the scale of turbulence predicted using ILES is dependent on the local grid resolution and dissipation this introduces, which stands in agreement with the observations made by Lloyd [136]. One could of course tune the mesh size and adjust the numerical schemes to achieve the desired amount of dissipation for a specific scenario, but as the grid becomes more complex and non-uniform, this process may become difficult. Furthermore, generalising such an approach would require a significant amount of experience and user skill, which is not desirable if the proposed method is to be more widely adopted by the maritime fluid dynamics community. It has therefore been decided to pursue more complex explicit models.

The final choice had to be made between the explicit LES and DDES model. The former has the advantage of offering more insight into the nature of the flow in the boundary layer region where many complex phenomena, such as re-entrant jets, take place in cavitating flows. It would therefore be recommended from the perspective of increasing accuracy and removing the amount of modelling assumptions. However, as

one aims to step away from the wall-modelled approach, the necessary grid resolution needed by the LES model increases rapidly with the Reynolds number. One therefore faces the choice of applying the wall function and accepting the inherent inaccuracies in regions of separated and recirculating flow, or moving to the DDES model and thus relying on solving the additional transport equations and suffering from more modelling assumptions in the boundary layer regions. Based on the studies by Bensow *et al.* [11] it is though that for low and medium Reynolds numbers the wall-modelled LES approach would offer more advantages. However, in maritime applications Reynolds numbers tend to be high and thus application of DES-based approaches has seen more use at present [159]. It has thus been decided to use the DDES model in the subsequent studies.

6.6 Results - Delft Twist 11

Figure 6.7 presents the result of the grid independence study carried out on the Delft Twist 11 hydrofoil in non-cavitating conditions. Subfigure 6.7a indicates how the integral force coefficients converged relative to the solution on the finest grid. It may be seen that beyond 7 million cells there is less than 0.1% variation in the predicted values. Results in Figure 6.7b show a similar plot for the predicted minimum and maximum pressure coefficient. The latter remains fairly constant, as expected from Bernoulli's equation, but the former shows very similar trends to the force coefficients. These results confirm that the steady state solution is grid-converged at 7.3 million cells used in the final grid.

Figure 6.8 presents the predicted distribution of pressure coefficient at various span-wise locations. For most measurement stations good agreement is seen, with the exception of one of the probes at x/c=0.3. This point appears to be an outlier, which puts the accuracy of the experiment at this location in question. Furthermore, there appears to be a consistent over-prediction of the pressure coefficient at the underside of the foil in the simulation. An important thing to note is that the minimum value of the pressure coefficient (-2.96) predicted in the current simulation is higher than what was reported by other authors (-3.17 to -3.23) [78]. This could limit the amount of cavitation inception and lead to smaller cavities being predicted.

For the cavitating flow simulation, the predicted mean lift coefficient was 0.412. This differs quite substantially from the experimentally reported value of 0.53, but stands in a relatively good agreement with other reported numerical results. For instance, Bensow [11] predicted mean lift coefficient values between 0.42 and 0.45 using RANS, ILES, and DES methods.

To better understand the origins of this discrepancy, it is worth to examine the the mean pressure coefficient and volume fraction distributions along the mid-span of the foil, shown in Figure 6.9. The latter shows that the attached cavities do no extend much further downstream than x/c=0.3. This compares well with the pressure coefficient

in Figure 6.9a, where the characteristic plateau associated with persistent presence of cavitation extends to the same chord-wise location. In the experiment, however, this was reported to reach x/c=0.4. In the measurement data, the pressure also increased much more gradually in the region of cavity closure. This observation is further supported by the mean distributions of the volume fraction along lines normal to the foil surface at several stations along the chord, shown in Figure 6.10. They show that beyond x/c 0.35 cavitation seldom reaches the foil surface. As one moves further downstream, the cavities appear to move away from the foil and the mean density quickly increases to nearly pure water at 0.6 x/c, which suggests that no cavitation structures make it this far downstream. Finally, it may be noted in Figure 6.9b that the mean value first nears pure water around x/c=0.05, then moves back towards vapour and only later moves to pure water region. This indicates that at a point during the cavitation cycle a substantial gap exists between the attached cavity at the leading edge and one located further downstream.

It also vital to gain insight into the unsteady cavitation behaviour occurring on the hydrofoil to ensure that cavitation noise will be able to be modelled in the upcoming studies. To begin with, it is worth examining consecutive snapshots of the flow over a single shedding cycle and comparing them to the experimental photographs, as shown in Figure 6.12. The simulated volume fraction iso-contours show how the cycle first involves the growth of a large cavity sheet. As this reaches its maximum stream-wise extent, necking takes place around the leading edge through the occurrence of a re-entrant jet. This process gives rise to the formation of the characteristic v-shaped notch in the sheet, which is followed by the sheet filling with vapour again. The predicted snapshots match the general behaviour reported in the experiments by Foeth [62] relatively well. The biggest discrepancy, already seen in the averaged data, stems from the under-prediction of the size of the cavity, both in the stream- and span-wise directions. This causes the sheet to be more stable off the centreline of the foil, which in turn inhibits the formation of the re-entrant jet closer to the tunnel walls, which was reported in the experiments. The jet behaviour seen around the centreline, where the sheet grows to a size more comparable with the experiments, matches the experimentally reported dynamics more closely.

Figure 6.11, shows how the distribution of the volume fraction changes in time across a line normal to the foil surface at x/c 0.15 at mid span. The data depict four shedding cycles, which begin with an attached cavity being present at that location. This is followed by a sudden destruction of the vapour volume and the subsequent appearance of small, intermittent pockets of vapour passing above the foil surface. One may begin to identify the shedding cycle period of approximately 26 miliseconds, which corresponds to a frequency of approximately 38 Hz.

The influence of the dominant shedding frequency is also visible in the time traces and power spectral density functions of the lift coefficient and total cavitation volume,

depicted in Figure 6.13 and 6.14. The latter reveals that both quantities of interest exhibit a pronounced contribution from the fundamental frequency of 38 Hz, with the lift coefficient also being affected by its higher harmonics. In the experiment, the shedding frequency was reported to be 32.5 Hz and numerical results from the 2011 SMP workshop ranged between 28 and 38 Hz [78]. Time series data in Figure 6.13 indicates that the cavity volume follows a relatively sinusoidal pattern, particularly at the lower volume fraction threshold which corresponds to regions of clearly-defined, coherent cavities. At higher threshold values the curves show less dependence on the shedding frequency and yield much greater total cavity volumes, suggesting the presence of large regions of intermediate liquid fraction values.

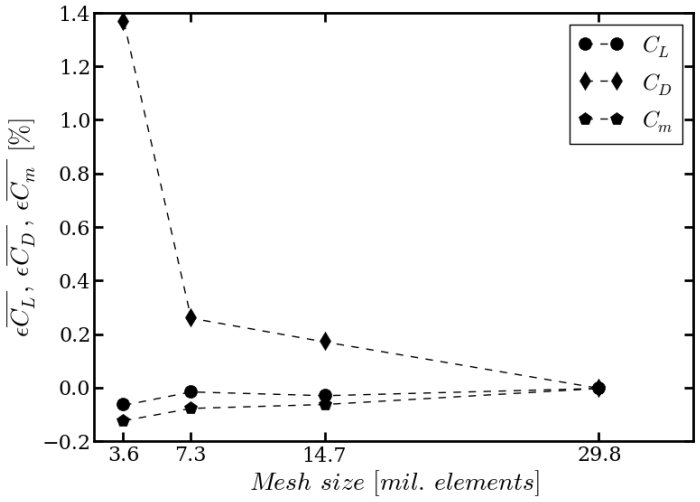

(a) Integral force coefficients

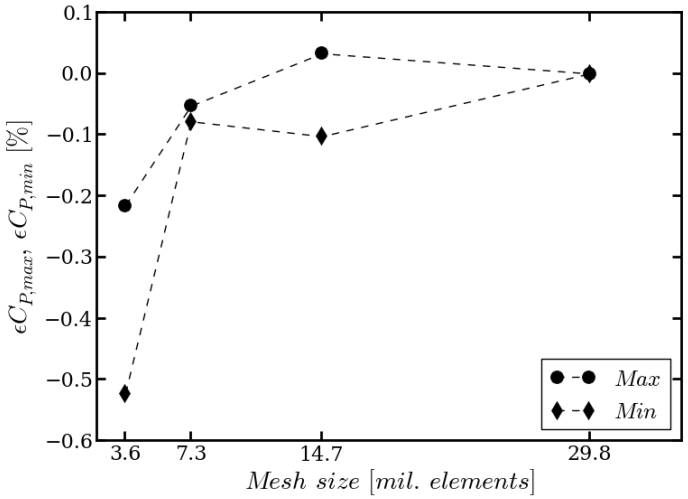

(b) Minimum and maximum pressure coefficient

Figure 6.7: Grid convergence of the Delft Twist 11 hydrofoil steady-state, non-cavitating simulation. Results show in relation to the finest grid solution.

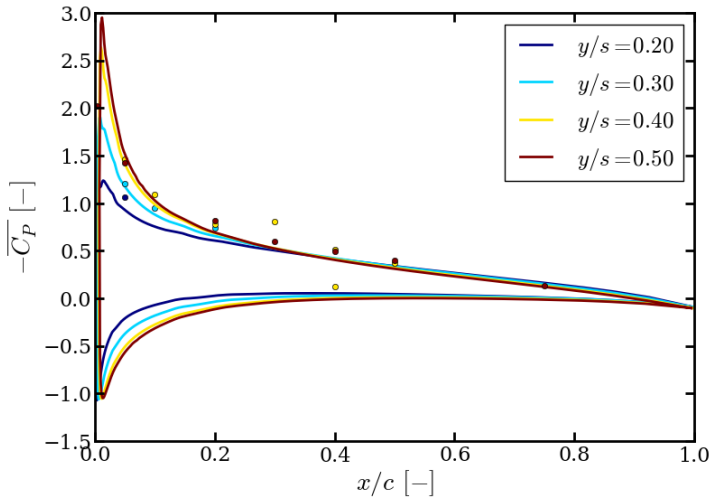

Figure 6.8: Non-cavitating surface pressure coefficient on the Delft Twist 11 hydrofoil compared to the experimental measurements at various span-wise locations.

6.7 Discussion - Delft Twist 11

In the present simulation the cavity extent has been under-predicted, as evident from the comparison of volume fraction iso-contours, mean pressure coefficient and vapour distribution along the foil. This has very likely led to the under-prediction of the mean lift coefficient and over-prediction of the shedding frequency observed. That is because a smaller cavity sheet induces a smaller effective change to the foil thickness, thereby reducing lift. It also takes less time to grow to its maximum length, a process which is expected to be largely controlled by the mean convection speed and chord-wise pressure gradient opposing the cavity growth [65]. This would reduce the shedding cycle period and thus raise the fundamental cavitation frequency.

The origin of this discrepancy could be due to the observed 6% under-prediction of the minimum pressure coefficient compared to other numerical studies, which could lead to smaller vaporisation rates near the leading edge and smaller cavities being created. At the same time, the study by Bensow [11] reported similarly under-predicted cavitation extents but the presented results showed shedding frequencies closer to the experimentally measured values, indicating that there could be more than one source of the discrepancy in the current results. Other potential culprits could have been the assumed constant nuclei size and density, which were not reported in the experiments, or possible misalignment of the foil in the experiments.

To verify this, two additional simulations were carried out with the foil angle of attack being changed by $\pm 0.5°$. These seemingly small variations resulted in significant changes to the cavitation behaviour, suggesting the shedding frequency may change by as much

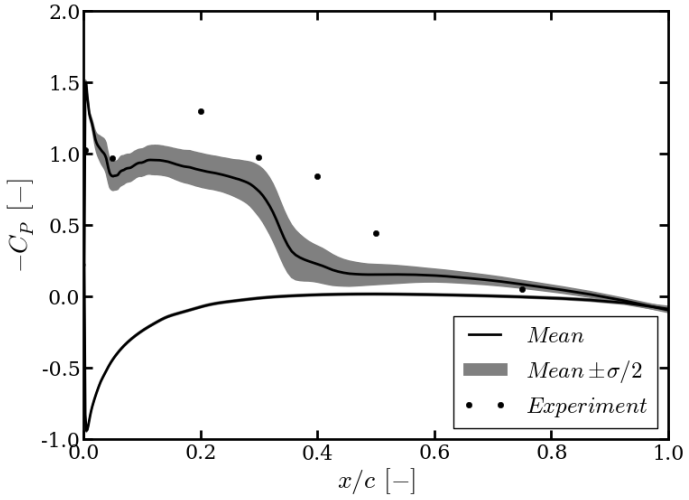

(a) Pressure coefficient

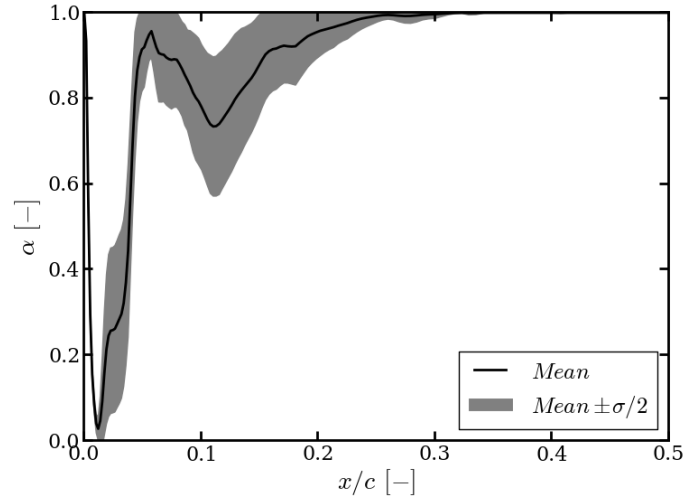

(b) Volume fraction

Figure 6.9: Mean surface pressure and volume fraction predicted at the mid-span of the Delft Twist 11 hydrofoil.

as 10 Hz per degree of angle of attack change. This possibility is further reinforced by data published by Leroux *et al.* [117], who have observed rapid changes to cavitation patterns on a 2D NACA 66 foil for angles of attack around 7 degrees at cavitation numbers similar to the one explored here. The point of the above argument is by no means to discredit the excellent experimental data set provided by Foeth [62], but rather to highlight than even a relatively small error in either the simulation set up or model itself could lead to large changes to the shedding behaviour predicted. Further sensitivity studies would therefore be needed to truly explore the origin of this behaviour.

It was also suggested that although the used mesh has been shown to be grid independent

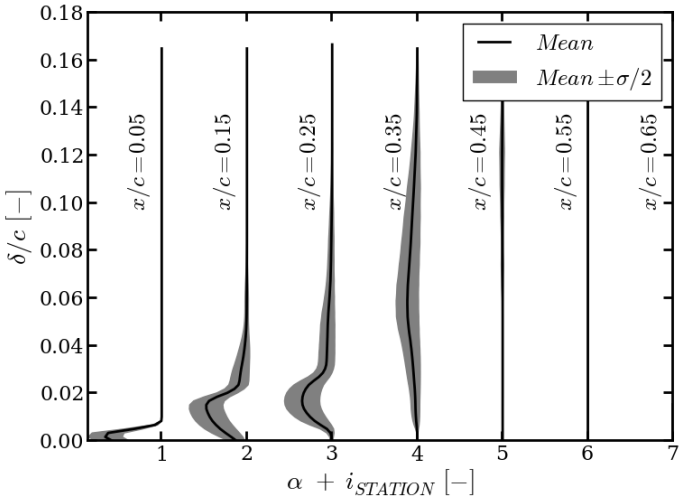

Figure 6.10: Mean value and standard deviation of the volume fraction along lines perpendicular to the Delft Twist 11 hydrofoil surface at mid-span, sampled at several x/c and plotted as a function of foil surface distance, δ.

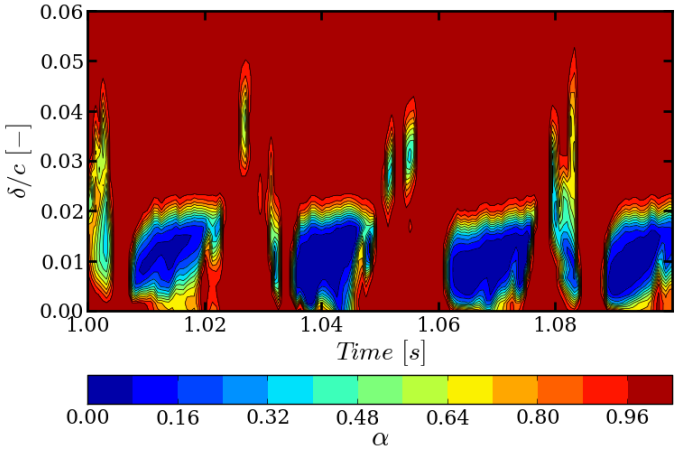

Figure 6.11: Time history of volume fraction at a station at x/c 0.15 from the leading edge of the Delft Twist 11 hydrofoil sampled at mid-span.

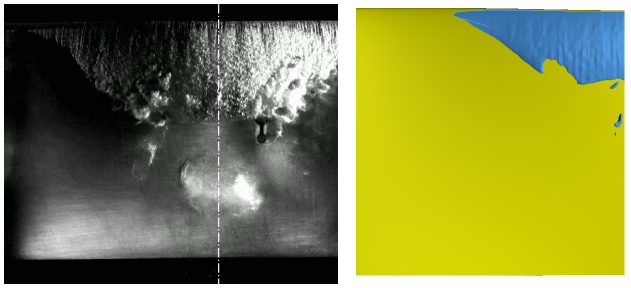

(a) Experiment - t_0 (b) CFD - t_0

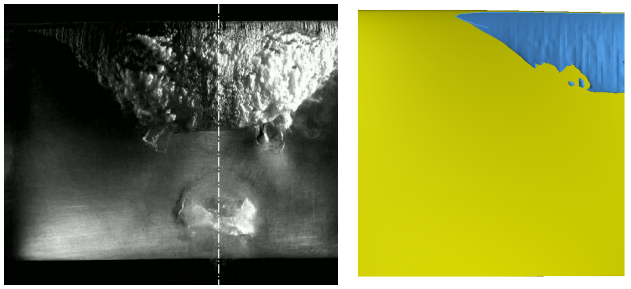

(c) Experiment - t_1 (d) CFD - t_1

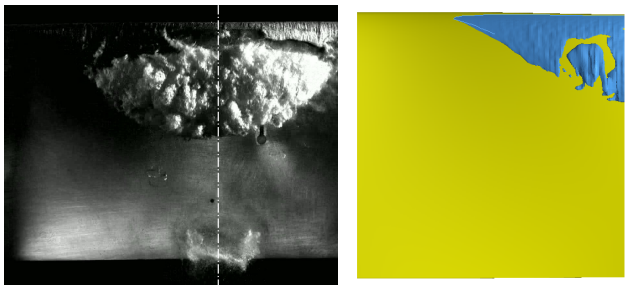

(e) Experiment - t_2 (f) CFD - t_2

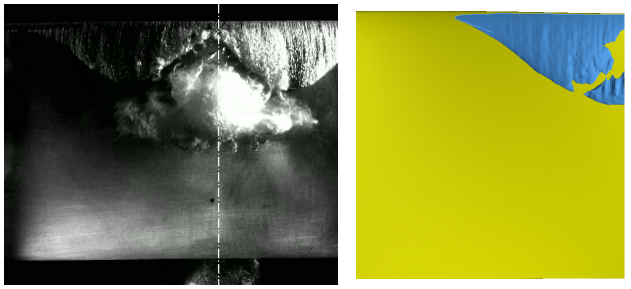

(g) Experiment - t_3 (h) CFD - t_3

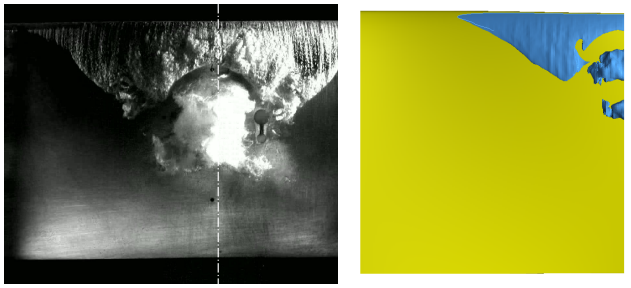

(i) Experiment - t_4 (j) CFD - t_4

Figure 6.12: Instantaneous iso-contours of vapour fraction ($\alpha = 0.5$) compared to the experimental cavitation observations on the Delft Twist 11 hydrofoil. Flow from top to bottom, CFD data only shows half of the foil while the experimental photopgraphs cover approximately three quarters of the span, which allows symmetry of the cavitation patterns to be appreciated.

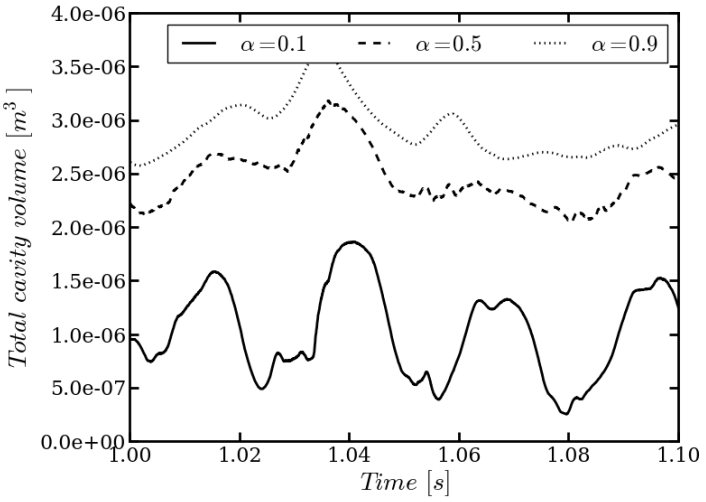

(a) Cavity volume

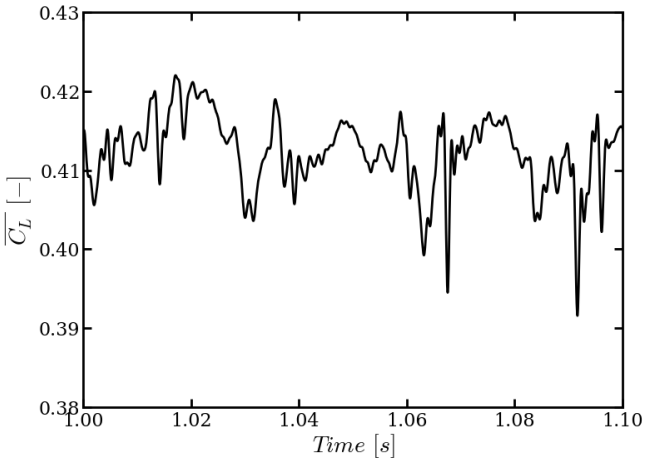

(b) Lift coefficient

Figure 6.13: Time histories of total cavity volume and lift coefficient on the Delft Twist 11 hydrofoil.

for steady-state flow, it may not necessarily be sufficiently dense to provide an accurate representation of the unsteady cavitating problem. Again, an additional simulation on a mesh with twice as many cells was undertaken, starting from the fully developed flow solution obtained on the main 7.3 million cells mesh. Due to the relatively high cost, few cavitating cycles were evaluated, but within that time no mentionable difference could be seen in the predicted cavity extent and shedding cycle period. A suggested improvement to the numerical grid would be to further refine the near-field region on the upper surface of the foil in the normal direction, in order to improve the resolution of the shed cavity clouds as they separate from the surface of the foil. It seems unlikely, however, that this would cause major changes to the shedding dynamics as the mesh used was fine enough to resolve the major motions of the fluid. This reinforces the

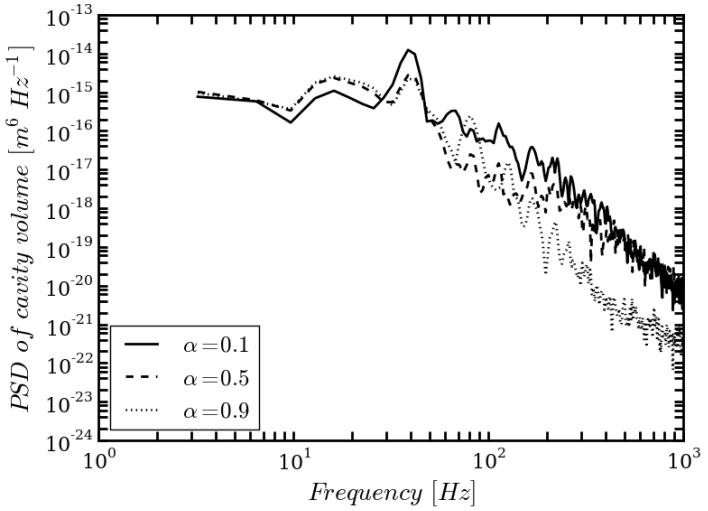

(a) Cavity volume

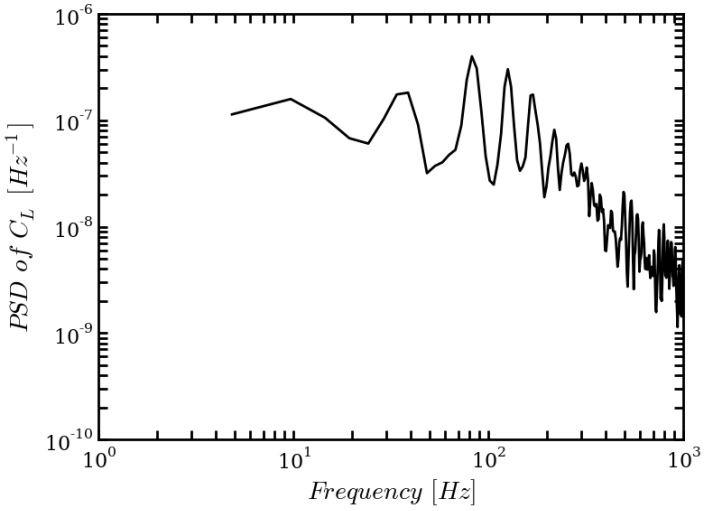

(b) Lift coefficient

Figure 6.14: Power spectral density functions of total cavity volume and lift coefficient on the Delft Twist 11 hydrofoil.

importance of the very recent works by Lloyd *et al.* [135], Negrato *et al.* [150] and Wu *et al.* [205] in the field of establishing mesh-independence estimation procedures for unsteady cavitating flows.

While the predictions made for the challenging Delft Twist 11 hydrofoil test case do leave room for improvement, they have been found to reproduce the key physical phenomena observed in reality quite closely. Given the significant sensitivity of the unsteady behaviour to even minor condition changes, it is thought that the transient cavitation behaviour was captured satisfactorily and with an accuracy level in line with the literature.

6.8 Summary

The presented results confirmed the claims made in the literature that unsteady RANS is less capable of predicting highly unsteady cavitation than more advanced turbulence modelling techniques. This was an important finding as it dictated that such more expensive methods must be used at the subsequent stages of the project if acoustic predictions are to be made about regarding cavitation induced pressures. The results for the Delft Twist 11 hydrofoil have shown reasonable agreement with the experimental data. The major discrepancies seen have been due to the limitations of the underlying cavitation model. However, it showed its capability to predict highly unsteady flows satisfactorily enough to be able to provide a description of the low-frequency noise source induced by oscillating cavitation. Studying this phenomenon is the main focus of this thesis and is addressed in the following Chapter.

Chapter 7

Application of the FW-H analogy to a NACA 0009 foil

7.1 Introduction

The purpose of this part of the project was to apply the newly developed Ffowcs Williams-Hawkings acoustic analogy to a hydrofoil undergoing significant unsteady cavitation and attempt to deduce the generated far-field pressure pulses. A successful attempt would imply that one of the major objectives of this thesis has been met. Because few detailed studies involving the FW-H analogy, advanced flow modelling techniques, and cavitation had been presented in the literature at the time of writing, the present study had to first gain practical insight into applying the methodology. In particular, appropriate ways to define the integration surfaces had to be devised and dependence of the results on the fundamental cavitation model assumptions, such as incompressibility and using the volume of fluid method, had to be studied.

The present part of the project focused on utilising the NACA 0009 test case, first introduced in Chapter 6, to study the aforementioned questions. This test case was chosen given its appreciable simplicity in terms of geometry, mesh and set up, as well as the complex, unsteady cavitation phenomena it generates. No experimental data readily usable for the purpose of validation of the acoustic predictions were found in the literature for a similar case and thus validation described on the basis on the Insean E779a propeller had to be relied upon.

7.2 Simulation set-up

7.2.1 General simulation parameters

A very similar numerical set-up to the one in Table 6.1 in the previous Chapter was used, employing the same flow conditions and fluid properties. However, unlike in the case of the Delft Twist 11, the present simulation utilised the dynamic mixed Smagorisnky model [69]. The purpose of this was to further advance the study conducted in Chapter 6, where different turbulence models were applied to the presently considered case. This model has also been used with reportedly promising results in the study by Lloyd [136], which meant it could be potentially very appealing if it could be shown to perform similarly to the DDES and ILES models investigated beforehand.

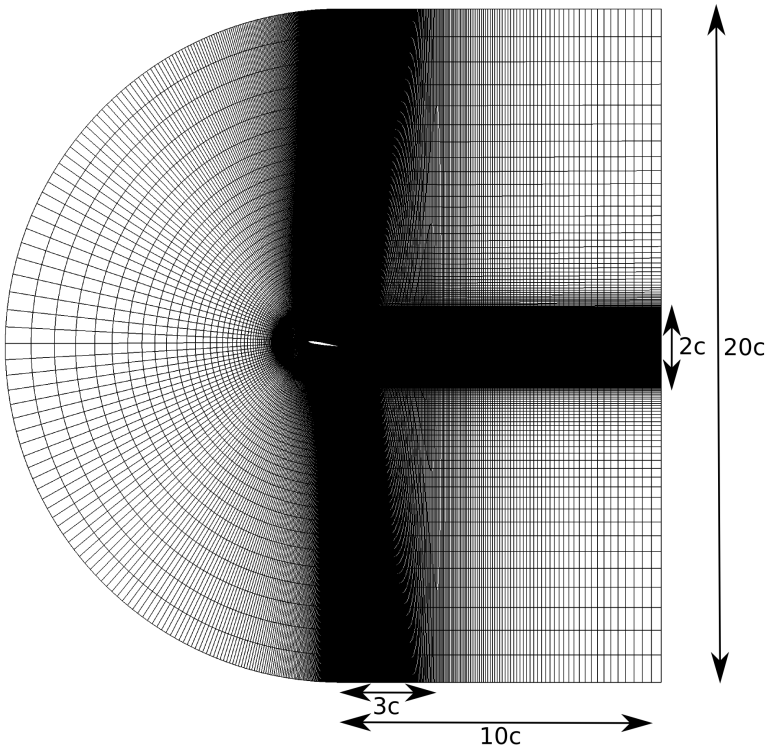

Figure 7.1: Overview of the C-grid topology used to simulate the NACA 0009 foil for acoustic analysis. Extents of the refinement region aimed at achieving good resolution in the wake also highlighted.

The second major difference in comparison to the original simulation was a modified domain layout, shown in Figure 7.1. This followed the same C-grid approach around the foil and H-grid in the wake, but the tunnel walls were not represented. Instead, the domain size was increased to 10 chord lengths in every direction to limit the possibility of the domain walls interacting with the FW-H integration surface. Moreover, mesh density in the wake region was increased. This was done following the E779a study

which indicated that resolving the turbulent wake may play an important role in determining the noise characteristics. The propeller study also highlighted the importance of resolving the flow field data accurately up to the FW-H integration surface, which would not have been likely had the original NACA 0009 grid been used. In total, 8.7 million cells were used with 50 grid points placed along the span of the foil.

The simulation was first run for 10 cavitation cycles in order to remove transient flow features present at the initialisation of the simulation. Collection of the data was then continued for 1 second. The computational expense amounted to approximately 360 hours on 128 processors and required approximately 40 gigabytes of RAM, which indicates a relatively high associated cost despite a simple geometry was being used. The acoustic analysis, carried out using the stand-alone executable version of the analogy, added little computational effort and could be run on a desktop machine. The saved flow field data, however, occupied approximately half a terabyte of hard drive space, which would present a challenge with present technology if data for several simulations was to be collected and kept for future use.

7.2.2 Span-wise domain size

The span of the domain was reduced to 0.16 chord lengths in order to keep the simulation feasible with the increased mesh density. This domain size could be considered sufficient for an aeroacoustic analysis, where it is often practical to simulate only a fraction of the span [18, 70, 72, 136]. Doing so limits the size of the largest turbulent length scale that may be captured [18]. For a compressible simulation, the maximum permitted wavelength propagating in the span-wise direction is similarly limited, effectively only allowing for certain frequencies to be resolved in a three-dimensional manner for a given domain width [136].

In aeroacoustics, a correction is usually applied to the numerical data in order to allow comparison with experimental results. A typical approach is outlined by Boudet *et al.* [18], who discuss a coherence function being used to correct the radiated sound pressure levels given the simulation and experimental domain sizes. To the authors' knowledge, no such correction has been developed for cavitating hydrofoils. This implies that unless sufficient understanding of the three-dimensional nature of the flow for a given cavitating hydrofoil is achieved and the characteristic span-wise lengths scales are identified, no definite conclusions may be drawn with respect to the total sound pressure levels which could be encountered in reality. A relevant study was undertaken by Ji *et al.* [99], where cavitating flow around a hydrofoil was computed using LES with three different span-wise mesh resolutions. The authors pointed out that the vortical structures in the wake of the sheet cavity are particularly affected by refining the grid. This may be expected to affect the noise, as turbulence in the wake of the cavity sheet will act to make shedding unsteady and thus affecting the dominant source frequency. From

a practical standpoint, the computational cost of carrying out a sensitivity study by looking at several span-wise domain sizes and mesh densities was considered too great for this investigation and therefore only a limited section of the foil was used.

7.2.3 Acoustic analogy set up

Two FW-H control surfaces were used, as depicted in Figure 7.2. The smaller one was defined to end just outside of the maximum cavity extents observed in the initial simulations, aiming to prevent any local density variations. Its downstream plane was still in the fine mesh region and placed in such a way as to enclose the convecting and collapsing cavities, as well as the most prominent wake structures.

A larger surface was also placed approximately twice as far away from the foil in a mesh region with a higher amount of cell stretching. This was intended to provide an estimate of how sensitive the acoustic solution is to the control surface location in a similar fashion to how this was conducted for the E779a propeller study. Moreover, each of the control surfaces was also evaluated in an open-ended variant in order to study how much spurious noise the turbulent structures penetrating the downstream-most extents will generate. This has already been studied for the Insean E779a propeller, but in that case the vortical structures were far more coherent and organised as they were associated with the slip stream of the propeller. In the present study, the turbulence was expected to be more incoherent and closer to isotropic, which would likely modify the effect of the downstream data surface.

Because slip boundaries were used in the span-wise direction, it was appropriate to include the outside domain faces in the FW-H surface. By examining Equations (5.10) and (5.14) one may note, however, that these would not contribute significantly to the predicted noise levels, because the angle between the radiation and normal directions would approach $\pi/2$, rendering the pseudo-loading term contribution small, except for receivers far away from the domain centre-plane. As the normal velocity on a slip wall is also zero, the pseudo-thickness is not expected to contribute at all to the predicted pressure.

Figure 7.2 and Table 7.1 show the locations of the receivers, which were placed around the foil, also highlighting the relative positions of the control surfaces employed. Six virtual hydrophones were placed directly above the foil at mid-chord in order to evaluate the rate of decay of sound with distance from the foil. Two single listeners were located below and in front of the foil in order to help evaluate the directionality of the sound sources. Furthermore, an additional receiver was placed close to the foil downstream of the trailing edge, in order to quantify the relative magnitudes of noise coming from the oscillating cavity and the turbulent wake. Two more receivers downstream on the centreline of the FW-H surface were used in order to shed more light on the directionality

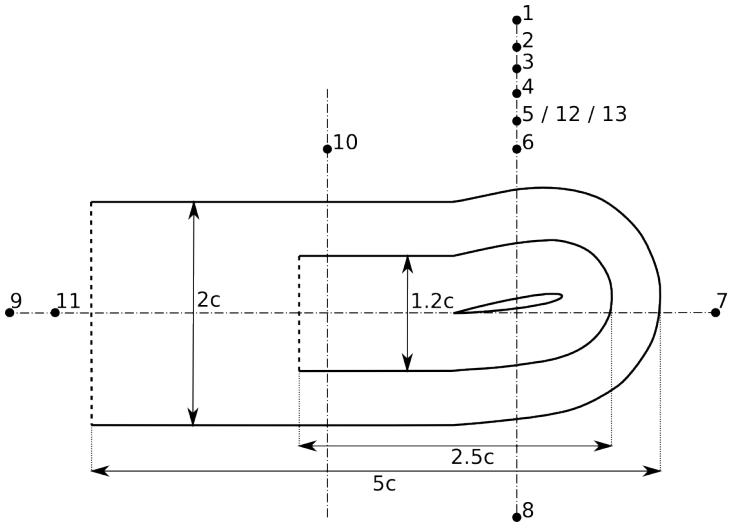

Figure 7.2: Positions of the hydrophones (black dots) used in the study relative to the foil and FW-H surfaces (solid lines), also indicating the downstream segments which were removed in the "open" configurations (thick dashed lines). Data surface dimensions given as a function of foil chord, c, distances of receives from the origin are not to scale.

of the noise source, the relative importance of turbulence noise, and the effect of the FW-H control surface definition on the predicted acoustic signature. Finally, two receivers were situated 1 and 2 span units away from listener 5 in the span-wise direction, in order to allow the effect of three-dimensionality of the noise source to be better understood.

Table 7.1: Locations of receivers used for the NACA 0009 acoustic analogy study.

Receiver	**x [m]**	**y [m]**	**z [m]**
1	0.00	100.00	0.05
2	0.00	75.00	0.05
3	0.00	50.00	0.05
4	0.00	25.00	0.05
5	0.00	12.00	0.05
6	0.00	3.00	0.05
7	50.00	0.00	0.05
8	0.00	-50.00	0.05
9	-50.00	0.00	0.05
10	-0.23	3.00	0.05
11	-3.00	0.00	0.05
12	0.00	12.00	-0.10
13	0.00	12.00	-0.25

7.3 Results

7.3.1 Identification of primary source mechanisms

Table 7.2 shows the convergence of the mean and standard deviation of the lift coefficient with extending the simulation duration. It may be seen that both of the quantities converge relatively quickly, suggesting that the simulation length has been sufficient and thus the mean quantities and Fourier analysis results are statistically significant.

Table 7.2: Convergence of the mean and standard deviation of the lift coefficient with extending time window.

Time window [s]	$\overline{C_L}$ [-]	σ_{C_L} [-]
0.00-0.25	0.8575	0.1553
0.00-0.50	0.8761	0.1809
0.00-0.75	0.8680	0.1805
0.00-1.00	0.8667	0.1828

Figure 7.3 depicts an instantaneous iso-contour of the volume fraction, $\alpha = 0.5$. Two large cavity structures are present above the mid-chord and downstream parts of the foil, with several smaller ones in between. A cavity sheet starting to develop around the leading edge of the foil may also be observed. Three-dimensionality of the flow is apparent from the cavity structures not being uniform in the span-wise direction across the foil.

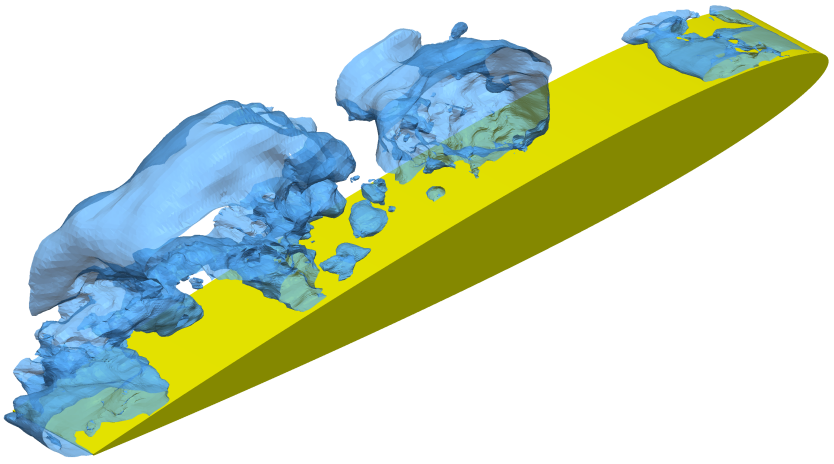

Figure 7.3: Sheet cavity growth and a set of large and smaller cavities present over the foil visualised using an instantaneous $\alpha = 0.5$ iso-contour.

Figure 7.4 presents a distribution of the axial velocity over a mid-span cut plane, with a black iso-contour denoting the cavity interface defined as $\alpha = 0.5$. A large cavity may be seen to be present just above the trailing edge of the foil and causing a severe

velocity disturbance, in effect creating several small regions where the flow is slowed down or made to recirculate. Cavity structures from the previous cavitation cycles may be seen to have affected the wake of the hydrofoil by also having created velocity perturbations. Finally, a cavity sheet that had just been sheared off by a re-entrant jet may be seen around the leading edge. It is worth noting how the flow accelerates while circumnavigating this structure, indicating why a cavity sheet may sometimes be seen as an effective modification to the shape of the foil section and increase its lift coefficient.

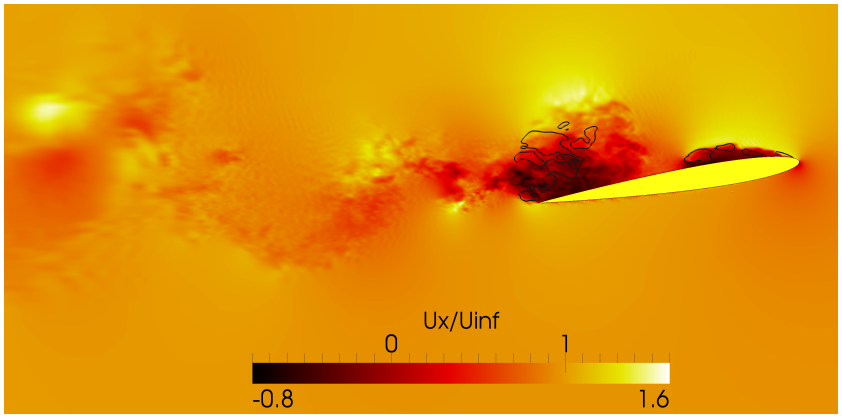

Figure 7.4: Span-normal cut showing stream-wise velocity distribution and the cavity interface ($\alpha = 0.5$).

Figure 7.5 shows the effect of the cavitation on the mean pressure coefficient distribution on the foil for cavitating and non-cavitating conditions. The latter corresponds to the initial condition of the transient simulation computed using steady-state RANS method. Figure 7.6 shows a similar plot for the surface distribution of the mean volume fraction value on the upper half of the hydrofoil.

The two figures show that there exist five distinguishable regions on the upper surface of the foil. Around the low pressure peak, x/c$\leq$0.15, where the foil is predominantly covered by sheet cavitation and experiences high fluctuations of the local volume fraction due to the periodic growth and destruction of the cavity sheet. Further downstream, for x/c$\in$(0.15,0.45), cavitation is still largely attached to the foil surface. The positive gradient of the mean VOF value may be explained by the cavity sheet growing at an approximately steady rate, thus periodically advancing along the foil. The mean pressure coefficient sees a characteristic plateau from the leading edge up to this point. For the mid-span section of the original twisted foil this extended up to x/c$\approx$0.4 [62], meaning that in the present simulation sheet cavitation extents approximately 5%c further downstream than in the case of the Delft Foil.

For x/c$\in$(0.45,0.65) there appears to be an intermediate region with little cavitation touching the hydrofoil surface and the pressure coefficient starting to tend to the trailing edge value. Notable features are the step changes in the standard deviation and in the rate of change of the local volume fraction. From this point downstream, fluctuations

in the local pressure coefficient may be seen to steadily increase. Beyond this region, the foil surface is almost entirely wetted with minimum fluctuations of the local volume fraction. Around the very trailing edge, x/c≥0.9, one may observe intermittent presence of cavities close to the foil surface.

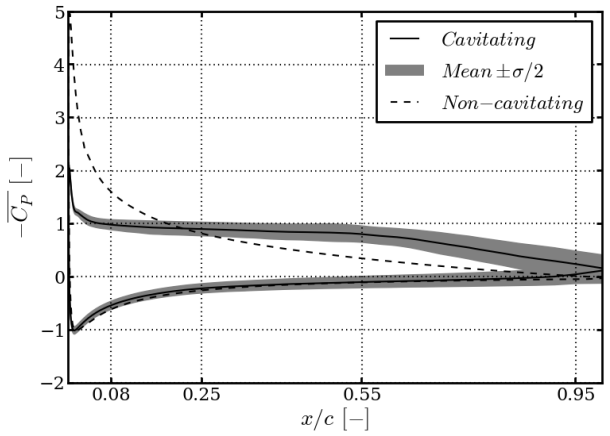

Figure 7.5: Time-averaged pressure coefficient distribution at mid-span of the foil surface, also showing the standard deviation, σ, at each location along the chord.

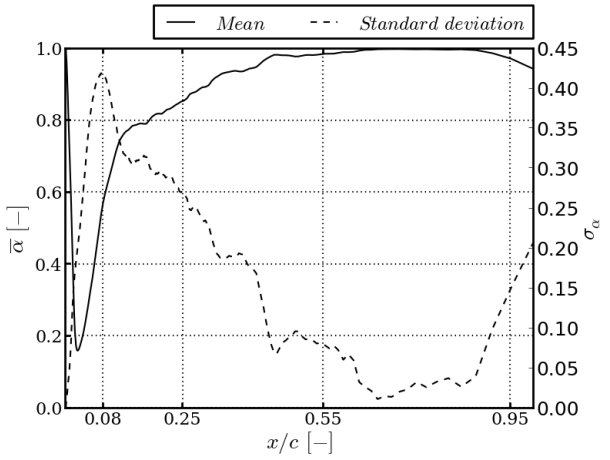

Figure 7.6: Distribution of the mean and standard deviation of the volume fraction on the upper surface of the foil, sampled at mid-span.

In order to allow a better explanation of the nature of the flow at the aforementioned stations along the foil, power spectral density function of the local pressure coefficient is presented in Figure 7.7. The data focus on four locations approximately in the middle of each of the described regions, omitting the one between x/c=0.65 and 0.9, as it provides little additional information. The results show that everywhere except at x/c=0.55, the local quantities are dominated by frequency of 22 Hz. This is similar to the results presented by Ji *et al.*, who found the surface pressure one the suction side of the foil

they studied to be affected predominantly by the cavity volume oscillation frequency [99].

Recalling the snapshot of the flow in Figure 7.4, one may see how the locations on the foil where the sheet is present see very periodic behaviour, but downstream of the cavity closure there exist more local flow instabilities. However, further downstream the flow is again dominated by regular passing of the shed clouds, explaining the periodicity of the signals around the trailing edge. The volume fraction there, however, gets affected by the shed clouds splitting into smaller elements and fluctuating in volume due to the action of vortical structures.

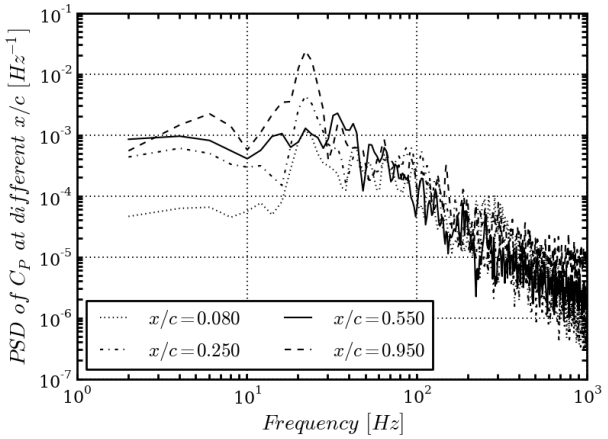

Figure 7.7: Power spectral density of the local pressure coefficient on the upper surface of the foil at x/c=0.08, 0.25, 0.55, and 0.95, sampled at mid-span.

It is important to look at the rate of change of the total cavity volume, as it is expected to be directly responsible for driving noise generation. Figure 7.8 shows a portion of the data for the three volume fraction values used and the power spectral density of the signals is shown in Figure 7.9. The rate of change of volume may be seen to experience a peak around the frequency of 22 Hz for all VOF values, which has already been identified as the main shedding frequency based on the pressure coefficient data. In the case of the lowest VOF threshold, there also exists a substantial amount of energy in the higher frequencies, which may indeed be seen by comparing the raw data in Figure 7.8.

7.3.2 Effect of FW-H control surface choice

Figure 7.10a shows the breakdown of the total sound pressure level (SPL) at receiver 3 into three terms, corresponding to the solutions of each of the integrals in Equation (5.12). Separate data series are plotted for each of the four control surface variants presented in Figure 7.2. It should be noted that for data shown in Figure 7.10a phase information has been lost and so adding the individual SPL spectra may not reproduce

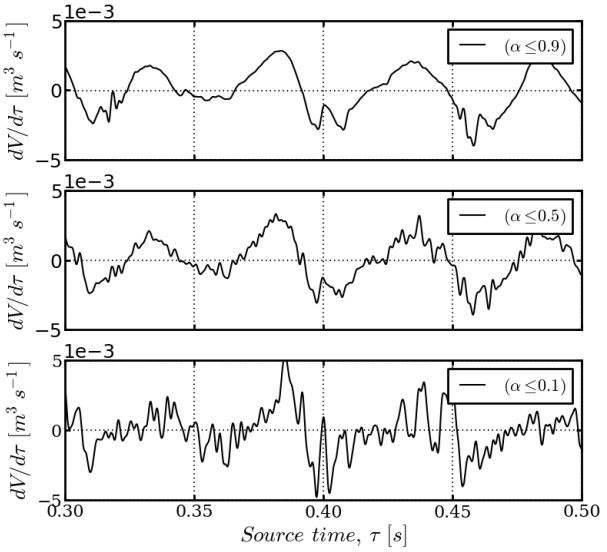

Figure 7.8: Source-time derivative of the total cavity volume time trace.

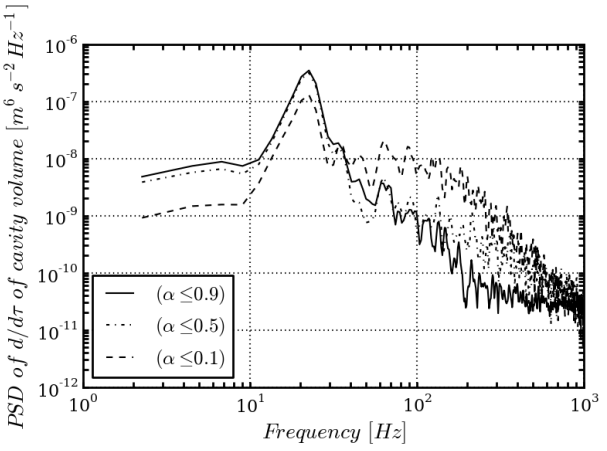

Figure 7.9: Power spectral density function of the time derivative of the total cavity volume for various volume fraction thresholds.

the actual total sound pressure level. SPL has been computed according to

$$SPL = 10 \log \left(\frac{p'}{p_{ref}} \right)^2, \tag{7.1}$$

with the reference pressure level p_{ref} of 1 μPa for water. The time trace of the pseudo-thickness and pseudo-loading pressure terms for this receiver is also depicted in Figure 7.11.

The first striking observation in these data is that the noise signal is predominantly dependent on the pseudo-thickness term associated with mass flow through the porous control surface. This may be associated with the action of the oscillating cavities periodically pushing mass out of the region surrounding the foil. This is also evident as the

spectral peak coincides with the 22 Hz frequency of the rate of change of total vapour volume signal. The pseudo-thickness term computed using all but the short-open control surface (CS) compares very well. For this particular CS, the peak value is overestimated by approximately 5 dB and the associated waveform may be seen to suffer from the negative pressure peaks being of substantially higher amplitude. This may be explained by the fact that the smallest control surface ends close to the region where cavities exist and when its downstream end is left open a substantial part of the normal flow velocity remains unaccounted for.

However, closing the downstream surface may cause a different set of problems associated with the p'_Q volume integral of the FW-H equations being ignored. This causes the noise sources leaving the closed control surface, such as turbulent eddies, not being accounted for well enough. This may be seen in the presented data as an increase in the pseudo-loading (proportional and derivative) terms of the acoustic analogy caused by strong peaks appearing in the time signals of these terms, as seen in Figure 7.11. A noteworthy fact is that despite the large control surface being placed in a coarser mesh region, the convected vortices still have a comparable effect on the predicted spurious noise as in the case of the small surface.

Another important obstacle in using an open-ended control surface is that, by virtue of the pseudo-loading terms being dependent on the dot product of radiation and normal directions, its faces will contribute more to the downstream receivers. This may potentially lead to the spurious noise source affecting them more than others. To evaluate the importance of this, the SPL of individual FW-H terms was plotted for receiver 6 in Figure 7.10b. One may note that, as expected, the relative importance of the pseudo-loading terms becomes higher and the result obtained using the short-closed control surface diverges the most of the remaining predictions. The latter indicates that the spurious noise source is indeed the strongest where the mesh is finest and the vortices are best preserved. This may be visualised by examining data in Figure 7.12, showing how the turbulence in the flow interacts with the control surface inducing localised noise sources. The presented noise data depicts the instantaneous FW-H contribution of each of the faces constituting the data surface. This has been divided by the face area of each face of the control surface, thus yielding a quantity which may be interpreted as an intensity. This allows a more accurate comparison of faces with different areas. It is also interesting to note the high turbulence levels around the foil where cavitation is present.

Based on the results from this part of the study it has been decided to use the open variant of the large control surface in the subsequent acoustic analysis, as it appears to be able to capture the dominant pseudo-thickness FW-H term and is not affected by the spurious noise sources in the wake. The drawback of this approach is that it may not capture all of the sound generation mechanisms in the wake and may affect the magnitude of the acoustic signals for the downstream receivers.

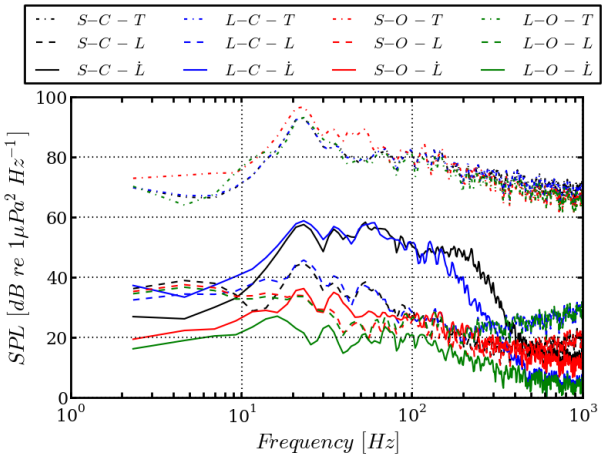

(a) Receiver 3 - above the foil

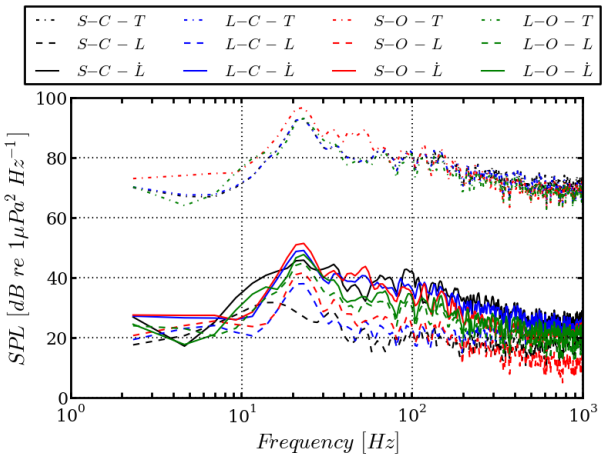

(b) Receiver 9 - downstream

Figure 7.10: Sound pressure level predicted at receivers 3 and 9 showing the contributions of different FW-H components, corresponding to individual terms in equations (5.12). Data for short (S) and large (L) control surfaces in closed (C) and open-ended (O) variants.

7.3.3 Sound source identification

Figure 7.13 shows time history of the acoustic pressure at receiver 1 plotted as a function of the source time by applying a phase shift of $|\mathbf{r}|_{median}/c_0$, where $|\mathbf{r}|_{median}$ is the median source-receiver distance of the control surface faces. Viewing the data in this way allows the sound history to be compared directly with the time derivative of the total cavity volume in Figure 7.8. A low-pass filter was applied to better visualise the low-frequency part of the waveform.

Points on the $dV/d\tau$ curves with steepest slope may be seen to coincide with the peaks and troughs in the pressure waveforms. This was expected as it is known from simple bubble theory that the second derivative of the bubble volume is directly linked to the

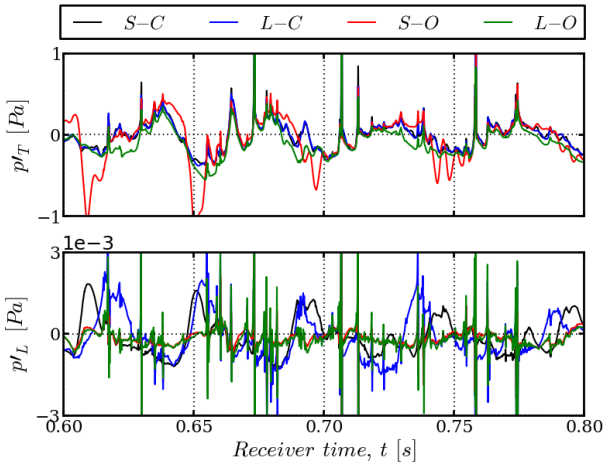

Figure 7.11: Time trace of the pseudo-thickness (T) and pseudo-loading (L) FW-H terms for receiver 3 for the four control surface variants used.

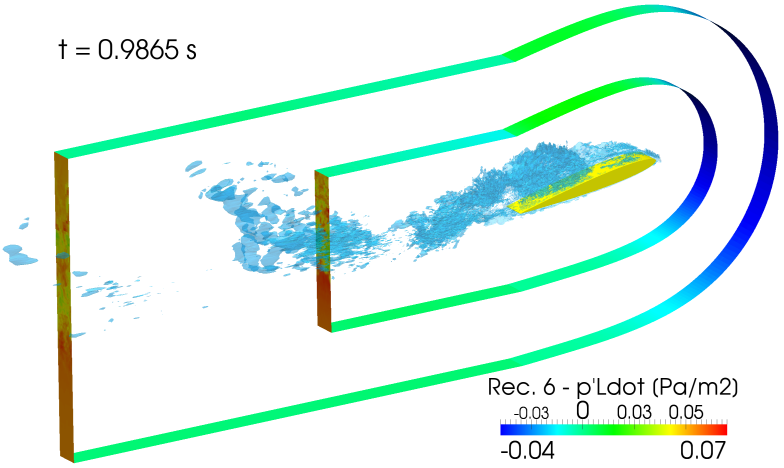

Figure 7.12: Distribution of the derivative part of the pseudo-loading FW-H term in Eq. (5.12b) for receiver 9 on both control surfaces used, also showing a vorticity iso-contour $|\omega| = 1000\,s^{-1}$.

strength of the monopole source associated with cavitation. Moreover, the noise signal has a certain amount of higher frequency components. These could be due to the pseudo-loading, but also the pseudo-thickness term, as seen in Figure 7.11. This shows that, while the dominant frequency of the signal seems to be excited by the entire vapour region up to high threshold VOF values, the perturbations in the more coherent cavity regions may also play an important role in deciding the final pressure signal.

An important observation is the presence of strong, impulse-like peaks in the pressure signals. These precede the occurrence of the maxima of the dominant 22 Hz waveform and may be seen to coincide in time with the troughs of the time derivative of the total cavity volume curves. Analysis of flow field snapshots has shown destruction of

a cloud cavity present downstream of the foil to occur at this point in the shedding cycle. Notably, the noise peaks are most prominent during the cavitation cycles when largest cloud cavity, corresponding to largest total vapour volume, is observed. Figure 7.14 shows two consecutive snapshots of the flow which indicate how a cloud around the trailing edge of the foil rapidly loses a significant part of its volume. The presented pressure contours indicate that a rapid increase in surface pressure on the foil is observed. It is this mechanism that is responsible for the generation of the discussed peaks in the integral forces and radiated pressure. A key thing to notice is that the magnitude of the narrow radiated pressure peaks is at least as large as that of the low-frequency oscillations, even after a low-pass filter has been applied. An important realisation is that the incompressible model may not predict the magnitude of the pressure peaks induced by the collapsing cavities accurately, and thus this part of the results is likely erroneous. This will affect the high frequency range of the noise spectrum and, to a certain extent, the overall sound pressure levels but not the conclusions drawn regardin the low-frequency noise, which was the primary focus of this work.

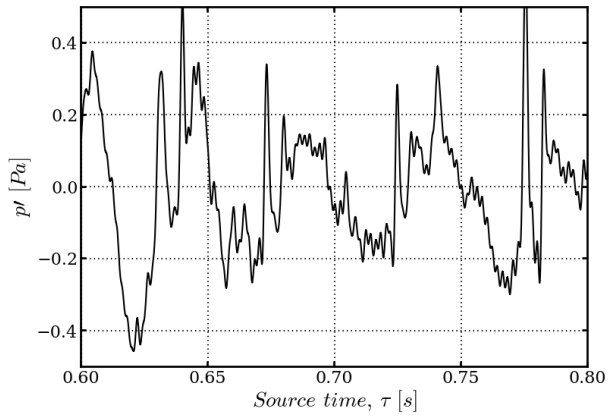

Figure 7.13: Time trace of the predicted acoustic pressure at receiver 3 shown as a function of the source time (corrected using median source-receiver distance). Data filtered with a low-pass filter at 500 Hz to better show the low-frequency contribution caused by the oscillations of the cavity volume.

7.3.4 Sound field characterisation

It is worth examining how the sound field radiated from the hydrofoil in order to better understand its directivity and the relative importance of particular flow regions in terms of noise generation. Figure 7.16a shows time series data for receivers displaced by 1 and 2 chord lengths in the span-wise direction from receiver 3. One may note very little difference between the waveforms. This may be explained by the radiated sound being dominated by the pseudo-thickness term contribution of the FW-H equations, which depends on the magnitude of the radiation vector, $|\mathbf{r}|$, and on the control surface normal direction, $\hat{n}$, and thus shows little directional behaviour.

Figure 7.16b presents time signals of the predicted radiated pressure for receivers 3 m away from the foil just above its mid-chord, above the wake, and directly downstream. The purpose of analysing these data was to examine whether with reducing the source-receiver distance the pseudo-loading FW-H terms will increase in magnitude sufficiently to start playing a significant role in the resultant total pressure waveform shape. As may be seen, this was not the case since the predicted signals resemble the ones at other receivers closely, apart from their magnitude being significantly higher, as expected. It is also worth noting how the same behaviour is observed for receivers below and in front of the hydrofoil, as shown in Figure 7.16c, hinting at a monopole nature of the dominant noise source. The only slight difference here may be seen for receiver 11, placed downstream of the foil, which sees fewer high-frequency oscillations. These have been shown to manifest themselves primarily through the pseudo-loading FW-H terms, which may not be predicted accurately for an open-ended control surface when source-receiver vectors pass through the "missing" part of the porous data surface, as is the case for this receiver.

Figures 7.17 and 7.18 present the radial variation of the sound pressure level emitted at the dominant 22 Hz frequency at receivers directly above the hydrofoil. An interesting observation is that at intermediate frequencies, the spectra see a falloff slightly slower than f^{-2}, which stands in general agreement with a range of cavitation noise experiments presented in the literature [22]. The receivers also experience a small amount of acoustic fluctuations at higher frequencies. These have been found to be related to the high-amplitude pressure peaks in the pressure time traces. Appearance of these peaks in the pseudo-loading FW-H terms suggests that they are the manifestations of collapsing cavities, as discussed for Figures 7.13 and 7.14.

It is worth recalling that for a porous FW-H formulation the individual terms lose their physical meaning and so the pseudo-thickness term, shown to play the dominant role in the presently compted acoustic data, may not be directly associated with a monopole source being present in the fluid. However, all of the result presented above indicate that the dominant noise source is indeed of monopole nature. In order to provide a final confirmation of this, it is worth to compare the noise levels predicted for the hydrofoil with those of an idealised acoustic source.

In the present simulation, the cavities are not spherical, but one may attempt to approximate the sound they radiate by finding their equivalent, idealised radius, and computing the pressure a spherical bubble of that size would produce in a quiescent liquid. This would allow the rate of decay of noise predicted in the current simulation to be compared to an idealised solution, thereby providing a degree of validaiton. From the time trace of the total cavity volume, depicted in Figure 7.15, the average maximum volume of the bubble during each cavitation cycle was found to be $V_{max} \approx 2.0 \cdot 10^{-5}\, m^{-3}$ using the $\alpha \leq 0.5$ curve. Assuming spherical shape, this yields $R_{max} \approx 0.017\, m$. The bubble may now be assumed to undergo simple harmonic motion with its radius oscillating

between R_{max} and zero at 22 Hz.The pressure radiated by a spherical bubble may then be described using Equation (5.15), where the source strength, Q, is the second time derivative of volume change of the bubble, and may be written for a spherical cavity of radius R as

$$Q = \ddot{V} = 4\pi(R^2\ddot{R} + 2R\dot{R}). \tag{7.2}$$

This yields radiated sound at a point [83]

$$p(\mathbf{x}, t) = \frac{\rho}{|\mathbf{x} - \mathbf{y}|}\left(R\ddot{R} + 2R\dot{R}^2\right)\Big|_{\tau}. \tag{7.3}$$

Naturally, both R and its source time derivatives in Equations (7.2) and (7.3) will be governed by the Rayleigh-Plesset equation [158], thus making determination of radiated pressure at a point more complex in reality [83, 143].

The equivalent radius derived from Figure 7.15 has been found to cause pressure oscillations of a much greater amplitude than was observed in the numerical data. By an empirical fit, the predicted noise data has been found to correspond to a bubble of radius with maximum radius of approximately 15% R_{max}. These data is also plotted in Figure 7.18 for comparison.

7.4 Discussion

Despite a different, more advanced LES model being used in the present investigation compared to the previously presented studies, the computed flow field does not differ significantly from the initial results presented in Chapter 6 in terms of the shedding frequency and the observed cavtation patterns. This further reinforces the conclusion that using the DDES model offers an advantage of being applicable to much higher Reynolds numbers without significant losses of accuracy when highly unsteady cavitating flows are concerned.

Furthermore, despite the foil considered here having a smaller span than in the initial simulations, the observed cavitation patterns are very similar. This indicates that, despite the cavitation having three-dimensional features, it is still largely governed by two-dimensional behaviour. Nonetheless, because of these span-wise features, a significant amount broadband pressure fluctuations on the foil has been observed. Referring to the data presented by Bretschneider *et al.* for a NACA0015 section, one may see that for foil experiencing sheet cavitation, severe amount of variation along the span may be seen at any one time. This reportedly also manifests itself in a fluctuating pressure signal for a transducer in direct vicinity of the foil, likely having a similar effect on the foil loading [27]. The matter of defining the characteristic span-wise length of cavitation as a function of governing flow parameters therefore remains an open question.

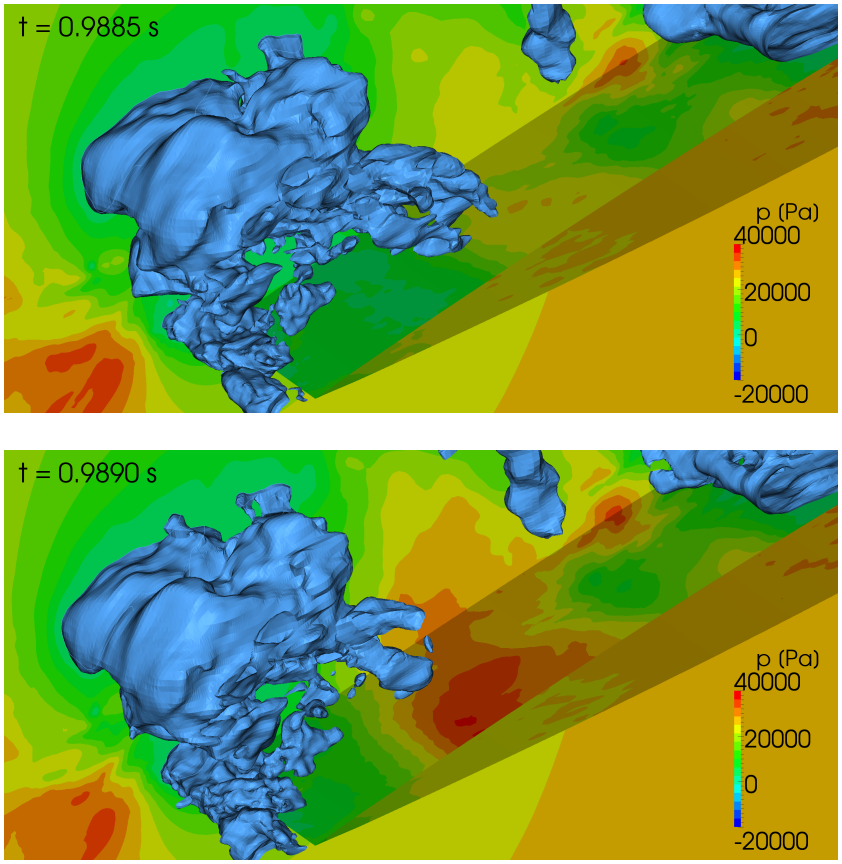

Figure 7.14: Consecutive snapshots of the cavity interface ($\alpha = 0.5$) and pressure on the surface of the foil and a span-wise extent of the domain before and after a violent collapse of a part of the cavity takes place. Cavity cloud is located above the trailing edge, downstream end of the growing sheet also seen in the top-right corner.

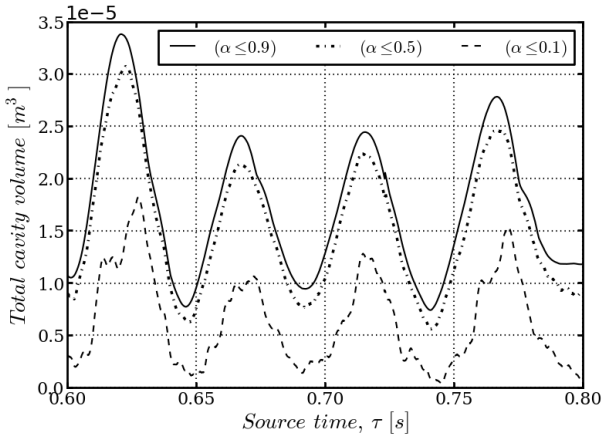

Figure 7.15: Time trace of the total cavity volume predicted over the NACA 0009.

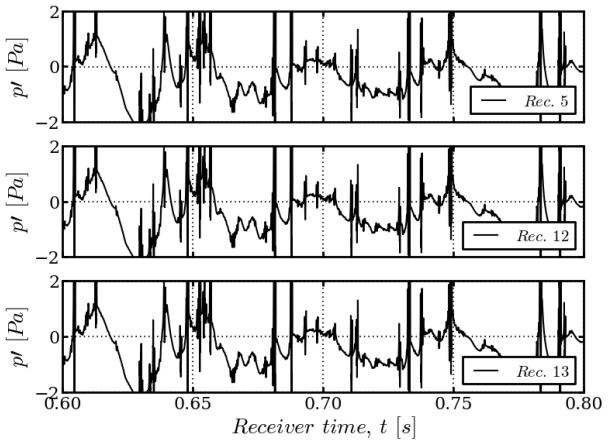

(a) Receivers spaced 1 chord away from each other along the span (5, 12 and 13)

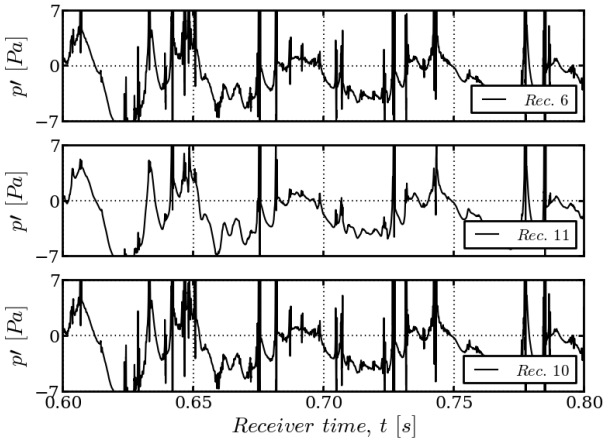

(b) Receivers in the near-field 12 m away from the foil (6, 10 and 11)

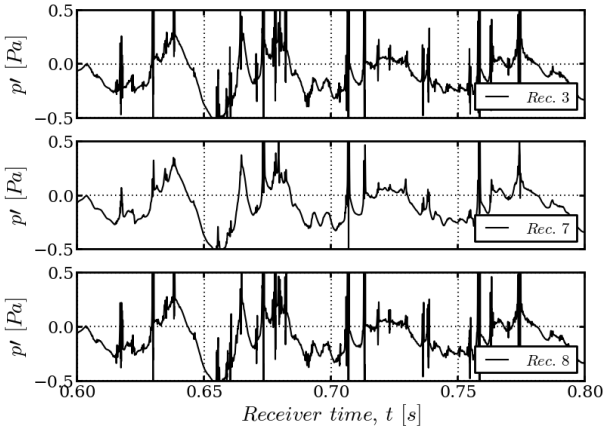

(c) Far-field receivers above, in front of, and below the foil (3, 7 and 8)

Figure 7.16: Pressure time histories predicted at different receivers around the foil.

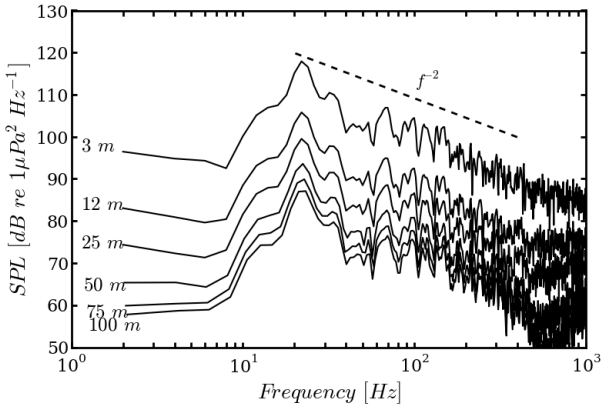

Figure 7.17: Variation of the predicted sound pressure level for receivers directly above the foil (1 to 6) with source-receiver distance.

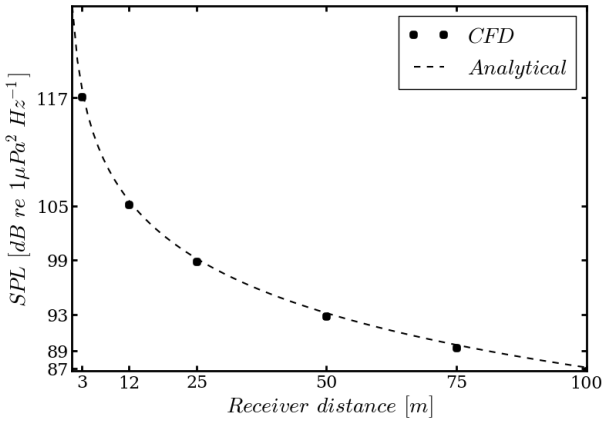

Figure 7.18: Decay of the sound pressure level predicted at the dominant frequency of 22 Hz with source receiver distance for receivers 1 to 6. Data for an idealised spherical bubble acting as a monopole noise source in accordance with Equation (7.3) plotted for comparison.

The presented data indicate that the cavitation mechanisms predicted for the foil are governed by periodic growth and collapse of a pronounced sheet cavity, as well as shedding of vapour clouds. These have been predicted to have a relatively constant cycle frequency apparent in most of the quantitative properties, such as pressure coefficient or total vapour volume, as well as qualitative characteristics like the wake.

In the present simulation, the three-dimensional shedding reported for the original Delft Twist 11 hydrofoil was not observed and instead much larger and persistent sheet cavitation was predicted. This also resulted in a lower shedding frequency, as the larger cavities took longer to grow to their maximum size. In the present study the Strouhal number defined based on the maximum sheet cavity length, taken as 0.6c, and free-stream velocity, has been computed to be 0.284. Experimental data by Ait Bouziad for

cavitation number 1.2 quoted this quantity to be 0.36 for a NACA 0009 foil at cavitation number 1.2, Reynolds number 2 million and angle of attack of 5 degrees [1]. It thus seems possible that the shedding frequency is under-predicted in the current simulation, which would have most likely been caused by the subgrid model introducing too much viscosity in the region of cavity closure [87, 202]. Interestingly, this finding would contradict the comparison for the full Delft Twist 11 foil for which the frequency was over-predicted. However, the measurements of flow past a NACA 66 reported by Leroux *et al.* [117] indicate that rapid changes in shedding frequency may occur for relatively small changes of the angle of attack and cavitation number. It is therefore likely that the higher cavitation number in the reference data by Ait Bouziad would induce a higher shedding frequency corresponding to a higher Strouhal number, which would stand in good agreement with trends observed by Leroux *et al.*.

Significant amounts of cavitation regions with intermediate vapour volume fractions between 0 and 1 have been predicted, particularly downstream of the sheet cavity. These regions of intermediate vapour fraction values may be physically interpreted as a mixture of smaller bubbles being carried by the fluid. Such cavities are known to have a high noise-generating potential as they oscillate subject to a varying pressure field [20, 35, 114, 163]. However, due to the way they are described in the volume-of-fluid approach this behaviour may not be captured.

Another limitation of the current methodology stems from the incompressible flow assumption and the nature of the mass transfer cavitation model. It has been shown that rapid desinence of cloud cavities may have a significant effect on the local pressure on the foil, the integral force coefficients, but also on the radiated noise. However, such a collapse mechanism is significantly affected by flow compressibility and requires the bubble mechanics to be resolved to very small spatial and temporal scales [9]. It thus follows that, because the adopted theoretical model cannot predict shock waves associated with cavity collapse, the impulse-like character of the associated radiated pressure may not be predicted accurately. This behaviour is further enhanced by the fact that while the numerical grid in this study may be considered fine when compared to those typically used in marine applications, it would be far too coarse to capture the final stages of the collapse, even if compressibility had been accounted for. One may thus argue that, while the noise due to large-scale cavity interface velocities may be predicted reasonably well using the presented method, the peak noise values associated with the final collapse events are likely to be predicted incorrectly due to insufficient mesh density and an incompressible flow assumption being invoked.

It has been shown that even for receivers in a relative proximity to the hydrofoil the dominant part of the noise is caused by the large-scale fluctuations of the cavities. This kind of excitation has been found to manifest itself through the pseudo-thickness term of the FW-H acoustic analogy, which is independent of the radiation vector and only on the radiation distance. Making use of this property, it has been demonstrated that ignoring

the volume integral and leaving the downstream end of the FW-H control surface open is a viable means of reducing the complexity of the simulations without introducing significant errors, even for downstream receivers.

However, if the amount of cavitation present would be smaller, such as could be expected on a well-designed ship propeller close to its operating point, one could expect the relative importance of the turbulent noise from the wake to become increasingly important. This would hold particularly true in the case of a propeller operating in a non-uniform, unsteady inflow. In such a case neglecting the volume integral and using an open-ended control surface could lead to errors, especially when considering radiation directions aligned with the flow, as pointed out by Ianniello *et al.* [88, 89]. This stresses the importance of searching for viable alternatives to using open FW-H control surfaces, such as the ones discussed by Rahier *et al.* [161] or Sinayoko *et al.* [181], if the studies are to be extended to more complex geometries.

The dominant noise source has also been demonstrated to be of monopole nature, as expected from the literature for oscillating vapour volumes. Because of this property and the way the Ffowcs Williams - Hawkings acoustic analogy is formulated, the noise field showed little variation in the span-wise direction, even if the radiation vector joining the surface of the foil and the virtual hydrophone does not penetrate the control surface. This could potentially mean that results obtained from a simulation similar to the one presented here could be used without much need for applying span corrections, like the ones discussed for turbulence noise over wings [18, 70, 72]. One has to be careful, however, as it has been shown in this work and in the literature that sheet cavitation is likely to develop three-dimensional features, even if the analogous wetted flow may well be two-dimensional [99]. At this stage it is therefore unclear how changing the span of the hydrofoil section would affect the radiated noise.

7.5 Summary

The present Chapter presented a comprehensive study of a NACA 0009 hydrofoil undergoing periodic sheet cavitation. The results described how the shedding mechanism affects the loading on the foil, as well as the velocity and pressure distributions around it and in its wake. The Ffowcs Williams-Hawkings acoustic analogy has then been successfully applied to study the radiated pressure produced by the sheet cavitation and clear connection between the predicted shedding mechanism and noise was shown in the data. Overall, the acoustic analogy has been demonstrated to cope well with accounting for the low-frequency part of the noise associated with oscillations of the volume of large sheet and cloud cavities. Furthermore, it has been shown that using an open-ended control surface, similarly to the E779a study, is a viable option for avoiding the expensive volume integral in the FW-H equation from a practical engineering standpoint. Areas

likely to be occupied by bubbles smaller than the grid size have been identified in the present simulations. These bubbles are not expected to drive the peak sound pressure levels at low frequencies, but have been reported in the literature to be the dominant noise source at medium and high frequencies in certain conditions. It has been decided to pursue a method capable of accounting for their contributions to the acoustic signature of a cavitating hydrofoil in the subsequent parts of this thesis. Beforehand, however, the next chapter aims to extend the current study by investigating a NACA 66 hydrofoil, which is much more representative of geometries seen on modern marine propellers than the NACA 0009 considered so far.

Chapter 8

Modelling pressures induced by a cavitating NACA 66 foil

8.1 Introduction

In the preceding chapters the implemented Ffowcs Williams-Hawkings acoustic analogy has been successfully applied to a non-cavitating properller and a heavily cavitating hydrofoil. Both of these test cases were established with the numerical solution in mind from the very beginning, in the sense that they did not replicate any particular experimental set ups directly. However, it has been recognised that most of the experimental data available for validation is available for geometries operating in a heavily constrained environment, mainly relatively narrow cavitation tunnel working sections. A hydrodynamic problem posed in such a way presents a significant challenge in the form of creating reflections and affecting the flow through blockage. All of these will affect the sound pressure levels measured in the experiments, and thus it is important to test the proposed acoustic method on a simulation representing an actual cavitation tunnel geometry.

This problem is addressed in the present chapter, which is focused on simulating the flow past a NACA 66 hydrofoil, following the experiments and simulations presented by Leroux, Astolfi and Ducoin *et al.* [6, 51, 116, 117]. The currently considered test case has been chosen because it represents hydrofoil shapes used on marine propellers more closely than the previously investigated NACA 0009, and the experimental studies reported the foil to undergo very dynamic cavitation. Data in the public domain also cover a range of angles of attack and cavitation numbers, modelling which would allow the limits of the used cavitation model to be further explored. Importantly, the experimental data provides time-resolved pressure measurements on the surface of the foil, which are deemed crucial from the cavitation model validation perspective.

Detailed aims of the present study were, therefore, to validate the currently used cavitation model across the wide range of conditions tested experimentally by Leroux, Astolfi and Ducoin *et al.*. Particular attention was paid to comparing the dynamic behaviour, such as the shedding frequency, unsteady pressure, and cavitation patterns, to the reported measurements. Following this, hydroacoustic analysis was carried out in a manner similar to the NACA 0009 hydrofoil, however without adjusting the domain size and grid topology to specifically meet the needs of the acoustic analogy. This will allow conclusions to be drawn about the limits of applicability of the FW-H method in terms of reproducing cavitation tunnel environments.

8.2 Background

The presently studied hydrofoil is very common on marine propellers. In fact, both of the propellers considered in the previous chapters, the Insean E779a and the PPTC, both employ that section shape, as do propellers on ship validation test cases such as the Kriso container ship (KCS), for example [180]. The reason for this is the round-back profile of the foil, which shifts the minimum pressure point aft and reduces its peak, thereby lowering the risk of cavitation inception. This also makes the foil particularly challenging to model, as it is expected that the mass transfer cavitation model source terms may be put to a difficult test when faced with relatively gentle pressure gradients.

The experimental data provided by Leroux *et al.* [117] for this test case covers two very different cavitation regimes. At low angles of attack and low cavitation numbers the authors report the sheet cavitation behaviour to be significantly affected by the pressure waves generated by the collapsing cavity clouds downstream of the foil. This has been reported to inhibit inception of new cavity sheets until the downstream clouds have disappeared completely. As the angle of attack and cavitation number are increased to a regime similar to the previously presented NACA 0009, however, sheet inception occurs soon after the passing of the re-entrant jet. Similar behaviour was also observed in the numerical results for the NACA 0009. Leroux *et al.* denote these two cavitation regimes as dynamics 1 and 2, respectively, and this notation is also followed in this chapter.

8.3 Simulation set-up

The numerical set up used for the present NACA 66 simulations derived substantially from the earlier studies of the Delft Twist 11 and NACA 0009. Namely, structured grid of similar topology were used, with an O-grid boundary layer region and a series of matching H-grids constituting the rest of the mesh. Domain size was chosen to match the height of the cavitation tunnel cross section used by Leroux *et al.*, namely 192 mm.

Chord length of the foil was 150 mm and the mesh was made to extend 3 chord lengths upstream and 10 downstream. The span-wise extent of 0.08 m, or 0.55 chord lengths was chosen based on the experience developed during the NACA 0009 simulations.

Density of the mesh was also chosen based on the grid convergence study carried out for the Delft Twist 11, as the present test case is expected to experience generally similar flow patterns. It is subject to an inflow speed of 5.33 ms^{-1}, which yields the chord-based Reynolds number of 800,000, which also compares closely with the 1 million experienced by the D11 test case. Consequently, a grid yielding x^+ of 82, $y^+ \leq 1$, and z^+ of 300 was designed using 7.3 million cells.

For the acoustic simulations, the porous data surface used to evaluate the FW-H integrals was chosen in such a way to encompass the entire region of cavitation, similarly to the large integration surface that was used for the NACA 0009 foil. In the present case, the upper limit on its size was dictated by the bounds of the cavitation tunnel section. Care was taken to extend the surface far enough downstream to enclose the shed cloud cavitation and corresponding regions of high turbidity. An outline of control surface is shown in Figure 8.1a, and the mesh, showing the wake refinement, is depicted in Figure 8.1b.

Turbulence was modelled using the Spalart-Allmaras DDES model and the boundary layer was fully resolved. A fixed velocity inlet and a pressure outlet were used. The horizontal cavitation tunnel walls and the sides of the numerical domain perpendicular to the foil span were treated as symmetry planes. Second order convection and time discretisation schemes were applied, and the turbulent viscosity transport equation was solved using the upwind scheme. The first series of simulations across a range of angles of attack and cavitation numbers was run by fixing the maximum Courant number at 0.5 and adjusting the time step dynamically. For the acoustic simulation being able to save the flow field data 40 kHz necessitated the simulation time step to be fixed at $2{\cdot}10^{-6}$ s, as the OpenFOAM time step adjusting algorithm could not cope well with such a stringent requirement.

The conditions reported in the experiments by Leroux *et al.* are summarised in Table 8.1. It should be noted that the authors highlighted the cases at 6 and 8° angles of attack to correspond to typical conditions representative of the dynamics 1 and dynamics 2 cavitation regimes discussed earlier. Table 8.1 also shows the cases investigated presently using CFD. It should be noted that the outlet pressure of the simulations has been iteratively adjusted to yield the mean cavitation number at the inlet of the numerical domain similar to the one reported in the experiments, thus maximising the flow similarity. Saturation pressure was assumed to be 3100 Pa based on the estimates quoted by [117]. An additional operating point at 9° was added by extrapolating from the experimental values in order to further explore the sensitivity of the cavitation model.

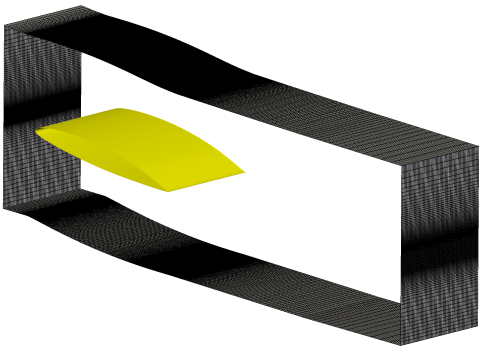

(a) FW-H integration surface

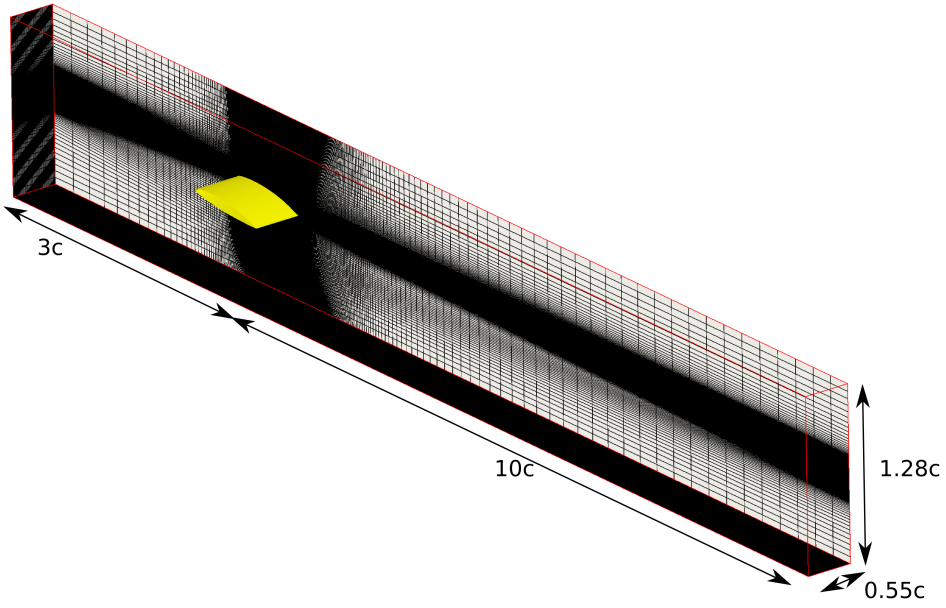

(b) Grid and numerical domain overview

Figure 8.1: FW-H integration surface and mesh used for the NACA 66 foil case.

Table 8.1: Flow conditions for the NACA 66 simulations replicating experiments by Leroux *et al.*. Data at 9 degrees angle of attack extrapolated from the experimental set up.

Angle of attack [deg]	$\sigma_{\mathbf{inlet}}$ [-]	**Outlet pressure [kPa]**
Experiments by Leroux *et al.* [117]		
6	0.99	-
7	1.13	-
8	1.27	-
Present CFD		
6	0.97	16.63
7	1.12	18.33
8	1.25	20.15
9	1.44	22.37

8.4 Results

8.4.1 Capturing different cavitation regimes

This part of the present investigation aimed to investigate how well the currently used cavitation model captures the different cavitation regimes described by Leroux *et al.* [117]. This was done by first analysing the time- and frequency-domain characteristics of cavitation volumes developed in the simulations, which are shown in Figure 8.2.

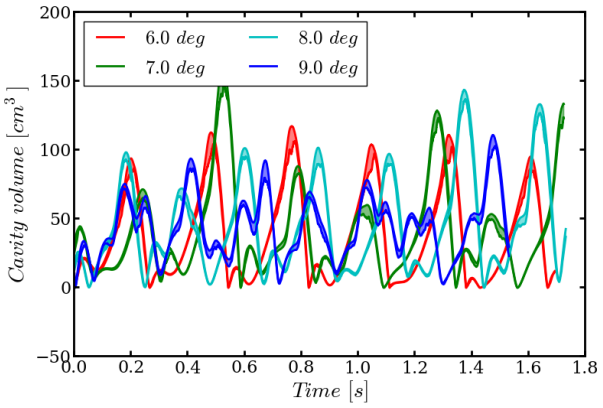

(a) Time history

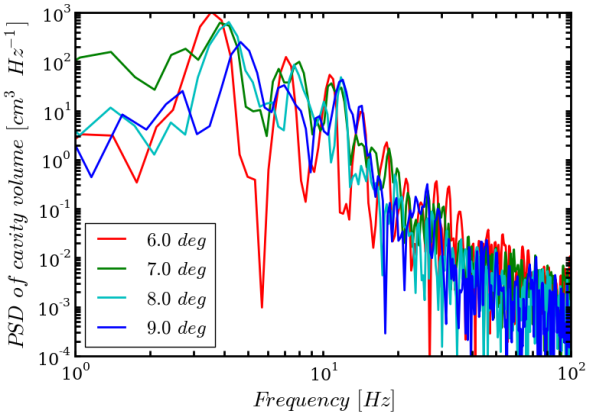

(b) Power spectral density function

Figure 8.2: Total cavity volume traces and spectral characteristics for NACA 66 across a range of conditions.

The power spectral density functions reveal that as the angle of attack is increased, the first harmonic shifts to a higher frequency. The low-frequency peaks in the spectra have been found to correspond to frequencies of 3.57, 3.96, 4.19, and 4.77 Hz for the cases between 6 and 9 degrees angle of attack, respectively. The key point to note is that for the dynamics 1 case at 6°, the fundamental frequency matches very well with the 3.5 Hz reported by Leroux *et al.* [117]. At 7°, the discrepancy with the experimentally

reported frequency of 4.5 Hz increases, but remains acceptable. However, the authors of the experiments reported a rapid increase in the shedding frequency beyond 7.5°, yielding 18 Hz for the dynamics 2 case, which may not be seen in the 1^{st} harmonics of the current simulation.

However, by analysing the time traces of the total cavity volume in Figure 8.2, one may note that the waveform for the highest angle of attack case differs significantly from the others. It shows a much more sinusoidal behaviour, while in the remaining scenarios a more complex, multi-modal pattern is observed. The latter behaviour is very consistent with the numerical data presented by Ji *et al.* for the same test case [99]. Differences between the cases are also evident in the higher harmonics of the signals, with the 9 degrees case being the only one showing higher spectral levels at the thirrd harmonic than at the second, the former corresponding to the frequency of 11.92 Hz. This also matches the mean peak-to-peak frequency of the signal, computed to be 11.76 Hz.

Turning attention to Figures 8.3 and 8.4, showing instantaneous volume fraction iso-contours and experimental cavitation pattern observations, yields further insight into the nature of the predicted cavitation behaviour. It should be noted that for the dynamics 2 case, the published experimental data does not include photographs along the span of the foil and hence comparison is made with numerical data by Seo & Lele [175], who applied a compressible cavitation model to the test case and obtained a very good agreement with the experiment in terms of shedding frequencies and predicted surface pressures. It has also been decided to compare the reference dynamics 2 data to the present 9 degrees case, since the time series analysis has revealed that the presently used cavitation model does not predict the transition to the high-frequency shedding regime until a more severe angular displacement is applied to the foil.

A relatively good agreement may be seen between the predicted cavitation patterns and experimental data by Leroux *et al.* for dynamics 1. A single cavitation cycle may be seen to start with the growth of a sheet, followed by the passing of a re-entrant jet and shedding of a prominent cloud. This then gets shed downstream while a new sheet begins to grow, but this process gets stopped by the collapse of the downstream cloud that induces high pressure. Hence, the new sheet growth may only really start when no cloud cavitation is present. The only major discrepancy seen is the very intermittent cavity occurring soon after the passing of the re-entrant jet. This is most likely caused by the source terms of the cavitation model not responding fast enough to the rapid change in the flow and hence causing cavitation inception over a large volume where there should be none.

The qualitative comparison of flow patterns shown in Figure 8.4 indicates that the currently used model yields similar behaviour to the reference data, although it predicts it to happen at a much lower frequency and only begins to capture the physics involved when

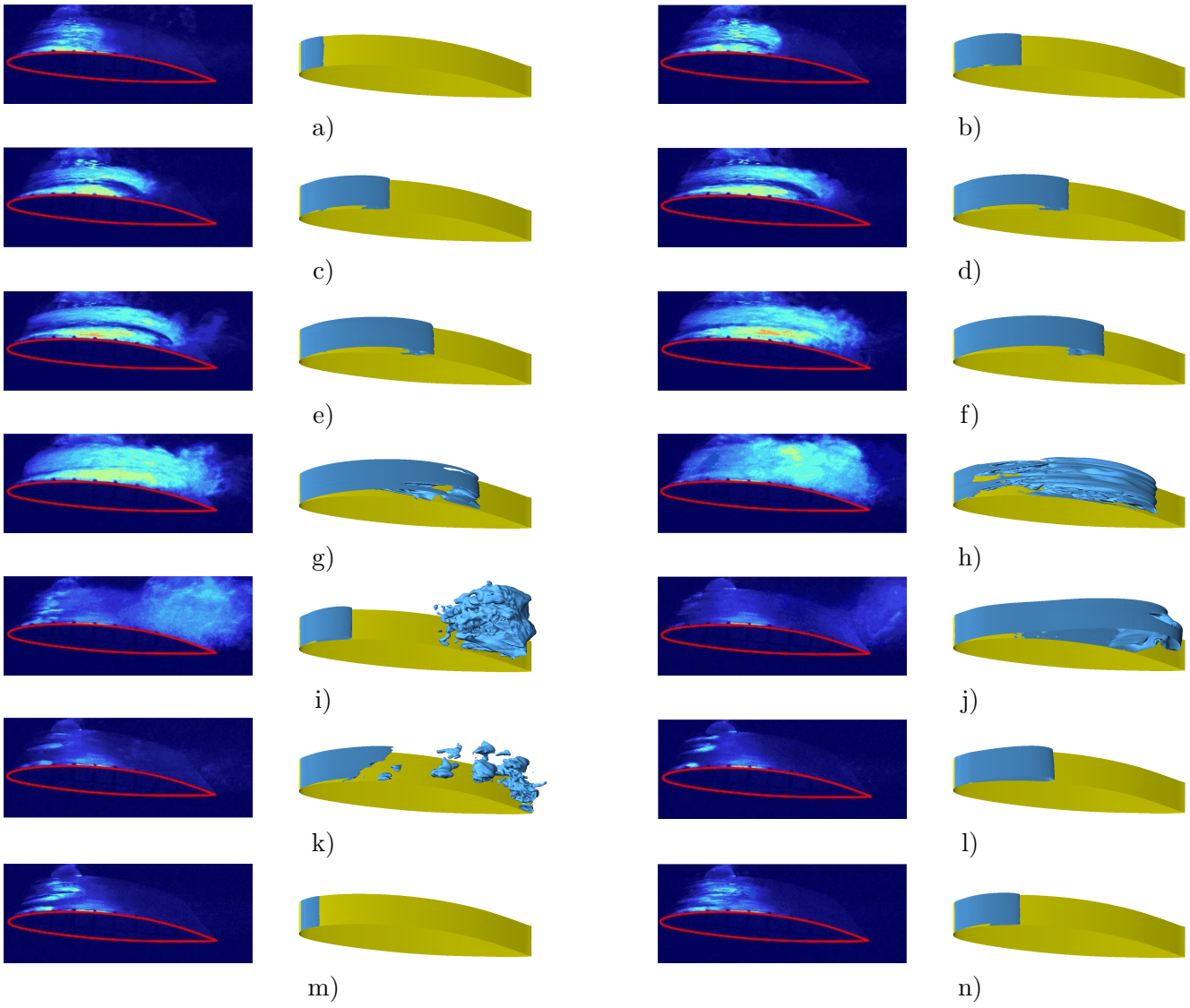

Figure 8.3: Snapshots of the experimental and computational cavity extents for NACA 66 - cavitation dynamics 1. Snapshots spaced evenly across a single cavitation cycle.

faced with much stronger pressure gradients. This corroborates the earlier observations made on the basis of frequency and time-series analyses.

8.4.2 Flow details for dynamics 1

Good comparison has been observed between the current results and experimental data at the dynamics 1 condition so far. This allows a more detailed investigation of the flow field data to be carried out. Firstly, Figure 8.5 presents the time history of lift-to-drag ratio on the hydrofoil. One may note the effect of the 3.5 Hz shedding frequency clearly.

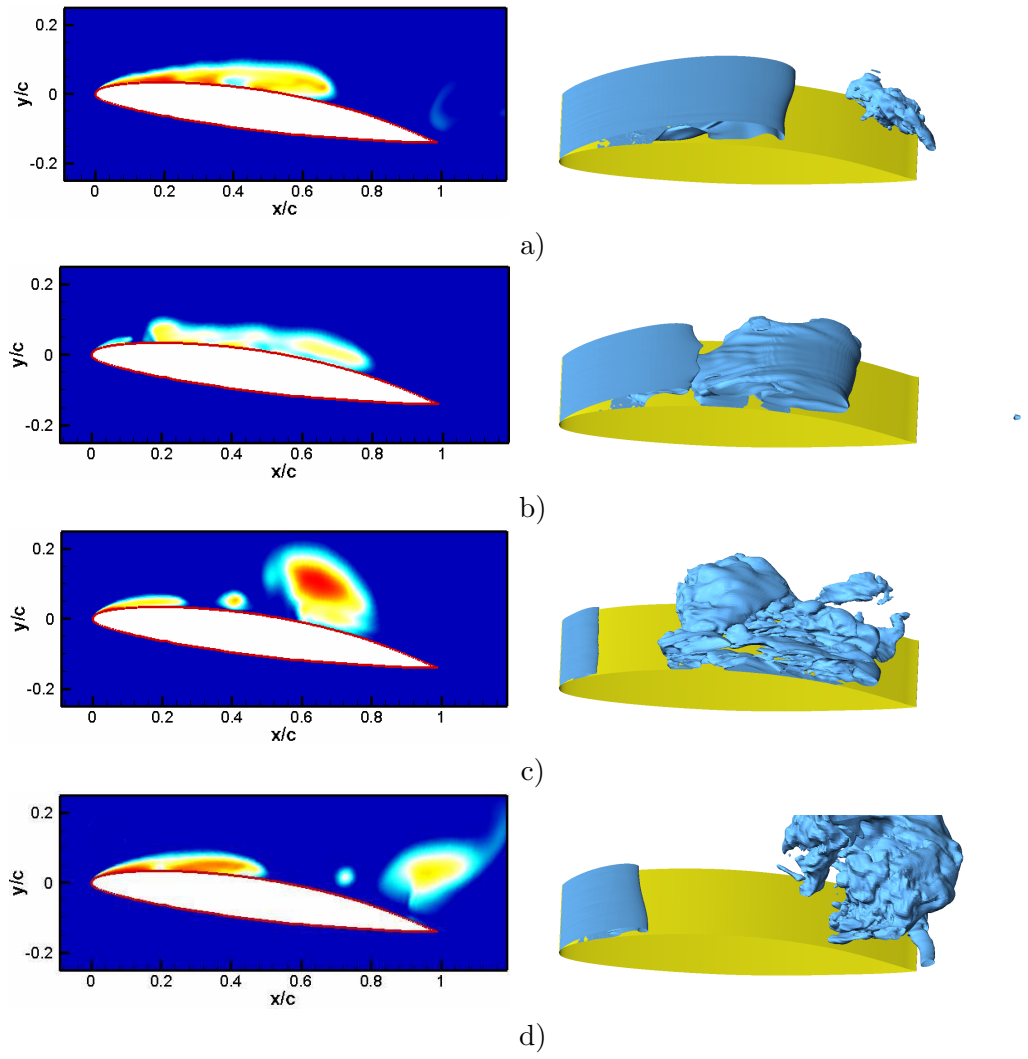

Figure 8.4: Snapshots of the cavity extents for NACA 66 - cavitation dynamics 2, also showing comparison with the numerical data obtained by Seo & Lele [175] (present CFD data plotted at 9 degrees while the reference CFD data are at 8 degrees). Snapshots span across a single cavitation cycle in both cases, although the two simulations yielded very different shedding frequencies.

The magnitude of the variations also agrees relatively well with the experiment, where L/D variations of ± 10 around the mean were reported.

Interesting observations may be drawn from Figure 8.6, which presents mean values and standard deviation bands of local volume fraction values and pressure coefficient on the surface of the foil. An immediately visible feature is the high variance of the pressure coefficient, significantly larger than what was predicted for the previously studied Delft Twist 11 and NACA 0009 hydrofoils. The flat part of the C_P curve also extends much further downstream then in the other investigated cases. This is partially due to the roundback shape of the currently considered foil, and also due to the presence of

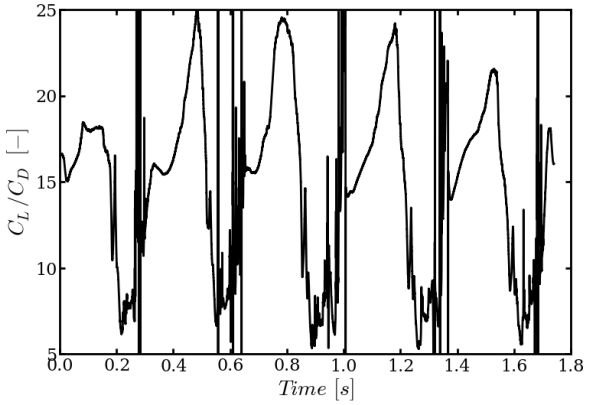

Figure 8.5: Time history of L/D ratio for the dynamics 1 NACA 66 simulation.

large sheet cavities encouraged by the gentle adverse pressure gradient towards the trailing edge of the foil. Notable regions where vapour touches the surface of the foil close to its downstream extent also suggest that the shed clouds impinge on the hydrofoil, which has indeed been seen in the snapshots shown in Figure 8.3.

8.4.3 Cavitation induced pressures for dynamics 1

Figure 8.7 shows the pressures predicted on the surface of the foil using the current simulation, compared to the numerical and experimental data by Leroux *et al.*, who used a compressible RANS solver in their work [117]. Very good agreement may be seen between the present data set and the measurements. Notable features are the regions of quasi-steady local pressure during the periods when attached cavitation is present and when the flow over the measurement point is fully wetted. When the re-entrant jet passes and a cavity cloud is being shed, the local pressure may be seen to experience very unsteady behaviour before it increases and adopts a relatively stable value until the next sheet occurs.

The relationship between the presence of cavitation or lack thereof and local pressure may be better seen in Figure 8.8. It depicts local pressure coefficient at various locations along the chord of the foil over the period of five cavitation cycles. Close to the leading edge small amounts of cavitation persist most of the time and only vanish for intermittent periods when abrupt cavitation collapse occurs in the entire domain. Further downstream cavitation is present for progressively smaller amounts of time and the magnitude of pressure disturbances caused by fluctuations of interface velocities of cavities are increasingly more pronounced.

In the previous chapters the relationship between the second time derivative of the total cavity volume and the associated induced pressure fluctuations has been highlighted

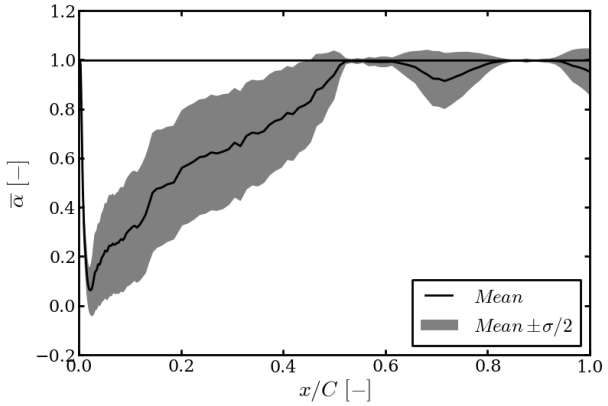

(a) Surface volume fraction values

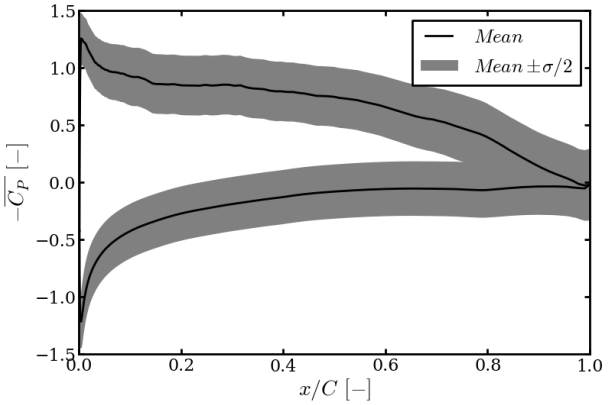

(b) Pressure coefficient

Figure 8.6: Surface distribution of mean flow quantities for the NACA 66 dynamics 1 case, also showing the local unsteadiness of each parameter in the form of standard deviation bands.

based on the Ffowcs Williams-Hawkings acoustic analogy predictions. Figure 8.9 shows $\partial^2 V_C/\partial t^2$ and pressure sampled from the direct CFD solution 2 chord lengths upstream of the hydrofoil leading edge. Dependence of the pressure on the time derivative is readily visible, further reinforcing the previously drawn observations. One may also note how the very abrupt pressure peaks are concentrated in specific periods of time corresponding to violent changes in the amount of cavitation in the numerical domain.

8.4.4 Acoustic analysis for dynamics 1

The main objective of the present study was to investigate how well the FW-H method can cope with being placed close to solid boundaries outside of the source region. Figure 8.10 presents pressure fluctuations upstream of the hydrofoil predicted using both

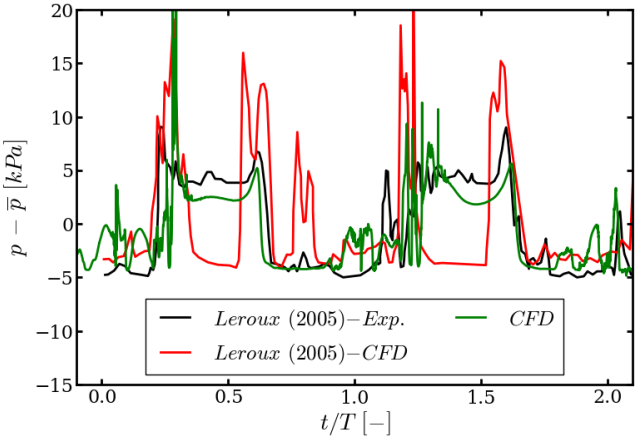

Figure 8.7: Local surface pressure time history at x/c 0.5 on the NACA 66 foil compared to experimental and numerical data by Leroux et al. [117]. Data presented in non-dimensional time to remove the effect of the slightly different shedding frequency predicted in the current simulation. Pressures quoted as the fluctuating component, or p'.

the FW-H method and sampled from the CFD solution directly. The most striking difference between the two signals is the greatly under-predicted amplitude of the induced pressures computed with the acoustic analogy. At the same time, when scaled to the same magnitude both signals show virtually identical time-domain characteristics.

Figure 8.11 presents a FW-H solution to a simplified representation of the current problem, namely an analytical monopole source inside a domain and data surface of identical size to the one used to model the NACA 66. It is known from potential flow theory that solid boundaries act as reflection planes, creating an infinite series of mirror images of the sound source inside the physical domain. In the presented simplified representation only two reflections were included on either side of the domain walls, as shown in Figure 8.12. As may be seen from the acoustic analysis, the FW-H method predicts the pressures induced by the main source very well, as has already been demonstrated in the previous chapters. However, because the mirror images due to reflection planes are outside of the integration surface, their effect is not accounted for and hence the pressure signal amplitude is notably under-predicted.

8.5 Discussion

The most important observation made in the present study has been the direct illustration of the inability of the present implementation of the acoustic analogy to cope with modelling reflections caused by the presence of solid walls close to the cavitating hydrofoil. This problem has not been dealt with or indeed widely mentioned in the open literature, as most authors tend to design their numerical domains to be big enough in

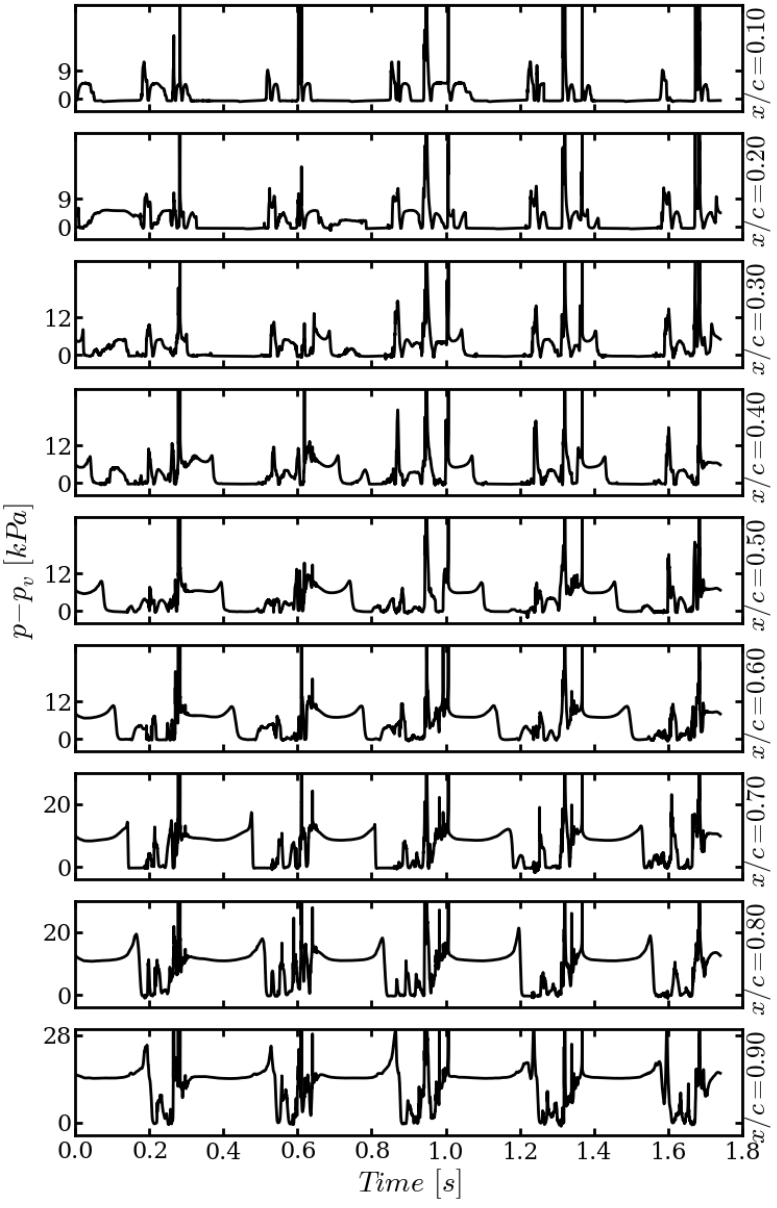

Figure 8.8: Time histories of local pressure on the suction of the NACA 66 foil undergoing dynamics 1 unsteady cavitation. Pressure values shifted to make zero coincide with the saturated vapour pressure.

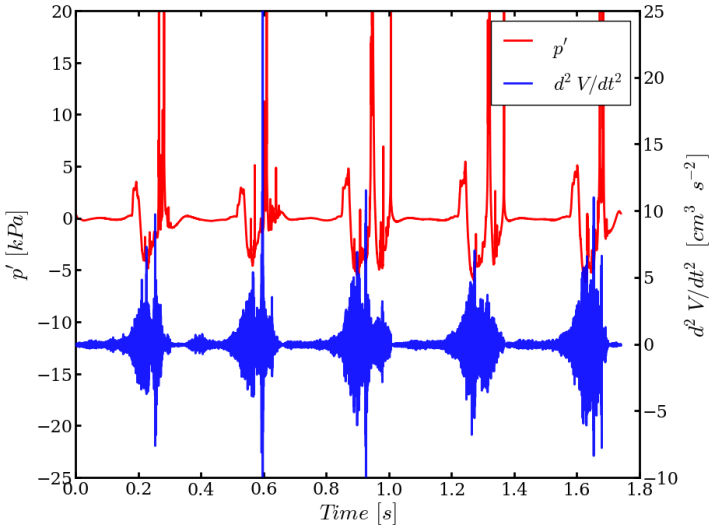

Figure 8.9: Time series of pressure and second derivative of the total cavity volume upstream of the NACA 66 (dynamics 1).

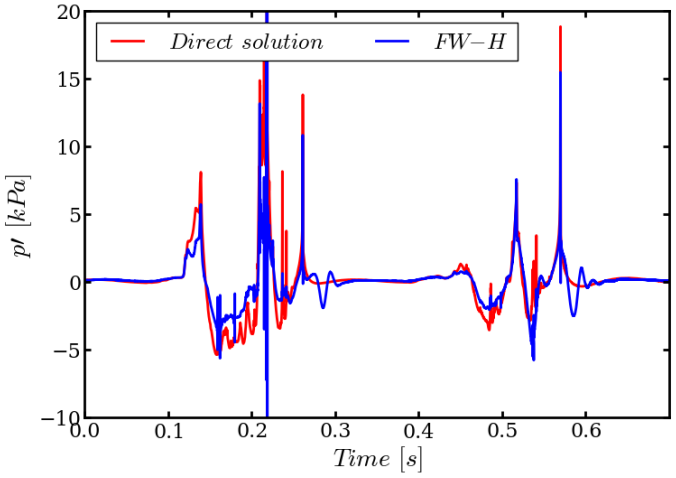

Figure 8.10: Comparison of the FW-H and direct pressures induced by cavitation in front of the NACA 66 (dynamics 1). The FW-H amplitude has been scaled up by a factor of 100.

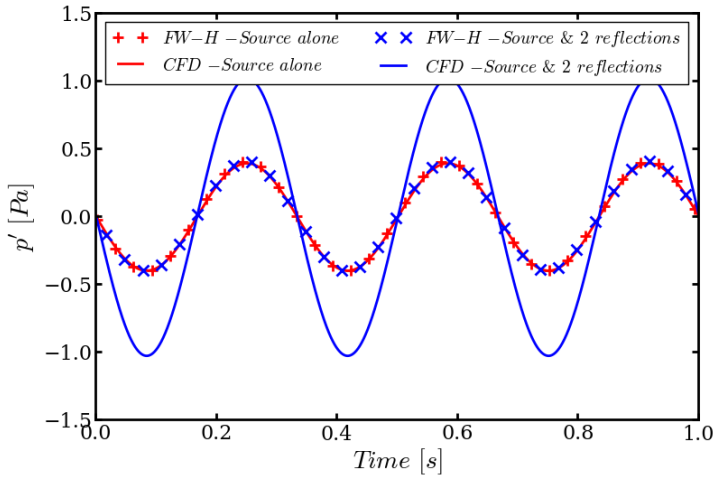

Figure 8.11: FW-H predictions for a monopole source and its reflections. FW-H signals show every 300th data point for clarity.

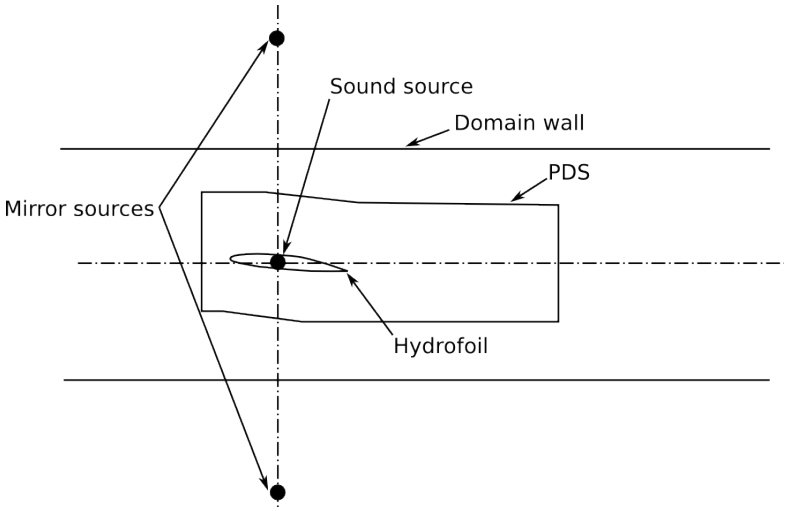

Figure 8.12: Illustration showing the effect of nearby solid walls on an acoustic source (only a single mirror source on the either side of the domain walls shown for brevity).

order to avoid the possibility of reflections [89, 132]. This approach has also been adopted in the earlier simulations presented in this thesis. One of the few works concerned with the effect of the solid boundaries is that by Salvatore [171], who investigated the effect of placing a plate 0.66D away from a propeller. The flow model used by the authors relied on potential flow theory, however, and did not account for the presence of a solid boundary explicitly, and thus the published results are of relatively little relevance here.

While using large numerical domains remains a valid solution to avoid the presented

problems, it excludes the possibility of validating the acoustic predictions against experimental data directly, as the latter will inherently be affected by the presence of solid boundaries. One might attempt to alleviate this by adopting a similar approach as has been undertaken presently, namely validating the cavitation model and the acoustic method independently, and then assembling the two methods together to make far-field predictions. An alternative would be to re-write the Green's function integrals used to derive the FW-H in such a way as to account for the series of reflections, or to devise a way to mirror the flow field data appropriately to mimic the effect of the solid boundaries.

Another relevant finding of the current investigation was the substantial inaccuracy of the mass-transfer cavitation model in capturing transition of cavitation from dynamics 1 to dynamics 2. This has not been previously reported by other authors for the currently used type of model, as the only published works concerned with both dynamics 1 and 2 have relied on compressible solvers [117, 175]. Authors employing incompressible approaches have typically restricted themselves to modelling the dynamics 1 condition only [99, 104].

This is a particularly important observation as it indicates that certain physics are omitted in the current approach but in a way which does not manifest itself in an obvious manner, unless when direct comparison with experimental data is available. This implies that even if the numerical set up is validated on certain test cases, such as the commonly used Delft Twist 11 foil, it may not remain valid as the flow conditions change by a relatively small amount. Such behaviour of the model may thus lead to substantial discrepancies as authors aim to expand the envelope of the predictions they make beyond what is covered by the experimental data.

At the same time, the flow behaviour predicted for dynamics 1 has stood in appreciably good agreement with the experiments. The computed cavitation patterns, variations in the lift-to-drag ratio, as well as the pressures on the surface of the foil matched the measurements by Leroux *et al.* closely. The use of a three-dimensional domain and advanced turbulence modelling has allowed a wide range of detailed flow features to be predicted and the dynamic cavitation behaviour to be captured well. As in the experimental data by Leroux *et al.*, the computed cavitation behaviour has been shown to first follow the typical sheet growth and cloud shedding, after which the cavities collapsing downstream inhibit growth of a new sheet until there is nearly no cavitation present in the entire numerical domain.

8.6 Summary

The present simulations have shown mixed results. On the one hand, the predictions made for the dynamics 1 case agreed very well with the experiments, but on the other

the presently used cavitation model struggled to capture the mechanisms involved in the dynamics 2 scenario. This highlights that the topic of cavitation modelling remains open for novel research, particularly from the point of view of including the effects of compressibility and refining the vaporisation and condensation modelling approaches. The Ffowcs Williams-Hawkings acoustic analogy has been shown to be incapable of accounting for the reflections caused by nearby solid boundaries, which had been expected from the way it is formulated. This does, however, indicate that special care must be taken when designing computational meshes to be used for acoustic predictions, especially if comparison to cavitation tunnel experiments is to be made. A major drawback of the presented method stems from its inability to account for the broadband noise contribution of small-scale bubbles, which cannot be accurately modelled using the volume of fluid approach on a standard CFD grid, but which play a significant role in the cavitation processes involved. These bubbles are not expected to drive the peak sound pressure levels at low frequencies, but have been reported in the literature to be the dominant noise source at medium and high frequencies in certain conditions. It has therefore been decided to further refine the present numerical framework to allow the behaviour of smaller-scale cavitation bubbles to be accounted for, which is addressed in the following Chapter.

Chapter 9

Multi-scale cavitation modelling

9.1 Introduction

The data presented in the Chapters until now has shown that the initially proposed methodology based on the Schnerr-Sauer mass transfer cavitation model, advanced turbulence modelling by means of LES or DES, and the Ffowcs Williams-Hawkings acoustic analogy, is capable of predicting the large-scale flow features induced by cavitation and the associated radiated pressures. However, it has been also demonstrated to be unable to resolve the large amounts of small scale bubbles present in the real flow unless very fine mesh resolutions are employed. Even then, the current model would struggle to accurately represent the final collapse stages of the bubbles due to it invoking fluid incompressibility. Finally, while the action of the small bubbles on the general flow may be represented with satisfactory accuracy through the solution of the volume of fluid transport equation, this approach is insufficient to describe the important acoustic contribution of the small-scale cavitation bubbles at medium and high frequencies.

For these reasons, the next stage of the project focused developing a hybrid cavitation model that would utilise the methodology introduced so far in order to model large cavities and a Lagrangian bubble tracking model in order to resolve the convecting clouds composed of small bubbles. Hybrid cavitation models are not a completely novel concept, but have been mainly used to study erosion rather than far-field noise [80, 196, 206]. In this Chapter, first a description of the exact theory behind the developed model is given and the undertaken implementation is outlined. Then, several verification studies are introduced, focusing on assessing the accuracy of the individual components of the model. Finally, the complete model is applied to the Delft Twist 11 hydrofoil test case, first introduced in Chapter 6, in order to provide basic validation and demonstrate the capability of the method.

9.2 Theory behind mixed Eulerian-Lagrangian modelling

9.2.1 Bubble motion

The basic idea behind a hybrid Lagrangian-Eulerian cavitation model is to use the volume of fluid approach in order to model large-scale cavities but switch to treating them in the Lagrangian mode once they become too small to be accurately captured on the Eulerian grid. The latter involves tracking the bubbles in space based on their equation of motion,

$$m_B \frac{\mathrm{d}\mathbf{U}_B}{\mathrm{d}t} = \mathbf{F}_a + \mathbf{F}_p + \mathbf{F}_{buoy} + \mathbf{F}_{drag} + \mathbf{F}_{lift}, \tag{9.1}$$

where m_B is the mass of a bubble with radius R and density ρ_B, $\mathbf{U}_B$ is the velocity of the centre of mass of the bubble located at $\mathbf{x}_B$, and $\mathbf{F}$ are individual force components. These correspond to

$$Added\,mass: \qquad \mathbf{F}_a = \frac{1}{2}\rho\frac{m_B}{\rho_B}\left(\frac{\mathrm{D}\mathbf{U}}{\mathrm{D}t} - \frac{\mathrm{d}\mathbf{U}_B}{\mathrm{d}t}\right), \tag{9.2a}$$

$$Pressure\,gradient: \qquad \mathbf{F}_p = -\frac{m_B}{\rho_B}\nabla p, \tag{9.2b}$$

$$Buoyancy: \qquad \mathbf{F}_{buoy} = m_B\left(1 - \frac{\rho}{\rho_B}\right)\mathbf{g}, \tag{9.2c}$$

$$Drag: \qquad \mathbf{F}_{drag} = C_D\rho\frac{m_B}{\rho_B}\frac{3}{8R}(\mathbf{U} - \mathbf{U}_B)\left|\mathbf{U} - \mathbf{U}_B\right|, \tag{9.2d}$$

$$Lift: \qquad \mathbf{F}_{lift} = C_L\frac{m_B}{\rho_B}(\mathbf{U} - \mathbf{U}_B) \times \omega, \tag{9.2e}$$

where ω is the vorticity and ρ is the density of the liquid surrounding the bubble [80, 153, 196, 206]. The lift coefficient, C_L, is assumed to be constant and equal to 0.5, and the drag coefficient may be computed as a function of the Reynolds number of the bubble,

$$Re_B = 2\left|\mathbf{U} - \mathbf{U_B}\right| R/\nu, \tag{9.3}$$

as [196]

$$C_D = 24.0/Re_B(1 + 0.15Re_B^{0.687}). \tag{9.4}$$

During its lifetime, a Lagrangian bubble experiences external pressure variations which affect its radius. This is governed by the Rayleigh-Plesset equation [158],

$$R\ddot{R} + \frac{3}{2}\left(\dot{R}\right)^2 = \frac{1}{\rho}\left(p_B - p_{ext} - \frac{2\sigma_{st}}{R} - \frac{4\mu}{R}\dot{R}\right), \tag{9.5}$$

where the term p_B refers to the pressure inside the bubble consisting of the sum of the saturated vapour pressure, p_v, and the local gas pressure, p_g. R is the bubble radius, σ_{st} is the surface tension of the vapour and μ is its dynamic viscosity. p_{ext} is the pressure of

fluid acting on the bubble, which is assumed to be equal to the pressure at the bubble centre, in accordance with classical Lagrangian theory. A more accurate representation would be to compute average pressure over the bubble surface [36], although this would result in an increased cost and code complexity and so is not done in the present model.

In order to account for the effect of compressibility of the gas enclosed inside the bubble, the perfect gas relationship,

$$p_B = p_v + p_{g0}\left(\frac{R_0}{R}\right)^{3k}, \tag{9.6}$$

is used. In the above, p_{g0} is the equilibrium gas pressure in the bubble, R_0 and R are the equilibrium and current bubble radii, respectively, and k is the polytropic compression constant [80, 206]. The latter is assumed equal to 1.4 as for air undergoing an adiabatic process, which is more suitable for describing the bubble physics during collapse [21]. For the growth phase assuming an isothermal process with $k = 1$ is more appropriate [21].

As the bubble enters the collapse phase, which is detected as a high inwards velocity consistent over several consecutive integration time steps, liquid compressibility becomes important to the bubble physics. This gives rise to an alternative form of the Rayleigh-Plesset equation,

$$\begin{aligned} R\ddot{R}\left[1-(1+\delta)\frac{\dot{R}}{c_0}\right] + \frac{3}{2}\dot{R}\left(\frac{4-\delta}{3} - \frac{4}{3}\frac{\dot{R}}{c_0}\right) = \\ \frac{1}{\rho}\left[p_v - p_{ext} - \frac{2\sigma_{st}}{R} + p_g m\left(\frac{R_{max}}{R}\right)^{3k}\right] \\ + \frac{1}{\rho}\left[-3kp_{gm}\left(\frac{R_{max}}{R}\right)^{3k} + \frac{2\sigma_{st}}{R^2}\dot{R}\right], \end{aligned} \tag{9.7}$$

expressed using the maximum radius, R_{max}, and the corresponding non-condensable gas pressure, p_{gm}, while neglecting the effect of viscosity [186, 192]. In the above, $\delta = \rho_g/\rho \approx 0.99882$ is a function of the gas density under atmospheric conditions and water density, while c_0 is the speed of sound in water. It should be noted that Equation (9.7) reduces to Eq. (9.5) if one assumes $c_0 \to \infty$ and $\delta \to 1$.

As each bubble undergoes oscillation of its radius, it induces pressure fluctuations. At an arbitrary point $\mathbf{x}$ these may be described for a bubble at $\mathbf{y}$ as [22, 83]

$$p\left(\mathbf{x}, t + \frac{c_0}{|\mathbf{x}-\mathbf{y}|}\right) = \frac{\rho}{|\mathbf{x}-\mathbf{y}|}\left(R^2\ddot{R} + 2R\dot{R}^2\right). \tag{9.8}$$

In order to arrive at a total pressure due to all the bubbles inside the numerical domain, each of their individual pressure signals must be interpolated onto a separate time axis

corresponding to the receiver time, similarly as in the case of accounting for the retarded time in acoustic analogy formulations discussed in Chapter 5.

As a new Lagrangian bubble is created, it is assumed to adopt an equilibrium pressure, p_{g0}, and radius, R_0, when subject to the outlet pressure, p_∞. Furthermore, it is assumed that at the moment of creation the bubble is also in equilibrium under its current p_{ext} [196]. These two assumptions give rise an equilibrium relationship,

$$\left(p_\infty - p_v\frac{2\sigma_{st}}{R_0}\right)\left(\frac{R_0}{R_{initial}}\right)^{3k} + p_v - \frac{2\sigma_{st}}{R_{initial}} - p_{ext} = 0, \tag{9.9}$$

which may be rearranged into a polynomial form and solved for the only unknown, R_0. This is then used to determine p_{g0} in accordance with ideal gas law in Equation (9.6) [196].

In order not to invalidate momentum conservation, the momentum the bubble exerts on the liquid should be accounted for in the form of a source term, thus providing two-way coupling [191]. This is done by calculating the momentum change of a bubble as it crosses a particular cell,

$$\Delta\mathbf{S}_B = -\frac{\Delta\mathbf{U}_B m_B}{V_i \Delta t}, \tag{9.10}$$

where V_i is the volume of the i-th cell, Δt is the time it takes the bubble to cross this cells, and $\Delta\mathbf{U}_B$ is the speed lost or gained by the bubble, and m_B is the bubble mass. Thus, by summing contributions of all bubbles crossing the cell, the total value of the momentum source, $\mathbf{S}_B$, to be added to the right-hand side of the Navier-Stokes equation, Eq. (3.5b), can be computed. In order to avoid invalidating the Lagrangian theory when a bubble becomes larger than the underlying mesh, it is more appropriate to spread its momentum across all cells within its zone of influence [196]. This is done by adopting a kernel function defined around the bubble centroid, $\mathbf{x}_B$,

$$K = (2\pi)^{\frac{-3}{2}} \exp\left(-\frac{1}{2}\left[\frac{|\mathbf{x} - \mathbf{x}_B|}{R}\right]^2\right), \tag{9.11}$$

as introduced by Vallier [196]. This leads to the momentum source being distributed in a smooth manner in such a way that most of its momentum is added to the cells within the distance of three radii away from the centroid. Hence, multiplying Equation (9.10) with the kernel value yields the contribution of an individual bubble to the momentum source field.

9.2.2 Eulerian cavity reconstruction

A critical step in the present model is determination where individual Lagrangian bubbles should be added. This first requires coherent cavitation structures to be reconstructed from the volume fraction field. The algorithm is depicted in Figure 9.1.

It starts by first identifying all cells with liquid volume fraction $\alpha < \alpha_{threshold}$, where the threshold value of 0.8 is used. Setting too low a value would limit the number of particles being created but setting it too high could cause blending of the Eulerian bubble interfaces. Once all vapour cells have been marked, one of them is selected at random and then a check is performed to establish if any of its neighbours are also filled with vapour. If yes, they are identified as a part of the same bubble. The process continues until no more cells may be added to the current bubble, at which point the next unassigned cell from the top list is chosen as a new starting point. The process continues until no more unassigned vapour cells exist in each subprocess domain. This is termed the flood-fill algorithm [196].

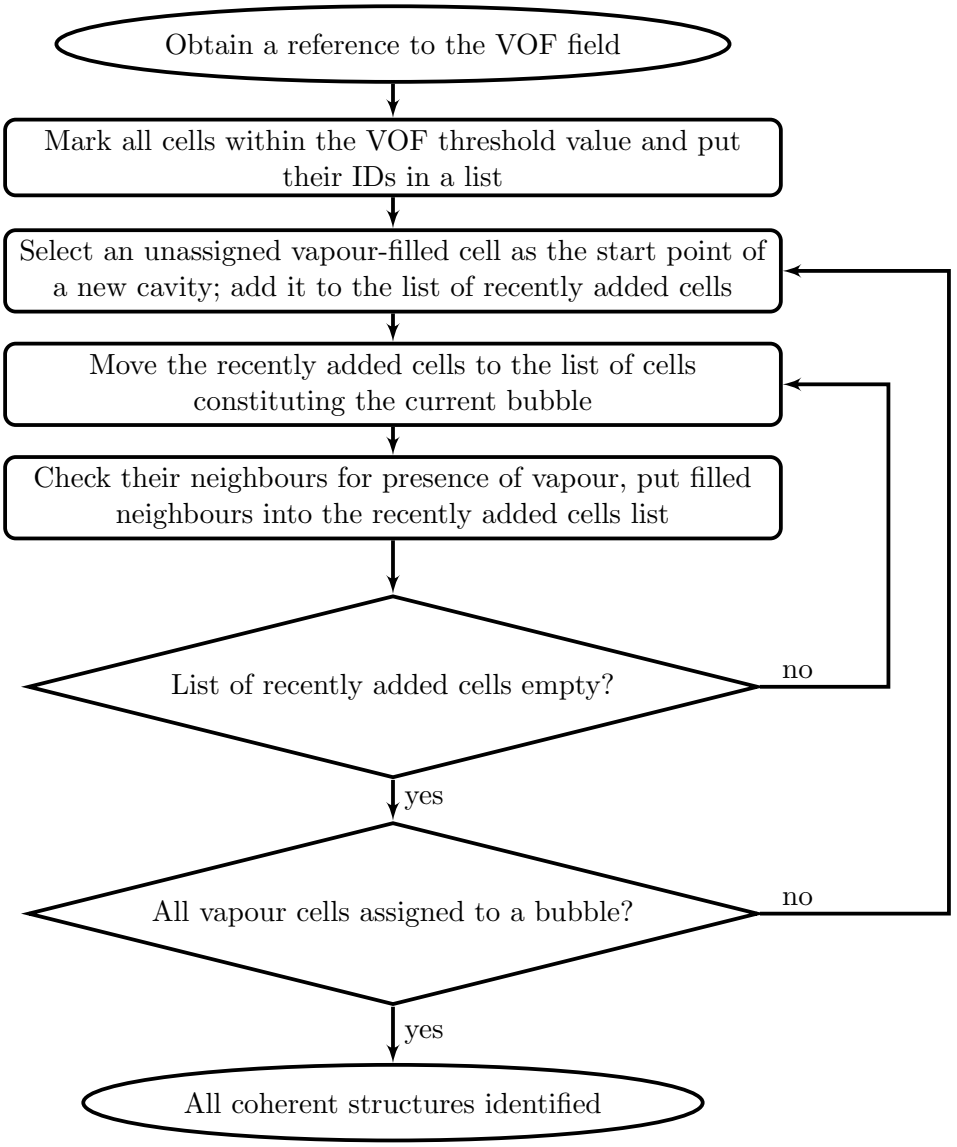

Figure 9.1: Principle of operation of the cavity reconstruction algorithm.

In order to enable parallel computation, the bubble connectivity information between

each subdomain must be exchanged, as shown in Figure 9.2. This is done by first identifying each local bubble lying on the edge of the subdomain, denoted as a processor patch in OpenFOAM terminology and noting which processor it neighbours with. This gives rise to a list of tuples of local bubble identifiers and processor numbers they neighbour with and a list face identifiers for each candidate neighbour bubble. The lists are then gathered and scattered across all processes. Each individual processor then sorts through them and looks for bubbles in other domains which may potentially connect to its own cavity structures. For each of them, it compares the face identifiers of own candidate bubbles with those of cavities on the neighbouring domains. As soon as a match is found the two bubbles are marked as connected and this information is stored. This is a major improvement introduced in the present work with respect to the model proposed by Vallier [196], as it allows massive parallel computations to be carried out without the model assumptions being invalidated.

Once individual connectivity for all bubbles has been established, the information is exchanged again. At this stage properties of each of the subdomain bubbles, such as centroid, volume and speed,

$$
\begin{aligned}
V_B &= \sum_{I}^{N_B} (1-\alpha_I) V_{cell,I}, \\
\overline{\mathbf{x}}_B &= \frac{1}{V_B} \sum_{I}^{N_B} \mathbf{x}_{cell,I} (1-\alpha_I) V_{cell,I}, \\
\mathbf{U}_B &= \frac{1}{V_B} \sum_{I}^{N_B} \mathbf{U}_I (1-\alpha_I) V_{cell,I},
\end{aligned}
\tag{9.12}
$$

may be added together to get a global picture. This yields a series of lists which allow net bubble properties to be associated with unique identifiers, shown in Figure 9.3 for an example time step of the present simulation.

9.2.3 Bubble transfer between Eulerian and Lagrangian frames

Once coherent Eulerian cavities have been identified, the algorithm must decide under what circumstances they are to be transferred to the Lagrangian phase. This is done following an approach similar to Vallier [196] and Tomar *et al.* [191], where the bubbles were moved to the Lagrangian frame if the number of cells constituting them was less than a given threshold N_{EL}, assumed equal to 15 in the present study. A second criterion has also been added which compares the physical size of the bubble, taken as cube root of the total volume of cells across which it spans, $R_{swept} = (\sum_I^{N_B} V_{cell,I})^{1/3}$, to the mean grid size inside the bubble. If this satisfies $R_{swept}/\Delta_{mean} < 3$, as well as $N_B < N_{EL}$, then the bubble is added to the Lagrangian frame. This is viewed as more physical

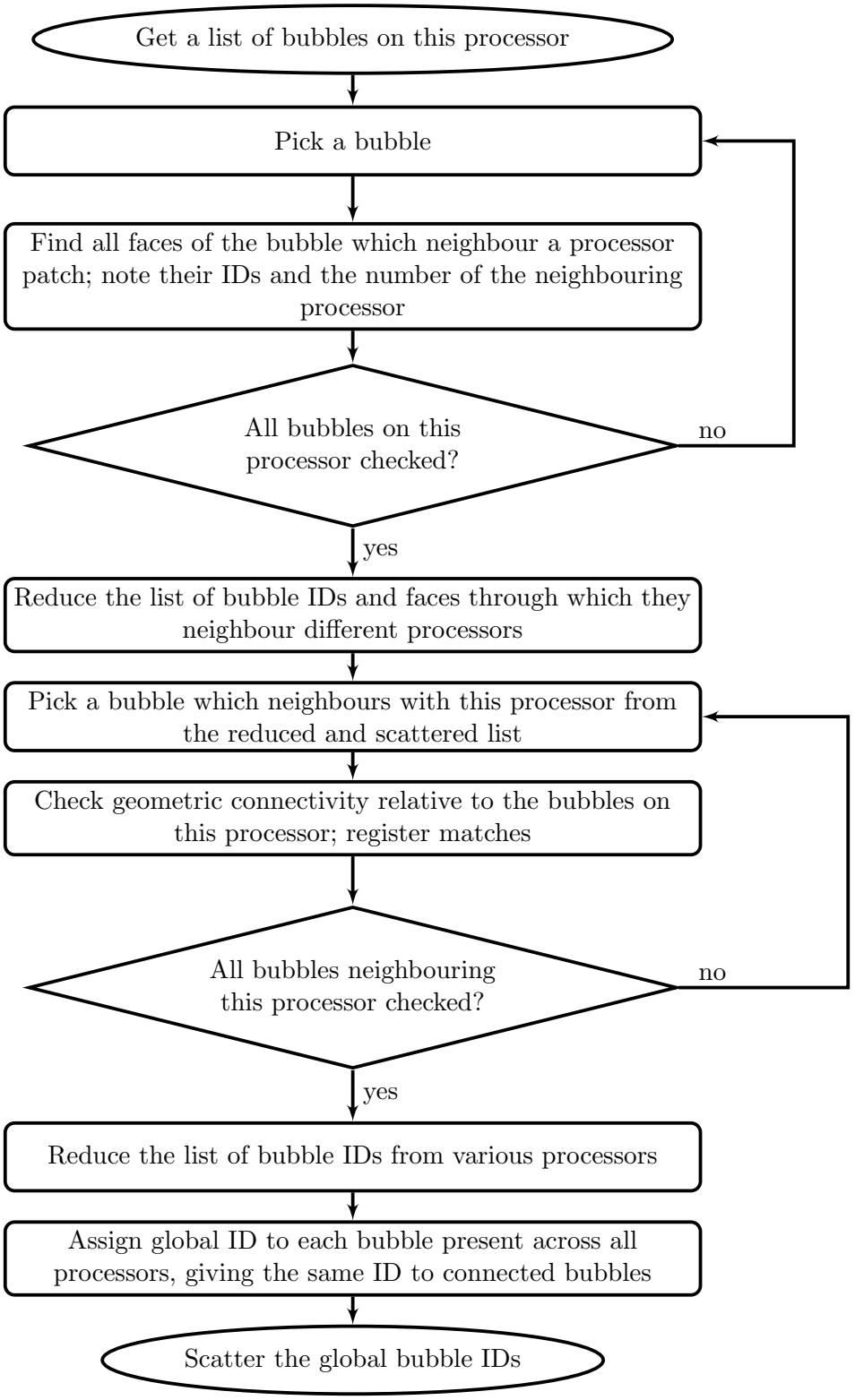

Figure 9.2: Parallel data exchange strategy for the cavity reconstruction algorithm.

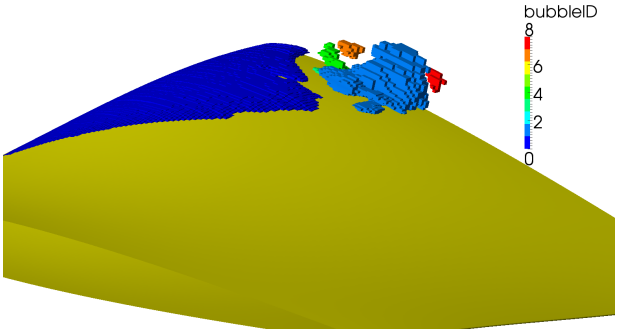

Figure 9.3: Example of cavities identified by the interface reconstruction algorithm during a simulation of the Delft Twist 11 hydrofoil with 128 processors.

as it moves the algorithm to being grid-independent. Following the transfer, the liquid fraction in the cells the bubble used to occupy is set to 1.

An inverse process is also allowed, where a Lagrangian bubble growing to above a certain threshold size is deleted and instead replaced with a vapour pocket in the Eulerian frame. This is done by inverting the criteria for the Eulerian-to-Lagranian transfer with a suitable margin allowing the newly added bubbles to grow and preventing the transfers from taking place too often. The same process is also applied when a bubble becomes trapped in a large Eulerian cavity. In practice, the latter process has been found to occur more frequently for bubbles created around dynamically deforming sheet and cloud cavities around the leading edges, where the likelihood of a bubble impacting on the interface of a larger cavity is much higher.

A critical issue with *ad hoc* modifications to the vapour fraction in this manner is the possible invalidation of the continuity equation. As a bubble is added or removed from the volume fraction field, its mass is effectively transferred or removed from the Lagrangian frame of reference and the inverse is true for the Eulerian simulation. Thus, a more suitable approach would be to compute the volume fraction of the Lagrangian bubbles, and include them in the volume fraction computed from the scalar convection equation, $\alpha_{Eulerian}$, as

$$\alpha = \alpha_{Eulerian} + \alpha_{nuclei} + \alpha_{Lagrangian}. \tag{9.13}$$

In this manner, no mass would be created or destroyed, irrespective of whether a particular amount of vapour would be accounted for in the Eulerian or Lagrangian frames. This issue did not affect the present simulations significantly, given the relatively small size of the Lagrangian bubbles considered. However, future versions of the model should implement the aforementioned improvement in order to avoid unnecessary inaccuracies.

9.3 Present implementation

9.3.1 Implementation strategy

The fundamental idea of the hybrid model is to first identify where, if at all, Lagrangian bubbles are to be introduced or deleted, which is done by executing the interface reconstruction algorithm and then comparing the properties of the present cavities with the transfer criteria. The deletion process simply removes the given bubble from the list storing all other bubble instances and adds to the vapour fraction field in the occupied cells. Addition of a new Lagrangian bubble first requires the initialisation step, described by Equation (9.9), to be undertaken. The bubble is then added to the main list.

The following step is the solving the coupled advection and radial displacement problem for each Lagrangian bubble, in accordance with Equations (9.1) and either (9.5) or (9.7). For the Rayleigh-Plesset equations, this is done by writing out a derivative vector of form $[\ddot{R}, \dot{R}]$ and integrating using the 4^{th}-order Runge-Kutta method with adjustable time step. For the convection equation, an approach discussed by Nordin [153] is followed, whereby the terms involving the continuous liquid phase are treated explicitly and implicit treatment is applied to the quantities associated with the bubble. This yields an expression which is then integrated using the Euler method.

The aforementioned steps are added as an additional stage of the outer loop of the baseline CFD solver, in this case `interPhaseChangeFoam`. The code may be integrated into almost any solver with the only major modification being the inclusions of the momentum source used to implement the two-way coupling.

9.3.2 Code organisation

OpenFOAM ships with a basic Lagrangian library that allows solid particles to be advected by the flow. This was used as a baseline for the present implementation, as it contained a number of useful classes and methods that the current solver derives from. The current solver, termed `interPhaseChangeBubbleFoam`, is divided into the following segments.

- **Core solver** - basic `interPhaseChangeFoam` solver with an added momentum source representing the two-way coupling with the Lagrangian bubbles. The solver follows the basic multiphase solver, `itnerFoam`, except it includes source terms in the volume fraction and pressure equations representing the evaporation and condensation terms delivered by the mass transfer model.

- **Mass transfer model** - this library, called `phaseChangeTwoPhaseBubbleMixtures`, implements the mass transfer cavitation model and is largely the same as the built-in OpenFOAM implementation under the name `phaseChangeTwoPhaseMixtures`.
- **Lagrangian phase solver** - this contains the main implementation of all the functionality of the hybrid solver implemented as the `bubbleParticles` library. This includes two major class definitions.
  - `bubbleParticle` - contains information and methods used to describe the physics of an individual Lagrangian bubble. The class is derived from the OpenFOAM-native `solidParticle`, which handles issues such as transfer between processors. Newly added members include implementation of the Runge-Kutta solver for the Rayleigh-Plesset equation, customised data output allowing time-series post-processing of the history of individual bubbles, modified equation of motion, initialisation of the bubble radius, and identification of the cells inside the sphere of influence of the bubble.
  - `bubbleParticleCloud` - derived from the base `solidParticleCloud` class definition and describes everything to do with a multiplicity of bubbles. It provides an interface to access the core flow solver fields from the individual bubble level, holds top-level control parameters, such as bubble properties contained in the `constant/bubbleProperties` dictionary, implements the interface reconstruction, bubble creation and destruction algorithms, and the two-way coupling via a momentum source.

It can be seen that the code follows suit with the OpenFOAM object-oriented programming strategy, which allows it to be modular and easily interfaced with the baseline flow solver. Thanks to this, it is straightforward to parallelise, as the physics of each bubble are solved by the processor it currently occupies. If the bubble crosses a processor patch, the responsibility for it is simply transferred to the neighbouring process. This also holds for output of the data describing the trajectory of the bubble. A disadvantage of this approach is the difficulty and relatively high communication cost associated with gathering data about all bubbles present in the simulation at any one time.

9.4 Verification

Following the implementation of the model, it was necessary to verify each of its segments - the solution of the Rayleigh-Plesset equation, transport of Lagrangian bubbles, and transfer of bubbles from Eulerian to Lagrangian frame and vice versa. The first step was verified by placing a single bubble in a quiescent fluid and subjecting it to known pressure excitations using a similar solver as the one to simulate ideal acoustic sources described in Chapter 5. Three different cases were considered - numerical one presented

by Vallier et al. [195], experimental by Ohl *et al.* [154], and numerical by Hilgenfeldt *et al.* [76] The former considered a linearly varying pressure and the latter two employed a sinusoidal excitation. A summary of the parameters used is given in Table 9.1.

The results for each of the three cases are presented in Figure 9.4. It may be seen that in all of the simulations the present and reference data agreed relatively well. Both the magnitudes and phases of the maximum radii are predicted accurately. Importantly, the signals following the bubble collapse, which will be responsible for the generation of radiated pressures, agree well with the validation data. Thus, the Rayleigh-Plesset solver may be considered accurate enough for the purpose of implementing a hybrid Eulerian-Lagrangian cavitation solver.

Table 9.1: Parameters describing idealised bubble simulations used to test the Rayleigh-Plesset equation solver for a range of cases by Vallier, Ohl *et al.*, and Hilgenfeldt *et al.* [76, 154, 195].

Parameter	**Vallier**	**Ohl**	**Hilgenfeldt**	**Unit**
Sinusoidal pressure ampl.	0	132000	141855	Pa
Sinusoidal pressure mean	0	100000	101325	Pa
Sinusoidal pressure freq.	0	21400	26500	Hz
Linear pressure change amp.	-18600	0	0	Pa
Linear pressure change time	$1.2{\cdot}10^{-4}$	0	0	s
Liquid visc., ν_l	$1{\cdot}10^{-6}$	$6{\cdot}10^{-6}$	$1{\cdot}10^{-6}$	$m^2\ s^{-1}$
Bubble visc., ν_B	$1.48{\cdot}10^{-5}$	$1.48{\cdot}10^{-5}$	$1.48{\cdot}10^{-5}$	$m^2\ s^{-1}$
Liquid density, ρ_l	1000	1000	1000	$kg^2\ m^{-3}$
Bubble density, ρ_B	0.023	0.023	0.023	$kg^2\ m^{-3}$
Surface tension, σ	0.0717	0.07	0.0728	$kg\ s^{-2}$

The interface reconstruction algorithm has been verified by execution on pre-computed flow field data for the Delft Twist 11 hydrofoil in single-threaded and parallel modes. The results were analogous to the already presented Figure 9.3 and have therefore shown the algorithm to function correctly. This set up was also used to verify the functionality of the bubble addition and removal methods, as well as the initial tuning of the criteria used to transfer the bubbles between the Eulerian and Lagrangian phases.

The convection of individual bubbles was tested by injecting a fixed amount of particles at a pre-determined location in a 2D diffuser geometry. The simulation was initialised using a RANS solutions and the injection point was placed to coincide with a streamline dividing the recirculation zone from the bulk of the flow. The result, shown in Figure 9.4, was the bubbles being convected along the streamline, as expected. This simulation was also used to verify parallel data exchange algorithms by subdividing the diffuser into several sub-domains along the axis of the flow. By controlling the outlet pressure, the response of the radius of the bubbles to slowly varying external pressures and the initialisation algorithm could also be verified.

Based on the aforementioned results, the individual elements of the hybrid solver were confirmed to function propely and, in the case of the Rayleigh-Plesset solver, validated. The next stage involved running a 2D variant of the NACA 0009 case, considered in the previous chapters, in order to ensure no obstacles existed at the interfaces of the inividual methods. These were encountered mainly in the parts of the code responsible for removal of the Eulerian cavities, but were alleviated by re-designing the designed code objects. Thus, the model became fully functional.

9.5 Application to the Delft Twist 11 hydrofoil

9.5.1 Aims of this study

Once the basic verification of the hybrid model was complete, it was necessary to apply it to a realistic test case and, as far as possible, compare the results to the available experimental data. Unfortunately, direct measurements of small, dispersed bubbles for representative geometries are, to the author's knowledge, not currently available in the open literature. Therefore, photographs of cavitation patterns had to be relied upon instead, and hence the validation was more qualitative than quantitiative in nature.

The proposed simulation utilised the Delft Twist 11 hydrofoil test case, first introduced in Chapter 6. Two main aims included comparing the predicted cavitation patterns to the experimental observations and identifying any changes with respect to the data obtained with the original model. Furthermore, pressure fluctuations induced by the large-scale Eulerian cavities were monitored at the wall of the numerical domain to simulate readings of pressure transducers in a cavitation tunnel. The data from the baseline Eulerian-only model were then compared with the hybrid model results and the effect of the small-scale bubbles was assessed.

9.5.2 Simulation set-up

No changes were made to the original set up from Chapter 6, except the simulation was now re-started from the final time step using the newly developed hybrid model. Moreover, six pressure probes were placed at the numerical domain wall directly above the foil centreline in order to monitor unsteady pressure fluctuations induced by the oscillating cavities. Their chord-wise positions are identical to the surface pressure probes used in the experiments by Foeth [62], as depicted in Figure 6.8.

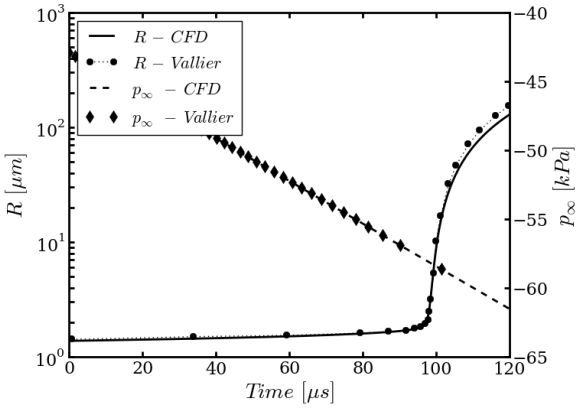

(a) Case 1 - Vallier [195]

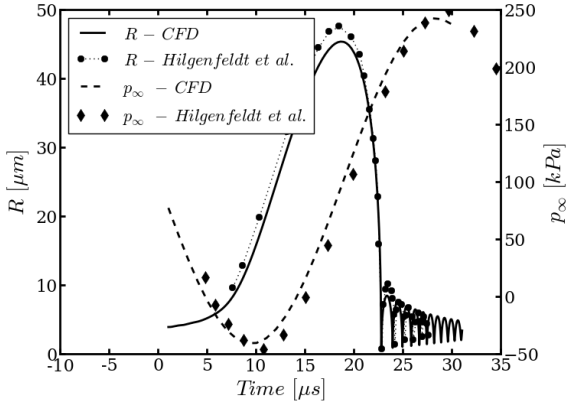

(b) Case 2 - Hilgenfeldt *et al.* [76]

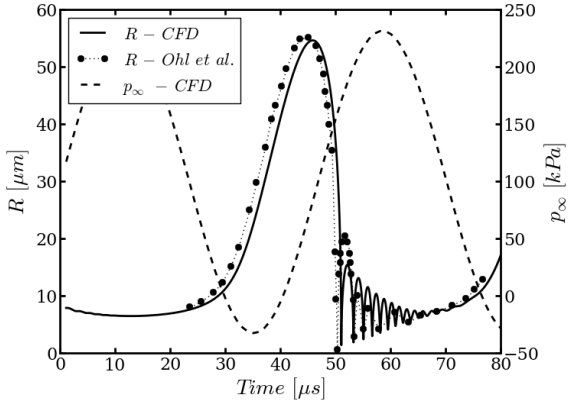

(c) Case 3 - Ohl *et al.* [154]

Figure 9.4: Time histories of bubbles used for validation of the Rayleigh-Plesset equation solver.

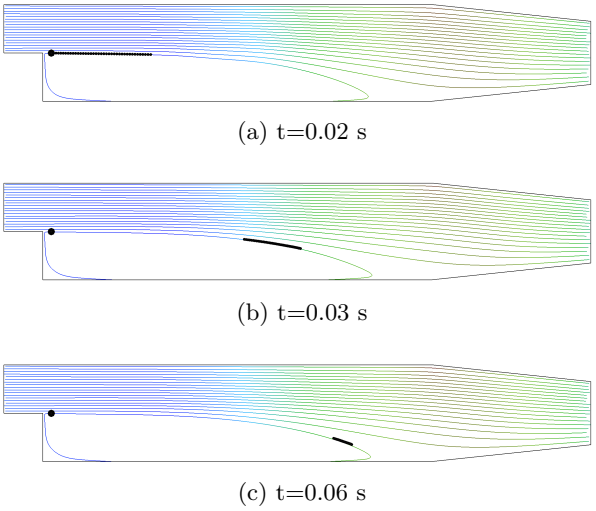

(a) t=0.02 s

(b) t=0.03 s

(c) t=0.06 s

Figure 9.5: Positions of bubbles over a backward facing step used for validation of the Lagrangian motion solver. Black dot at the close to the inlet on the left-hand side is the injection point of new particles, small black dots are the instantaneous positons of the bubbles added to the domain.

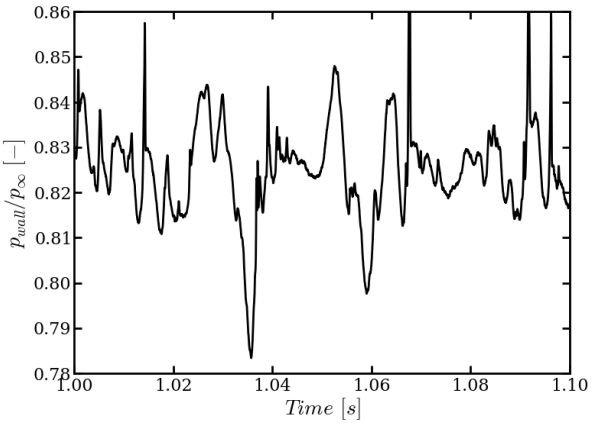

Figure 9.6: Wall pressure as a function of outlet pressure predicted for a probe above the leading edge of the foil at the centreline (probe 6). Eulerian flow solution only.

9.5.3 Results

Figure 9.6 presents cavitation-induced pressure at the top wall of the virtual cavitation tunnel directly above the leading edge of the foil obtained using the baseline cavitation model without Lagrangian bubbles. The signal shows fluctuations of approximately ±3% of the reference pressure and, at the first glance, does not show direct dependence on the shedding frequency. However, spectral analysis, shown in Figure 9.7, indicates that the wall pressure is directly related to the cavity sheet behaviour and its higher harmonics, as expected.

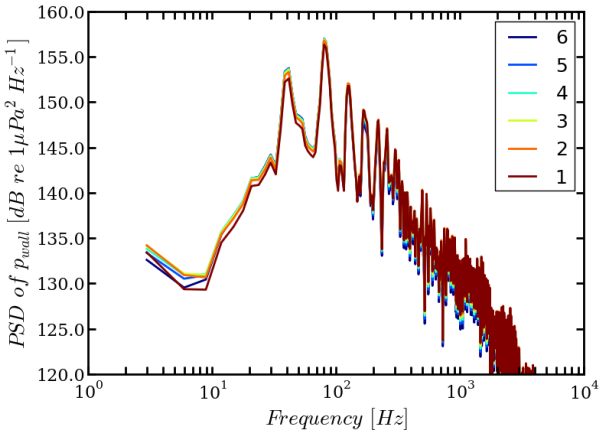

Figure 9.7: Power spectral density function of the wall pressure for a series of probes placed along the centreline of the foil, from the trailing edge (probe 1) to the leading edge (probe 6). Eulerian flow solution only.

Figure 9.8 shows the distribution of Lagrangian bubbles at an instant in the cavitation cycle similar to the one in the included experimental photograph. One may note that the volume-of-fluid field behaves in a very similar to the previously used baseline model, thus yielding similar iso-contours. An important observation is also that the baseline mass transfer model fails to convect cavities down to the trailing edge to the foil, causing to a discrepancy with the experimental observations. The new hybrid model, however, predicts this behaviour successfully.

Closer analysis of Figure 9.9 allows one to observe where the Lagrangian bubbles get created. It may be seen that two primary scenarios exist in which transfer from the Eulerian frame occurs. First, when a well-defined cavity with high vapour fraction significantly reduces in size. The second instance, by far appearing to be more common in the present simulation, is when there exists a region of intermediate vapour fraction values and when at some point, either by becoming physically separated or when local volume fractions exceed the pre-set thresholds, a certain sub-region gets identified as a separate cavity by the reconstruction algorithm. In Figure 9.9 this may be seen to occur primarily close to the centreline of the foil, where large interface displacements and velocities take place, causing injection of relatively large Lagrangian bubbles, predominantly just after the occurrence of the re-entrant jet. This appears to stand in good agreement with the experimental observations. A second region where Lagrangian bubbles get created is at around 35% of span from the wall, where the cavity sheet also experiences substantial deformations. This behaviour may also be seen in the experimental data (Figure 6.12 a) and c)), although more bubbles appear to have been created at this location during experimental tests. This discrepancy could be due to the unsteadiness of the volume fraction field being under-predicted, the shortcomings of the Euler-to-Lagrange transition algorithm or its settings.

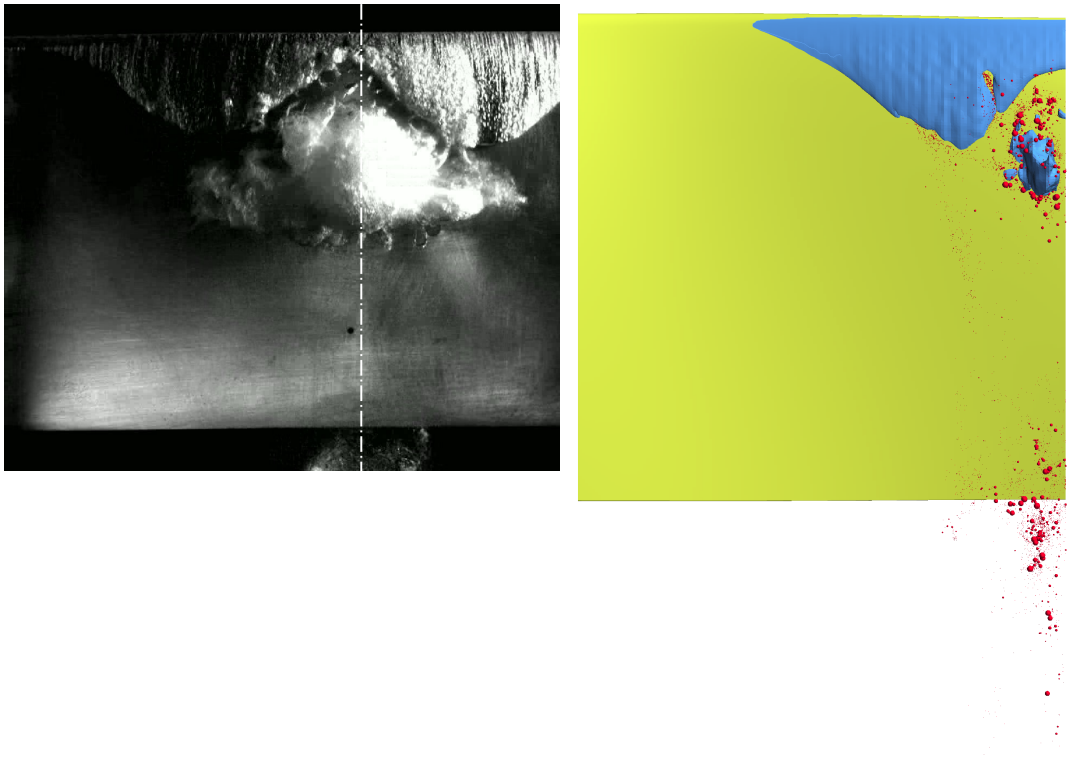

(a) Experiment (b) Hybrid cavitation model

Figure 9.8: Comparison of the cavitation pattern on the Delft Twist 11 foil between the experiment by Foeth [62] and the present hybrid Eulerian-Lagrangian cavitation model. Volume-of-fluid cavities represented as blue $\alpha = 0.5$ iso-contours, Lagrangian bubbles shown as red spheres with appropriate instantaneous radius.

A key aim of the present study was to investigate how much the Lagrangian bubbles contribute to the induced wall pressures, which is depicted in Figures 9.10 and 9.11 in the form of time- and frequency-domain plots. The former shows pressure at the probe above the leading edge of the foil over the duration of approximately one cavitation cycle. One may note that the pressure caused by the presence of small bubbles exhibits a broadband nature without immediately obvious concentrations along the time axis. Closer analysis reveals, however, that the magnitude of the Lagrangian contributions increases when spikes in the Eulerian pressure field, visible around times 0.006 and 0.012 s, occur. This may be explained by an increased likelihood of collapse of the Lagrangian bubbles being induced by the higher external pressures associated with collapsing Eulerian cavities, which further reinforces the magnitudes of the predicted noise.

Figure 9.11 shows that including the pressure induced by the Lagrangian bubbles in the spectral analysis causes an 8 dB increase in the spectral levels around the shedding frequency and makes the higher harmonics more clearly defined than when just the Eulerian pressure is considered. One may thus readily see the relationship between the rise in local pressure causing an increased number of Lagrangian collapses, which then

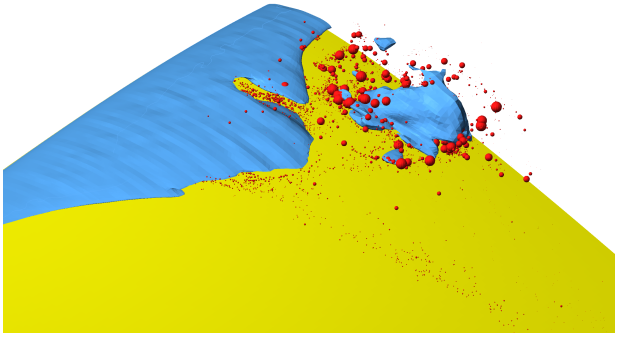

(a) Leading edge region

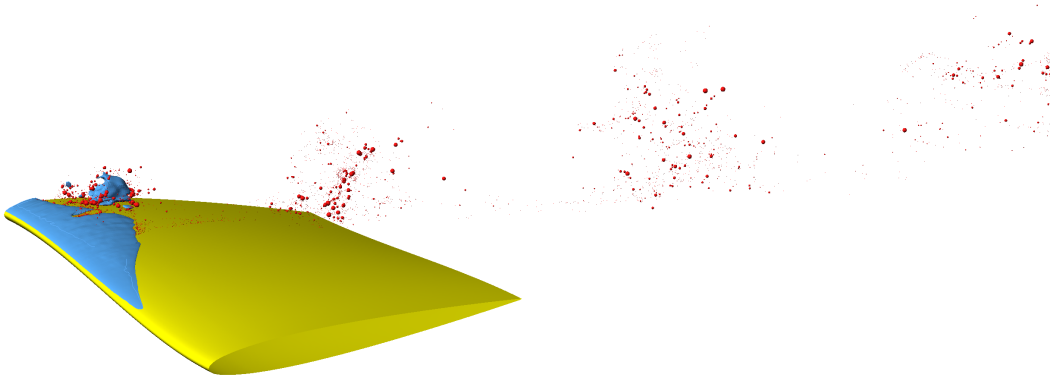

(b) Wake structure

Figure 9.9: Detailed view of cavitation patterns predicted by the hybrid cavitaiton model for the Delft Twist 11 foil. Volume-of-fluid caivties represented as blue $\alpha = 0.5$ iso-contours, Lagrangian bubbles shown as red spheres with appropriate instantaneous radius.

contribute to the predicted wall pressures. It should be noted that the low-frequency range of the spectra in Figure 9.11 is different than in Figure 9.7 due to the hybrid model simulation having been run for a smaller number of cavitation cycles due to the increased computational and data storage costs.

In total, over 15000 Lagrangian bubbles have been introduced to the numerical domain over the period of 4 cavitation cycles. It has thus proven challenging to analyse their individual lifetimes in detail. An interesting hand-picked example is shown in Figure 9.12, where the time history of the evolution of the radius of a bubble and the external pressure acting on it are shown. One may note how, first, the bubble was in a region of constant pressure and thus experienced little variation in radius due to the equilibrium assumption. It was then subjected to a rise in the external pressure, leading to a decrease in radius. This was followed by the bubble being swept closer to the centreline of the foil to a region of lower pressure, leading to a significant expansion, followed by a collapse downstream and a series of rebounds. A sudden spike in the external pressure may then be seen, which appears to have altered the oscillation frequency and reduced the amplitude of the radius. The bubble was then convected by the flow towards the outlet,

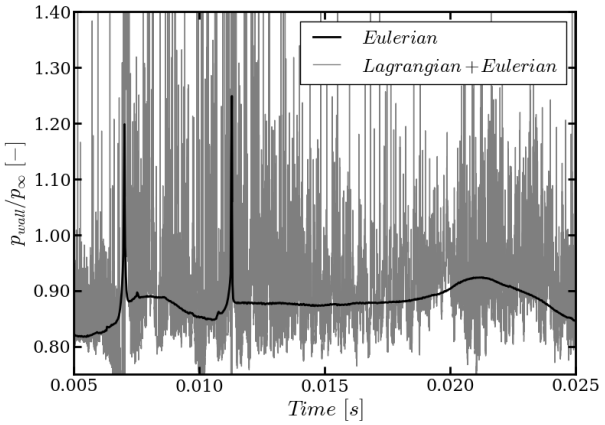

Figure 9.10: Direct Eulerian wall pressure at probe 6 also showing values with superimposed Lagrangian bubbles pressures.

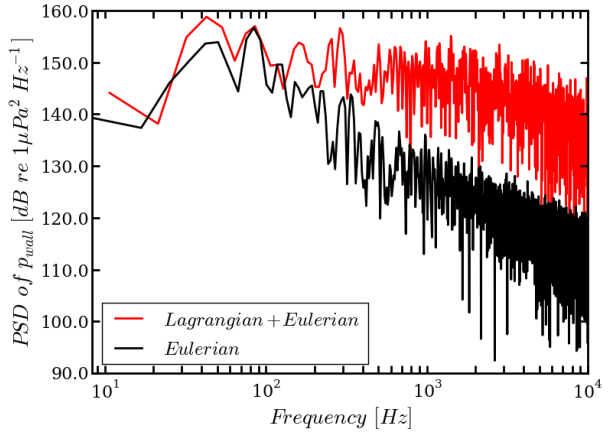

Figure 9.11: Power spectral density function of the direct CFD and combined Euler-Lagrange wall pressures at the location of probe 6.

which was accompanied by a steady rise in local pressure and decay of the oscillation of the radius as the bubble gradually approached the equilibrium condition.

9.5.4 Discussion

Analysis of the predicted time histories of radius as a function of local pressure for the bubbles present in the simulation revealed significant similarities to the validation data presented for individual bubbles. This shows that, while the actual geometry contains far more complex phenomena and thus pressure excitation, baseline mechanisms of bubble growth, collapse, and rebound have been predicted to take place. This, first of all, hints and the hybrid model being representative of actual physics and, secondly, highlights the relevance of the studies presented in the literature which only concern themselves with the motion of a single bubble.

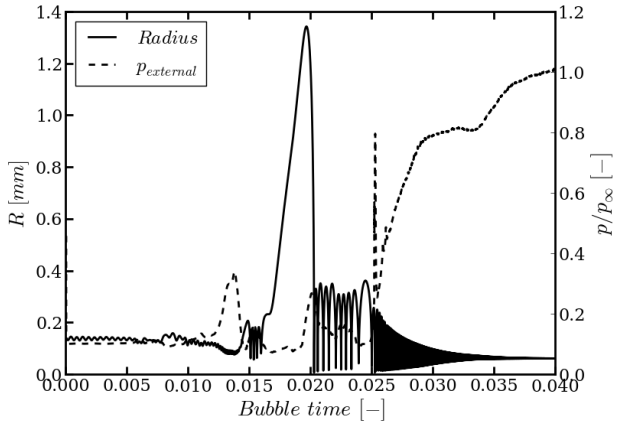

Figure 9.12: Time history of the radius and external pressure acting on a selected bubble which was created 0.1 s off-centreline close to the beginning of the simulation.

Comparison of the predicted and experimentally observed distributions and locations of Lagrangian bubbles during the cavitation cycle has revealed promising agreement. This indicates that, despite the simplicity of its current implementation, the hybrid Eulerian-Lagrangian cavitation model accounts for the dominant physical phenomena. A key observation in this regard has been the importance of local cavity interface deformations, most likely related to the presence of shear layers and varying pressure gradients, on where regions of intermediate volume fractions occur and spawn potential injection sites for Lagrangian bubbles. Although no experimental data exist in the public domain to validate the predicted wall pressures, the predicted broadband contributions of the small-scale bubbles, superimposed on the underlying low-frequency oscillations induced by the large-scale cavity sheet and clouds, stand in qualitative agreement with what is understood about multi-scale cavitation noise [22, 27, 143].

As expected, the wall pressures induced by the cavitation modelled using the baseline Eulerian model were predicted to be primarily dependent on the shedding frequency. The data did also show a substantial amount of higher harmonics. Inclusion of the broadband signals from the dispersed bubbles led to a significant increase in the sound pressure levels predicted for medium and high frequencies. Similar observations were also made by numerical studies by Park *et al.* [157], and Sunil *et al.* [186], who considered noise from convected Lagrangian bubbles only, as well as in the investigation by Matusiak [143], who implemented a hybrid Lagrangian-BEM (boundary element method) coupled with a potential flow solver. This is a key observation, as it firstly provides more confidence in the present method. It also shows the significant increase in the noise prediction capabilities offered by the new model compared to what is discussed in the open literature.

Several areas for improvement have been identified in the current multi-scale cavitation model. It has been seen that a small number of the Lagrangian bubbles come in close

contact with each other and thus could be expected to merge in reality [196]. Accounting for this is, however, was expected to be computationally expensive due to the added cost of a global reduce operation required for bubbles in each sub-domain to contain information on all the other Lagrangian parcels in the simulation. It has been seen that a vast amount of data gets generated from the Lagrangian tracking algorithm, which makes it difficult to utilise using more basic CFD post-processing techniques. It is thus hoped that more robust and statistically sound approaches can be devised in the future to better inform the user on what the results mean in practice. Moreover, the current model assume that large coherent clouds act as single cavities, as long as they meet the prescribed size criterion. In reality this is not always the case as cloud cavities often consist of a large amount of small bubbles interacting with each other. It would therefore be beneficial to build upon the current interface reconstruction method to be able to distinguish between large coherent structures or concentrations of small bubbles. The final, and most pressing, issue with the present implementation is to do with the continuity equation not being strictly observed when transferring bubbles to the Lagrangian phase. While this has not been seen to cause major problems from a practical standpoint, a more mathematically strict version of the model should be sought. A possible route to achieve this is through including the Lagrangian bubbles in the volume fraction scalar field so that the transfer operation does not destroy or create vapour but merely relocates it slightly in space.

9.6 Summary

The implementation of a hybrid Eulerian-Lagrangian cavitation model has been introduced and the principles of operation of the new solver were described. The model was then verified and partially validated based on a series of simple but representative test cases. Finally, an application to the Delft Twist 11 hydrofoil was presented. The study showed that accounting for the effect of the Lagrangian bubbles allows for the medium and high frequency content of cavitation-induced pressures to be modelled in the simulation, which was not possible with the baseline Eulerian-only solver. This is an important step towards direct prediction of the full-spectrum of cavitation noise and brings the current computational method closer towards the ultimate goal of being able to compete with a real-life cavitation tunnel at making noise predictions of marine propellers.

Chapter 10

Conclusions and future work

10.1 Conclusions

A wide range of cavitating flow cases including propellers and hydrofoils have been modelled and the results were compared against available experimental results, as well as benchmarked against published numerical data. In most of the cases, relatively good agreement has been achieved, indicating relative maturity of the underlying mass-transfer cavitation models and turbulence modelling techniques. The major discrepancies observed have been identified to be due to the mass transfer model itself and were particularly evident in under-predicted cavitation volumes and the inability to accurately resolve transition between different shedding dynamics for the NACA 66 case.

Despite these drawbacks, mass-transfer models remain a useful prediction tool and are still the workhorse of the marine propeller community. However, increasingly more authors have moved towards using compressible methods, such as the barotropic equilibrium models. Arguably, these approaches remain expensive, primarily due to the high mesh density and very small time step requirements. However, the constantly increasing computational power available will likely bring them to the realm of everyday use in the not-so-distant future. Whatever the future advancements, it is likely that the models used will still share the common assumptions and features of the model used in the present work, namely finite volume discretisation, reliance on Eulerian grids, and utilisation of the volume fraction transport equation. This means the problems from the hydroacoustic side, such as having to deal with small amplitude acoustic waves, high sound speeds, the need for large domains, and inability to resolve small cavitation scales, will still persist. Hence, the methods proposed here will be directly transferable and applicable as much as they were in the present context.

A major step forward relative to the state of the art made in this work has been the implementation of the porous Ffowcs Williams-Hawkings acoustic analogy into the open-source OpenFOAM framework. This approach has the potential to be highly flexible

in terms of tackling complex problems and should be able to account for noise sources associated both with cavitation and turbulence. While it has seen wide use in the aeroacoustic community, it has gained ground in the hydroacoustic field only fairly recently, partially thanks to the work presented here.

The first important finding in terms of applicability of this acoustic method to marine propeller problems has been that typical mesh and simulation arrangements used to predict the cavitating flows should be suitable to account for the major part of the low-frequency noise spectrum. This is a highly relevant observation as it promises that acoustic signature assessment could be made part of the final design stages of future vessles, thus paving the way for quieter oceans. A key limitation in this respect is the minimum mesh resolution needed to accurately predict the flow field data in the nearlfield where it is sampled for the acoustic analysis.

Through a range of applications to propeller and hydrofoil cases, it has been shown that the currently used acoustic method can acount for cavitation and turbulence noise. However, if these phenomena are to be accounted for accurately, more advanced turbulence modelling techniques, such as DES or LES, should be used in lieu of the presently prevalent unsteady RANS methods. It has also been found that the currently implemented form of the FW-H analogy, ignoring the volume integral and leaving the porous data surface open in the downstream region, requires a certain amount of skill to be applied successfully to a new case for which the flow pattern is not know *a priori*. This could be alleviated by further improvements to the present implementation, such as employment of outlet disc averaging techniques, which is encouraged if the method is to be used regularly for a wide range of applications.

The acoustic analogy has also been used to confirm that the low-frequency cavitation noise is primarily dependent on the fluctuations of the large cavity volumes and is monopole in nature. These observations had already been made based on experimental observations and theoretical analysis. However, the present work was able to arrive at the same conclusions from a fundamentally different angle, which increases the confidence in the present method and promises more interesting findings in the future as the acoustic analogy becomes more widely adopted by the maritime CFD community.

A major problem encountered has been the inability of the current cavitation model to resolve small-scale cavitation. This is not typically assumed to be the major noise source on marine propellers over most operating conditions. One may thus argue that a mass transfer model and acoustic analogy alone are capable enough to make engineering estimates of peak sound pressure levels. However, it is expected that high-frequency cavitation noise will occupy similar frequency ranges as the noise due to turbulence and hence understanding it better is an important step in truly being able to model propeller noise across the full frequency spectrum.

For this reason, hybrid Eulerian-Lagrangian cavitation modelling approaches combining the single-fluid and Lagrangian bubble models have been identified as appealing to the scope of work undertaken in this project. Their principle advantage is that they offer the possibility to resolve both the large and small scales of the cavitating flow without requiring a substantial increase in the density of the mesh. Such a model has also been implemented in OpenFOAM, with particular focus on robust use on massively parallel architectures. While detailed validation of this method was difficult to undertake due to lack of applicable experimental data, qualitative validation with the Delft Twist 11 hydrofoil has shown the results to be promising both in terms of the cavitation patterns and tunnel wall pressures predicted. Importantly, the broadband noise induced by the Lagrangian cavities was not predicted to affect the dominant, low-frequency harmonics of the wall pressures significantly, but was observed to extend the range of frequencies generated by cavitation well above a kilohertz. It is believed that, following the inclusion of several additional physical mechanisms, the current model will form a useful tool for cross-examination of cavitation tunnel noise measurements and will contribute towards a better understanding of shipping noise. An advantage of this method is that it could be readily used with the FW-H acoustic analogy, yielding a much fuller description of the cavitation-related noise sources across a wide range of frequencies.

10.2 Review of scientific contributions

To sum up, the presented work has contributed the following novel developments, results and observations to the field of marine propeller cavitation and noise modelling.

- Implemented the porous Ffowcs Williams-Hawkings acoustic analogy to the OpenFOAM framework, building on the experience of the aeroacoustic community. Viability of the method in the marine propeller noise prediction context was studied and it was shown to be a promising tool that may be used with modern CFD techniques, which stands in line with recent literature [89].
- Applied FW-H, Large Eddy Simulation, as well as Detached Eddy Simulation, and mass transfer cavitation models together in order to analyse the relationship between the predicted flow field and the radiated noise around a cavitating hydrofoils. This was described in one the first such studies in the public domain [118, 123], thus paving the way for a wider adoption of the described methods.
- Confirmed the monopole character of the sheet cavity noise using an acoustic method and a cavitation model which make no assumptions on the nature of the noise sources. The direct link between the induced pressures and the second time derivative of the total cavity volume has also been shown.

- Conducted a comprehensive study of the effect of choosing the extent of the acoustic analogy integration surface on the predicted near- and far-field pressure fluctuations, in application to a propeller and cavitating hydrofoil. This adds to the better understanding of how to use the method efficiently and accurately, hence improving the collective ability of the martime fluid dynamic community.

- Implemented a hybrid Eulerian-Lagrangian cavitation model with the aim of resolving the broadband part of the cavitation-induced noise spectrum better than with a standard mass transfer cavitation model alone. The present model derives from published work by Vallier [196], but extends its capability by allowing far-field noise to be studied.

- Performed qualitative validation of the model based on cavitating hydrofoil simulations, highlighting the potential advantages it offers to modelling cavitation-induced pressures, particularly when cloud cavitation is likely to occur.

These contributions have been published in the following journal and conference articles.

Peer-reviewed journal articles

- Lidtke, A. K., Turnock, S. R. and Humphrey, V. F. (2016), "Characterisation of sheet cavity noise of a hydrofoil using the Ffowcs Williams-Hawkings acoustic analogy". Computers & Fluids, 130, 8-23. (doi:10.1016/j.compfluid.2016.02.014)

- Lidtke, A. K., Humphrey, V. F. and Turnock, S. R. (2015), "Feasibility study into a computational approach for marine propeller noise and cavitation modelling". Ocean Engineering, 1-8. (doi:10.1016/j.oceaneng.2015.11.019).

Peer-reviewed conference articles

- Lidtke, A. K., Turnock, S. R. and Humphrey, V. F. (2016), "Multi-scale modelling of cavitation-induced pressure around the delft twist 11 hydrofoil", In 31st Symposium on Naval Hydrodynamics (SNH), Monterey, CA, USA, 11 - 16 Sep 2016

- Lidtke, A. K., Humphrey, V. F. and Turnock, S. R. (2015), "Use of Acoustic Analogy for Marine Propeller Noise Characterisation", In Fourth International Symposium on Marine Propulsors (SMP), Autsin, TX, USA, 12-15 Jun 2015

Conference articles and workshop items[1]

- Lloyd, T. P., Lidtke, A. K., Rijpkema, D. R., van Wijngaarden, H. C. J., Turnock, S. R. and Humphrey, V. F., "Using the FW-H equation for hydroacoustics of propellers", In 18th Numerical Towing Tank Symposium (NuTTS), Cortona, Italy, 28-30 Sep 2015
- Lidtke, A. K., Turnock, S. R. and Humphrey, V. F., "The influence of turbulence modelling techniques on the predicted cavitation behaviour on a NACA0009 foil", In 17th Numerical Towing Tank Symposium (NuTTS), Gothenburg, Sweden, 28-30 Sep 2014
- Lidtke, A. K., Turnock, S. R. and Humphrey, V. F., "Outlook on Marine Propeller Noise and Cavitation Modelling", A. Yucel Odabasi (AYO) Colloquium Series, Istanbul, Turkey, 6-7 November 2014

Periodical articles

- Lidtke, A. K., Turnock, S. R. and Humphrey, V. F. (2016), "Saving ocean sound scapes", The Naval Architect, pp. 36-38

10.3 Future work

During the project several future research questions relating to marine propeller noise and cavitation modelling have been identified.

- The proposed numerical framework for evaluating marine propeller noise has now been developed to a sufficient stage to allow application to a more demanding test case. The most promising one identified to date is the R/V Princess Royal, for which detailed full- and model-scale noise measurements have been presented by Brooker *et al.* [28] and Aktas *et al.* [2, 3]. It would thefore seem as the natural choice for any future investigations.
- The current framework could readily be used in application to a rotating marine propeller. Doing so accurately would require substantial computational resources, although not beyond the current top-of-the-line capabilities. Moving on to such a test case would allow direct comparison with measurements done in cavitation tunnels across a wide range of frequencies and would move the developed method another step closer to wider adoption by the maritime community.

[1]The first listed paper is a collaborative work between all authors

- Calibration of the Schnerr-Sauer cavitation model by using several most common validation test cases simultaneously could allow for a more robust set of tuning coefficients to be arrived at. This could, in theory, make the model less dependent on the experience of the individual user and deliver more repeatable performance across a broad range of applications. Possible routes for its further refinement, such as addition of second order corrective terms, might also be found.

- In the present form, the acoustic analogy, by definition, cannot account for the reflections caused by the presence of solid boundaries. It is perfectly feaible to design numerical domains limiting the likelihood of reflections, as in the presented E779a and NACA 0009 simulations, but introducing modifications to the FW-H to allow it to cope with the presence of solid boundaries would increse its range of applicability.

- The incompressibility assumption invoked in the current method raises numerous difficulties, discussed at length throughout this thesis. The growing computational resources available indicate that it should soon be possible to switch to a compressible or pseudo-compressible flow solver when dealing with cavitating flows. It is therefore recommended to study this path, so that the overall cavitation modelling framework becomes more realiable.

- Current algorithms used to transfer bubbles between the Eulerian and Lagrangian frames of reference are rather simplistic and it is possible that they do not represent some of the more complex cavitation break-up physics well. Advancing this part of the code would make it more accurate and provide a better representation of reality. In order to succeed, a hypothetical project would need access to a rich experimental data base. This could allow the assumptions on how to model cavity break up to be devised.

- Investigating the effect of span-wise domain extent on the predicted cavitaiton on hydrofoils could lead to an interesting study. This would be applicable in helping guide future experimental studies as well as shedding light on best practices in running simulations of idealised hydrofoils.

Furthermore, areas for improvement in the already developed method have also been identified. While these are not critical to the overall conclusions drawn about the methods, they would have a substantial positive impact on increasing the applicability and generality of the methodology proposed.

- To make the acoustic analogy less dependent on the skill of an individual user, it would be worth implementing the volume integral term and/or an approach for the treatment of the outlet porous data surface part to remove spurious noise sources due to penetrating vortices. This should make the FW-H method more

easily applicable to complex geometries, such as propellers operating near the hull in a fully appended configuration.

- The current FW-H implementation relies on several dictionary files and a long list of command line arguments to work due to the rather hasty development cycle. Rewriting the code to make it more transparrent would have a positive effect on its user-friednliness.

- The entire framework has been intially implemented in OpenFOAM 2.2.2 and then migrated to version 3.0.1, as it became available. At the time of writing, the newest available official OpenFOAM release has already moved to version 4.1. While this is a never-ending process, updating the code to work with the most recent version is a must if it is to be picked up by the users.

Appendix A

Schnerr-Sauer model derivation

One may sum the transport equations for liquid and vapour mass,

$$\frac{\partial}{\partial t}\left(\alpha\rho_l\right) + \nabla\cdot\left(\alpha\rho_l\right) = 0, \tag{A.1a}$$

$$\frac{\partial}{\partial t}\left((1-\alpha)\rho_v\right) + \nabla\cdot\left((1-\alpha)\rho_v\right) = 0, \tag{A.1b}$$

to obtain the non-divergent continuity equation,

$$\nabla\cdot\mathbf{U} = \left(\frac{1}{\rho_\mathrm{v}} - \frac{1}{\rho_\mathrm{l}}\right)\dot{m}, \tag{A.2}$$

which denotes the velocity divergence due to the mass transfer between the two phases present. This indicates that the source terms will affect both the α transport equation and the pressure equation [11], as shown in By rearranging the above, an expression for the mass transfer rate may be obtained

$$\dot{m} = \left(\frac{\rho_\mathrm{l}\rho_\mathrm{v}}{\rho_\mathrm{v} - \rho_\mathrm{l}}\right)\nabla\cdot\mathbf{U}. \tag{A.3}$$

By considering the full version of the continuity equation,

$$\frac{\partial\rho}{\partial t} + \nabla\cdot\left(\rho\mathbf{U}\right) = 0, \tag{A.4}$$

one may formulate an expression for the density variation which assumes the lack of spatial variation in the liquid and vapour densities (incompressible flow):

$$\nabla\cdot\left(\mathbf{U}\right) = -\frac{1}{\rho}\frac{\mathrm{d}\rho}{\mathrm{d}t}. \tag{A.5}$$

Using the expression for fluid properties interpolated as a function fo the volume fraction field,

$$\rho = \alpha\rho_{\mathrm{v}} + (1-\alpha)\rho_{\mathrm{l}}, \tag{A.6a}$$

$$\mu = \alpha\mu_{\mathrm{v}} + (1-\alpha)\mu_{\mathrm{l}}, \tag{A.6b}$$

the time-derivative term in (A.5) may be written as:

$$\frac{\partial\rho}{\partial t} = (\rho_{\mathrm{l}} - \rho_{\mathrm{v}})\frac{\partial\alpha}{\partial t}, \tag{A.7}$$

which reduces to the required form if the partial derivative is dropped. Hence the following may be written:

$$\nabla\cdot\mathbf{U} = -\frac{1}{\rho}(\rho_{\mathrm{l}} - \rho_{\mathrm{v}})\frac{\partial\alpha}{\partial t}. \tag{A.8}$$

Schnerr-Sauer model assumes that the vapour originates from small nuclei present in the fluid and described by the characteristic radius, R_0, and density, n_0. Hence an expression for the *vapour* volume fraction may be written as:

$$\alpha_{\mathrm{v}} = \frac{\frac{4}{3}\pi R^3 n_0}{1+\frac{4}{3}\pi R^3 n_0}. \tag{A.9}$$

In order to rearrange (A.8) a time derivative of the α field is required which may be obtained by differentiating the above expression and allowing the bubble radius to vary with time, which represents the expansion and contraction of the individual nuclei:

$$\frac{\partial\alpha}{\partial t} = -\alpha\frac{\frac{4}{3}\pi R^3 n_0}{\left(1+\frac{4}{3}\pi R^3 n_0\right)^2}\frac{3\dot{R}}{R}. \tag{A.10}$$

Using (A.9) this may be reduced to

$$\frac{\partial\alpha}{\partial t} = -\alpha(1-\alpha)\frac{3\dot{R}}{R}. \tag{A.11}$$

The bubble radius derivative may be obtained directly from the Rayleigh-Plesset equation:

$$R\ddot{R} + \frac{3}{2}\left(\dot{R}\right)^2 = \frac{1}{\rho}\left(p_i - p_\infty - \frac{2\sigma}{R} - \frac{4\mu}{R}\dot{R}\right). \tag{A.12}$$

Upon rearranging, neglecting the high-order term and the effects of viscosity and surface tension, as well as assuming that pressure inside the bubble is equal to the saturated vapour pressure, p_v, and the pressure at the bubble interface is the same as the local fluid pressure this yields:

$$\dot{R} = \text{sign}(p_\text{v} - p)\sqrt{\frac{\frac{2}{3}|p_\text{v} - p|}{\rho_l}}. \tag{A.13}$$

Use may now be made of the following relationship in order to separate the contribution of the nuclei volume, which remains unaltered for constant R_0 and n_0, from the volume fraction field (α_nuc denotes the contribution of the nuclei to the vapour volume fraction, as given by (A.9) for $R = R_0$):

$$n_0 \frac{4}{3}\pi R^3 = \frac{\alpha_\text{v}}{\alpha} = \frac{1 + \alpha_\text{nuc} - \alpha}{\alpha}. \tag{A.14}$$

This may be rearranged to yield an expression for the reciprocal of the bubble radius:

$$\frac{1}{R} = \left(\frac{4}{3}\pi n_0 \frac{\alpha}{1 + \alpha_\text{nuc} - \alpha}\right)^{\frac{1}{3}}. \tag{A.15}$$

Finally, combining equation (A.8) with (A.11), (A.13) and (A.15) yields the final expression for the Schnerr-Sauer model:

$$\dot{m} = \frac{3\rho_\text{l}\rho_\text{v}}{\rho}(1 - \alpha)\alpha \left(\frac{4}{3}\pi n_0 \frac{\alpha}{1 + \alpha_\text{nuc} - \alpha}\right)^{\frac{1}{3}} \text{sign}(p_\text{v} - p)\sqrt{\frac{\frac{2}{3}|p_\text{v} - p|}{\rho_\text{l}}} \tag{A.16}$$

In the actual implementation, the terms are split into condensation and vaporisation parts and see slightly different treatment depending on whether they are being used in the pressure or the volume fraction transport equations, as shown in Eq. (A.17).

$$
\begin{aligned}
\dot{m}_{\alpha,c} &= C_c \alpha \, \max(p - p_v, 0) \\
&\quad \left[\frac{3\rho_l \rho_v}{\rho} \sqrt{\frac{2}{3\rho_l}} \left(\frac{4}{3} \pi n_0 \frac{\alpha}{1 + \alpha_{\text{nuc}} - \alpha} \right)^{\frac{1}{3}} \sqrt{\frac{1}{|p_{\text{v}} - p|}} \right] \\
\dot{m}_{\alpha,v} &= C_v (1 + \alpha_{\text{nuc}} - \alpha) \, \min(p - p_v, 0) \\
&\quad \left[\frac{3\rho_l \rho_v}{\rho} \sqrt{\frac{2}{3\rho_l}} \left(\frac{4}{3} \pi n_0 \frac{\alpha}{1 + \alpha_{\text{nuc}} - \alpha} \right)^{\frac{1}{3}} \sqrt{\frac{1}{|p_{\text{v}} - p|}} \right] \\
\dot{m}_{p,c} &= C_c (1 - \alpha) \alpha \, \text{pos}(p - p_v) \\
&\quad \left[\frac{3\rho_l \rho_v}{\rho} \sqrt{\frac{2}{3\rho_l}} \left(\frac{4}{3} \pi n_0 \frac{\alpha}{1 + \alpha_{\text{nuc}} - \alpha} \right)^{\frac{1}{3}} \sqrt{\frac{1}{|p_{\text{v}} - p|}} \right] \\
\dot{m}_{p,v} &= -C_v (1 + \alpha_{\text{nuc}} - \alpha) \alpha \, \text{neg}(p - p_v) \\
&\quad \left[\frac{3\rho_l \rho_v}{\rho} \sqrt{\frac{2}{3\rho_l}} \left(\frac{4}{3} \pi n_0 \frac{\alpha}{1 + \alpha_{\text{nuc}} - \alpha} \right)^{\frac{1}{3}} \sqrt{\frac{1}{|p_{\text{v}} - p|}} \right]
\end{aligned}
\tag{A.17}
$$

$$
\begin{aligned}
\dot{V}_{\alpha,c} &= \left[\frac{1}{\rho_l} - \alpha \left(\frac{1}{\rho_l} - \frac{1}{\rho_v} \right) \right] C_c \alpha \, \max(p - p_v, 0) \\
&\quad \left[\frac{3\rho_l \rho_v}{\rho} \sqrt{\frac{2}{3\rho_l}} \left(\frac{4}{3} \pi n_0 \frac{\alpha}{1 + \alpha_{\text{nuc}} - \alpha} \right)^{\frac{1}{3}} \sqrt{\frac{1}{|p_{\text{v}} - p|}} \right] \\
\dot{V}_{\alpha,v} &= \left[\frac{1}{\rho_l} - \alpha \left(\frac{1}{\rho_l} - \frac{1}{\rho_v} \right) \right] C_v (1 + \alpha_{\text{nuc}} - \alpha) \min(p - p_v, 0) \\
&\quad \left[\frac{3\rho_l \rho_v}{\rho} \sqrt{\frac{2}{3\rho_l}} \left(\frac{4}{3} \pi n_0 \frac{\alpha}{1 + \alpha_{\text{nuc}} - \alpha} \right)^{\frac{1}{3}} \sqrt{\frac{1}{|p_{\text{v}} - p|}} \right] \\
\dot{V}_{p,c} &= \left(\frac{1}{\rho_l} - \frac{1}{\rho_v} \right) C_c (1 - \alpha) \alpha \, \text{pos}(p - p_v) \\
&\quad \left[\frac{3\rho_l \rho_v}{\rho} \sqrt{\frac{2}{3\rho_l}} \left(\frac{4}{3} \pi n_0 \frac{\alpha}{1 + \alpha_{\text{nuc}} - \alpha} \right)^{\frac{1}{3}} \sqrt{\frac{1}{|p_{\text{v}} - p|}} \right] \\
\dot{V}_{p,v} &= \left(\frac{1}{\rho_l} - \frac{1}{\rho_v} \right) (-C_v) (1 + \alpha_{\text{nuc}} - \alpha) \alpha \, \text{neg}(p - p_v) \\
&\quad \left[\frac{3\rho_l \rho_v}{\rho} \sqrt{\frac{2}{3\rho_l}} \left(\frac{4}{3} \pi n_0 \frac{\alpha}{1 + \alpha_{\text{nuc}} - \alpha} \right)^{\frac{1}{3}} \sqrt{\frac{1}{|p_{\text{v}} - p|}} \right]
\end{aligned}
\tag{A.18}
$$

Appendix B

Ffowcs Williams-Hawkings acoustic analogy derivation

The following derivation largely follows the steps presented by Brentner and Farassat [26], with modifications introduced to arrive at the porous rather than impermeable FW-H formulation. The process is also supported by noting the steps presented by Farassat [60] and Di Francescantonio [48].

The derivation utilises the generalised function theory, described by Farassat [58, 59] and summarised by Brentner and Farassat [26], which allows the fluid properties to be extended into the moving surface through the use of artificial discontinuities where the flow meets the surface. The advantage of applying generalised function theory is that it allows for the derivatives of flow parameters with discontinuities to be obtained and subsequently used in manipulations such as Green's function integration.

A key property of a generalised derivative, denoted as $\overline{\partial}$, of a function $q(\mathbf{x})$ with a discontinuity of Δq at $f(\mathbf{x}) = 0$ is that

$$\frac{\overline{\partial} q}{\partial x_i} = \frac{\partial q}{\partial x_i} + \Delta q \frac{\partial f}{\partial x_i} \delta(f), \tag{B.1}$$

with $\delta(f)$ denoting the Dirac delta function with respect to the surface f.

Another important characteristic has to do with integrating $\delta(f)$

$$\int Q(\mathbf{x}) \left|\nabla f\right| \delta(f) \mathrm{d}\mathbf{x} = \int_{f=0} Q(\mathbf{x}) \mathrm{d}S. \tag{B.2}$$

In the above, $\int_{f=0}$ denotes a surface integral over the surface $f = 0$ and Q is an arbitrary function defined on that surface.

The first step in deriving the Ffowcs Williams-Hawkings analogy is the definition of the moving surface $f(\mathbf{x}, t) = 0$, with $f > 0$ corresponding to its exterior. The surface

is assumed to have a normal vector, $\nabla f = \hat{\mathbf{n}}$ (or $\partial f/\partial x_i = \hat{n}_i$ in tensor notation), defined everywhere. In the derivation it is assumed that the fluid extends into the data surface and adopts the properties of the undisturbed fluid there. Next, taking P_{ij} to denote the compressive stress tensor, the momentum and continuity equations (neglecting viscosity),

$$\frac{\partial \rho}{\partial t} + \frac{\partial \left(\rho u_i\right)}{\partial x_i} = 0, \tag{B.3a}$$

$$\frac{\partial}{\partial t}\left(\rho u_i\right) + \frac{\partial}{\partial x_j}\left(\rho u_i u_j + P_{ij}\right) = 0, \tag{B.3b}$$

defined outside of the data surface are rewritten using the generalised function theory to incorporate the $f < 0$ region and the discontinuity it introduces,

$$\begin{aligned} \frac{\overline{\partial}\rho}{\partial t} + \frac{\overline{\partial}\left(\rho u_i\right)}{\partial t} &= \frac{\partial \rho}{\partial t} + (\rho - \rho_0)\frac{\partial f}{\partial t}\delta(f) + \frac{\partial(\rho u_i)}{\partial x_i} + (\rho u_i)\frac{\partial f}{\partial x_i}\delta(f) \\ &= \left[\rho_0 v_n + \rho(u_i \hat{n}_i - v_n)\right]\delta(f), \end{aligned} \tag{B.4a}$$

$$\begin{aligned} \frac{\overline{\partial}(\rho u_i)}{\partial t} + \frac{\overline{\partial}}{\partial x_j}\left(\rho u_i u_j + P_{ij}\right) &= \frac{\partial(\rho u_i)}{\partial t} + \rho u_i \frac{\partial f}{\partial t}\delta(f) \\ &+ \frac{\partial}{\partial x_j}\left(\rho u_i u_j + P_{ij}\right) + \left(\rho u_i u_j + \Delta P_{ij}\right)\frac{\partial f}{\partial x_j}\delta(f) \\ &= \left[\rho u_i (u_i \hat{n}_i - v_n)_\Delta P_{ij}\hat{n}_j\right]\delta(f). \end{aligned} \tag{B.4b}$$

In the above, the local velocity of the data surface is defined as $v_n = -\partial f/\partial t$. The equations also utilise the first generalised derivative property, given in Eq. (B.1), with the jumps in fluid properties at the data surface being $(\rho - \rho_0)$ and ρu_i in the continuity equation and $\Delta P_{ij} n_j$ and $\rho u_i(u_i \hat{n}_i - v_n)$ in the momentum equations.

In order to arrive a the Ffowcs Williams-Hawkings analogy, it is now necessary to take the generalised derivative $\overline{\partial}/\partial t$ of Eq. (B.4a) and $\overline{\partial}/\partial x_i$ of Eq. (B.4b) and subtract the latter from the former. Then, it is necessary to rearrange the result by subtracting $\overline{\nabla}^2[c^2(\rho - \rho_0)]$ from both sides. Finally, one can assume linear propagation of sound outside of the source region, thus allowing $p' = c^2\rho'$ to be used to simplify the resultant expression. The outcome is the permeable FW-H equation

$$\begin{aligned} \overline{\mathbb{D}}^2 p'(\mathbf{x}, t) = &\frac{\overline{\partial}}{\partial t}\left\{\left[\rho_0 v_n + \rho(u_n - v_n)\right]\delta(f)\right\} \\ &- \frac{\overline{\partial}}{\partial x_i}\left\{\left[\Delta P_{ij}\hat{n}_j + \rho u_i(u_n - v_n)\right]\delta(f)\right\} \\ &+ \frac{\overline{\partial}^2}{\partial x_i \partial x_j}\left[T_{ij}H(f)\right], \end{aligned} \tag{B.5}$$

where $u_n = u_i \hat{n}_i$, $H(f)$ is the Heaviside function and T_{ij} is the Lighthill stress tensor introduced in Chapter 5. The first term may be interpreted as a monopole and the second as a dipole source, both of which are defined on the surface $f = 0$. Due to

the presence of the Heviside function the last term is defined over a volume $f > 0$ and represents a quadrupole source. An important observation is that the above equation is an inhomogeneous wave equation for and external flow problem.

The key step involved in deriving the FW-H formulation used in practice is rearranging Eq. (B.5) into a summation of surface and volume integrals by using the free-space Green's function,

$$g(\mathbf{x},t;\mathbf{y},\tau) = \begin{cases} 0, \tau > t \\ \delta(\tau - t + r/c)/(4\pi r), \tau \leq t \end{cases} \tag{B.6}$$

for a receiver distance is defined as $r = |\mathbf{x} - \mathbf{y}|$. This is applied to the FW-H equation in order to eliminate the Dirac delta functions through the process of changing the variables and noting that the wave operator is linear and thus allows the spatial and temporal derivatives to commute. Thus, Eq. (B.5) may be written as

$$\begin{aligned} 4\pi p'(\mathbf{x},t) = &\frac{\partial}{\partial t}\int_{-\infty}^{t}\int_{-\infty}^{\infty}\frac{[\rho_0 v_n + \rho(u_n - v_n)]\delta(f)\delta(g)}{r}\mathrm{d}\mathbf{y}\mathrm{d}\tau \\ &- \frac{\partial}{\partial x_i}\int_{-\infty}^{t}\int_{-\infty}^{\infty}\frac{[\Delta P_{ij}\hat{n}_j + \rho u_i(u_n - v_n)]\delta(f)\delta(g)}{r}\mathrm{d}\mathbf{y}\mathrm{d}\tau + p'_Q(\mathbf{y},\tau)|_{ret}, \end{aligned} \tag{B.7}$$

where the last term is the quadrupole source which becomes a volume integral and has been defined with subscript *ret* denoting that the source contribution affecting the receiver at $(\mathbf{x}, t)$ must be evaluated at the retarded time. For the sake of brevity this terms is not expanded in the present derivation. Now, the divergence operator, $\partial/\partial x_i$ acting on the Green's function Dirac delta must be taken into the integral. This may be done by first noting that $\partial r/\partial x_i = \hat{r}_i$, which may be applied to the Green's function definition in Eq. (B.6) to yield

$$\frac{\partial}{\partial x_i}\left(\frac{\delta(g)}{r}\right) = -\frac{\delta'(g)}{c_0 r}\hat{r}_i - \frac{\delta(g)}{r}\hat{r}_i, \tag{B.8}$$

which may be simplified using $-\delta'(g)/r = \partial(\delta(g)/r)/\partial t$ as

$$\frac{\partial}{\partial x_i}\left(\frac{\delta(g)}{r}\right) = -\frac{1}{c_0}\frac{\partial}{\partial t}\left(\frac{\delta(g)}{r}\right) - \frac{\delta(g)}{r}\hat{r}_i. \tag{B.9}$$

The above expression may be substituted directly into Eq. (B.7), which upon collecting the terms, yields

$$\begin{aligned} &4\pi p'(\mathbf{x},t) = \\ &\quad\frac{1}{c_0}\frac{\partial}{\partial t}\int_{-\infty}^{t}\int_{-\infty}^{\infty}\frac{[\rho_0 c_0 v_n + c_0\rho(u_n - v_n) + \Delta P_{ij}\hat{n}_j\hat{r}_i + \rho u_i\hat{r}_i(u_n - v_n)]}{r}\mathrm{d}\mathbf{y}\mathrm{d}\tau \\ &\quad+ \int_{-\infty}^{t}\int_{-\infty}^{\infty}\frac{[\Delta P_{ij}\hat{n}_j\hat{r}_i + \rho u_i\hat{r}_i(u_n - v_n)]}{r^2}\mathrm{d}\mathbf{y}\mathrm{d}\tau + p'_Q(\mathbf{y},\tau)|_{ret}. \end{aligned} \tag{B.10}$$

The final step before arriving at the Farassat 1 formulation is exchanging the variables in Eq. (B.10) as $(\tau, \mathbf{y}) \rightarrow (g, d)$. As shown by Brentner and Farassat [26], the following is true

$$\mathrm{d}\mathbf{y}\mathrm{d}\tau = \frac{\mathrm{d}S\mathrm{d}f\mathrm{d}g}{|1 - M_r|}, \tag{B.11}$$

where $\mathrm{d}S$ is the infinitesimal element of the data surface $f = 0$ and $M_r = v_i\hat{r}_i/c_0$ is the Mach number of a point on the surface in the radiation direction. Thus, Equation (B.10) becomes

$$\begin{aligned} 4\pi p'(\mathbf{x}, t) = \\ \frac{1}{c_0}\frac{\partial}{\partial t}\int_{f=0}\left[\frac{\rho_0 c_0 v_n + c_0\rho(u_n - v_n) + \Delta P_{ij}\hat{n}_j\hat{r}_i + \rho u_i\hat{r}_i(u_n - v_n)}{r|1 - M_r|}\right]_{ret}\mathrm{d}S \\ + \int_{f=0}\left[\frac{\Delta P_{ij}\hat{n}_j\hat{r}_i + \rho u_i\hat{r}_i(u_n - v_n)}{r^2|1 - M_r|}\right]_{ret}\mathrm{d}S + p'_Q(\mathbf{y}, \tau)|_{ret}. \end{aligned} \tag{B.12}$$

Before continuing the derivation, it is useful to simplify the above expression by introducing intermediate acoustic variables,

$$U_i = \frac{\rho}{\rho_0}u_i, \tag{B.13a}$$

$$L_i = P_{ij}\hat{n}_j + \rho u_i(u_i \cdot \hat{n}_i), \tag{B.13b}$$

and assuming the control surface is stationary, $v_i = v_n = 0$. Furthermore, by denoting a dot product of the radiation vector $\hat{r}$ with any quantity by subscript r, the FW-H equation becomes

$$\begin{aligned} 4\pi p'(\mathbf{x}, t) = &\frac{1}{c_0}\frac{\partial}{\partial t}\int_{f=0}\left[\frac{c_0\rho_0 U_n + L_r}{r|1 - M_r|}\right]_{ret}\mathrm{d}S + \int_{f=0}\left[\frac{L_r}{r^2|1 - M_r|}\right]_{ret}\mathrm{d}S \\ &+ p'_Q(\mathbf{y}, \tau)|_{ret}. \end{aligned} \tag{B.14}$$

In order to arrive at Frassat 1A formulation used in this project the following identity must be used in order to bring the time derivative in Eq. (B.14) into the integral

$$\begin{aligned} \left.\frac{\partial}{\partial t}\right|_{\mathbf{x}} = &\left(\frac{1}{1 - M_r}\left.\frac{\partial}{\partial \tau}\right|_{\mathbf{x}}\right)_{ret} \\ &+ p'_Q(\mathbf{y}, \tau)|_{ret}, \end{aligned} \tag{B.15}$$

where the $|_{\mathbf{x}}$ denotes the receiver position as fixed during the integration. Applying this to Eq. (B.14) and noting that for a stationary surface and receiver $M_r = 0$, $\dot{n}_i = 0$, and $\dot{r}_i = 0$,

$$4\pi p'(\mathbf{x}, t) = \int_{f=0}\left[\frac{\rho_0\dot{U}_n}{r}\right]_{ret}\mathrm{d}S + \frac{1}{c_0}\int_{f=0}\left[\frac{\dot{L}_r}{r}\right]_{ret}\mathrm{d}S + \int_{f=0}\left[\frac{L_r}{r^2}\right]_{ret}\mathrm{d}S, \tag{B.16}$$

which is identical to Equation (5.12).

References

[1] Ait Bouziad, Y. (2005). *Physical Modelling of Leading Edge Cavitation: Computational Methodologies and Application To Hydraulic Machinery.* PhD thesis, Ecole Polytechnique Federale de Lausanne.

[2] Aktas, B., Atlar, M., Turkmen, S., Korkut, E., and Fitzsimmons, P. (2016a). Systematic cavitation tunnel tests of a Propeller in uniform and inclined flow conditions as part of a round robin test campaign. *Ocean Engineering*, 120:136–151.

[3] Aktas, B., Atlar, M., Turkmen, S., Shi, W., Sampson, R., Korkut, E., and Fitzsimmons, P. (2016b). Propeller cavitation noise investigations of a research vessel using medium size cavitation tunnel tests and full-scale trials. *Ocean Engineering*, 120:122–135.

[4] Aktas, B., Turkmen, S., Sampson, R., Shi, W., Fitzsimmons, P., Korkut, E., and Atlar, M. (2015). Underwater radiated noise investigations of cavitating propellers using medium size cavitation tunnel tests and full-scale trials. In *Fourth International Symposium on Marine Propulsors (SMP)*, Austin, Texas, USA, June.

[5] Arndt, R. E., Song, C., Kjeldsen, M., He, J., and Keller, A. (2000). Instability of Partial Cavitation: A Numerical/Experimental Approach. In *Twenty-Third Symposium on Naval Hydrodynamics*, Val de Reuil, France.

[6] Astolfi, J. A., Leroux, J.-B., Dorange, P., Billard, J.-Y., Deniset, F., and de La Fuente, S. (2000). An Experimental Investigation of Cavitation Inception and Development on a Two-Dimensional Hydrofoil. *Journal of ship research*, 44(4):259–269.

[7] Bailly, C. and Juvé, D. (1999). A stochastic approach to compute subsonic noise using linearized Euler's equations. *5th AIAA/CEAS Aeroacoustic Conference and Exhibit*, (c):496–506.

[8] Bardina, J. E., Ferziger, J. H., and Reynolds, W. C. (1980). No Title. In *AIAA Fluid and Plasma Dynamics Conference*, 14-16 July, Snowmass, USA.

[9] Benjamin, T. B. and Elis, A. T. (1996). The collapse of cavitation bubbles and the pressures thereby produced against solid boundaries. *Philosophical Transactions of the Royal Society of London*, 260(1110):221–240.

[10] Bensow, R. and Liefvendahl, M. (2008). Implicit and explicit subgrid modeling in les applied to a marine propeller. In *38th Fluid Dynamics Conference and Exhibit*, pages 1–12, 23 - 26 June, Seattle, Washington, USA.

[11] Bensow, R. (2011a). Simulation of the unsteady cavitation on the the Delft Twist11 foil using RANS, DES and LES. In *2nd International Symposium on Marine Propulsors, June*, Hamburg, Germany.

[12] Bensow, R. E., Bark, G., and Lu, N. (2012). Hydrodynamic Mechanisms in Cavitation Erosion. In *International Symposium on Cavitation*, number 148, pages 1–6, Singapore.

[13] Bensow, R. E. and Bark, G. (2010a). Implicit LES predictions of the cavitating flow on a propeller. *Journal of fluids engineering*, 132(4).

[14] Bensow, R. E. and Bark, G. (2010b). Simulating cavitating flows with LES in OpenFOAM. In *European Conference on Computational Fluid Dynamics*, number June, pages 14–17, Lisbon, Portugal.

[15] Bensow, R. E. and Liefvendahl, M. (2016). An acoustic analogy and scale-resolving flow simulation methodology for the prediction of propeller radiated noise. In *31st Symposium on Naval Hydrodynamics*, Monterey, CA, USA, 11-16 September.

[16] Bensow, R. E. (2011b). Capturing Secondary Cavitation A Step Towards Numerical Assessment of Cavitation Nuisance. *Ship Technology Research*, 69(3):70–81.

[17] Bertschneider, H., Bosschers, J., Choi, G. H., Ciappi, E., Farabee, T., Kawakita, C., and Tang, D. (2014). Specialist Committee on Hydrodynamic Noise. Technical report, ITTC.

[18] Boudet, J., Grosjean, N., and Jacob, M. C. (2005). Wake-airfoil interaction as broadband noise source: a large-eddy simulation study. *Aeroacoustics*, 4(1):93 – 115.

[19] Brennen, C. (1993). Cavitation Bubble Dynamics and Noise Production. In *6th International Workshop on Multiphase Flow*, pages 3–28.

[20] Brennen, C. E., Colonius, T., and D'Auria, F. (1998). Computing shock waves in cloud cavitation. In *Third International Symposium on Cavitation*, pages 287–294, Grenoble, France.

[21] Brennen, C. E. (2009a). Bubble growth and collapse. In *Fundamentals of Multiphase Flow*, chapter 4, pages 73–96. Cambridge University Press, Cambridge, 2 edition.

[22] Brennen, C. E. (2009b). Cavitation. In *Fundamentals of Multiphase Flow*, chapter 5, pages 97–115. Cambridge University Press, Cambridge, 2 edition.

[23] Brennen, C. E. (2009c). *Fundamentals of Multiphase Flow*. Cambridge University Press, Cambridge, 2 edition.

[24] Brennen, C. E. (2009d). Introduction to multiphase flow. In *Fundamentals of Multiphase Flow*, chapter 1, pages 1–28. Cambridge University Press, Cambridge, 2 edition.

[25] Brentner, K. S. and Farassat, F. (1997). An analytical comparison of the acoustic analogy and Kirchhoff formulation for moving surfaces. In *American Helicopter Society 53rd Annual Forum*, volume 36, pages 1–17, Virginia Beach, Virginia, USA, April 29-May 1.

[26] Brentner, K. S. and Farassat, F. (2003). Modeling aerodynamically generated sound of helicopter rotors. *Progress in Aerospace Sciences*, 39(2-3):83–120.

[27] Bretschneider, H., Lydorf, U., and Johannsen, C. (2008). Experimental Investigation to Improve Numerical Modeling of Cavitation. Technical report, HSVA GmbH.

[28] Brooker, A. and Humphrey, V. (2016). Measurement of radiated underwater noise from a small research vessel in shallow water. *Ocean Engineering*, 120:182–189.

[29] Brooker, A. and Humphrey, V. F. (2014). Measurement of Radiated Underwater Noise from a Small Research Vessel in Shallow Water. In *A. Yücel Odabas Colloquium Series*, pages 47–55, 6th-7th November, Istanbul, Turkey.

[30] Brooks, T. (1984). Airfoil tip vortex formation noise. In *American Institute of Aeronautics and Astronautics and NASA, Aeroacoustics Conference*, Williamsburg, VA.

[31] Brooks, T. F., Pope, D. S., and Marcolini, M. A. (1989). *Airfoil self-noise and prediction*. NASA.

[32] Budich, B., Schmidt, S. J., and Adams, N. A. (2015). Numerical Investigation of a Cavitating Model Propeller Including Compressible Shock Wave Dynamics. In *Fourth International Symposium on Marine Propulsors (SMP)*, Austin, Texas, USA.

[33] Calcagno, G., Di Felice, F., Felli, M., Franchi, S., Pereira, F., and Salvatore, F. (2003). The INSEAN E779a Propeller Test Case: a Database For CFD Validation. In *Marnet-CFD Final Workshop*.

[34] Casper, J. and Farassat, F. (2004). Broadband trailing edge noise predictions in the time domain. *Journal of Sound and Vibration*, 271:159–176.

[35] Ceccio, S. L. and Brennen, C. E. (2006). Observations of the dynamics and acoustics of travelling bubble cavitation. *Journal of Fluid Mechanics*, 233.

[36] Chahine, G. (2004). Nuclei effects on cavitation inception and noise. In *5th Symposium on Naval Hydrodynamics*, pages 8–13, St. John's, Newfoundland and Labrador, Canada, August.

[37] Chahine, G. L. (2008). Numerical Simulation of Bubble Flow Interactions. Technical Report July, Warwick IMRC.

[38] Chapman, R. (2014). Ambient Noise in the Ocean. *Journal of Ocean Technology*, 9(1):21–26.

[39] Chen, X., Sandham, N. D., and Zhang, X. (2007). Cavity flow noise predictions. Technical Report February, Aerodynamics & Flight Mechanics Group, University of Southampton.

[40] Choi, H. and Moin, P. (2012). Grid-point requirements for large eddy simulation : Chapman s estimates revisited. *Physics of Fluids*, 24.

[41] Choi, J., Hsiao, C.-T., Chahine, G., and Ceccio, S. (2009). Growth, oscillation and collapse of vortex cavitation bubbles. *Journal of Fluid Mechanics*, 624:255.

[42] Choi, J.-K. and Chahine, G. L. (2003). Noise due to extreme bubble deformation near inception of tip vortex cavitation. In *International Symposium on Cavitation Inception*, volume 16, page 2411, Honolulu, Hawaii, USA.

[43] Crighton, D. (1975). Basic principles of aerodynamic noise generation. *Progress in Aerospace Sciences*, 16(1):31–96.

[44] Curle, N. (1955). The Influence of Solid Boundaries upon Aerodynamic Sound.

[45] Davidson, L. (2006). Transport Equations in Incompressible URANS and LES. Technical Report May, Chalmers University of Technology.

[46] de Lange, D. F. and DeBruin, G. J. (1998). Sheet cavitation and cloud cavitation, re-entrant jet and three-dimensionality. *Applied Scientific Research*, 58:91–114.

[47] Dekeling, R. (2014). Underwater Soundscapes. *Journal of Ocean Technology*, 9(1):2–10.

[48] Di Francescantonio, P. (1997). A new boundary integral formulation for the prediction of sound radiation. *Journal of Sound and Vibration*, 202(4):491–509.

[49] Dieste, M. and Gabard, G. (2010). Predicting broadband fan interaction noise using a random-vortex-particle method. In *Proceedings of 20th International Congress on Acoustics*, number 2327 August, Sydney, Australia, pages 1–10.

[50] Ducoin, A., André, J., and Sigrist, J.-f. (2012a). An experimental analysis of fluid structure interaction on a flexible hydrofoil in various flow regimes including cavitating flow. *European Journal of Mechanics B/Fluids*, 36:63–74.

[51] Ducoin, A., Huang, B., and Young, Y. L. (2012b). Numerical Modeling of Unsteady Cavitating Flows around a Stationary Hydrofoil. *International Journal of Rotating Machinery*, 2012:1–17.

[52] Ebert, E., Kleinwachter, A., Kostbade, R., and Damaschke, N. (2016). HDNC - Nuclei Size and Number Concentration Estimation with Detection Volume Correction. In *31st Symposium on Naval Hydrodynamics*, Monterey, CA, USA, 11-16 September.

[53] Eskilsson, C. and Bensow, R. E. (2011). A mesh adaptive compressible Euler model for the simulation of cavitating flow. In *V International Conference on Computational Methods in Marine Engineering - MARINE*.

[54] EU FP7 (2014a). AQUO Project.

[55] EU FP7 (2014b). SONIC Project.

[56] Ewert, R., Meinke, M., and Schroder, W. (2003). Computation of Aeroacoustic Sound Via Hybrid CFD/CAA-Methods. *Ageing Mechanisms and Control: Part A Developments in Computational Aero- and Hydro-Acoustics*, 079(October):8–11.

[57] Farassat, F. and Myers, M. K. (1987). Extension of Kirchhoff's formula to radiation from moving surfaces. Technical Report May, NASA, Hampton, VA, USA.

[58] Farassat, F. (1996a). Introduction to generalized functions with applications in aerodynamics and aeroacoustics. In *NASA-TP-3428, L-17300, NAS 1.60:3428*.

[59] Farassat, F. (1996b). The Kirchhoff formulas for moving surfaces in aeroacoustics the subsonic and supersonic cases. In *NASA-TM-110285, NAS 1.15:110285*.

[60] Farassat, F. (2007). Derivation of Formulations 1 and 1A of Farassat. *Nasa/Tm*, 214853(March):1–25.

[61] Ffowcs Williams, J. and Hawkings, D. L. (1969). Sound generation by turbulence and surfaces in arbitrary motion. *Philosophical Transactions of the Royal Society of London Series A, Mathematical and Physical Sciences*, 264(1151):321–342.

[62] Foeth, E. (2008). *The structure of three-dimensional sheet cavitation*. PhD thesis, TU Delft, The Netherlands.

[63] Foeth, E. J., Doorne, C. W. H., van Terwisga, T., and Wieneke, B. (2006). Time resolved PIV and flow visualization of 3D sheet cavitation. *Experiments in Fluids*, 40(4):503–513.

[64] Foeth, E. J. and van Terwisga, T. (2006). An attached cavity on a three-dimensional hydrofoil. In *International Symposium on Cavitation*, number September 2006, pages 1–18, Wageningen, The Netherlands.

[65] Franc, J. P. (2001). Partial Cavity Instabilities and Re-Entrant Jet. In *Fourth International Symposium on Cavitation*, number June 20-23, Pasadena, CA, USA.

[66] Fréchou, D., Dugué, C., Briançon-Marjollet, L., Fournier, P., Darquier, M., Descotte, L., and Merle, L. (2000). Marine propulsor noise investigations in the hydroacoustic water tunnel "G.T.H.". In *23rd Symposium on Naval Hydrodynamics (SNH)*, pages 262–278, Washington, DC, USA.

[67] Fujiyama, K. (2015). Numerical Simulation of Ship Hull Pressure Fluctuation Induced by Cavitation on Propeller with Capturing the Tip Vortex. In *Fourth International Symposium on Marine Propulsors (SMP)*, Austin, Texas, USA.

[68] Georgiadis, N. J., Rizzetta, D. P., and Fureby, C. (2010). Large-Eddy Simulation: Current Capabilities, Recommended Practices, and Future Research. *AIAA Journal*, 48(8):1772–1784.

[69] Germano, M., Piomelli, U., Moin, P., and Cabot, W. H. (1991). A dynamic subgridscale eddy viscosity model. *Physics of Fluids*, 3(7):1760–1765.

[70] Giret, J. C., Sengissen, A., Moreau, S., Sanjosé, M., and Jouhaud, J. C. (2012). Prediction of the sound generated by a rod-airfoil configuration using a compressible unstructured LES solver and a FW-H analogy. *18th AIAA/CEAS Aeroacoustics Conference (33rd AIAA Aeroacoustics Conference)*, pages 1–18.

[71] Godderidge, B., Tan, M. Y., Earl, C., and Turnock, S. R. (2007). Grid resolution for the simulation of sloshing using CFD. In *Numerical Towing Tank Symposium*, pages 3–8.

[72] Greschner, B., Grilliat, J., Jacob, M. C., and Thiele, F. (2010). Measurements and wall modeled LES simulation of trailing edge noise caused by a turbulent boundary layer. *International Journal of Aeroacoustics*, 9(3):329–356.

[73] Gröschel, E., Schröder, W., Renze, P., Meinke, M., and Comte, P. (2008). Noise prediction for a turbulent jet using different hybrid methods. *Computers & Fluids*, 37(4):414–426.

[74] Haigermoser, C. (2009). Application of an acoustic analogy to PIV data from rectangular cavity flows. *Experiments in Fluids*, 47(1):145–157.

[75] Hildebrand, J. (2009). Anthropogenic and natural sources of ambient noise in the ocean. *Marine Ecology Progress Series*, 395:5–20.

[76] Hilgenfeldt, S., Brenner, M. P., Grossmann, S., and Lohse, D. (1998). Analysis of RayleighPlesset dynamics for sonoluminescing bubbles. *J. Fluid Mech.*, 365:171–204.

[77] Hirschberg, A. and Rienstra, S. W. (2004). *An introduction to aeroacoustics*. Eindhoven University of Technology, Eindhoven, The Netherlands.

[78] Hoekstra, M., van Terwisga, T., and Foeth, E. J. (2011). SMP11 Workshop - Case 1: DelftFoil. In *Second International Symposium on Marine Propulsors*, Hamburg, Germany.

[79] Howe, M. (1998). *Acoustics of fluid-structure interactions*. Cambridge University Press, Cambridge.

[80] Hsiao, C., Ma, J., Chahine, G. L., Ynaflow, D., and Nc, I. (2014). Multi-Scale Two-Phase Flow Modeling of Sheet and Cloud Cavitation. In *30th Symposium on Naval Hydrodynamics*, Hobart, Tasmania, Australia, 2-7 November.

[81] Hsiao, C.-t. and Chahine, G. (2012). Effect of a propeller and gas diffusion on bubble nuclei distribution in a liquid. *Journal of Hydrodynamics*.

[82] Hsiao, C.-T. and Chahine, G. L. (2005). Scaling of Tip Vortex Cavitation Inception Noise With a Bubble Dynamics Model Accounting for Nuclei Size Distribution. *Journal of Fluids Engineering*, 127(1):55.

[83] Hsiao, C. T. and Chahine, G. L. (2008). Scaling of tip vortex cavitation inception for a marine open propeller. In *27th Symposium on Naval Hydrodynamics*, Seoul, Korea, October.

[84] Hsiao, C.-t., Jingsen, M., and Georges L., C. (2015). Simulation of Sheet and Tip Vortex Cavitation on a Rotating Propeller Using a Multiscale Two-phase Flow Model. In *Fourth International Symposium on Marine Propulsors (SMP)*, Austin, Texas, USA.

[85] Hu, Z., Morfey, C. L., and Sandham, N. D. (2006). Sound radiation from a turbulent boundary layer. *Physics of Fluids*, 18(9):17–20.

[86] Huang, B., Zhao, Y., and Wang, G. (2014). Computers & Fluids Large Eddy Simulation of turbulent vortex-cavitation interactions in transient sheet / cloud cavitating flows. *Computers & Fluids*, 92:113–124.

[87] Huuva, T. (2008). *Large eddy simulation of cavitating and non-cavitating flow*. PhD thesis, Chalmers University of Technology.

[88] Ianniello, S. and Bernardis, E. D. (2015). Farassat s formulations in marine propeller hydroacoustics. *International Journal of Aeroacoustics*, 14(1 & 2):87–103.

[89] Ianniello, S., Muscari, R., and Mascio, A. (2013a). Ship underwater noise assessment by the acoustic analogy. Part I: nonlinear analysis of a marine propeller in a uniform flow. *Journal of Marine Science and Technology*, 18(4):547–570.

[90] Ianniello, S., Muscari, R., and Mascio, a. (2013b). Ship underwater noise assessment by the Acoustic Analogy part II: hydroacoustic analysis of a ship scaled model. *Journal of Marine Science and Technology*, 19(1):52–74.

[91] Ianniello, S., Muscari, R., and Mascio, A. D. (2012). Hydroacoustic characterization of a marine propeller through the acoustic analogy. *Sustainable Maritime Transportation and Exploitation of Sea Resources*, pages 991–1000.

[92] Ianniello, S., Muscari, R., and Mascio, A. D. (2013c). Ship underwater noise assessment by the acoustic analogy, part III: measurements versus numerical predictions on a full-scale ship. *Journal of Marine Science and Technology*.

[93] Ianniello, S. (2016). Hydroacoustic analysis of a marine propeller through the Ffowcs Williams-Hawkings equation. In *31st Symposium on Naval Hydrodynamics*, Monterey, CA, USA, 11-16 September.

[94] International Maritime Organization (IMO) (2014). Guidelines for the reduction of underwater noise from commercial shipping to address adverse impacts on marine life. Technical Report 7 April, London, United Kingdom.

[95] ITTC (2005). ITTC Recommended Procedures and Guidelines: Cavitation Induced Erosion on Propellers, Rudders and Appendages, Model Scale Experiments. Technical report.

[96] ITTC (2008). Specialist Committee on Cavitation Final Report and Recommendations to the 25th ITTC. *The 25th International Towing Tank Conference*, II:473–533.

[97] Jacobsen, F. and Juhl, P. (2011). Radiation of sound. Technical report.

[98] Jasak, H. (1996). *Error analysis and estimation for the finite volume method with applications to fluid flows*. PhD thesis, Imperial College London.

[99] Ji, B., Luo, X., Arndt, R. E., Peng, X., and Wu, Y. (2015). Large Eddy Simulation and theoretical investigations of the transient cavitating vortical flow structure around a NACA66 hydrofoil. *International Journal of Multiphase Flow*, 68:121–134.

[100] Ji, B., Luo, X., Peng, X., Wu, Y., and Xu, H. (2012). Numerical analysis of cavitation evolution and excited pressure fluctuation around a propeller in non-uniform wake. *International Journal of Multiphase Flow*, 43:13–21.

[101] Ji, B., Luo, X., Wu, Y., Peng, X., and Duan, Y. (2013a). Numerical analysis of unsteady cavitating turbulent flow and shedding horse-shoe vortex structure around a twisted hydrofoil. *International Journal of Multiphase Flow*, 51:33–43.

[102] Ji, B., Luo, X.-w., Peng, X.-x., and Wu, Y.-l. (2013b). Three-dimensional large eddy simulation and vorticity analysis of unsteady cavitating flow around a twisted hydrofoil. *Journal of Hydrodynamics, Ser. B*, 25(4):510–519.

[103] Jones, L., Sandberg, R., and Sandham, N. (2008). Direct numerical simulations of forced and unforced separation bubbles on an airfoil at incidence. 602:175–207.

[104] Kanfoudi, H., Lamloumi, H., and Zgolli, R. (2012). Numerical Investigation for Steady and Unsteady Cavitating Flows. In *Advances in Modeling of Fluid Dynamics*, chapter Chapter 4, pages 87–96.

[105] Kastengren, A. L., Swantek, A. B., Sovis, N., Fezzaa, K., Neroorkar, K., Moulai, M., Powell, C. F., and Schmidt, D. P. (2014). Comparing Simulations and X-ray Measurements of a Cavitating Nozzle. In *ILASS-Americas 26th Annual Conference on Liquid Atomization and Spray Systems*, number May, Portland, OR, USA.

[106] Kellet, P., Turan, O., and Incecik, A. (2014). Underwater Noise and Marine Wildlife: Current and Future Implication and Assessment. In *A. Yücel Odaba Colloquium Series*, pages 63–69, 6th-7th November, Istanbul, Turkey.

[107] Kirsteins, I., Clark, P., and Atlas, L. (2011). Maximum-likelihood estimation of propeller noise modulation characteristics. In *Proc. Underwater Acoustic Measurements*.

[108] Kolmogorov, a. N. (1941). The local structure of turbulence in incompressible viscous fluid for very large Reynolds numbers.

[109] Kolmogorov, a. N. (1962). A refinement of previous hypotheses concerning the local structure of turbulence in a viscous incompressible fluid at high Reynolds number. *Journal of Fluid Mechanics*, 13(01):82.

[110] Koop, A. H. (2008). *Numerical simulation of unsteady three-dimensional sheet cavitation*. PhD thesis, University of Twente, Enschede, The Netherlands.

[111] Kubota, A., Kato, H., and Yamaguchi, H. (1992). A new modelling of cavitating flows: a numerical study of unsteady cavitation on a hydrofoil section. *Journal of Fluid Mechanics*, 240:59.

[112] Kunz, R. F., Boger, D. A., Stinebring, D. R., Chyczewski, S., Lindau, J. W., Gibeling, H. J., Venkateswaran, S., and Govindan, T. R. (2000). A preconditioned Navier - Stokes method for two-phase flows with application to cavitation prediction. *Computers & Fluids*, 29:849–875.

[113] Leaper, R., Renilson, M., and Ryan, C. (2014). Reducing underwater noise from large commercial ships: current status and future directions. *Journal of Ocean Technology*, 9(1):65–83.

[114] Leighton, T. G., Turangan, C. K., Jamaluddin, a. R., Ball, G. J., and White, P. R. (2012). Prediction of far-field acoustic emissions from cavitation clouds during shock wave lithotripsy for development of a clinical device. *Proceedings of the Royal Society A: Mathematical, Physical and Engineering Sciences*, 469(2150).

[115] Leighton, T. G. and Walton, a. J. (1987). An experimental study of the sound emitted from gas bubbles in a liquid. *European Journal of Physics*, 8(2):98–104.

[116] Leroux, J.-b., Astolfi, J. a., and Billard, J.-Y. (2004). An Experimental Study of Unsteady Partial Cavitation. *Transactions of ASME*, 126(January):94–101.

[117] Leroux, J.-b., Coutier-delgosha, O., and Astolfi, J. A. (2005). A joint experimental and numerical study of mechanisms associated to instability of partial cavitation on two-dimensional hydrofoil. *Physics of Fluids*, 17(5):1–20.

[118] Lidtke, A., Lakshmynarayanana, A., Camilleri, J., Banks, J., Phillips, A., Turnock, S., and Badoe, C. (2015a). RANS computations of flow around a bulk carrier with energy saving device. In *Tokyo 2015 Workshop on CFD in Ship Hydrodynamics*, December 2-4, NMRI, Tokyo, Japan.

[119] Lidtke, A. K., Humphrey, V. F., and Turnock, S. R. (2016a). Feasibility study into a computational approach for marine propeller noise and cavitation modelling. *Ocean Engineering*, 120(1 July):152–159.

[120] Lidtke, A. K., Turnock, S. R., and Humphrey, V. F. (2014a). Outlook on Marine Propeller Noise and Cavitation Modelling. In *A. Yücel Odaba Colloquium Series*, number November, 6th-7th November, Istanbul, Turkey.

[121] Lidtke, A. K., Turnock, S. R., and Humphrey, V. F. (2014b). The influence of turbulence modelling techniques on the predicted cavitation behaviour on a NACA0009 foil. In *Numerical Towing Tank Symposium (NuTTS)*, Marstrand, Sweden.

[122] Lidtke, A. K., Turnock, S. R., and Humphrey, V. F. (2015b). Use of Acoustic Analogy for Marine Propeller Noise Characterisation. In *Fourth International Symposium on Marine Propulsors (SMP)*, Austin, Texas, USA.

[123] Lidtke, A. K., Turnock, S. R., and Humphrey, V. F. (2015c). Use of Acoustic Analogy for Marine Propeller Noise Characterisation. In *Fourth International Symposium on Marine Propulsors (SMP)*, Austin, Texas, USA.

[124] Lidtke, A. K., Turnock, S. R., and Humphrey, V. F. (2016b). Characterisation of sheet cavity noise of a hydrofoil using the Ffowcs Williams-Hawkings acoustic analogy. *Computers & Fluids*, 130:8–23.

[125] Lidtke, A. K., Turnock, S. R., and Humphrey, V. F. (2016c). Multi-Scale Modelling of Cavitation-Induced Pressure Around the Delft Twist 11 Hydrofoil. In *31st Symposium on Naval Hydrodynamics*, Monterey, CA, USA.

[126] Lidtke, A. K., Turnock, S. R., and Humphrey, V. F. (2016d). Saving ocean sound scapes. *The Naval Architect*.

[127] Lighthill, M. J. (1952). On Sound Generated Aerodynamically. I. General Theory. *Proceedings of the Royal Society A: Mathematical, Physical and Engineering Sciences*, 211(1107):564–587.

[128] Lighthill, M. J. (1954). On Sound Generated Aerodynamically. II. Turbulence as a Source of Sound. *Proceedings of the Royal Society A: Mathematical, Physical and Engineering Sciences*, 222(1148):1–32.

[129] Lilly, D. K. (1992). A proposed modification of the German0 closure method. *Physics of Fluids A: Fluid Dynamics*, 4(3):633–635.

[130] Liu, D.-M., Liu, S.-H., Wu, Y.-L., and Xu, H.-Y. (2009). LES numerical simulation of cavitation Bubble shedding on ALE 25 and ALE 15 hydrofoils. *Journal of Hydrodynamics, Ser. B*, 21(6):807–813.

[131] Liuzzi, D. (2012). *Two-Phase Cavitation Modelling.* PhD thesis, University of Rome.

[132] Lloyd, T., Rijpkema, D., and Wijngaarden, E. V. (2015a). Marine propeller acoustic modelling : comparing CFD results with an acoustic analogy method. In *Fourth International Symposium on Marine Propulsors (SMP)*, May-June, Austin, Texas, USA.

[133] Lloyd, T. P., Lidtke, A. K., Rijpkema, D., Van Wijngaarden, E., Turnock, S. R., and Humphrey, V. F. (2015b). Using the FW-H equation for hydroacoustics of propellers. In *Numerical Towing Tank Symposium (NuTTS)*, Cortona, Italy.

[134] Lloyd, T. P., Rijpkema, D., and Van Wijngaarden, E. (2014). Implementing the Ffowcs Williams-Hawkings acoustic analogy into a viscous CFD solver. In *17th Numerical Towing Tank Symposium (NuTTS)*, 28-30th September, Marstrand, Sweden.

[135] Lloyd, T. P., Vaz, G., Rijpkema, D., and Schuiling, B. (2015c). The Potsdam Propeller Test Case in oblique flow : prediction of propeller performance , cavitation patterns and pressure ... propeller performance , cavitation patterns and pressure pulses. In *Second International Workshop on Cavitating Propeller Performance*, number July, Austin, Texas, 4th June 2015.

[136] Lloyd, T. P. (2013). *Large eddy simulations of inflow turbulence noise: application to tidal turbines.* PhD thesis, University of Southampton.

[137] Lloyd, T. P. (2014). *Private communication.*

[138] Lu, N.-x., Bensow, R. E., and Bark, G. (2010). LES of unsteady cavitation on the delft twisted foil. *Journal of Hydrodynamics, Ser. B*, 22(5):784–791.

[139] Lu, N.-x. (2013). *Modelling Cavitation Mechanisms Using Large Eddy Simulation.* PhD thesis, Chalmers University of Technology.

[140] Luebke, L. and Barkmann, U. (2015). 2nd International Workshop on Cavitating Propeller Perfomance. Technical report, Austin, Texas, USA.

[141] Lurton, X. and Leviandier, L. (2010). Underwater acoustic wave propagation. In *An introduction to underwater acoustics: principles and applications*, chapter 2. Praxis Publishing, Chichester, 2 edition.

[142] Lyrintzis, A. S. (2002). Surface Integral Methods in Computational Aeroacoustics - From the CFD Near-Field to the Acoustic Far-Field. In *CEAS Workshop "From CFD to CAA"*, pages 1–53, Athens, Greece.

[143] Matusiak, J. (1992). *Pressure and noise induced by a cavitating marine screw propeller*. PhD thesis, Helsinki University of Technology.

[144] Mckenna, M. F., Ross, D., Wiggins, S. M., and Hildebrand, J. A. (2012). Underwater radiated noise from modern commercial ships. *J. Acoust. Soc. Am.*, 131(1):92–103.

[145] Ménard, T., Tanguy, S., and Berlemont, A. (2007). Coupling level set/VOF/ghost fluid methods: Validation and application to 3D simulation of the primary break-up of a liquid jet. *International Journal of Multiphase Flow*, 33(5):510–524.

[146] Menter, F. (1994). Two-equation eddy-viscosity turbulence models for engineering applications. *AIAA Journal*, 32(8):1598–1605.

[147] Menter, F. R., Kuntz, M., and Langtry, R. (2003). Ten Years of Industrial Experience with the SST Turbulence Model. In Hanjalic, K., Nagano, Y., and Tummers, M., editors, *Turbulence, Heat and Mass Transfer 4*, pages 625 – 632, Antalya, Turkey, 12-17 October. Begell House, Inc.

[148] Murthy, J. Y. (2002). Numerical Methods in Heat , Mass and Momentum Transfer. *Lecture*, pages 1–196.

[149] National Maritime Research Institute (NMRI) (2015). Tokyo 2015 - A Workshop on CFD in Ship Hydrodynamics. Technical report, Tokyo, Japan, December 2-4.

[150] Negrato, C., Lloyd, T. P., van Terwisga, T., and Bensow, R. E. (2016). Influence of grid setup on the prediction of hydrofoil cavitation. In *Numerical Towing Tank Symposium (NuTTS)*, number 3-4 October, St Pierre d'Oleron, France.

[151] Niedzwiedzka, A., Schnerr, G. H., and Sobieski, W. (2016). Review of numerical models of cavitating flows with the use of the homogeneous approach. *Archives of Thermodynamics*, 37(2):71–88.

[152] Nitzkorski, Z. and Mahesh, K. (2016). Computational Noise Prediction from Trailing Edge Flows. In *31st Symposium on Naval Hydrodynamics*, Monterey, CA, USA, 11-16 September.

[153] Nordin, N. P. A. (2001). *Complex chemistry modelling of diesel spray combustion*. PhD thesis, Chalmers University of Technology.

[154] Ohl, C.-D., Kurz, T., Geisler, R., Lindau, O., and Lauterborn, W. (1999). Bubble dynamics, shock waves and sonoluminescence. *Philosophical Transactions of the Royal Society A: Mathematical, Physical and Engineering Sciences*, 357(1751):269–294.

[155] Pan, Y.-C. and Zhang, H.-X. (2013). Numerical prediction of marine propeller noise in non-uniform inflow. *China Ocean Engineering*, 27(1):33–42.

[156] Park, C., Seol, H., Kim, K., and Seong, W. (2009a). A study on propeller noise source localization in a cavitation tunnel. *Ocean Engineering*, 36(9-10):754–762.

[157] Park, K., Seol, H., Choi, W., and Lee, S. (2009b). Numerical prediction of tip vortex cavitation behavior and noise considering nuclei size and distribution. *Applied Acoustics*, 70(5):674–680.

[158] Plesset, M. S. and Prosperetti, A. (1977). Bubble dynamics and cavitation. *Annual Review of Fluid Mechanics*, 9(1):145–185.

[159] Ponkratov, D. and Caldas, A. (2015). Prediction of Cavitation Erosion by Detached Eddy Simulation (DES) and its Validation against Model and Ship Scale Results. In *Fourth International Symposium on Marine Propulsors (SMP)*, Austin, Texas, USA.

[160] Pope, S. B. (2000). *Turbulent flows*. Cambridge University Press, Cambridge.

[161] Rahier, G., Huet, M., and Prieur, J. (2015). Additional terms for the use of Ffowcs Williams and Hawkings surface integrals in turbulent flows. *Computers & Fluids*, 120:158–172.

[162] Rahier, G., Prieur, J., Vuillot, F., Lupoglazoff, N., and Biancherin, A. (2004). Investigation of integral surface formulations for acoustic post-processing of unsteady aerodynamic jet simulations. *Aerospace Science and Technology*, 8(6):453–467.

[163] Raju, R., Singh, S., Chao-tsung, H., and Georges, C. (2010). Study of pressure wave propagation in a two-phase bubbly mixture. In *ASME International Mechanical Engineering COngress & Exposition*, pages 1–36, Vancouver, British Columbia, Canada.

[164] Rayleigh, L. (1917). On the pressure developed in a liquid during the collapse of a spherical cavity. *Philosophical Magazine Series*, 34(6):94–98.

[165] Roohi, E., Zahiri, A. P., and Passandideh-Fard, M. (2013). Numerical Simulation of Cavitation around a Two-Dimensional Hydrofoil Using VOF Method and LES Turbulence Model. *Applied Mathematical Modelling*, 37(9):6469–6488.

[166] Rumpfkeil, M., Robertson, D., and Visbal, M. (2014). Comparison of Aerodynamic Noise Propagation Techniques. In *52nd Aerospace Sciences Meeti*, number January, pages 1–13, National Harbor, Maryland, USA.

[167] Russel, P. S., Giosio, D. R., Venning, J. A., Pearce, B. W., Brandner, P. A., and Ceccio, S. L. (2016). Microbubble Generation from Condensation and Turbulent Breakup of Sheet Cavitation. In *31st Symposium on Naval Hydrodynamics*, Monterey, CA, USA, 11-16 September.

[168] Sagaut, P. (2006). *Large eddy simulation for incompressible flows*. Springer-Verlag, Berlin.

[169] Salvatore, F. and Ianniello, S. (2002). Preliminary results on acoustic modelling of cavitating propellers. In *IABEM 2002, International Association for Boundary Element Methods*, UT Austin, TX, USA.

[170] Salvatore, F., Testa, C., and Greco, L. (2009). Coupled Hydrodynamics Hydroacoustics BEM Modelling of Marine Propellers Operating in a Wakefield. In *First International Symposium on Marine Propulsors*, number June, Trondheim, Norway.

[171] Salvatore, F. (2009). Propeller cavitation modelling by CFD-Results from the VIRTUE 2008 Rome workshop. In *Proc. Of 1st international Symposium on Marine Propulsors*, Trondheim, Norway.

[172] Sandberg, R. D., Jones, L. E., Sandham, N. D., and Joseph, P. F. (2009). Direct numerical simulations of tonal noise generated by laminar flow past airfoils. *Journal of Sound and Vibration*, 320(4-5):838–858.

[173] Sauer, J. and Schnerr, G. H. (2001). Development of a new cavitation model based on bubble dynamics. *Zeitschrift für Angewandte Mathematik und Mechanik*, 81:561–562.

[174] Self, R. H. (2004). Jet noise prediction using the Lighthill acoustic analogy. *Journal of Sound and Vibration*, 275(3-5):757–768.

[175] Seo, J. H. and Lele, S. K. (2009). Numerical investigation of cloud cavitaiton and cavitation noise on a hydrofoil section. In *Proceedings of the 7th International Symposium on Cavitation*, Ann Arbor, USA.

[176] Seo, J. H., Moon, Y. J., and Shin, B. R. (2008). Prediction of cavitating flow noise by direct numerical simulation. *Journal of Computational Physics*, 227(13):6511–6531.

[177] Seol, H., Suh, J.-C., and Lee, S. (2005). Development of hybrid method for the prediction of underwater propeller noise. *Journal of Sound and Vibration*, 288(1-2):345–360.

[178] Shur, M. L., Spalart, P. R., Strelets, M. K., and Travin, a. K. (2003). Towards the prediction of noise from jet engines. *International Journal of Heat and Fluid Flow*, 24(4):551–561.

[179] Shur, M. L., Spalart, P. R., and Strelets, M. K. (2009). Noise prediction for increasingly complex jets. Part II: Applications. *International Journal of Aeroacoustics*, 4(3):247–266.

[180] SIMMAN 2008 Workshop (2008). KCS Test Case.

[181] Sinayoko, S., Wright, M. C. M., and Sandberg, R. D. (2015). A generalised Ffowcs-Williams and Hawkings formulation applied to flow simulations with vortical outflow. In *22nd International Congress on Sound and Vibration*, 12-16 July, Florence, Italy.

[182] Singhal, A. K., Athavale, M. M., Li, H., and Jiang, Y. (2002). Mathematical Basis and Validation of the Full Cavitation Model. *Journal of Fluids Engineering*, 124(3):617.

[183] Spalart, P. R. and Allmaras, S. R. (1992). A one equation turbulence model for aerodinamic flows. *AIAA Journal*, 94(439).

[184] Spalart, P. R. and Shur, M. L. (2009). Variants of the Ffowcs Williams - Hawkings equation and their coupling with simulations of hot jets. *International Journal of Aeroacoustics*, 8(5):477–491.

[185] Srinivasan, V., Salazar, A., and Saito, K. (2009). Numerical simulation of cavitation dynamics using a cavitation-induced-momentum-defect (CIMD) correction approach. *Applied Mathematical Modelling*, 33(3):1529–1559.

[186] Sunil, M., Keith, T. G., and Nikolaidis, E. (2006). Numerical simulation of traveling bubble cavitation. *International Journal of Numerical Methods for Heat & Fluid Flow*, 16(4):393–416.

[187] SVA Hydrodynamic Solutions (2011). Potsdam Propeller Test Case (PPTC) 1.

[188] SVA Hydrodynamic Solutions (2015). Potsdam Propeller Test Case (PPTC) 2.

[189] Tasker, M. L., Amundin, M., Andre, M., Hawkins, A., Lang, W., and Merck, T. (2010). Marine Strategy Framework Directive - Task Group 11 Report and other forms of energy Underwater noise. Technical Report 31210.

[190] The OpenFOAM Foundation (2014). OpenFOAM.

[191] Tomar, G., Fuster, D., Zaleski, S., and Popinet, S. (2010). Multiscale simulations of primary atomization. *Computers and Fluids*, 39(10):1864–1874.

[192] Tomita, Y. and Shima, A. (1977). On the behavior of a spherical bubble and the impulse pressure in a viscous compressible liquid. *Bulletin of the JSME*, 20(149):1453–1460.

[193] Tran, T. D., Nennemann, B., Vu, T. C., and Guibault, F. (2014). Numerical simulation of unsteady sheet/cloud cavitation. In *27th IAHR Symposium on Hydraulic Machinery and Systems*, Montreal, Canada.

[194] Urik, R. J. (1984). Ambient noise in the sea, Naval Sea Systems Command Department of the Navy, Washington, DC. Technical report.

[195] Vallier, A., Revstedt, J., and Nilsson, H. (2013). A multi-scale approach for modelling cavitation on hydrofoils , implemented in OpenFOAM. In *8th International OpenFOAM Workshop*, Jeju, Korea.

[196] Vallier, A. (2013). *Simulations of cavitation-from the large vapour structures to the small bubble dynamics*. PhD thesis, Lund University.

[197] Van der Graaf, A., Ainslie, M., André, M., Brensing, K., Dalen, J., Dekeling, R., Robinson, S., Tasker, M., Thomsen, F., and Werner, S. (2012). European Marine Strategy Framework Directive Good Environmental Status (MSFD-GES). Technical Report February.

[198] Verhoeven, O. (2011). Trailing Edge Noise Simulations using IDDES in OpenFOAM. Technical report, TU Delft, The Netherlands.

[199] Wan, B., Benra, F. K., and Dohmen, H. J. (2013). Application of a new numerical solver to turbomachinery flow problems. *Proceedings of the Institution of Mechanical Engineers, Part A: Journal of Power and Energy*, 227(6):628–636.

[200] Wang, G. and Ostoja-Starzewski, M. (2007). Large eddy simulation of a sheet/cloud cavitation on a NACA0015 hydrofoil. *Applied Mathematical Modelling*, 31(3):417–447.

[201] Wang, X. and Walters, K. (2012). Computational Analysis of Marine-Propeller Performance Using Transition-Sensitive Turbulence Modeling. *Journal of Fluids Engineering*, 134(7):71107.

[202] Wikstrom, M. (2006). *Approaching Large eddy simulation of cavitating flows for marine applications*. PhD thesis, Chalmers University of Technology.

[203] Wittekind, D. and Schuster, M. (2016). Propeller cavitation noise and background noise in the sea. *Ocean Engineering*, 120:116–121.

[204] Woo Shin, K. (2010). *Cavitation simulation on marine propellers*. PhD thesis, Technical University of Denmark.

[205] Wu, X. C., Wang, Y. W., and Huang, C. G. (2016). Effect of mesh resolution on large eddy simulation of cloud cavitating flow around a three dimensional twisted hydrofoil. *European Journal of Mechanics B / Fluids*, 55:229–240.

[206] Yakubov, S., Cankurt, B., Abdel-Maksoud, M., and Rung, T. (2013). Hybrid MPI/OpenMP parallelization of an Euler-Lagrange approach to cavitation modelling. *Computers and Fluids*, 80(1):365–371.

[207] Yakubov, S., Maquil, T., and Rung, T. (2015). Experience using pressure-based CFD methods for Euler Euler simulations of cavitating flows. *Computers and Fluids*, 111:91–104.

[208] Zang, Y., Street, R. L., and Koseff, J. R. (1993). A dynamic mixed subgrid-scale model and its application to turbulent recirculating flows. *Physics of Fluids A: Fluid Dynamics*, 5(12).